NASA CR–134615
MTI 74TR29

SMALL, HIGH-SPEED BEARING TECHNOLOGY FOR CRYOGENIC TURBO-PUMPS

(NASA-CR-134615) SMALL, HIGH-SPEED BEARING TECHNOLOGY FOR CRYOGENIC TURBO-PUMPS (Mechanical Technology, Inc.) 224 p HC $7.25 CSCL 13I
N75-11349
Unclas
G3/37 02776

by

Leo W. Winn
Martin W. Eusepi
Anthony J. Smalley

MECHANICAL TECHNOLOGY INCORPORATED

Prepared for

NATIONAL AERONAUTICS AND SPACE ADMINISTRATION
Washington, D. C.

Contract NAS3–17773

C. J. Morgan, Program Manager

NOTICE

Requests for copies of this report should be referred to

National Aeronautics and Space Administration
Scientific and Technical Information Facility
P.O. Box 33
College Park, Md. 20740

1. Report No. NASA CR-134615	2. Government Accession No.	3. Recipient's Catalog No. N75-11349
4. Title and Subtitle SMALL, HIGH-SPEED BEARING TECHNOLOGY FOR CRYOGENIC TURBO-PUMPS		5. Report Date July 1974
		6. Performing Organization Code
7. Author(s) Leo W. Winn, Martin W. Eusepi and Anthony J. Smalley		8. Performing Organization Report No. MTI 74TR29
9. Performing Organization Name and Address Mechanical Technology Incorporated 968 Albany-Shaker Road Latham, New York 12110		10. Work Unit No.
		11. Contract or Grant No. NAS3-17773
12. Sponsoring Agency Name and Address National Aeronautics and Space Administration Washington, D. C. 20546		13. Type of Report and Period Covered Contractor Report
		14. Sponsoring Agency Code

15. Supplementary Notes

Project Manager - C. J. Morgan

16. Abstract

This report describes in detail the design of 20-mm bore ball bearings for cryogenic turbomachinery applications, operating up to speeds of 120,000 rpm. The report includes also a special section on the design of hybrid bearings, each hybrid bearing being composed of a ball bearing in series with a conventional pressurized fluid-film journal bearing.

In addition to the bearing design, full details are also presented on the design of a test vehicle which possesses the capability of testing the above named bearings within the given speed range under externally applied radial and axial loads.

PRICES SUBJECT TO CHANGE

17. Key Words (Suggested by Author(s))	18. Distribution Statement Unclassified - Unlimited

19. Security Classif. (of this report) Unclassified	20. Security Classif. (of this page) Unclassified	21. No. of Pages 223	22. Price* $3.00

* For sale by the National Technical Information Service, Springfield, Virginia 22151

FOREWORD

The work reported herein was performed by Mechanical Technology Incorporated within the scope of NASA-Lewis Research Center Contract No. NAS3-17773. The NASA Program Manager is Mr. C. J. Morgan. The MTI Program Manager is Mr. Leo W. Winn.

Our appreciation is extended to Dr. V. N. Constantinescu, who provided consultation in the early stages of this fluid-film bearing design work and was instrumental in identifying the important physical phenomena and the means to analyze them, to Mr. H. F. Jones for his design critique and suggestions, and Mr. A. Artiles for help extended in the thermal and rotor-dynamic analyses.

ABSTRACT

This report describes in detail the design of 20-mm bore ball bearings for cryogenic turbo-machinery applications, operating up to speeds of 120,000 rpm. The report includes also a special section on the design of hybrid bearings, each hybrid bearing being composed of a ball bearing in series with a conventional pressurized fluid-film journal bearing.

In addition to the bearing design, full details are also presented on the design of a test vehicle which possesses the capability of testing the above named bearings within the given speed range under externally applied radial and axial loads.

TABLE OF CONTENTS

TABLE OF CONTENTS (Continued)

LIST OF FIGURES

LIST OF FIGURES (Continued)

LIST OF FIGURES (Continued)

LIST OF FIGURES (Continued)

LIST OF FIGURES (Continued)

LIST OF TABLES

LIST OF TABLES (Continued)

SUMMARY

This report describes the design of a test vehicle and bearing components for testing and evaluation of bearing systems operating at high speeds in LH_2. The test program will be carried out at NASA-Lewis facilities.

Within the scope of this program, two rotor supports were considered -- one consisting exclusively of ball bearings, and the other of hybrid bearings.

The ball bearing supported rotor employs two duplex-mounted pairs of 20 mm bore bearings. The results of the ball bearing analyses indicate that a light series 20 mm bore bearing employing a complement of nine - 6.35 mm (0.250 in.) diameter balls, and Armalon or lead-alloy coated, outer ring guided cages, represents an optimized selection for this application from the standpoint of fatigue life and wear. The conditions at which these bearings are required to operate do exceed the present state-of-the-art, and no reliable quantitative estimates regarding bearing life can be made at this time.

The hybrid bearing design consists of a pair of hybrid assemblies, each of which employs a duplex-mounted ball bearing in series with a hydrostatic fluid-film journal bearing. The fluid-film bearing is located on the outer diameter of the duplex bearing housing. To minimize power loss, the ball bearing outer diameter had to be reduced, resulting in the use of an extra-light series 20 mm bore ball bearing with ten 4.76 mm (.1875 in.) diameter balls. Analyses indicate that a hybrid bearing mode of operation can be achieved over a wide range of conditions. When the bearings operate in the hybrid mode, the ball bearings should approach solid body rotation, at which point fatigue and wear life problems become minimized. The fluid-film bearings are designed to operate on a film of LH_2. Contact between the stationary and rotating elements should take place normally at start or stop only. Starts and stops will be performed primarily on the ball bearings, thus, minimizing wear in the fluid-film bearings.

The test vehicle is designed to alternately accept the two types of rotor supports. Both test systems have undergone an extensive design study which

included the following:

- Geometric Configuration Study
- Rotor Dynamics Investigation
- Thermal Analysis
- Seal Investigation
- Turbine Design
- Instrumentation
- Selection of Materials

The final tester configuration which evolved from the design analysis represents a reasonable compromise between the requirements of the tester and the limitations placed on it by physical restraints. A comprehensive discussion of the design details, together with a detailed description of each tester and its associated instrumentation, is presented.

INTRODUCTION

The objective of this program is to design and manufacture rolling-element bearings, hybrid bearings, and a test vehicle capable of operation at 120,000 rpm with controlled thrust and radial loading applied to the rotary system.

The operational requirements of the Shuttle Program impose severe conditions upon the operation of rotary shaft systems employed in the Tug's LH_2 turbo-pump engines. Most, if not all, liquid hydrogen pumps developed to date use rolling-element bearings for rotary supports. Operation of actual pumps as well as rolling-element bearing tests performed in LH_2 media have, so far, disclosed that lack of lubrication is one of the most serious problems which limit the life of the rolling-element bearing. One practical way of bearing lubrication most frequently employed, consists of the incorporation of bearing retainers made of materials known to possess good lubricating characteristics. Using this approach, the life of the rolling-element bearings has been limited mainly to the progression of wear. Bearing lives of 20 hours and above have not been uncommon in some up-to-date pump applications where the DN values did not exceed 1.8 million. The new generation of pumps, however, requires high speeds of operation (DN of 2.4 million) which exceed the limits of the present-day experience. This extension of the state-of-the-art, in turn, calls for a new developmental effort.

As an alternate to the ball bearing system, fluid-film bearings operating in liquid hydrogen on the hydrostatic or externally pressurized principle have been designed and tested (References 1, 2). The major problems encountered with these bearings fall within the area of high-speed rubs and wear at lift-off or shut-down. High-speed rubs occur as a result of excessive rotor excursions caused by sudden shock or transient operation through regimes of inherent rotor instability. The extent of wear at lift-off or shut-down depends upon the speed at which a machine is capable to develop the pressure differentials required to sustain hydrostatic (or for that matter also hydrodynamic) lubrication.

In order to by-pass the fatigue life and wear problems inherent in rolling-element bearings or journal bearings operating at cryogenic conditions, combinations of hydrostatic journal bearings and ball bearings known as hybrid bearings have been tried. The results of design studies and tests performed to date indicate that the hybrid bearings possess good potential for reduction of the major problems inherent in either the ball bearing or the hydrostatic journal bearing systems. Within the scope of this program, two approaches to the high-speed bearing design problem were undertaken, i.e., rolling-element bearings, and hybrid bearings were designed and manufactured.

In parallel with the bearing work, a test vehicle capable of accepting the contemplated bearing geometries has been designed. The test vehicle operational parameters such as thrust load range, radial load range, flow range, speed range and temperature and pressure ranges have, in most cases, been specified by NASA Program Management.

The Final Report presents the results of the rolling-element bearing design, hybrid bearing design, and the design of the test vehicles to be used in the bearing evaluation program. Principal calculations are performed in English units.

TECHNICAL DISCUSSION

A. Ball Bearing Design

One of the requirements of the design study was that the rolling-element bearing consist of an angular contact, separable, 20 mm bore ball bearing.

The angular contact ball bearing can be employed either as a singular bearing element, located at each end of the rotating shaft, or in a duplex bearing arrangement — in which case, two ball bearings are employed at each rotor support position.

The decision as to whether a singular or a duplex-mounted bearing arrangement should be used depends upon the type of the vehicle as well as upon various design details incorporated in the vehicle in which the bearings are to be used. Whereas, in most applications, singular ball bearing components preloaded so as to minimize excessive sliding of the balls are successfully used, in high-pressure turbo-machinery, the thrust and sometimes also radial loads are high enough to preclude their use. Instead, the bearings are mounted in duplex pairs. The duplex bearing design arrangement affords the opportunity of preloading one bearing against the other at each rotor support position. As a result of this type of preload, the bearings can be mounted so as to permit axial floatation of the rotor bearing system. This has its advantages inasmuch as a balance piston can be then employed to automatically balance out the axial loading during operation, thus reducing the thrust load capability requirements of the ball bearings and rendering the ball bearings less susceptible to the wear and fatigue life problems normally encountered.

Within the scope of this program, a singular and duplex bearing arrangement was designed. The singular arrangement will be employed in tests designed to establish the preload requirements for the ball bearings. Once the minimum amount of preload required to prevent excessive skidding within the ball bearing has been established, this preload will be built into the duplex bearing arrangement and a new series of tests performed utilizing the duplex bearing set-up.

Another aspect of the duplex ball bearing design is also covered in this report. This aspect pertains to the utilization of the duplex-mounted bearing pair as a component of a series hybrid bearing arrangement. The performance characteristics ofthe series hybrid bearing are discussed in Section B. The different mode of the ball bearing operation within a hybrid bearing arrangement requires angular contact ball bearings which are compatible with this mode of operation. Hence, the basic objectives of the ball bearing design became to design bearings capable of supporting the shaft at the given conditions of operation when employed independently, or in conjunction with a fluid-film bearing as is the case in the hybrid bearing arrangement.

The design process consisted of the establishment of the physical envelope limitations, selection of bearing materials, selection of the cage configuration, and an analytical optimization study. The final bearing geometries, which were arrived at as a result of the above study, were then subjected to a performance analysis. During this stage, thermal and centrifugal expansion and/or contraction was accounted for as was operation at various speeds and loads.

1. Envelope Limitations

The overall bearing dimensions, i.e., its bore diameter, outer diameter and width, as well as the ball size, have been selected from standard AFBMA sizes. The maximum speed of 120,000 rpm and bore diameter of 20mm initially specified as design goals, permit the use of either the extra-light or the light series ball bearing. The standard envelope defining a light series ball bearing, as well as that defining an extra-light bearing, is given in Table I.

TABLE I

BEARING ENVELOPE DIMENSIONS

	INNER DIAMETER mm (inches)	OUTER DIAMETER mm (inches)	WIDTH mm (inches)
LIGHT SERIES (L)	20 (.7874)	42 (1.6535)	12 (.4724)
EXTRA-LIGHT SERIES (LL)	20 (.7874)	37 (1.4567)	9 (.3543)

The envelope dimensions specified in Table I impose physical limitations upon the ball diameter and number of balls that can be utilized. The combination of the number of balls and ball diameter is limited by the available pitch circumference, by the minimum spacing between balls (from here on identified as the web thickness) required to maintain a sound cage design, and by the minimum outer and inner ring wall thickness. Utilizing a minimum cage web thickness of 3.81 mm (.150 in.) recommended by Reference 3, as a limiting factor, and a minimum of 1.575 mm (.062 in.) as a minimum wall thickness for the outer and inner rings, the permissible ball size as well as the maximum number of balls can be calculated. The results of this calculation are shown in Table 2.

TABLE 2

APPLICABLE BALL SIZE AND NUMBER OF BALLS

	PITCH CIRCUMFERENCE mm (inches)	PERMISSIBLE BALL SIZE mm (inches)	MAXIMUM BALL NUMBER mm (inches)
LIGHT SERIES (L)	97.38 (3.834)	4.76 (.1875) 5.55 (.2187) 6.35 (.25)	10 10 9
EXTRA-LIGHT SERIES (LL)	89.5 (3.5250)	4.76 (.1875)	10

2. Bearing Materials

Bearings for process fluid lubrication in systems employing LH_2 have, in the past, been made of SAE 52100 or AISI 440 C stainless steel. The 440 C stainless steel has been more frequently used, mainly because of its better corrosion resistance. The original NASA specifications call for the use of 440 C stainless steel bearings.

The fatigue life of a 440 C stainless steel bearing is a function of material cleanliness (Ref. 3) and hardness (Ref. 4). The cleanest bearing material is obtained through the consumable electrode vacuum melting technique (CEVM). Hence, the materials to be used in this application will all be produced by CEVM processes. The hardness of the material can be controlled through proper heat treatment. Bearing hardness in general, should not fall below 58 R_C. A normal, acceptable bearing material hardness range runs from 58 to 63 R_C.

Another aspect of proper material utilization involves the dimensional stability of the bearing material selected. Dimensional stability can be obtained through a stabilization process consisting of repeated cycling down to LN_2 temperatures followed by tempering. The stabilization of the 440 C stainless steel bearings for cryogenic use has been included in the overall bearing specifications.

The selection of the cage materials forms a critical part of the bearing design. The cage, in addition to serving the function of a ball separator, also acts as the main reservoir of the lubricant. The material acting as the lubricant can be either incorporated into the basic matrix of the material structure or deposited in the form of a solid film on the outer cage surfaces. Cage materials which have been tried in LH_2 applications are:

- Reinforced PTFE (Armalon, Rulon)
- Salox-M Bronze-filled PTFE
- Polyimide Bronze (60% - 40% by volume)
- Silver Polyimide Tungsten Diselenide (75% - 20% - 5% by volume)
- Reinforced Polymers of the PBI type (Polyimide reinforced with Brass)
- Silver matrix composites
- P-77 Lead alloy coated steel (87.5 Pb, 10 Sn, 2.5 Cu)

Of the above materials, Armalon performed consistently well in a number of high-speed, cryo-turbo-pump applications, (Reference 5). In recent testing performed at NASA, (Ref. 6), the lead alloy coatings on metal substrates also provided promising results. In view of the past experience, it is recommended that Armalon and P-77 coated steel cages be selected for test in the ball bearing supported rotor.

In hybrid bearing designs, the ball bearing cage is expected to operate at the full speed of rotation of 120,000 rpm. In normal ball bearing installations, the cage speed would not exceed 60,000 rpm at a shaft speed of 120,000 rpm. Because of the speed difference, the cage material used in the hybrid bearing must be capable of sustaining the high stress levels expected at these speeds. Only steel or titanium alloy cages possess this capability. Hence, in hybrid bearing applications, P-77 - coated 440 C stainless steel and/or P-77 - coated Ti - 5 Al - 2.5 Sn should be employed. Physical properties of the selected bearing materials can be found in Appendix A.

3. Cage Configuration

At present, a bearing operating above 600,000 DN is considered to be a high-speed bearing and a bearing operating above 1,000,000 DN an ultra-high-speed bearing. These lines of demarcation were arrived at by experience and usually as a result of a given cage design becoming inadequate beyond a given speed range. The question of cage adequacy gains in importance when the bearing is deprived of good lubrication and must depend upon the cage to serve as a reservoir and supply source for the lubricant. In this case, factors affecting cage guidance, cage geometry and cage materials must be given special considerations.

a. Inner Versus Outer Ring Riding Cages

Although most of the high-speed cage designs presently in use are outer riding, and considerable theoretical and practical experience indicates the desirability of such configurations, it may be of interest to describe the relative merits of inner versus outer ring riding cages, particularly in view of the controversial manner in which this problem is regarded in the industry. The following advantages and disadvantages are based upon adequate lubrication.

Applicable advantages of outer (versus inner) ring riding cages:

- Better lubrication is afforded both rolling elements and cage control surface.
- Lower relative rubbing velocity on control surface.

- Lower bearing pressure per unit area on control surface.
- Control surface contacting cooler outer ring permits easier heat removal from separator. Inner ring controlled separator is fed heat from hotter inner ring.

Disadvantages of outer (versus inner) ring riding cages:

- High mass moment of inertia and weight.
- Lower strength-to-weight ratio.
- Careful attention must be given to clearance between cage O.D. and outer ring guiding lands to avoid possibility of seizure due to different expansion rates.

Cryogenic lubrication is in a sense unique since the problems normally associated with heat are non-existent, i.e., there is normally ample cooling available to remove most of the heat generated, thus drastically reducing the problems due to high temperature. Moreover, low temperature operation with lubricant containing cages imposes also several unique problems in the choice of cage guidance. Because the coefficient of thermal expansion of self-lubricating cages is much higher than that of the bearing material, cage-to-land clearances are easier to control at a nominal value when the design is inner race riding. This is, however, counter-balanced by higher wear rates due to higher rub velocity at the inner race and enhanced possibility of cage excitation due to inner race runouts. In armoured cages, because of structural weakness encountered in the cage material, the centrifugal retention occurs at the outer diameter; hence, inner race guidance becomes mandatory.

It is a fact that most LH_2 high-speed bearing configurations employ outer race guidance, (Ref. 5, 7). Recent test results for bearings operating in LH_2 published by NASA (Ref. 6), also indicate, on the average, a higher degree of success in terms of longer lives achieved with the outer race guided cage.

b. Cage Geometry

The selection of a machined outer race guided cage eliminates, for all practical purposes, designs employing armoured cages. The machined cage has been extensively used in the NERVA LH_2 turbomachinery design (Ref. 5, 7), as well as in the NASA tests.

The machined cage, with chamfers around the ball pockets is ideally suited to accommodate the materials and lubricants, the selection of which has been discussed in the preceding sub-section.

4. Analysis

Having established the physical limitations of the bearing envelope, the pertinent ball sizes, applicable bearing materials, and cage geometry, the next step was directed toward the optimization of the bearing geometry. The optimization study was performed utilizing the Rolling-Element Bearing Computer Program available at MTI.

The variables of particular interest in the optimization study were:

- Number of Balls
- Ball Size
- Curvature Ratios
- Contact Angle

The relative soundness of the design evolving from this study was measured by the following parameters:

- Fatigue Life
- SV Values
- Maximum Stress
- Torque

A description of the above parameters is given in what follows.

Fatigue Life - The fatigue life is indicative of the statistical fatigue life of a bearing designed to operate with a 90% probability of survival. The higher the fatigue life, the greater the improvement in system reliability. The fatigue life calculations cited in this report are based on modified AFBMA procedures (Reference 8) employed in the rolling-element bearing computer program which, in the past, have proven to be extremely conservative for oil lubricated systems. There are some indications that in well lubricated oil systems, the actual fatigue life may be as high as 10 times that calculated by the AFBMA methods, but under conditions of marginal bearing lubrication, the fatigue life may turn out to be appreciably lower than that predicted by the computer program. How this life compares with that obtained in LH_2 lubricated systems is difficult to establish. Considering the uncertainties involved in fatigue life calculation, the designer must minimize the chances of failure by attempting to obtain as high a fatigue life as possible.

SV - The SV value represents the maximum product of stress times velocity of spin in the Hertzian contact zones. Experience has shown that the higher the SV value, the higher the potential for material removal through the process of wear. In the past, successful ball bearing operation in LH_2 was achieved up to SV values of 12×10^5 ($lb/in^2 \times ft/sec$* - Reference 7). Operation at higher values, to the best of the author's knowledge, has not been attempted. Considering the past experience, to render the bearing less susceptible to wear, the SV values should be maintained at as low levels as possible.

Stress - The maximum stress criterion is used in order to assure that the stress levels during operation are low enough to avoid permanent deformation. According to the criteria established in Reference 4, the maximum deformation must be maintained below 0.0001 d where "d" is the ball diameter. More recent results (Reference 9) indicate that for 440 C stainless steel, a mean contract stress below 330,000 (maximum stress of 495,000 psi) represents a safer standard of acceptability than the 0.0001 d deflection.

Torque - The value of torque enters into the system efficiency calculations. Excessive bearing torques cause high heat rejection which, in turn, requires high rates of coolant flow. Consequently, bearing torque should be maintained at as low a level as possible. The hybrid bearing arrangement presents

---

*The SV product will be from hereon used without reference to dimensions.

an exception to that rule. Here, the ball bearing acts as a clutch through which sufficient torque must be transmitted to drive the fluid-film bearing. This requires a certain minimum torque load at the ball bearing.

a. Effects of Ball Diameter Change

The study of envelope limitations resulted in the definition of an applicable ball size range. The permissible ball diameters fall within 4.76 mm (0.1875 in.) to 6.35 mm (0.25 in.). To evaluate the effect of ball size on bearing performance, the number of balls, thrust load, radial load, pitch diameter, outer race curvature and inner race curvature, as well as the contact angle have been maintained constant at the values shown in Figure 1.

Bearings with variable ball diameters have been analyzed in the Rolling Element Bearing Program at a speed of 120,000 rpm of inner race rotation. The effect of ball size on fatigue life, SV value, torque and maximum stress is plotted in Figures 1 through 4.

Within the range of ball diameters examined, the fatigue life increases with ball size, the difference between the 4.76 mm (.1875 in.) ball diameter and the 6.35 mm (.25 in.) ball diameter being about 8%. The SV value decreases with an increase in ball diameter by 21% and the maximum stress which is encountered on the outer race increases by 3%. This increase is, however, accompanied by a considerable decrease in the stress at the inner race. The maximum stress is still well below the brinelling stress limit of 3.41×10^9 N/m^2 (495,000 psi).

The increase in fatigue life accompanied by a substantial decrease in the SV values characteristic of the increased ball size, suggests that the largest possible ball size, i.e., 6.35 mm (.25 in.) should be used in order to maximize the fatigue and wear life of the bearing. The torque increase which accompanies that selection is still reasonable and the maximum stress is maintained well below the brinelling limit.

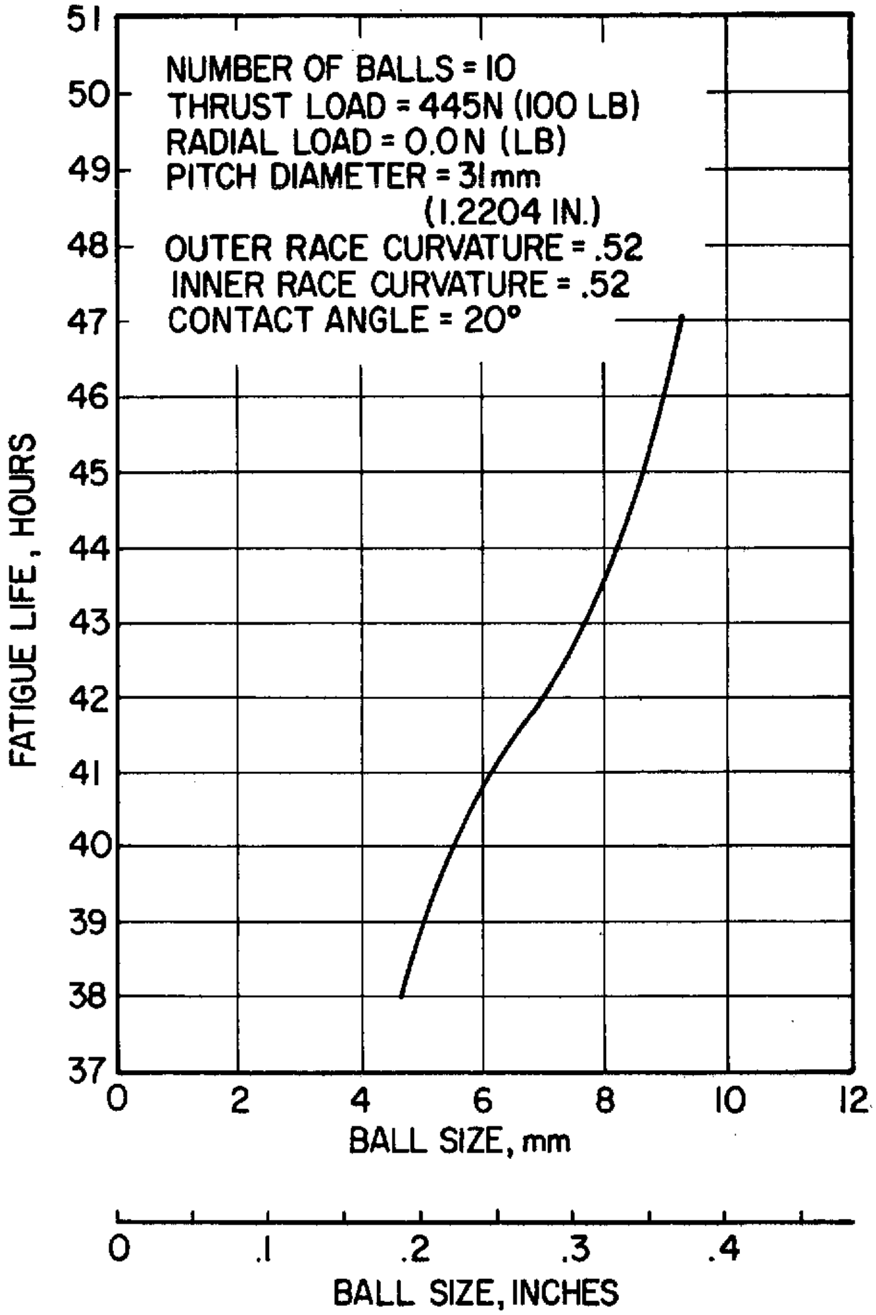

Fig. 1 Effects of Ball Diameter on Bearing Fatigue Life

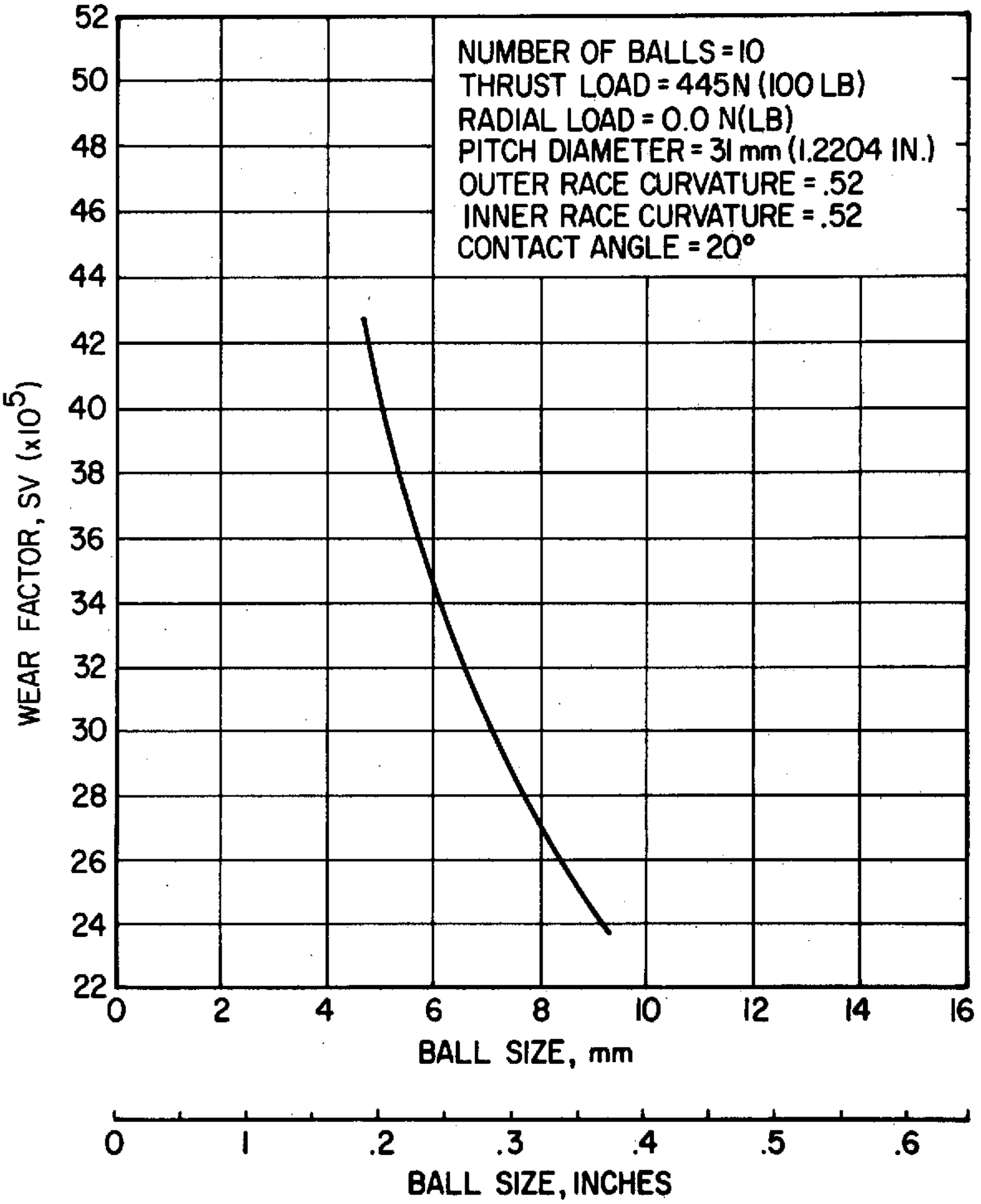

Fig. 2 Effects of Ball Diameter on Wear Factor

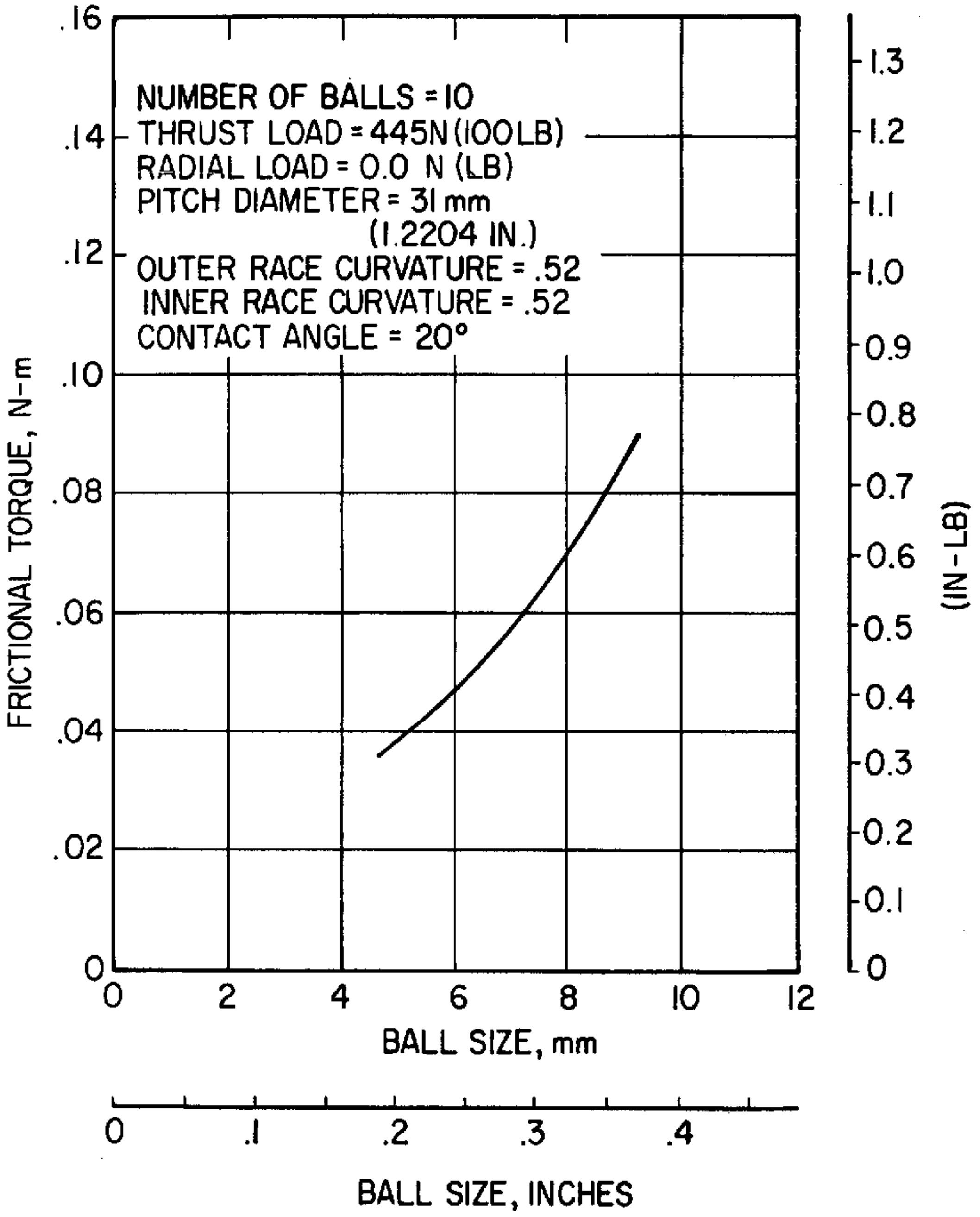

Fig. 3 Effects of Ball Size on Frictional Torque

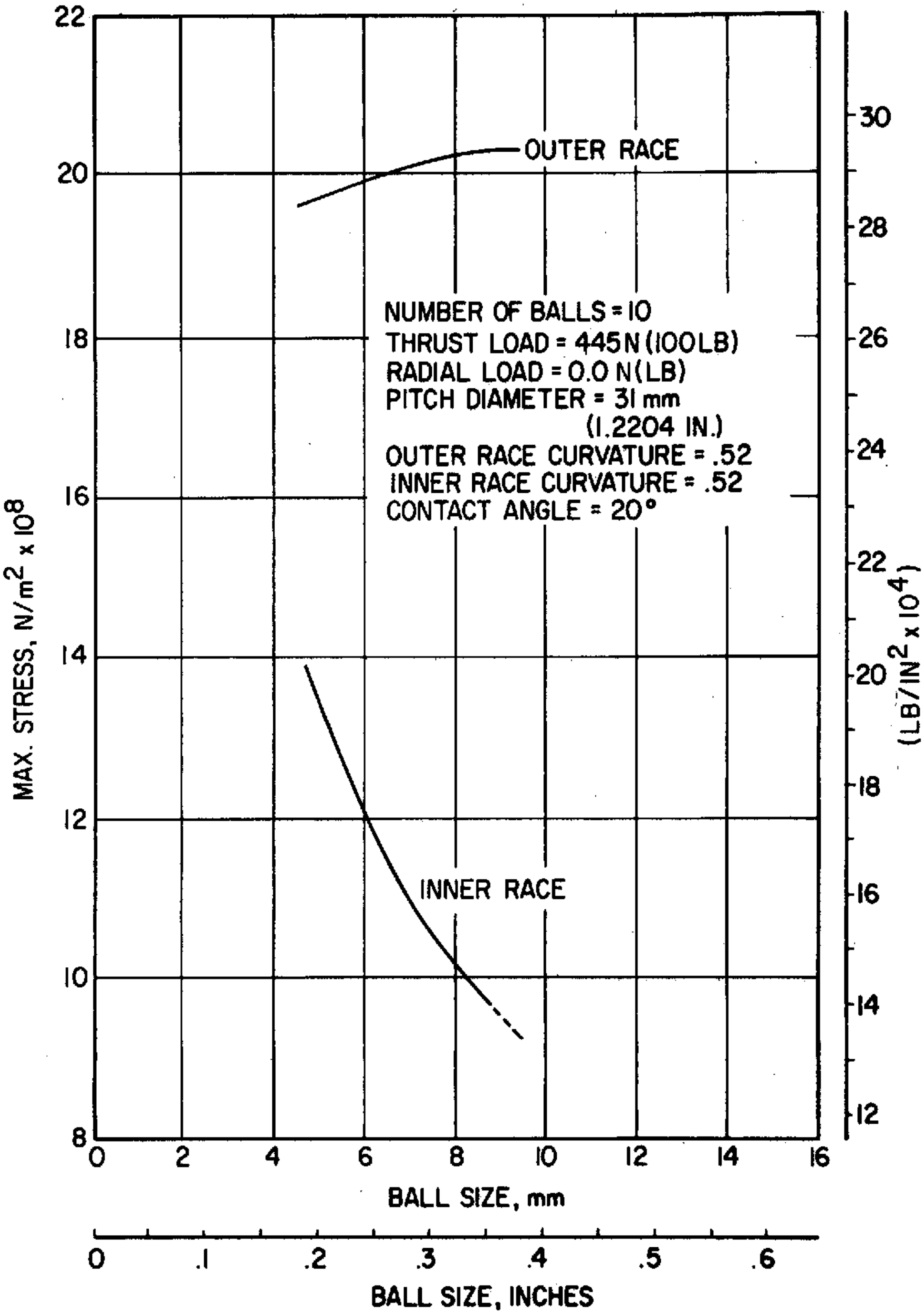

Fig. 4 Effects of Ball Diameter on Compressive Hertz Stress

b. Selection of the Number of Balls

The effect of the number of balls on the selected design criteria, is shown in Figures 5 through 8. Because of envelope and ball diameter limitations, the number of balls cannot exceed 10. Examining the differences between an 8 and 10 ball complement bearing - the bearing fatigue life decreases as the number of balls increases. This holds true for high-speed applications only, where the beneficial effects, accomplished through the reduction in the externally imposed loading per ball, are offset by the increased number of stress cycles at the races. The difference in fatigue life, between an 8 and 10 ball complement is, however, small and may be considered, for all practical purposes, negligible.

The SV value decreases as the number of balls is increased, the SV value with 10 balls being approximately 11% lower than that with 8 balls.

The effects of the number of balls, between the 8 and 10 ball complement, on torque and outer race stress, are considered negligible.

Although the reduction of the SV values indicates that the bearing wear rate could be minimized with a further increase in the number of balls, cage web thickness limitations dictate that the maximum number of balls for the extra-light series bearing be kept at 10 and that for the light series bearing at 9.

Having established the ball size and number of balls, the next factors to be evaluated are those of inner and outer race curvatures and the contact angle. These factors, in combination with the ball size, number of balls and pitch diameter, define the internal bearing geometry.

c. Race Curvature Optimization

Race curvature is defined as the ratio of the radius of curvature of the race to the ball diameter. The closer this ratio approaches 0.5, the better the conformity and the lower the Hertzian stresses. There are,

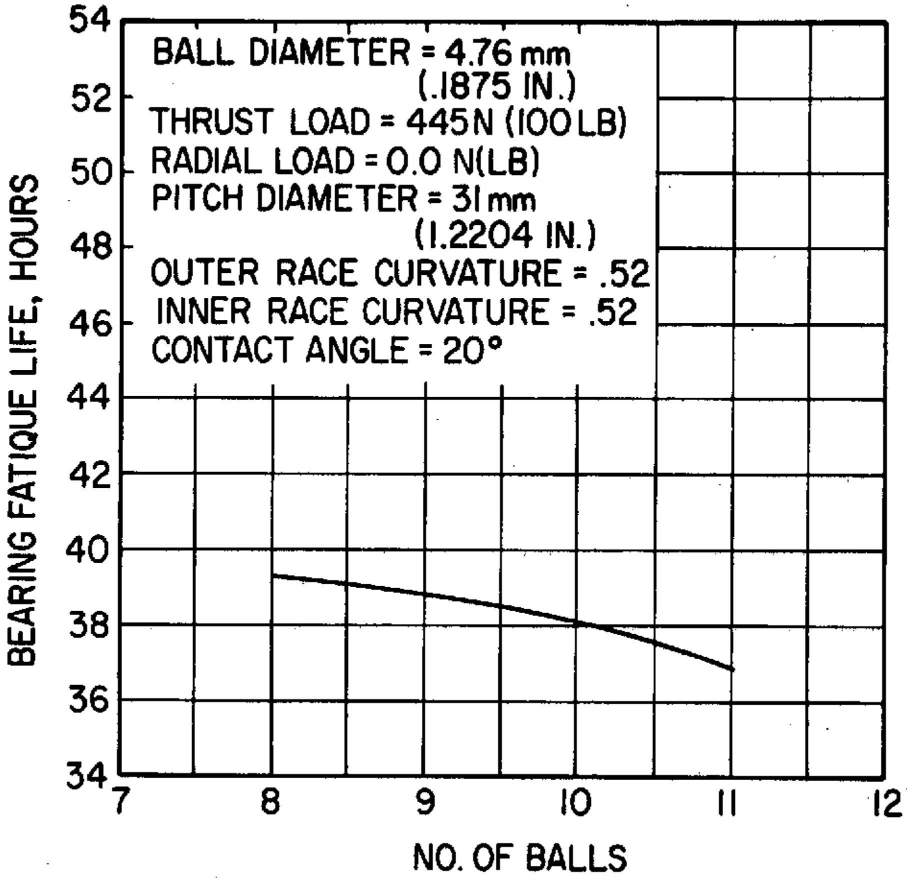

Fig. 5 Effects of Number of Balls on Fatigue Life

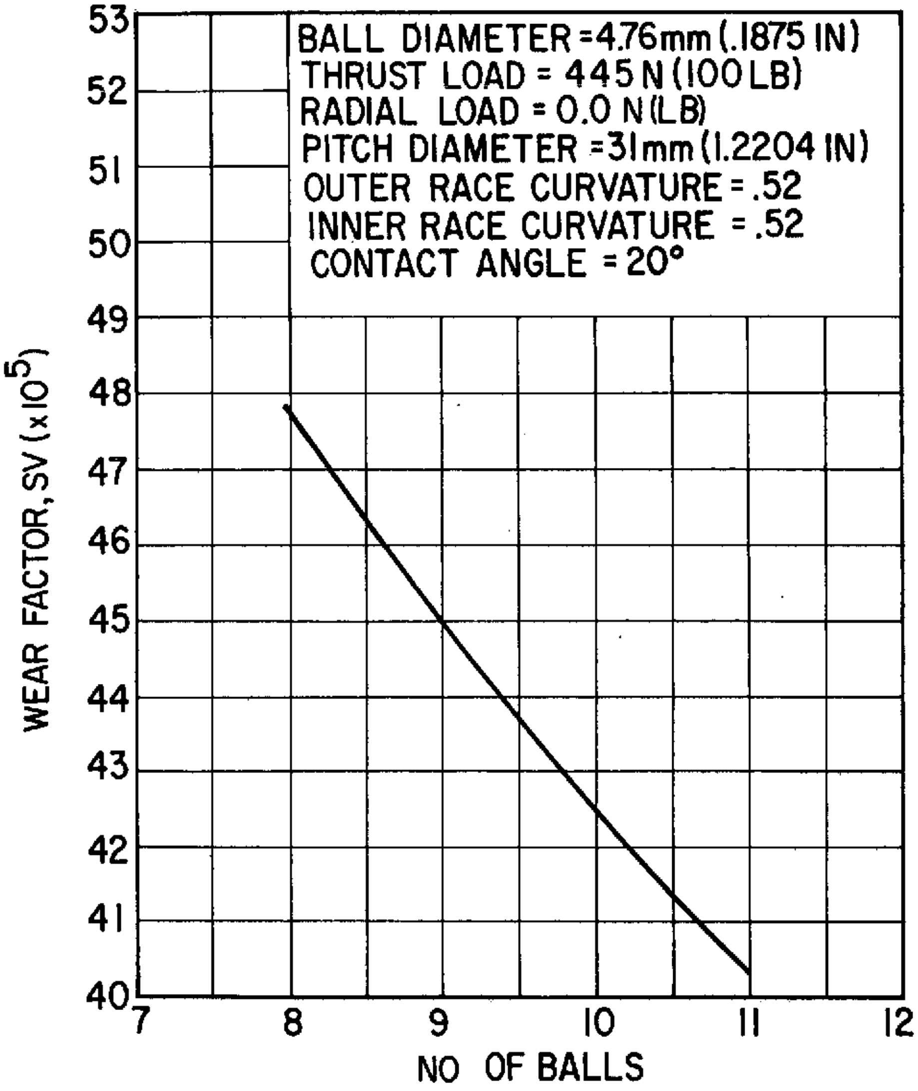

Fig. 6 Effects of Balls on Wear Factor

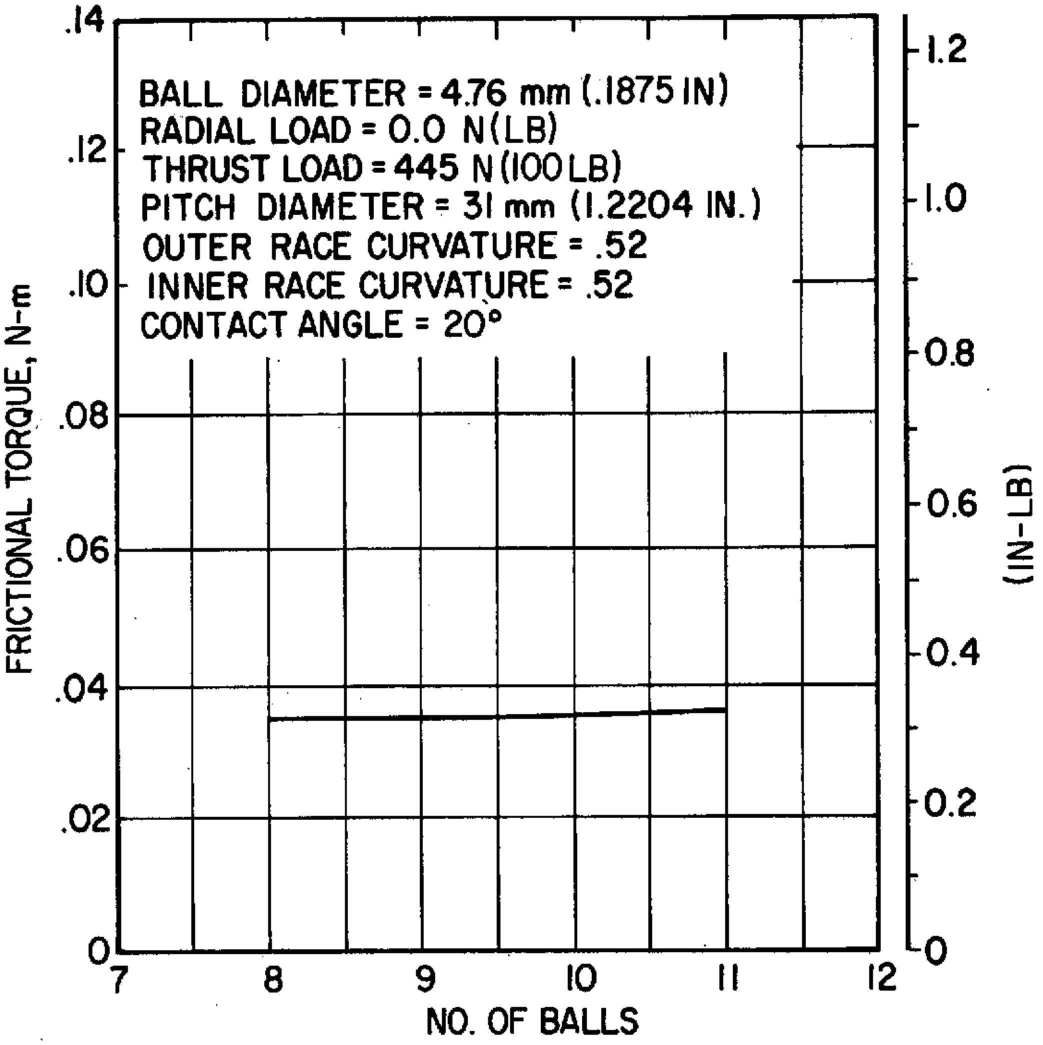

Fig. 7 Effects of Number of Balls on Torque

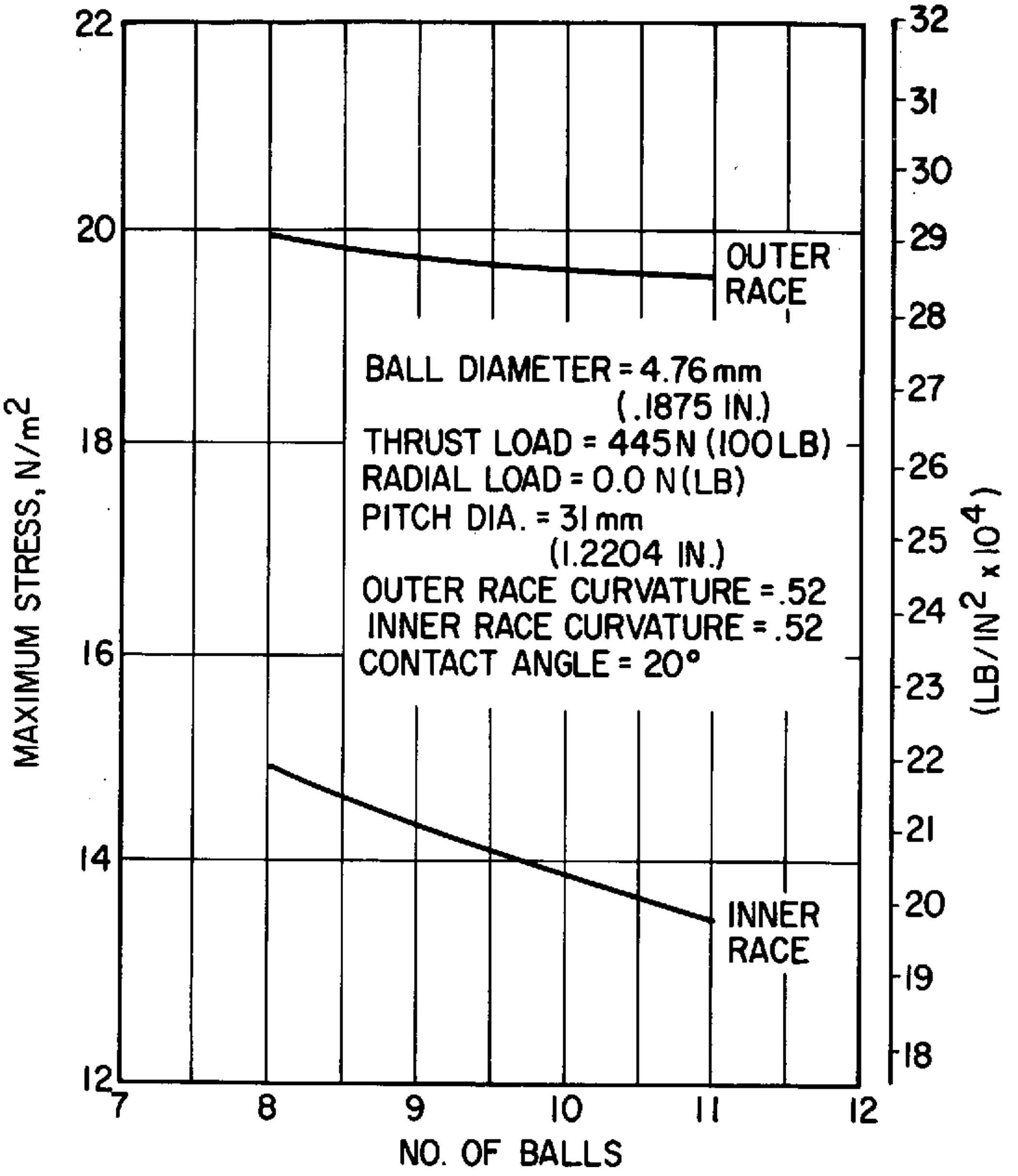

Fig. 8 Effects of Number of Balls on Compressive Hertz Stress

however, physical limitations imposed by the need to maintain a certain ball-to-race clearance and by machineability tolerance requirements which limit this ratio to a minimum of about 0.52. The fatigue life of a bearing normally decreases with an increase in the curvature ratio. Because of the low fatigue lives calculated for the 0.52 curvature ratios assumed in the preceding examples and the anticipated further decrease as the curvature ratio increases, a maximum curvature limit of 0.56 was set for the inner and outer races in the race curvature optimization calculations.

The effect of outer race curvature (f_o) and that of inner race curvature (f_i) on the performance of the bearing design parameters previously selected, is shown in Figures 9 through 12 for the 4.76 mm (0.1875 in.) diameter balls, and in Figures 13 through 16 for the 6.35 mm (.250 in.) diameter balls.

Comparing the fatigue life results presented in Figure 9 for the small size balls, and Figure 13 for the larger ball size, it is apparent that for any given outer race and inner race curvature combination (with the exception of $f_o = 0.56$ and $f_i = 0.52$) the B_{10} fatigue life of the bearing will be higher when the larger size ball is used. The fatigue life decreases at a fast rate with an increase in outer race curvature because of reduction in Hertzian contact area and high load at the outer race, due to centrifugal inertia effects. Inner race curvature effects on the fatigue life are pronounced only at 0.52 outer race curvature ratios when the smaller size balls are employed.

The trends shown in Figure 10 and 14 for the SV value variation with inner race and outer race curvatures are similar, the exception being that the SV values for the larger size balls are appreciably lower than those with the smaller size balls. In general, the SV value decreases with increase in inner race curvature. The reverse holds true for the outer race curvature. Here, however, the increase in SV with increasing outer race curvature is not very pronounced.

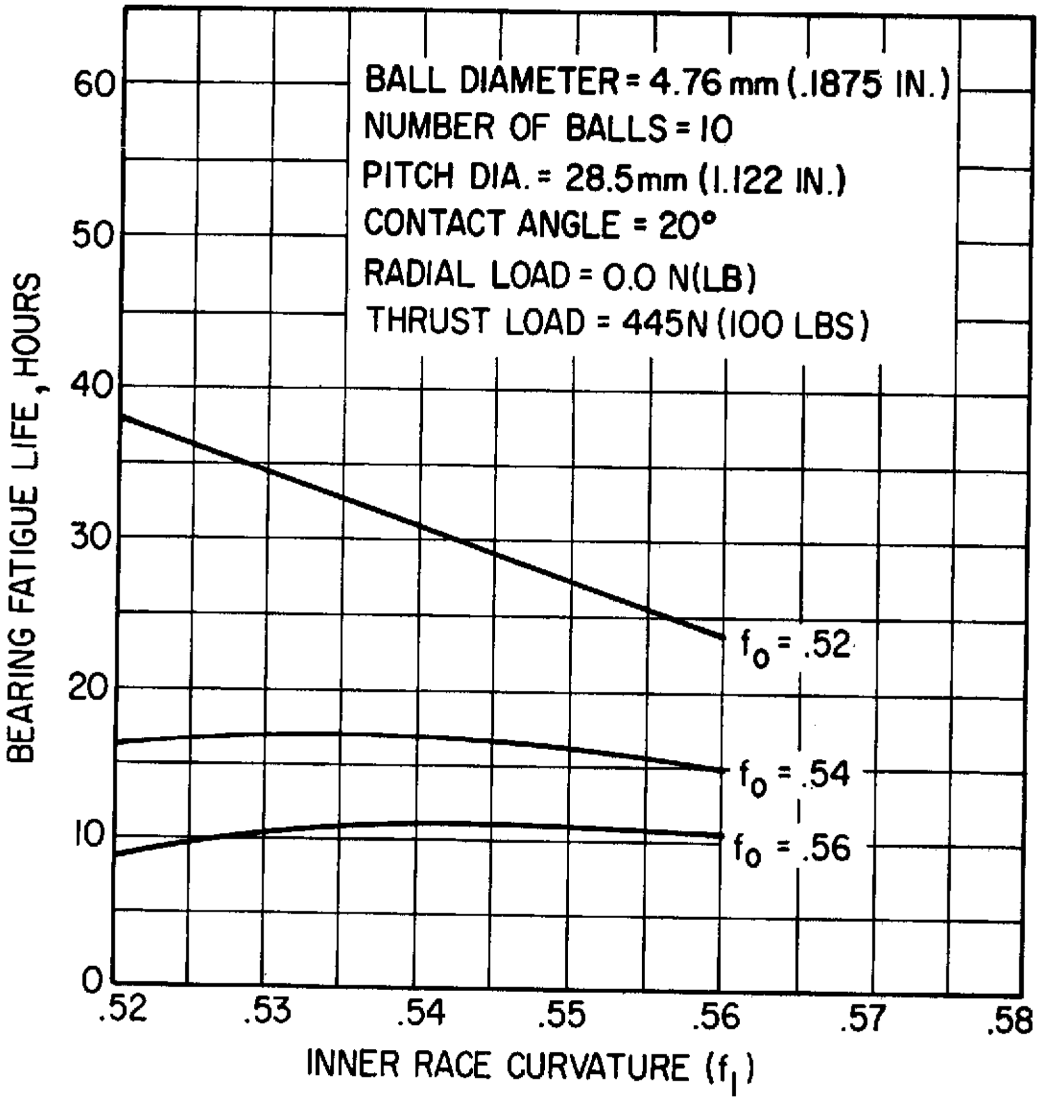

Fig. 9 Effect of Race Curvature on Bearing Fatigue Life

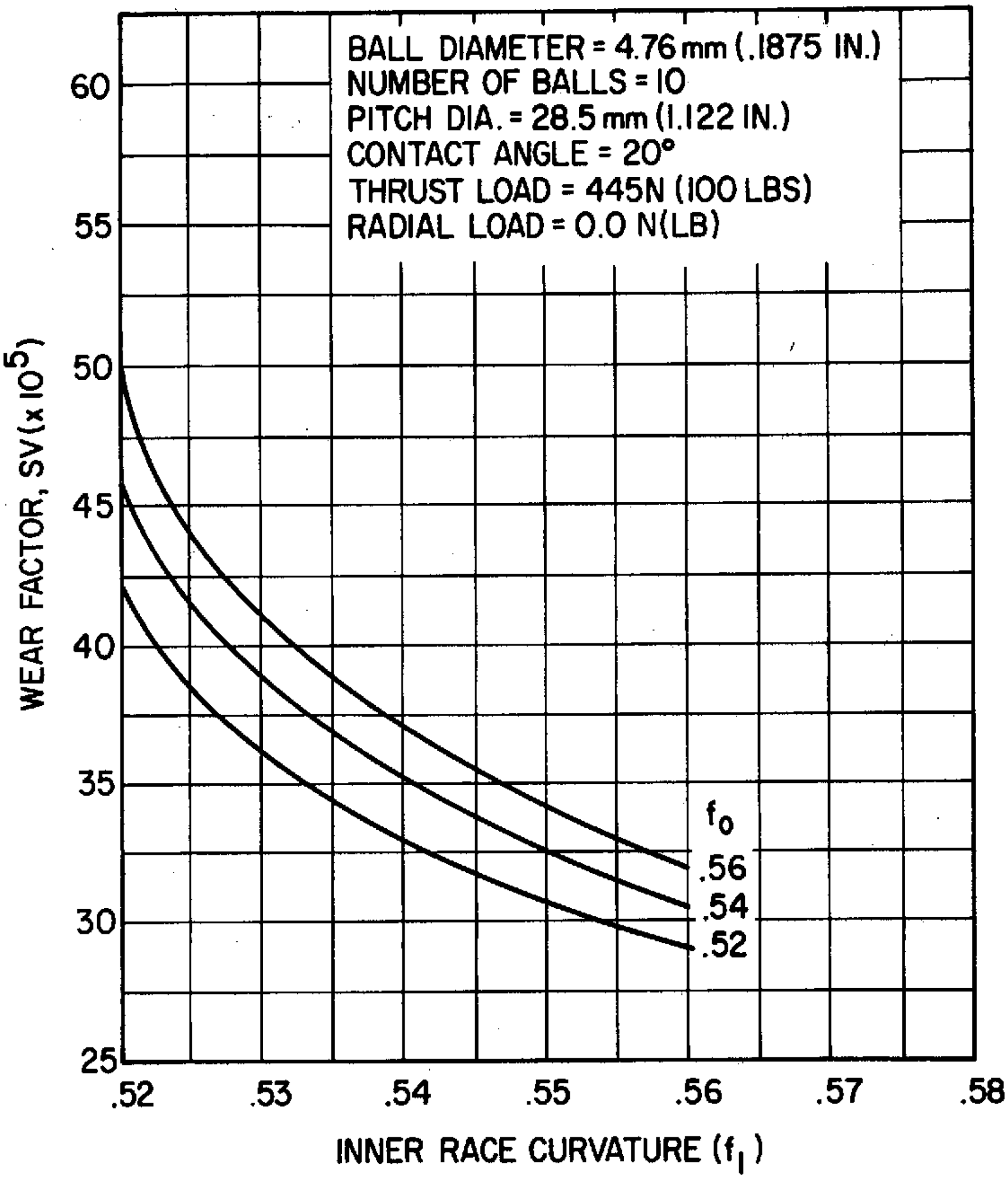

Fig. 10 Effect of Race Curvature on Wear Factor

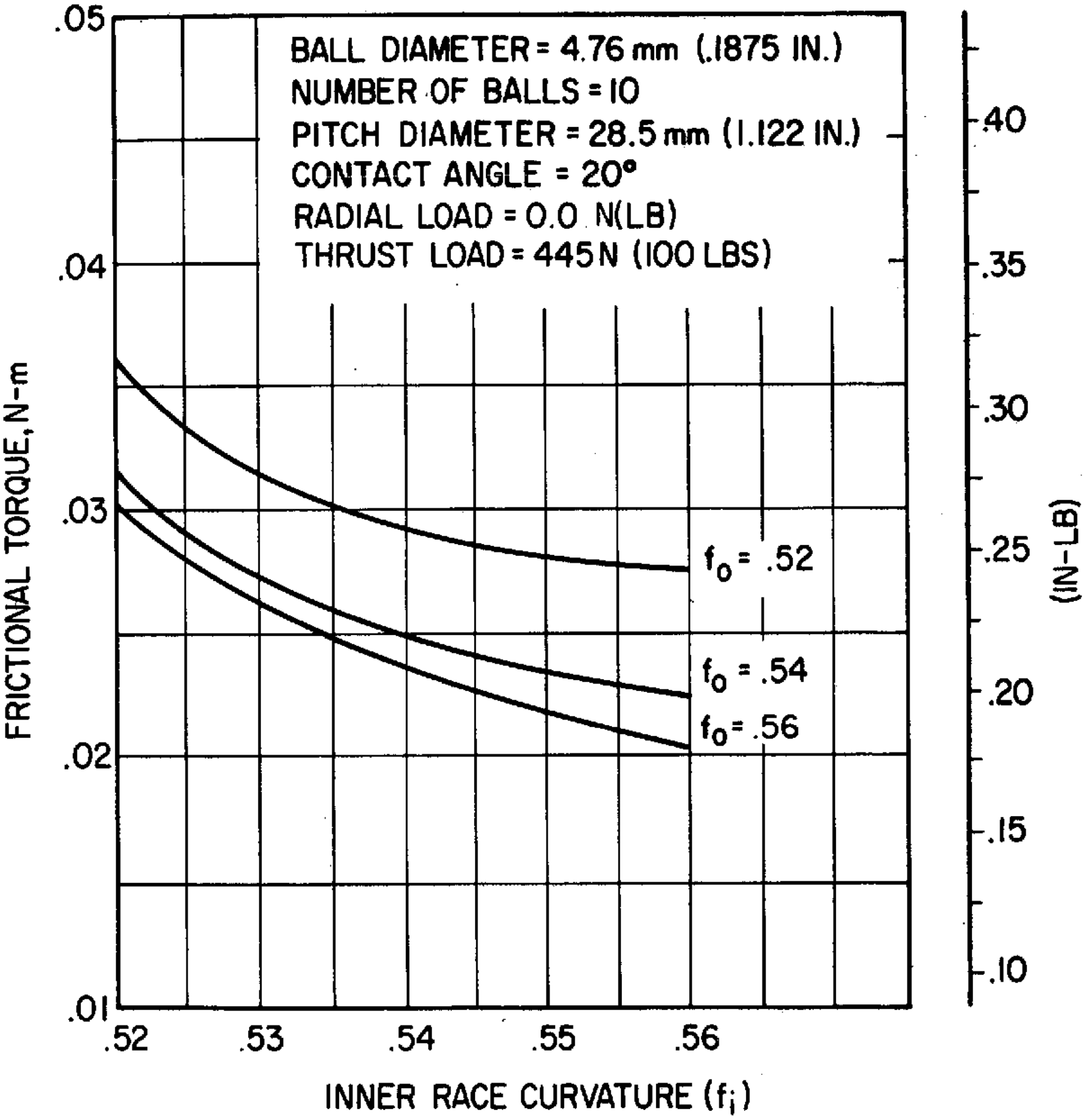

Fig. 11 Effect of Race Curvature on Frictional Torque

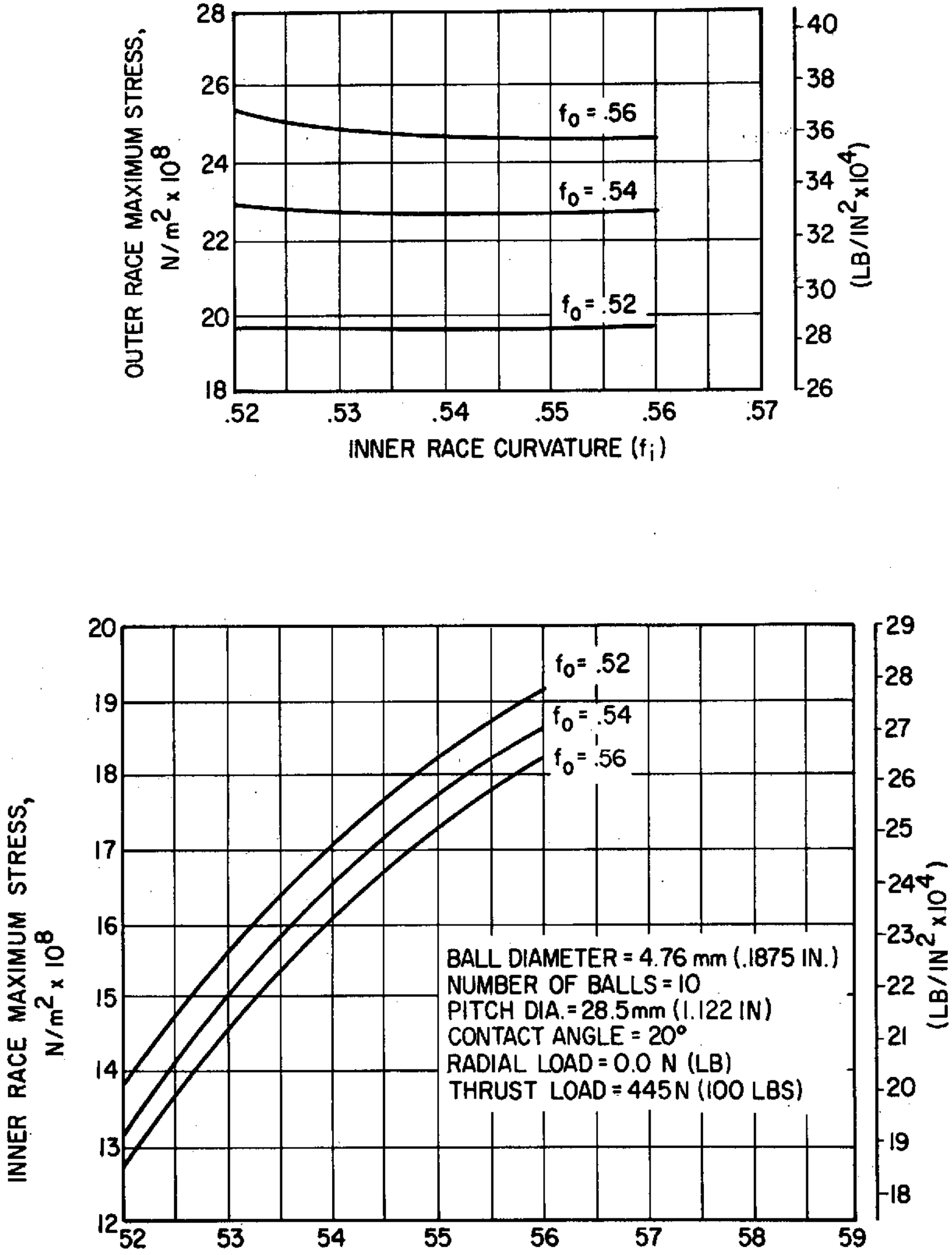

Fig. 12 Effect of Race Curvature on Compressive Hertz Stress

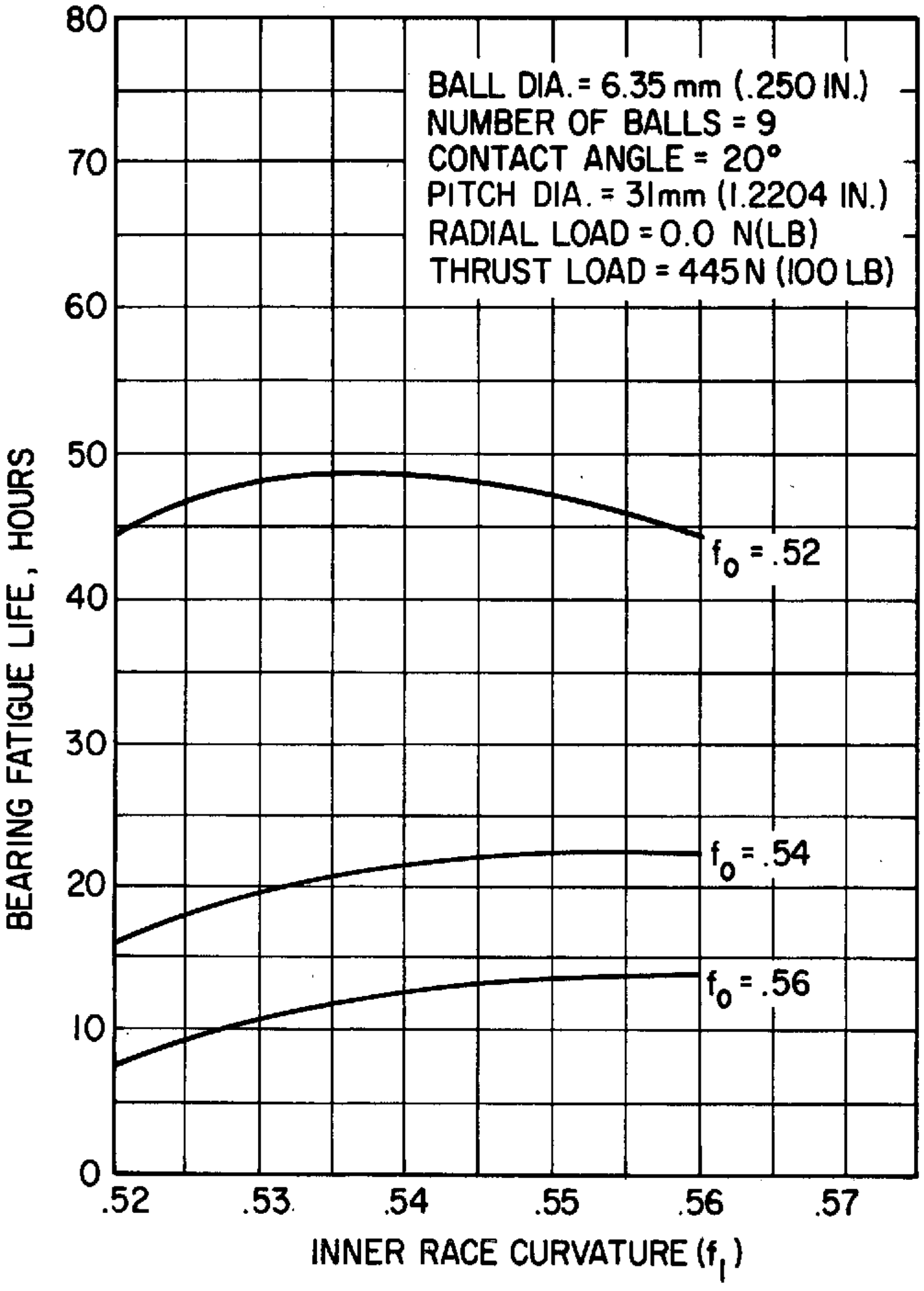

Fig. 13 Effect of Race Curvature on Bearing Fatigue Life

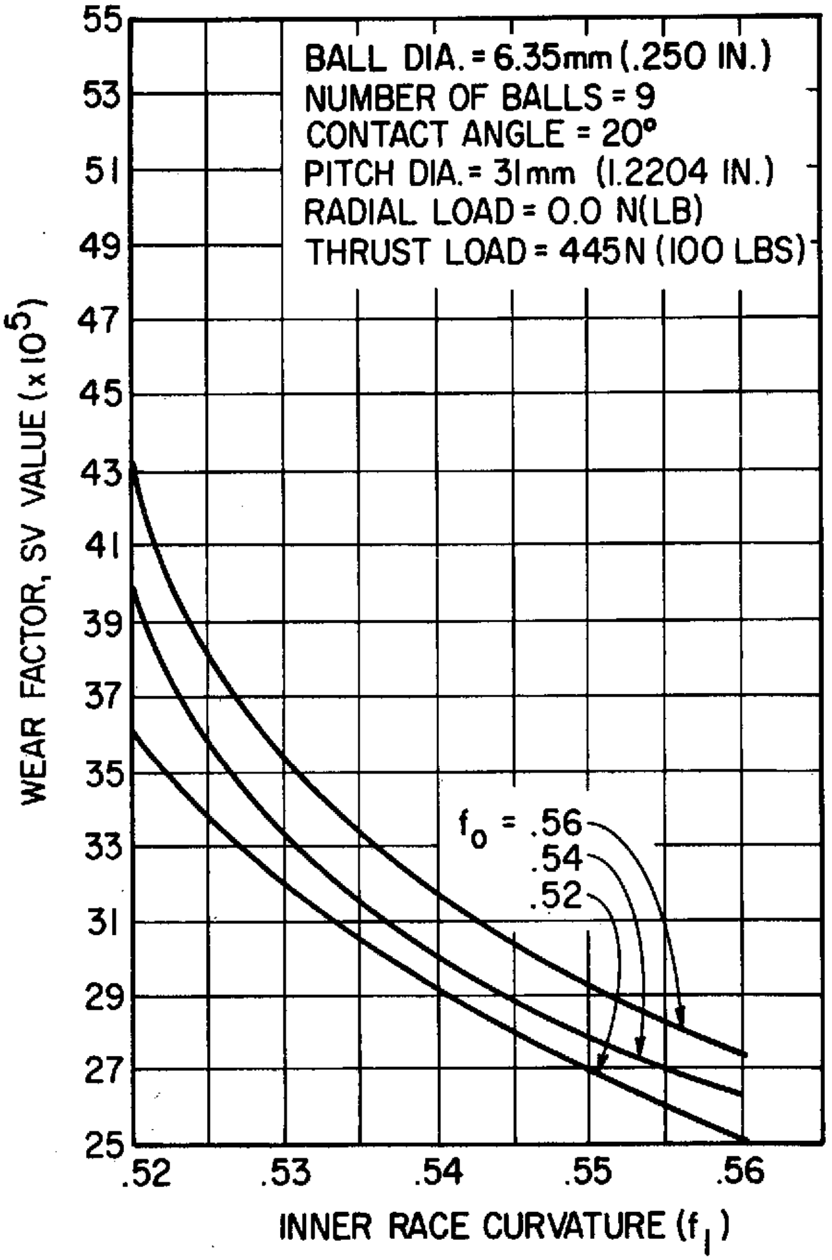

Fig. 14 Effect of Race Curvature on Wear Factor

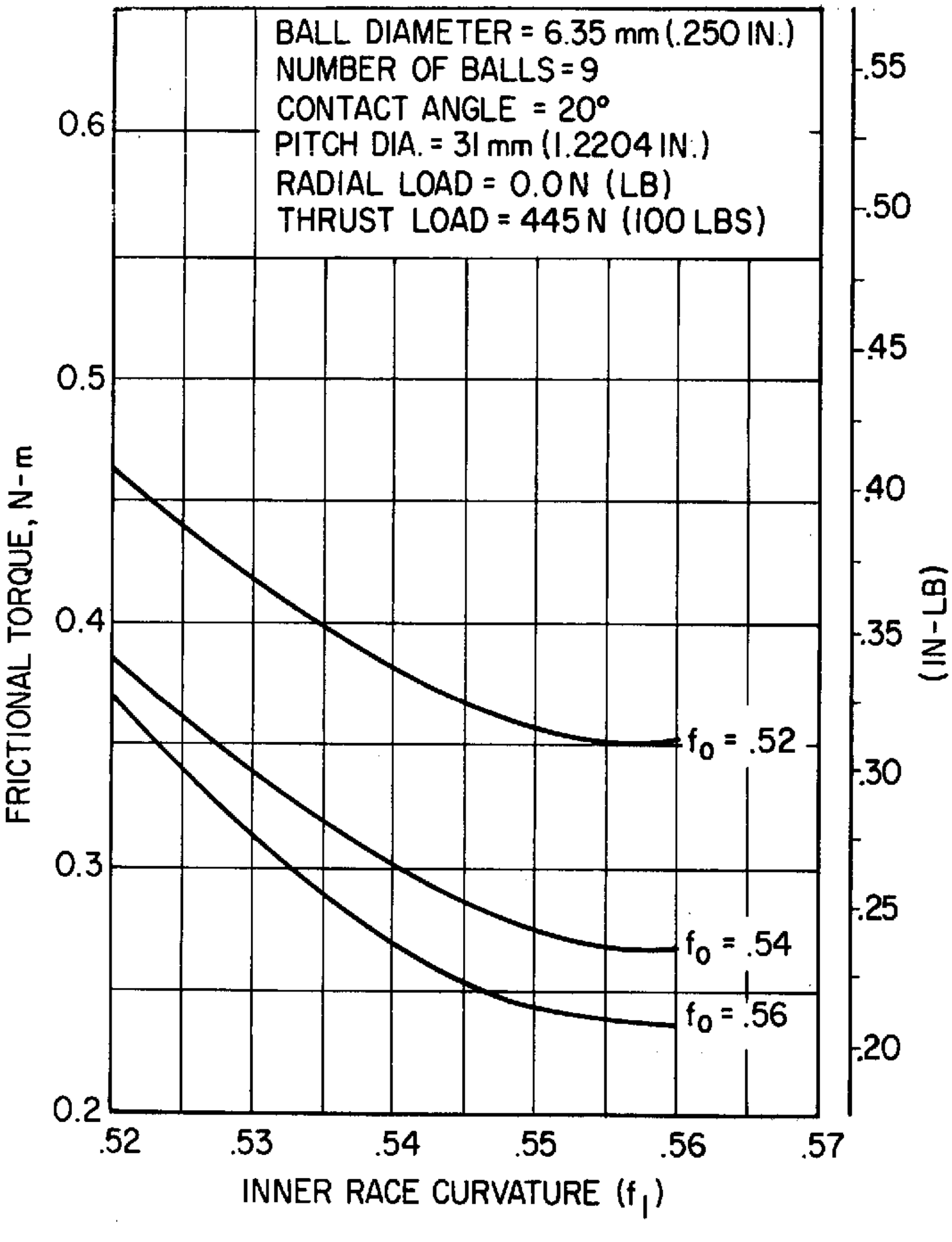

Fig. 15 Effect of Race Curvature on Frictional Torque

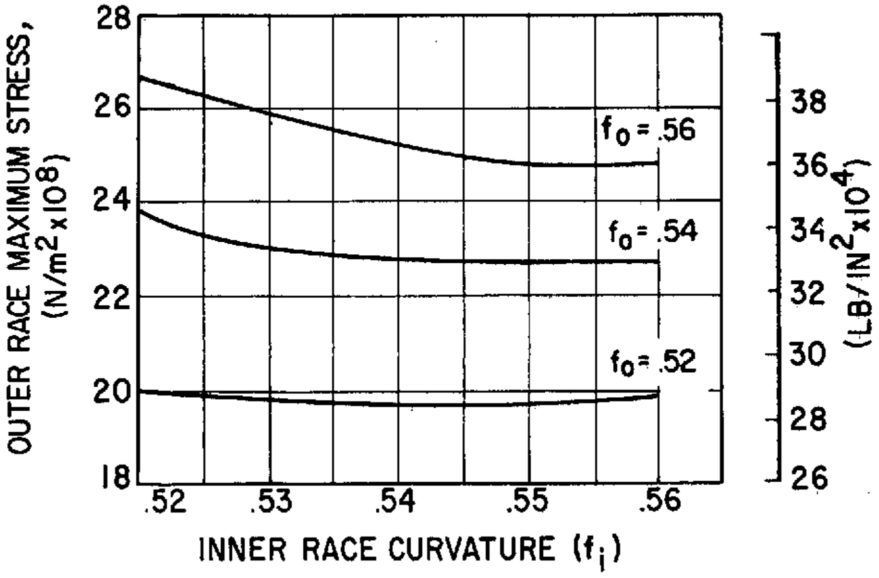

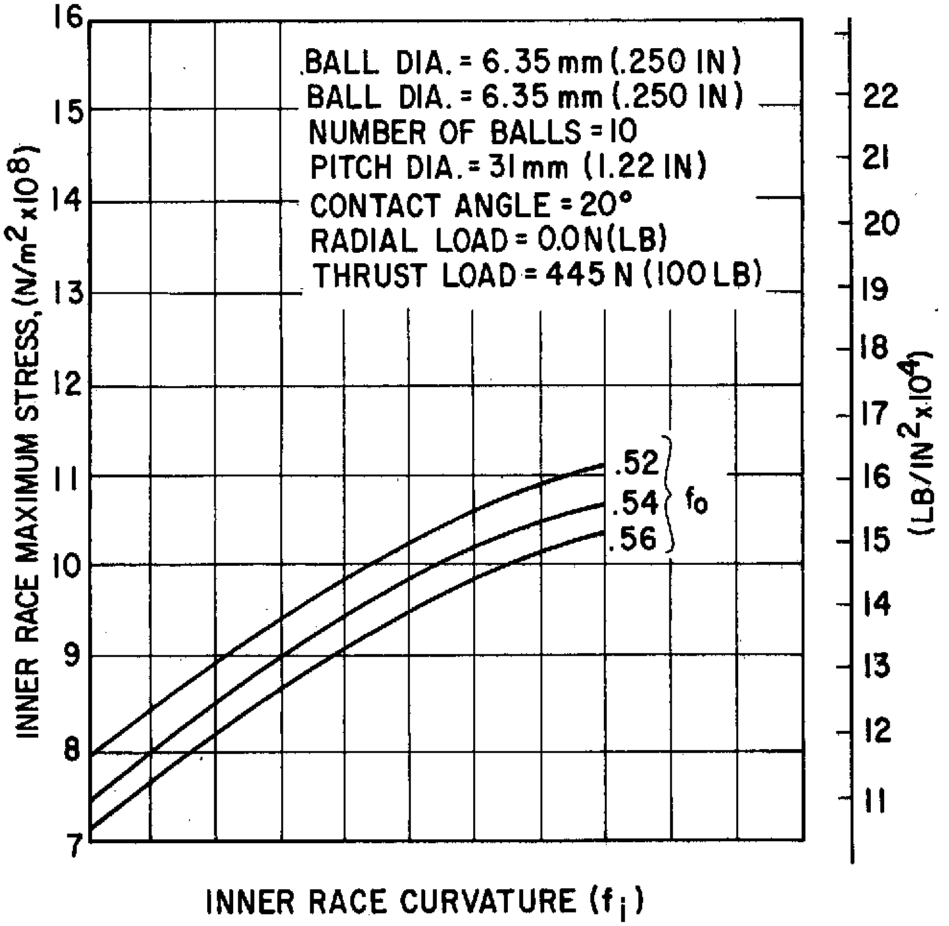

Fig. 16 Effect of Race Curvature on Compressive Hertz Stress

The frictional torque is larger for the large ball size because the centrifugal inertia effects are more pronounced due to larger ball mass. Comparing the plots shown in Figures 11 and 15, appreciable decreases in torque can be obtained through an increase in the inner race curvature. The same trend is also apparent from an increase in the outer race curvature.

The maximum stress values at the inner and outer races, shown in Figures 12 and 16, for the smaller and larger size balls, remain still well within the limits specified for permanent deformation.

Summarizing the results of the examination of the plots shown in Figures 9 through 16, the indications are clear that the outer race should be maintained at the curvature ratio of 0.52, in order to obtain the highest fatigue life, as well as the lowest SV values. This holds true for the bearing with the 6.35 mm (.250 in.) diameter ball and the bearing with the 4.76 mm (.1875 in.) diameter ball. In the process of using $f_o = 0.52$, one must realize that the frictional torque would be somewhat higher over that obtained with higher curvature ratios at the outer race, but this appears to be the only penalty involved in the overall compromise. The maximum stresses are greatly reduced through the use of the low curvature ratio, 0.52.

Having selected an outer race curvature of 0.52, one can examine now the inner race curvature behavior in greater detail. Turning to Figures 9 - 12 for the small diameter ball bearing, the fatigue life drops off as the inner race curvature increases. The change in inner race curvature from 0.52 to 0.56 represents a 32 percent drop in fatigue life. At the same time, the SV value also decreases.

The overall drop between the inner race curvature of 0.52 and that of 0.56 is equal to 32%. Thus, the drop in fatigue life appears to have been made up, to some extent, by a similar decrease in the SV values. The slope of the SV curve is low between f_i values of 0.54 and 0.56 and high between the 0.52 and 0.54. A value of 0.54 would thus represent a reasonable compromise. At this point, the fatigue life decreases by only 18% over that at 0.52 and the SV value decreases by 23.5%. The torque at $f_i = 0.54$ is not very much different from that at 0.56. However, a reasonable torque reduction can be obtained between 0.52 and 0.54. The maximum stress is still well below the specified safety limits. On the basis of the above observations, a curvature ratio at the inner race of 0.54 was selected.

With the 6.35 mm (0.25 in.) ball (see Figures 13-16), the variation of the inner race curvature does not seem to appreciably affect the fatigue life, however, a significant decrease in the SV values can be obtained through an increase in the inner race curvature. The torque value for the bearing also appreciably decreases as the inner race curvature is increased, and the maximum stress remains relatively unaffected by the inner race curvature. Because of this behavior, an inner race curvature of 0.56 would be highly advisable for this type of a design; the only factor adversely affected by it (the bearing fatigue life) shows an insignificant change within this range of curvatures.

Based upon the above examination of the data, the outer race curvature ratio for both bearings should be fixed at 0.52. The inner race curvature ratio for the 4.76 mm (0.1875 in.) ball bearing should be 0.54 and that of the 6.35 mm (0.250 in.) ball bearing, 0.56.

d. Effect of Operational Contact Angle

Once the ball size, number of balls, and the outer and inner race curvatures have been established, it remains to define the operational contact angle in order to fix the bearing geometry. The operational contact angle represents the actual contact angle in the bearing as it would appear in its fully assembled state, at the given speed, and temperature of operation. In order to arrive at the design, or initial contact angle, the effects of shrink-fit, centrifugal growth, and temperature have to be compensated for. This will be done in a later section, dealing with the examination of the bearing performance over its full operating range. In this section, the number of balls, ball diameter and curvature ratios arrived at above, were used as constants and the contact angle was varied between 12° and 25°. Two sets of curves were prepared, one for the 4.76 mm (0.1875 in.) ball and one for the 6.35 mm (0.250 in.) ball diameters. The results are shown in Figures 17 - 24.

Regarding the effects of contact angle, the following conclusions hold for either the small or the larger size bearing:

- The bearing fatigue life increases with the contact angle.
- The bearing SV values increase with the contact angle.
- The bearing torque remains essentially constant.
- The bearing outer race stresses remain constant.
- The bearing inner race stresses decrease as the contact angle is increased.

The key compromise to be struck in the selection of contact angle, involves thus, the fatigue life and the SV values. Examining the curves for the smaller diameter balls, the fatigue life increases by 30% as the contact angle is raised from 12° to 22°, and remains reasonably constant from 22° up to the maximum value of 25°. With the larger diameter balls, an increase of 48% can be obtained over a similar contact angle range. The increase in SV values is 25% for either the smaller or the larger ball size, over a similar range of contact angles. The design contact angle can be expected to vary by ± 2°, under the best of manufacturing conditions. In view of this, an angle of 20° - 24° should represent a reasonable compromise between the bearing fatigue and SV values.

e. Preliminary Bearing Geometry Specifications

The preceding sections outlined in detail the reasoning behind the selection of the bearing geometry. A summary of the effects of the bearing variables on the design parameters is presented in Table 3.

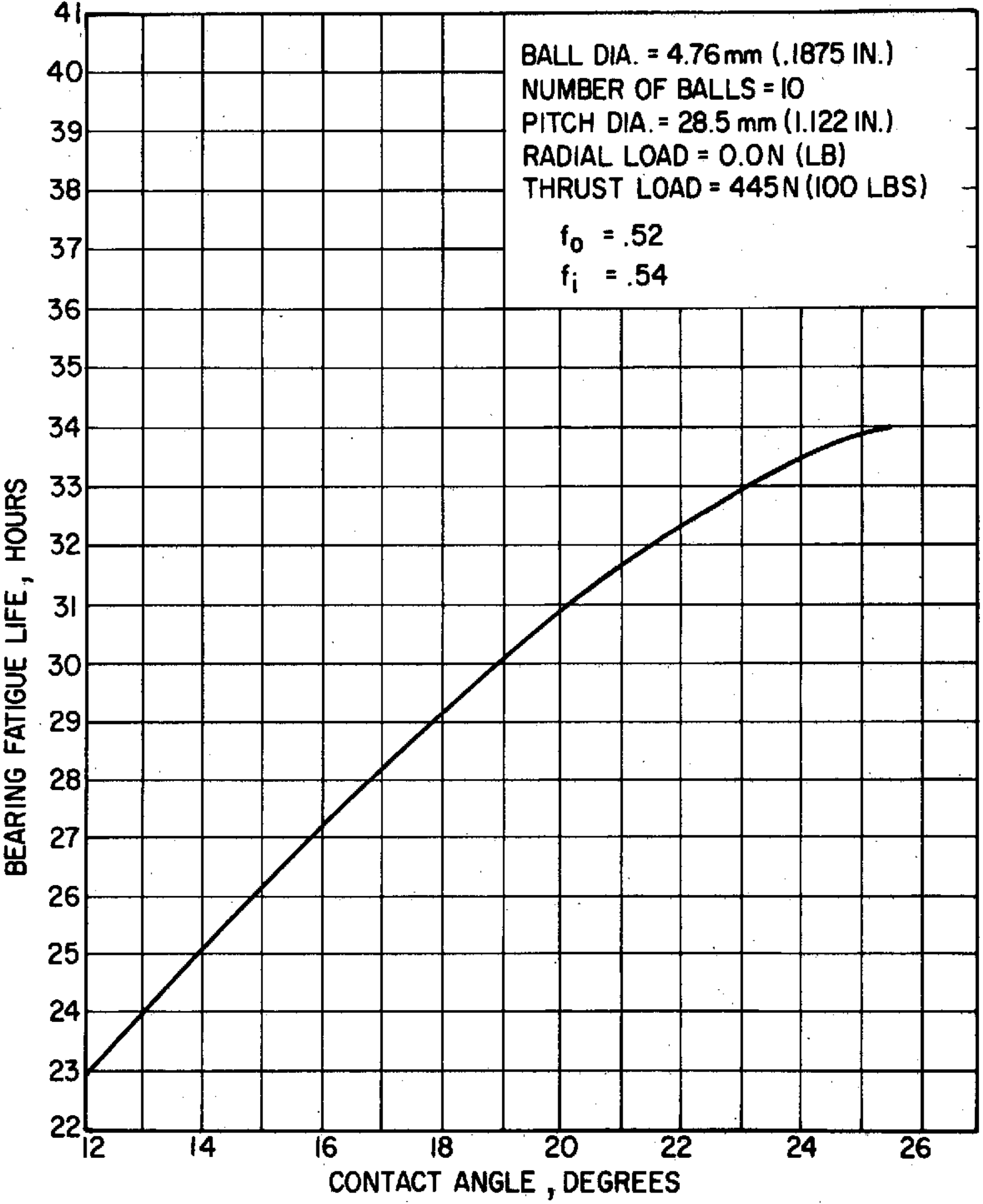

Fig. 17 Effect of Contact Angle on Bearing Fatigue Life (f_o = 0.52, f_i = 0.54)

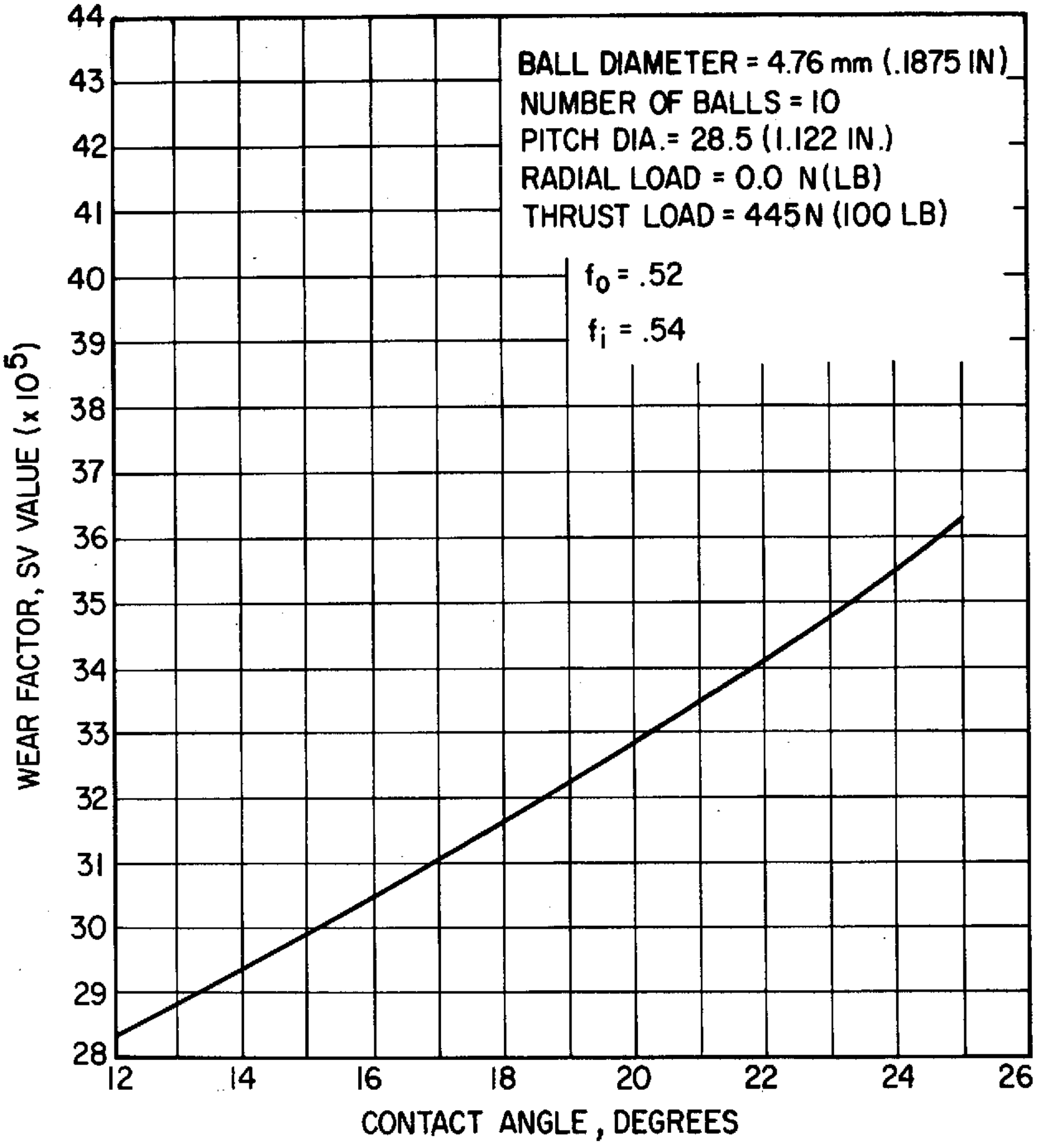

Fig. 18 Effect of Contact Angle on Wear Factor ($f_o = 0.52$, $f_i = 0.54$)

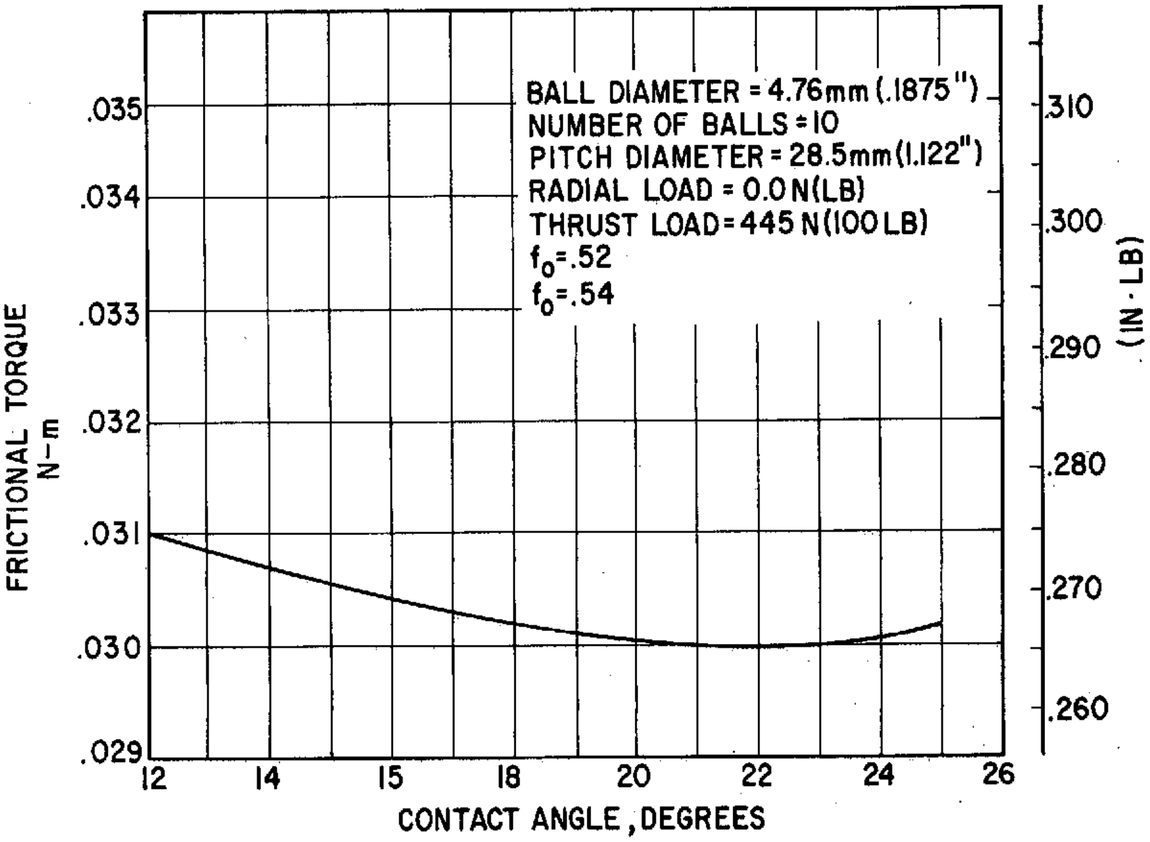

Fig. 19 Effect of Contact Angle on Bearing Frictional Torque ($f_o = 0.52$, $f_i = 0.54$)

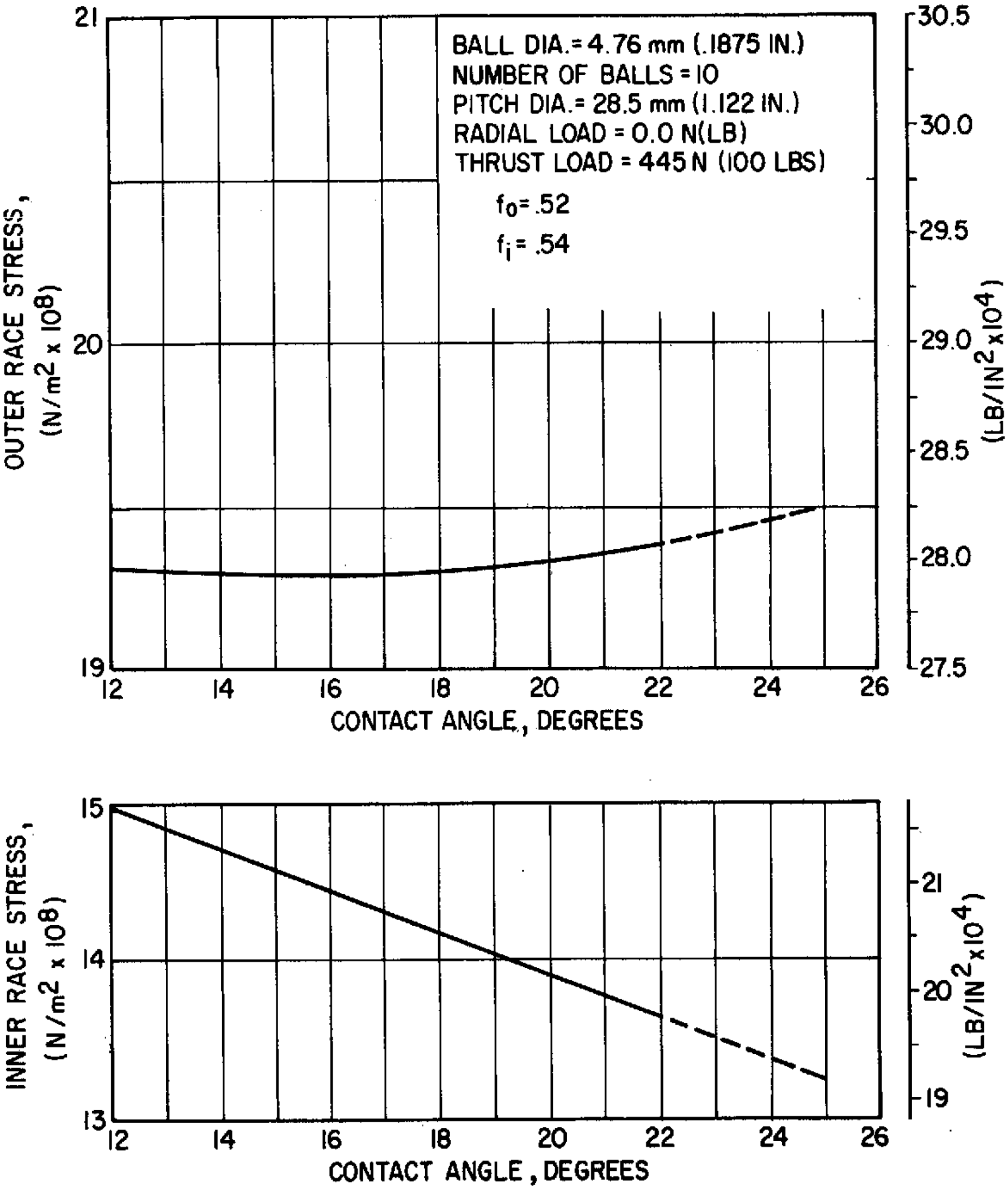

Fig. 20 Effect of Contact Angle on Compressive Hertz Stress (f_o = 0.52, f_i = 0.54)

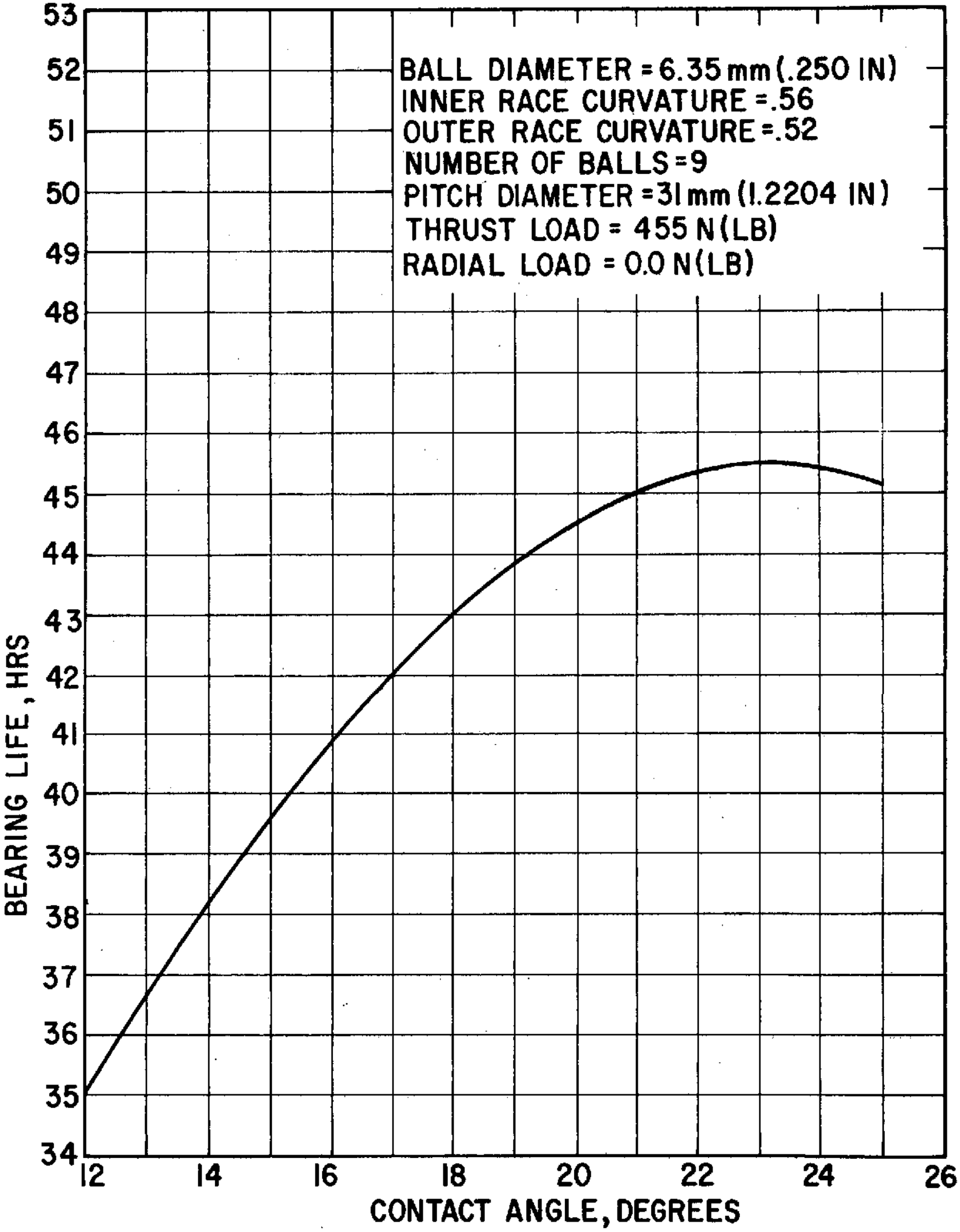

Fig. 21 Effect of Contact Angle on Bearing Fatigue Life (f_o = 0.52, f_i = 0.56)

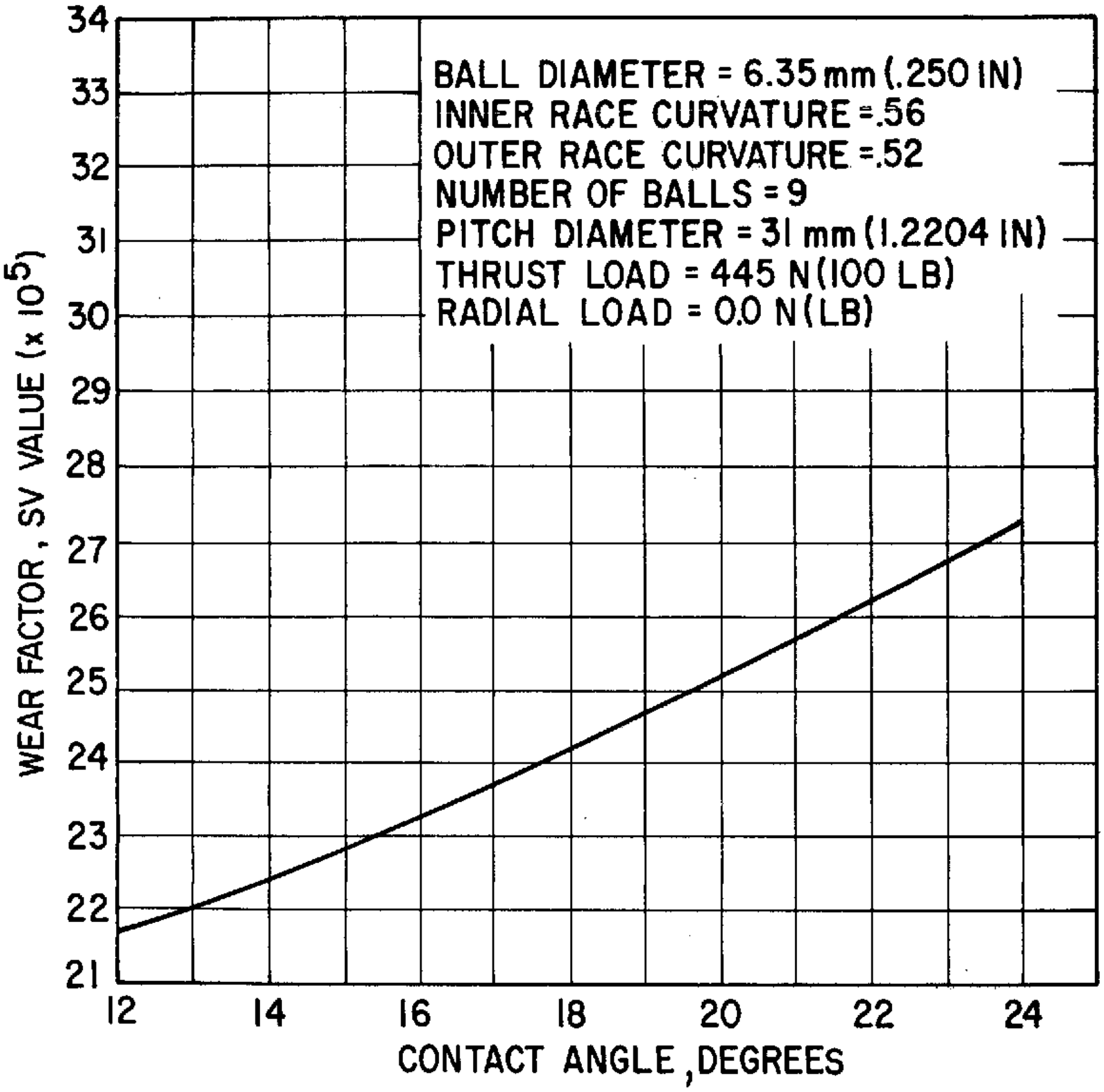

Fig. 22 Effect of Contact Angle on Wear Factor
(f_o = 0.52, f_i = 0.56)

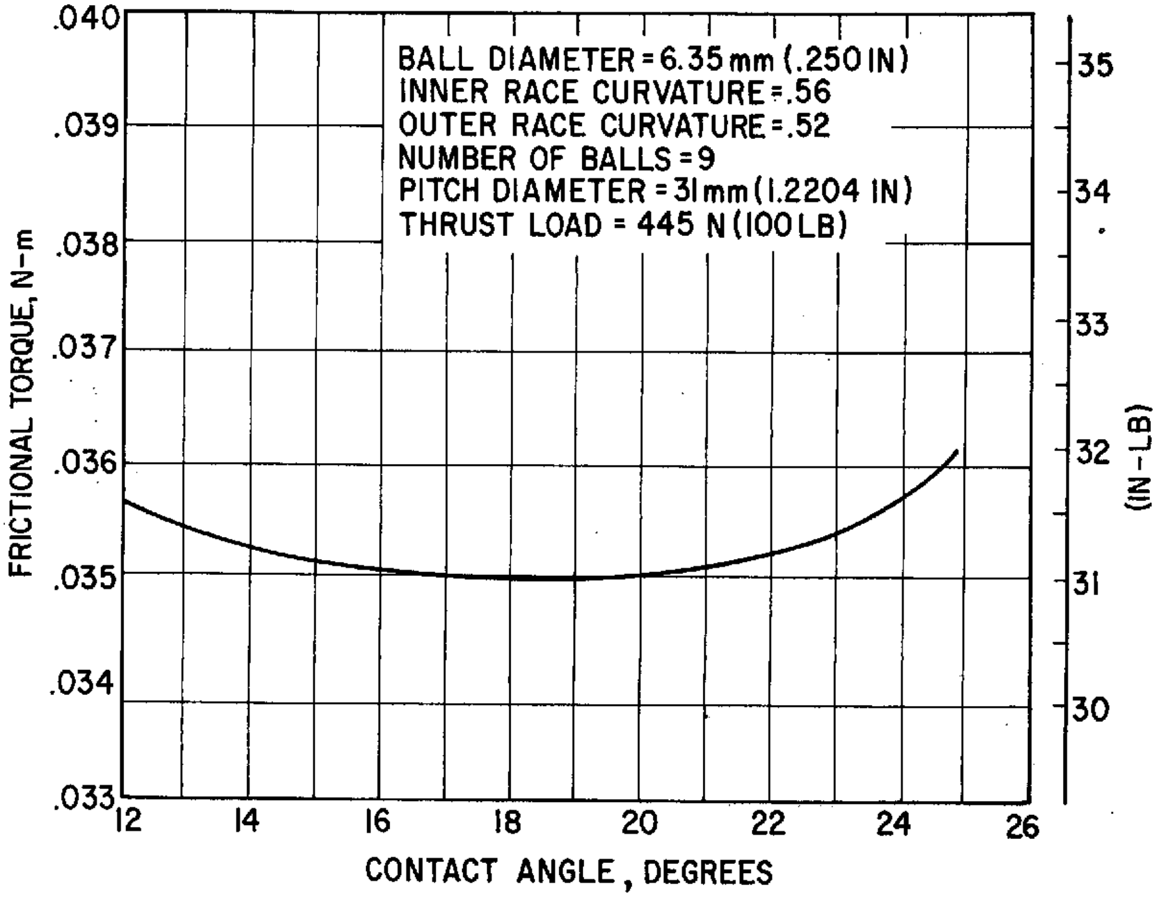

Fig. 23 Effect of Contact Angle on Frictional Torque ($f_o = 0.52$, $f_i = 0.56$)

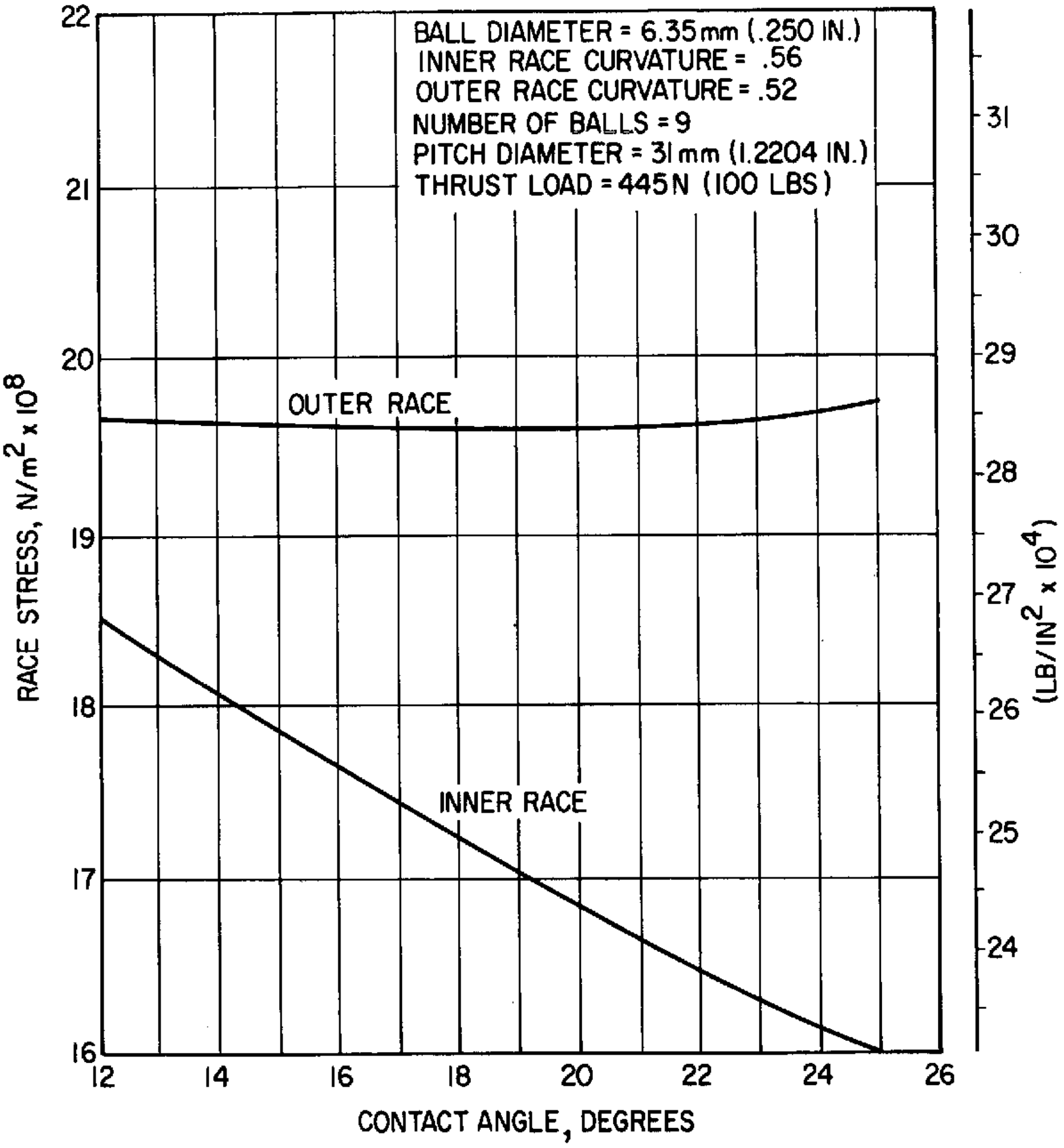

Fig. 24 Effect of Contact Angle on Compressive Hertz Stress

TABLE 3

EFFECT OF BEARING VARIABLES ON DESIGN PARAMETERS AND BALL BEARING INTERNAL GEOMETRY RECOMMENDATIONS

Variable (Increase in:)	Design Parameters				Recommended Values	
	Fatigue Life	SV*	Torque	Maximum Stress	Extra-Light Series	Light Series
Ball Size	Incr.	Decr.	Incr.	Incr.	4.76 mm (0.1875 inch)	6.35 mm (0.250 inch)
Number of Balls	Decr.	Decr.	N.C.	Decr.	10	9
Outer Race Curvature	Decr.	Incr.	Decr.	Decr.	0.52	0.52
Inner Race Curvature	N.C.-Decr.	Decr.	Decr.	N.C.	0.54	0.56
Contact Angle	Incr.-N.C.	Incr.	N.C.	N.C.	20° - 24°	20° - 24°

NOTES:
Incr. = Increase
Decr. = Decrease
N.C. = No change

*The SV value represents the maximum product of stress times velocity of spin in the Hertzian contact zones. See page 12.

The same table also specifies the dimensional value of the variable to be employed in two selected bearing configurations - one extra-light series, and one light series bearing. The light series bearing is superior to the extra-light bearing from the standpoint of fatigue life and wear resistance. These characteristics place the light series bearings as a prime candidate for use in exclusively ball bearing supported systems.

Systems employing hybrid bearings require as low an outer diameter as possible primarily because of the high fluid-film bearing losses associated with the larger diameter (power loss in fluid-film bearings is proportional to D^4). Because the relative rotation between the ball bearing elements is expected to be greatly reduced in the Hybrid Bearing System, the fatigue life and wear limitations presented by the extra-light series ball bearing components greatly diminish in importance. The use of the extra-light series bearing in the hybrid bearing will thus enhance the possibility of successful operation. The extra-light bearing, because of its reduced size can also be considered as a potential substitute for the light bearing in exclusively supported ball bearing systems, when size, weight and torque losses are at a premium.

As a result of the bearing optimization study, the following recommendations apply:

- For the single bearing pair rotor supported system light series bearings should be used.
- The duplex pair supported system should also employ the light series bearings.
- Extra-light bearings should be employed in the hybrid system.

5. Examination of Changes in Bearing Geometry Induced by the Conditions of Operation

The rolling-element bearings proposed for this application will undergo dimensional changes during installation and operation at test conditions.

Within the scope of this program, the bearings are expected to pass through four stages, each of which will contribute to a change in the bearing dimensions. These stages are:

- Free State
- As Assembled
- As Assembled at Test Temperature
- At Test Temperature and Speed

The bearing free-state dimensions must correspond to those specified in the procurement drawings and specifications.

During assembly, the bearing internal clearances will undergo a change because of the strains enforced by the fits of the bearing rings on the shaft and bearing housings. Cooling of the assembled bearing down to the temperature of operation will introduce additional changes in the bearing dimensions. These changes will result mainly from the differences in the coefficients of thermal expansion of the shaft, bearing housing, and ball bearing materials and will again affect the bearing internal clearance.

Finally, operation at full speed imposes centrifugal growth on the rotating parts which, in turn, produce internal clearance changes within the bearing.

The effects common to each of the above stages have been accounted for in detailed calculations. The results of these calculations are summarized in Tables 4 - 9. The predominant changes introduced in the bearing as it passes through the four stages are reflected mainly in the internal clearance of the bearing; this, in turn, affects the contact angle. The pertinent ball bearing and cage diameters are shown in Figure 25.

In the preceding sections, it was pointed out that the test plan includes tests of single, duplex and hybrid bearing configurations. The single bearing pair and duplex pair rotor supported systems are subject to the same dimensional changes, hence, the analysis of one light series bearing will apply to both rotor systems. The extra-light series bearing to be employed in the hybrid bearing system will be mounted in duplex pairs. Since the

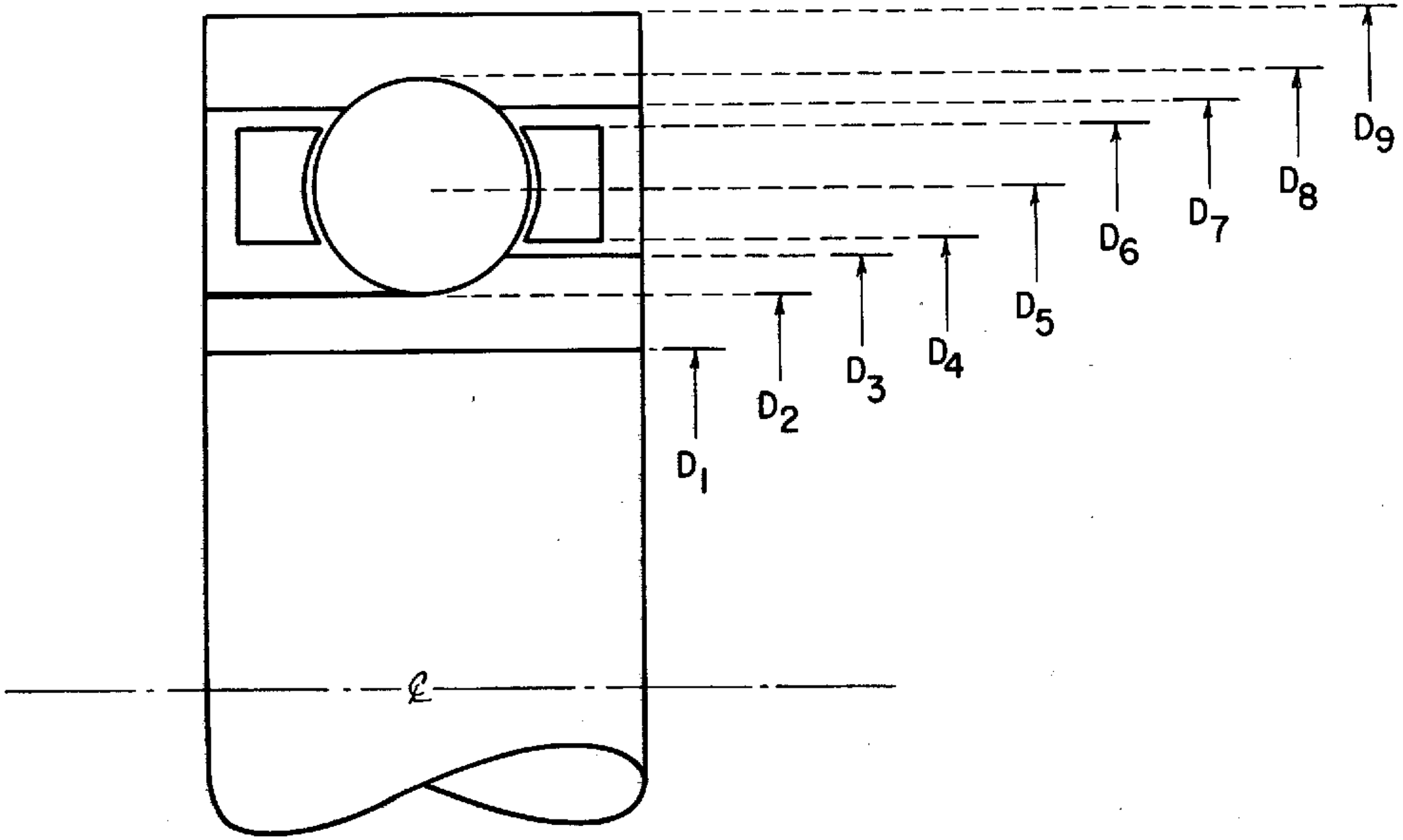

Fig. 25 Ball Bearing Diameter Code

bearings are identical in size, the examination of the behavior of a single extra-light series bearing will also apply to the duplex mount.

As has been previously mentioned, the bearing materials consist of 440 C for balls and races, and either glass-filled Teflon (Armalon), or lead coated 440 C stainless steel will be used for the cages. The shaft will be made of Inconel X-718.

The coefficients of thermal expansion of each one of the materials of construction used in the bearing as well as in the forthcoming test vehicle design are given in Appendix A.

a. Effects of Dimensional Changes - Light Series Bearing

To avoid excessive dynamic excursions caused by loose inner rings, the bearing has to be designed to operate with an interference fit at full speed in the expected LH_2 environment. Centrifugal growth and thermal shrinkage calculations were performed, the results of which indicate that a nominal shrink fit of 0.028 mm (0.0011 in.) will be sufficient to maintain interference at speeds up to 120,000 rpm. A listing of the changes in the critical diameters as a function of temperature and speed is given in Table 4. This table represents the values of the inner and outer race groove diameters at room temperature, at room temperature as assembled after the initial interference fit, at the cryogenic temperature of -420°F, and finally, at the cryogenic temperature as a function of speed, the speed running from 0 to 120,000 rpm.

The internal clearance of the bearing can be expressed as being equal to:

$$D_8 - D_2 - 2d = P_D \tag{1}$$

The relationship between the contact angle, curvature and the internal clearance is as given in Eq. [2]:

$$\cos \alpha_i = \frac{2Bd - P_D}{2Bd} \tag{2}$$

TABLE 4

CLEARANCES AND FITS FOR LIGHT SERIES BEARING

(Initial Interference = .0279mm (.0011")

TEMP		SPEED, RPM	D_2***		D_8***		P_E		P_D		α
			mm	(in)	mm	(in)	mm	(10^{-3}in)	mm	(10^{-3}in)	Deg.
°K	°R										
293	(528)	0*	24.65	(.9704)	37.44	(1.474)	0.41	(16)	0.09	(3.63)	24.6
293	(528)	00**	24.67	(.9713)	37.44	(1.474)	0.37	(14.7)	0.07	(2.73)	21.3
22	(40)	0	24.62	(.9693)	37.4	(1.4714)	0.38	(15)	0.08	(3.15)	23
22	(40)	40,000	24.62	(.9694)	37.4	(1.4714)	0.38	(15)	0.76	(3)	22.5
22	(40)	60,000	24.62	(.9694)	37.4	(1.4714)	0.38	(15)	0.76	(3)	22.5
22	(40)	80,000	24.62	(.9694)	37.4	(1.4714)	0.38	(15)	0.76	(3)	22.5
22	(40)	100,000	24.62	(.9695)	37.4	(1.4714)	0.38	(15)	0.76	(3)	22.2
22	(40)	120,000	24.62	(.9695)	37.4	(1.4714)	0.38	(15)	0.76	(3)	22.2

*Bearing in free state

**Installed bearing

P_E - Axial play in ball bearing

P_D - Radial Play in ball bearing

***D_2 and D_8 are defined in Figure 25 where $B = f_o + f_i - 1$, f_o = outer race curvature ratio, f_i = inner race curvature ratio and d is the ball diameter.

The relationship between P_E (axial play) and P_D is:

$$P_E = \sqrt{4Bd\ P_D - P_D^2} \tag{3}$$

The values of P_E, P_D, and the contact angle calculated for this particular bearing assembly over the full range of speeds and operating conditions are also given in Table 4.

The results indicate that the initial contact angle of 24.6° (prior to assembly) will result in a contact angle of about 22° after the interference, temperature, and speed effects have been accounted for. This value is in line with the results of the optimization study discussed in Section A-1.

The maximum hoop stress occurs in the inner ring with the bearing fully installed. The stress is equal to 35,840 psi. At cryogenic conditions, this stress decreases to 21,309 psi, and at full speed of 120,000 rpm, the stress is 27,654 psi. These values are well below the yield point of 440 C stainless steel.

Because of the relatively low speeds of cage rotation, (30,000 rpm max) operation with Armalon cages is possible. Calculations of the effect of cage speed on growth and stress produced the results shown in Table 5. The maximum tangential stress at 60,000 rpm is less than 2,000 psi, which is well below a 7,000 psi limit specified for this type of material. The net maximum growth of the cage is only .013 mm (.52 x 10^{-3} in.). The outer and inner diameters, as well as the operational diametral clearance for the Armalon cage are also given in Table 5.

As a back up to the Armalon cage, a lead alloy coated steel cage will also be manufactured. Since the cage will be made of the same material as the bearing, the relative clearances should not change as the bearing

TABLE 5

ARMALON CAGE DIMENSIONS

TEMP °K	(°R)	SPEED RPM	D_6* (mm)	D_6* (in)	D_7* (mm)	D_7* (in)	C_D** (mm)	C_D** (mils)
293	(528)	0	34.4	(1.356)	34.5	(1.3604)	0.114	(4.45)
22	(40)	0	34.2	(1.3476)	34.5	(1.3581)	0.267	(10.5)
22	(40)	40,000	34.2	(1.3478)	34.5	(1.3581)	0.261	(10.3)
22	(40)	60,000	34.2	(1.3481)	34.5	(1.3581)	0.254	(10.0)

*See Figure 25 for definition of D_6 and D_7.

**$C_D = D_7 - D_6$

is submerged in LH_2. Because the cage speed is close to one-half of the bearing inner ring speed, centrifugal growth will be minimal. A tabulation of centrifugal growth, shrinkage, and clearance effects is presented in Table 6. The maximum hoop stress of the steel cage at 120,000 rpm of bearing rotation is 12,700 psi.

b. Effects of Dimensional Changes - Extra-Light Series Bearing Hybrid Mode

When used as a component of the hybrid bearing, the ball bearing is expected to approach solid body rotation. A drawing of the hybrid bearing is given in Figure 26.

Since the bearing outer ring is expected to rotate at a speed close to that of the shaft, the bearing housing will also rotate at the same speed. The differences in the size and thickness of the bearing housing and the bearing outer ring will cause the housing to grow centrifugally at a rate faster than that of the bearing outer ring.

In order to maintain a close fit at the full speed of rotation (120,000 rpm) an interference of 0.018 mm (0.0007 in.) on radius between the bearing housing and bearing outer ring is required at room temperature.

The fit at the inner race remains essentially the same as the one specified for the light series bearing, i.e., 0.0127 mm (0.00055 in.). The combination of a high interference fit at the outer and inner races may critically affect the internal bearing clearance.

The variation in clearance and contact angle with each stage of operation is given in Table 7. With the assumed interference fits, the worst situation develops when the fully assembled unit is cooled down to the levels of operation. At this point, the internal clearance is nearly 0.008 mm (0.0003 in.) when an initial free contact angle of 24° is assumed. To avoid total loss of clearance, the initial free contact angle cannot be permitted to drop below 24°.

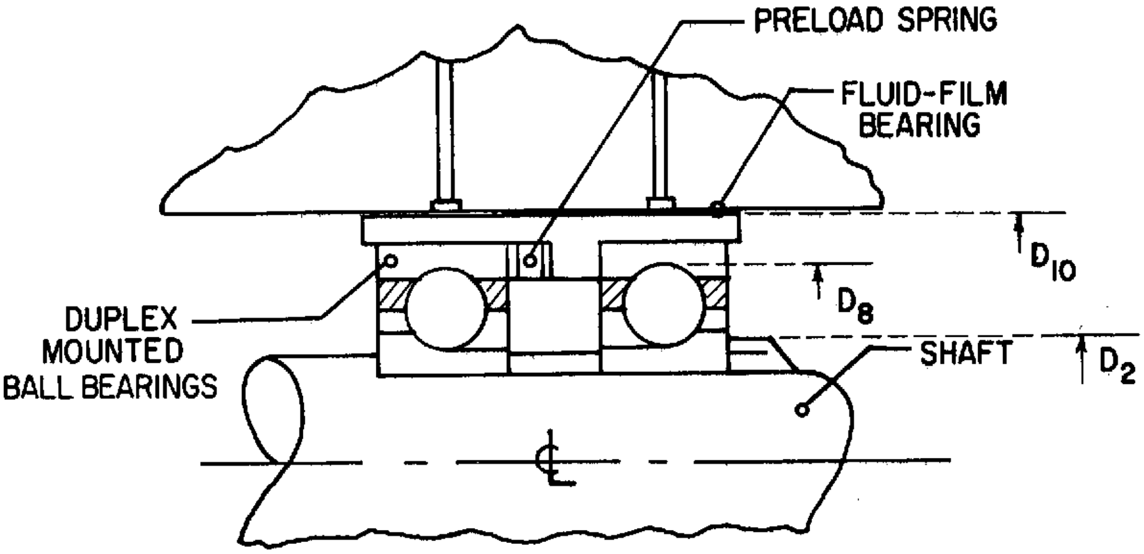

Fig. 26 Hybrid Bearing Assembly

TABLE 6

440 C STAINLESS STEEL CAGE DIMENSIONS

TEMP °K	 (°R)	SPEED (RPM)	D_6 * (mm)	 (in)	D_7 * (mm)	 (in)	C_D ** (mm)	 (mils)
293	(528)	0	34.26	(1.3490)	34.54	(1.360)	0.15	(11)
22	(40)	0	34.20	(1.3466)	34.48	(1.3576)	0.15	(11)
22	(40)	20,000	34.21	(1.3467)	34.48	(1.3576)	0.15	(10.9)
22	(40)	40,000	34.21	(1.3468)	34.48	(1.3576)	0.15	(10.6)
22	(40)	60,000	34.21	(1.3471)	34.48	(1.3576)	0.14	(10.5)

---

*See Figure 25 for definition of D_6 and D_7.

**$C_D = D_7 - D_6$

TABLE 7

CLEARANCES AND FITS FOR EXTRA-LIGHT SERIES BEARING – HYBRID ASSEMBLY

(Initial Interference at Bearing Bore = 0.0279 mm (0.0011"), at Bearing O.D. = 0.0355 mm (0.0014")

TEMP		SPEED	D_2 *		D_8 *		D_{10} *		P_D		α
°K	(°R)	RPM	mm	(inch)	mm	(inch)	mm	(inch)	mm	(inch)	Deg
293	(528)	0**	23.74	(.9345)	33.82	(1.3114)	41.76	(1.6440)	.033	(.0013)	24.0
293	(528)	0***	23.76	(.9354)	33.29	(1.3108)	41.78	(1.6448)	.010	(.0004)	11.0
22	(40)	0	23.71	(.9334)	33.23	(1.3081)	41.69	(1.6412)	.008	(.0003)	9.5
22	(40)	40,000	23.71	(.9335)	33.23	(1.3084)	41.70	(1.6416)	.013	(.0005)	12.0
22	(40)	60,000	23.71	(.9335)	33.24	(1.3088)	41.71	(1.6420)	.023	(.0009)	16.3
22	(40)	80,000	23.71	(.9335)	33.26	(1.3094)	41.72	(1.6426)	.033	(.0015)	21.0
22	(40)	100,000	23.71	(.9336)	33.28	(1.3101)	41.74	(1.6433)	.053	(.0021)	25.0
22	(40)	120,000	23.71	(.9336)	33.30	(1.3110)	41.75	(1.6438)	.076	(.0030)	30.0

*For definition of D see Figure 26.

**Bearing in free state

***Installed Bearing

P_D: Axial Play of Ball Bearing

α: Contact Angle

With the initial free contact angle of 24°, the contact angle at full speed of 120,000 rpm will be close to 30°. Since, however, the relative rotation between the bearing will be minimal at that speed, the fatigue and wear aspects are less important. The major concern is that the Hertzian zone of the ball to inner race contact does not extend beyond the bearing shoulder. The shoulder height ("H") at the inner race is:

$$H = \frac{D_3 - D_2}{2} = 1.07 \text{ mm } (0.042 \text{ inches})$$

The ratio of the shoulder height to ball diameter is:

$$\frac{H}{d} \times 100 = 22.3\%$$

According to the computer calculations, the maximum ratio anticipated at the extremity of the Hertzian contact zone is 20.7%. This ratio represents a very conservative estimate and will occur at the full speed of 120,000 rpm with an initial preload of 100 lb. Although a larger margin of safety in this area may be desirable, further increase in D_3 will impose greater restrictions on the flow through the bearings.

The dimensional changes introduced in the cages selected for this application are shown in Table 8, for the 440 C and Ti-5Al-2.5 Sn titanium alloy. The dimensions for the two materials are the same because the differences in density are counteracted by similar differences in the moduli of elasticity, and the coefficients of thermal expansion are closely matched.

The relatively tight clearances imposed in the cage-to-land area are necessary to reduce the magnitude of unbalance caused by the eccentric displacement of the cage within the bearing. The maximum eccentricity is equal to the radial clearance, hence:

Max. Unbalance = we

where w = grams (oz)

e = eccentricity - mm (in)

TABLE 8

CAGE DIMENSIONS AFTER PLATING
(440 C Stainless Steel and Ti - 5Al - 2.55Sn)

TEMP		SPEED	D_6*		D_7 *		C_D	
°K	(°R)	RPM	mm	(inch)	mm	(inch)	mm	(inch)
293	(528)	0	30.378	(1.1960)	30.498	(1.2007)	0.119	(.0047)
22	(40)	0	30.325	(1.1939)	30.444	(1.1986)	0.119	(.0047)
22	(40)	40	30.327	(1.1940)	30.444	(1.1986)	0.117	(.0046)
22	(40)	60	30.333	(1.1942)	30.444	(1.1986)	0.112	(.0044)
22	(40)	80	30.340	(1.1945)	30.444	(1.1986)	0.104	(.0041)
22	(40)	100	30.348	(1.1948)	30.444	(1.1986)	0.096	(.0038)
22	(40)	120	30.358	(1.1952)	30.444	(1.1986)	0.086	(.0034)

*See Figure 25 for definition of D_6 and D_7

C_D: Diametral Cage Clearance

With 440 C stainless steel for the cage material, the cage nominal weight is 7 gms. (.25 oz.). At 120,000 rpm, the maximum eccentricity is 0.043 mm (0.0017 inches). The maximum unbalance caused by the steel cage is thus equal to .301 gm-mm (0.00042 oz-in). The effect of this unbalance on the dynamic performance of the test vehicle will have to be established in the test phase.

Should this unbalance prove to be excessive, the titanium cage can be employed. With titanium, the unbalance is reduced to .172 gm-mm (0.00024 oz-in).

The reason for the expressed preference of steel to titanium is the lack of experience in the deposition of the recommended lead-alloy coatings on titanium, and the adhesion of the coatings to a titanium substrate at cryogenic temperatures.

c. Bearing Loads

Loads acting upon bearings in a turbo-pump can be classified as falling into the following categories:

- Preload
- Thrust Load
- Radial Load
- Dynamic Load

All loads, no matter what their origin, have to be accounted for in the design and selection of the bearing configuration.

Preload - Ball bearings have to be initially preloaded in order to avoid excessive skidding. Past experience has shown that the onset of skidding in ball bearings is a function of speed, preload and lubrication. The higher the speed of operation, the higher the preload requirements for the ball bearing.

For bearings operating at ultra-high-speeds, one of the most significant bearing load components is due to the high centrifugal ball loads. High ball loading brings about high Hertzian stresses and invariably results in a substantial reduction in fatigue life. The addition of high bearing preloads to stabilize the bearing and prevent it from reaching the onset of skidding during operation at ultra-high-speeds acts then in the direction of further reducing the bearing fatigue life. Hence, for bearings operating at ultra-high-speeds, it becomes imperative that the minimum preload required to stabilize the bearings be used, inasmuch as any excess of additional preload will have a tendency to further reduce the fatigue life which is already heavily taxed by the presence of high internal centrifugal ball loads.

All the effort expended to date in the direction of determination of the factors responsible for ball bearing skidding leads distinctly to the conclusion that skidding is an instability introduced through the interaction of a tractive slip (defined as the difference between the ring and ball orbital velocity in the direction of rolling) and gyroscopic slip (resulting from the gyroscopic moments operating on a ball at high speeds and the tractive forces present within the Hertzian contact zones which counteract the moments to achieve equilibium). Most of the data accumulated pertains to oil lubricated bearings. The requirements of the turbo-pump are unique inasmuch as the speed levels, accelerations, and lack of elastohydrodynamic traction in the ball-to-race contact zones place this application into a new, not yet explored region. For this reason, the optimum preload requirements will have to be established on test. For the purpose of bearing analysis, a preload of 100 lbs. was assumed. This preload is, in all probability, on the conservative side. High-speed bearings as a rule require a minimum preload equal to about 5% of the dynamic capacity. The 445 N (100 lb) assumed represents 10% of the capacity of the extra-light series bearing and 7% of the light series bearing.

Thrust Loads - The overall thrust load levels can be extremely high in a turbo-pump operating at discharge pressures of 4000 to 5000 psi. At the speeds considered for this application, the imposition of high thrust loads on the ball bearings will have serious consequences. To remedy this situation, balance pistons are normally employed. The balance pistons are designed to automatically thrust balance the rotor during operation. Because balance pistons are contemplated for the turbopump design, the assumption was made that the thrust loads will be fully balanced, and any residual loading will be of negligible proportions. A more detailed discussion of the thrust loading is given in Appendix B.

Radial Loads - The magnitudes of radial loading expected on the bearings in a typical turbo-compressor has been calculated in Appendix B. Based on these calculations a radial load per bearing of 25 lbs. represents a reasonable estimate. This load can, however, appreciably vary depending upon the volute design. Because of these, and other uncertainties due to dynamic loads, a load range of 44.5 - 445 N (10 - 100 lb) is assumed in the bearing performance calculations discussed in the next section.

Dynamic Loads - Dynamic bearing loads develop as a result of residual unbalance present in the rotor during operation. Preliminary rotor response calculations performed as an aid in the design layouts, indicate that dynamic radial loading per bearing should not exceed 267 N (60 lb.).

Additional dynamic loading develops within the bearing due to the high centrifugal ball inertia. The centrifugal load per ball in the hybrid mode of operation is 1000 N (225 lb.) for the extra-light bearing operating in the hybrid mode at 120,000 rpm, and 500 N (113 lb.) for the light series bearing in a usual set up at 120,000 rpm. These loads are accounted for in the performance calculations. In view of the relatively large magnitude of the ball inertia forces, the ball bearing life should not be very sensitive to variations in the externally imposed radial loading, as long as the radial loading does not exceed in magnitude the per ball inertia load.

d. Calculated Bearing Performance

The analyses performed up to this point resulted in two optimized bearing designs (one for the ball bearing supported system, and one in the hybrid bearing system), a detailed definition of the anticipated dimensional changes, and an estimate of the loading expected during operation.

The above factors were fed into the Rolling Element Computer Program and new calculations performed to define the effect of those changes on bearing performance. In addition to the fatigue life, SV and torque parameters, the variation in bearing stiffness with speed and load was also established. The stiffness values will be used in the test vehicle design phase concerned with the critical speed and rotor response calculations.

The results of this analysis are shown in Figures 27 - 30 for the ball bearing supported system. Figures 31-34 present plots for the ball bearing employed in the hybrid bearing system. The bearing preload in each case was 445 N (100 lb). All data is presented for a single bearing only. Hence the stiffness and torque of a duplex bearing system will be twice that shown in the drawings. As was pointed out in another section of this report, the actual bearing torque in LH_2 applications is about three times that of the torque calculated by the RECAP program.

Ball Bearing Supported System - For the ball bearing supported system (light series bearing) the fatigue life, SV, and friction torque values are not appreciably different from those originally obtained in the optimization study at 120,000 rpm. The effect of speed, however, is quite pronounced. A decrease in speed from 120,000 to 100,000 rpm will bring about an appreciable increase in fatigue life. At the speed of 120,000 rpm, the fatigue life is relatively insensitive to the increase in radial load between 44.5 N (10 lb) and 445. N (100 lb). Radial load sensitivity increases with decrease in speed. This behavior is mainly due to the ball inertia loading.

Maximum SV values are appreciably increased within the given speed range of 60,000 rpm - 120,000 rpm with increased radial loading. Up to 60,000 rpm, the change in SV appears to be minor. SV vs. inner race speed is shown in Figure 28. The ball bearing stiffness K_z varies as a function of speed. The variation is less pronounced under heavy loading. Plot of stiffness vs. inner race speed is shown in Figure 29.

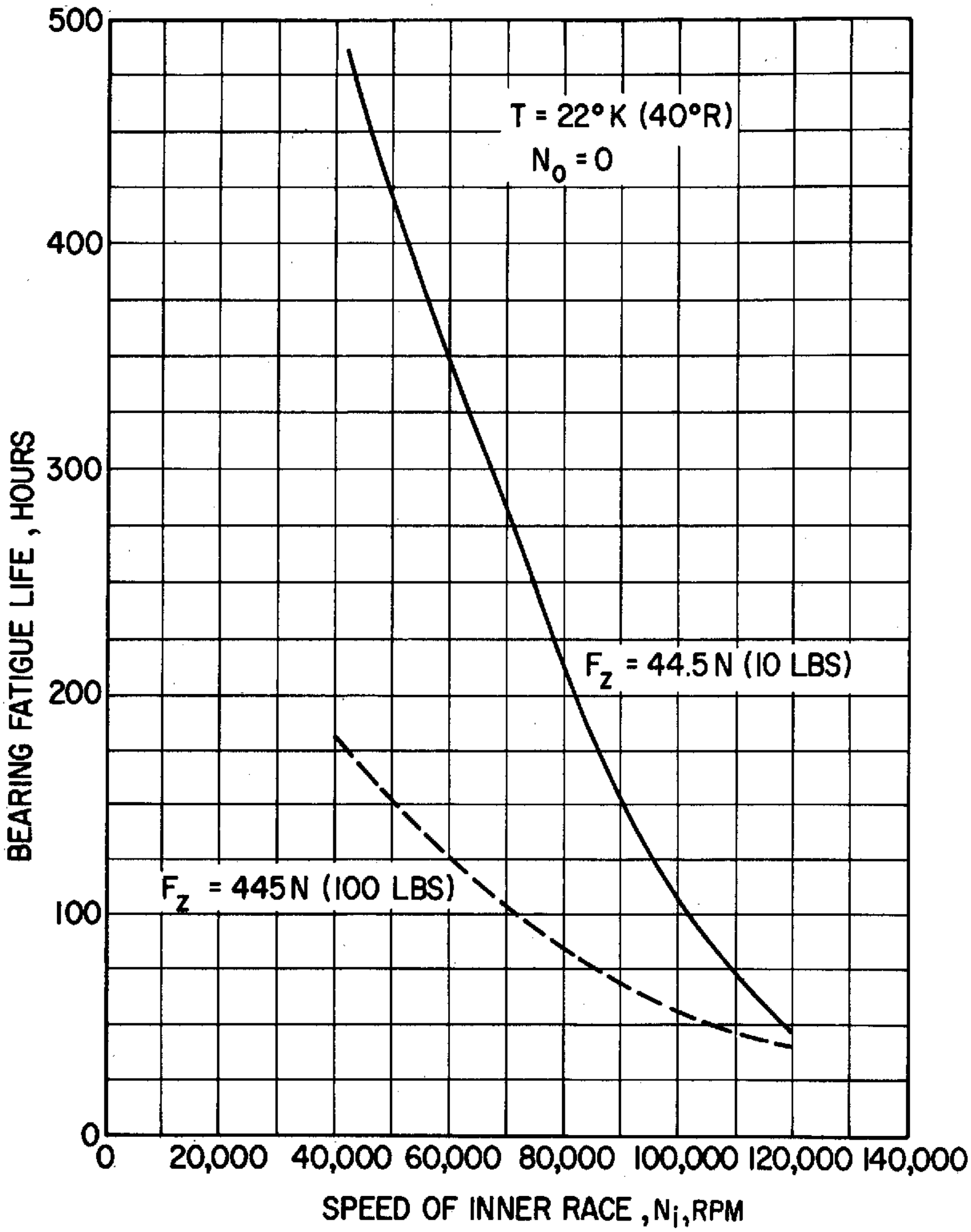

Fig. 27 Effect of Speed on Fatigue Life - Single Bearing Set-Up

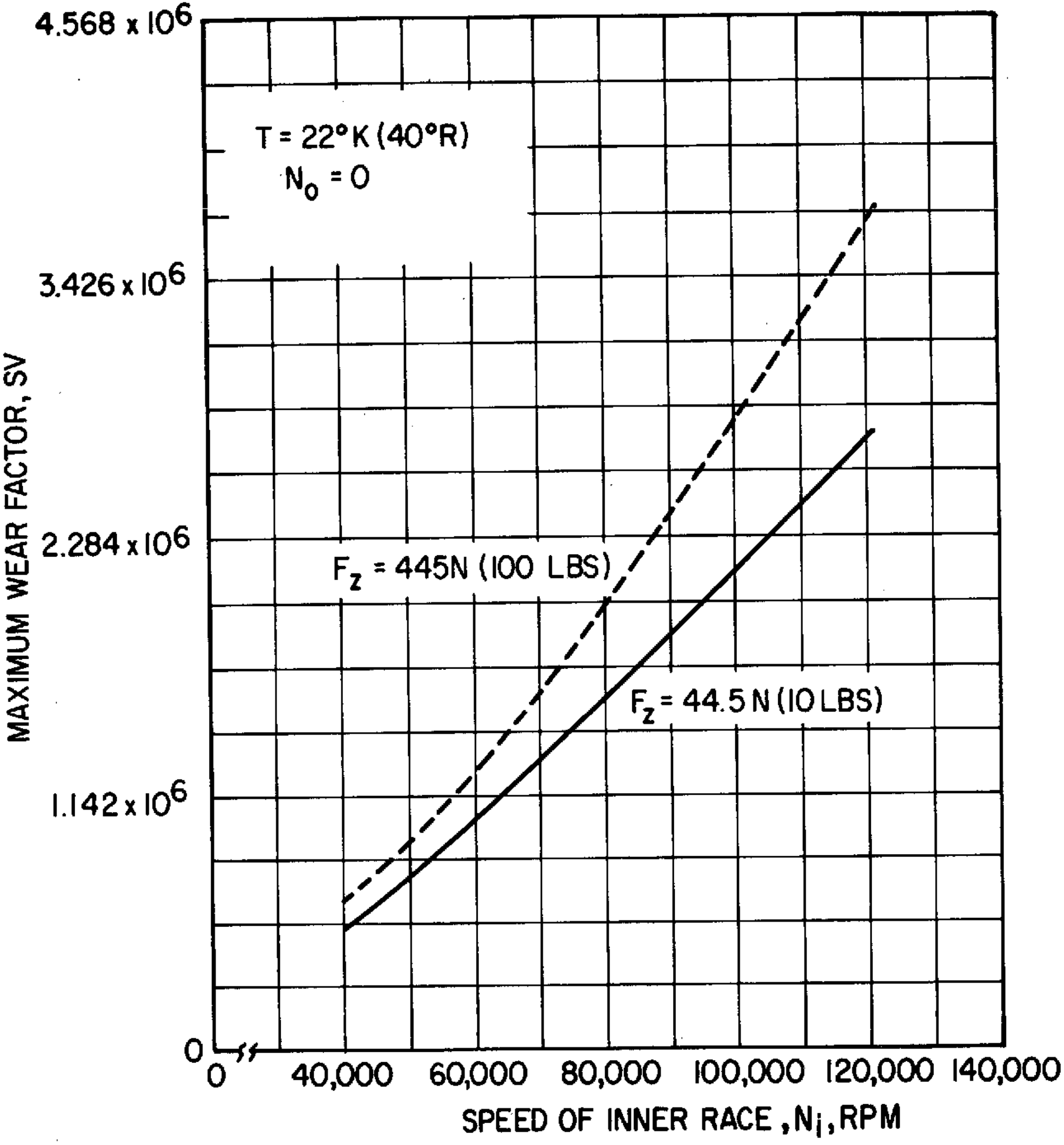

Fig. 28 Effect of Speed on Wear Factor — Single Bearing Set-Up

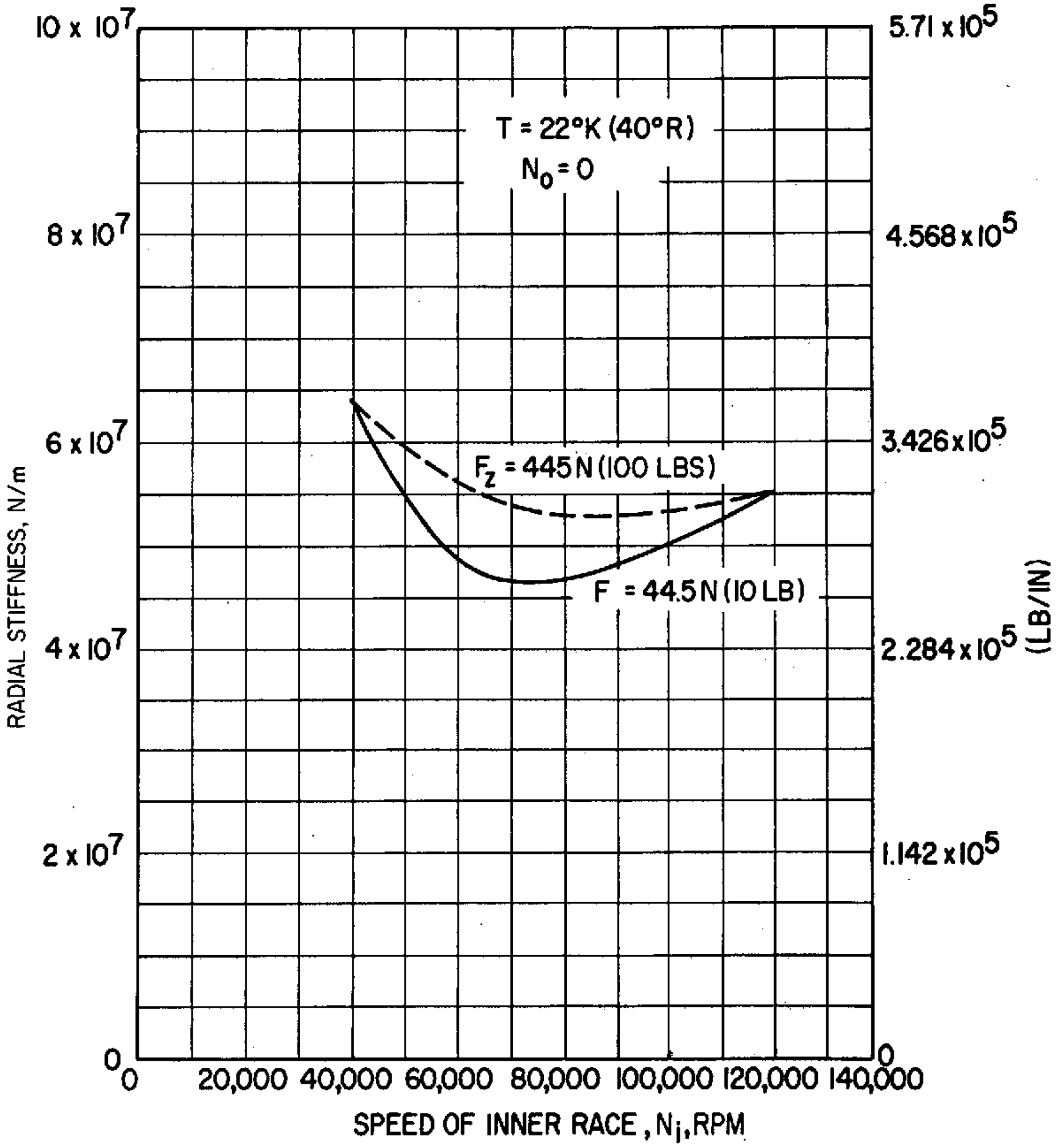

Fig. 29 Effect of Speed on Radial Stiffness - Single Bearing Set-Up

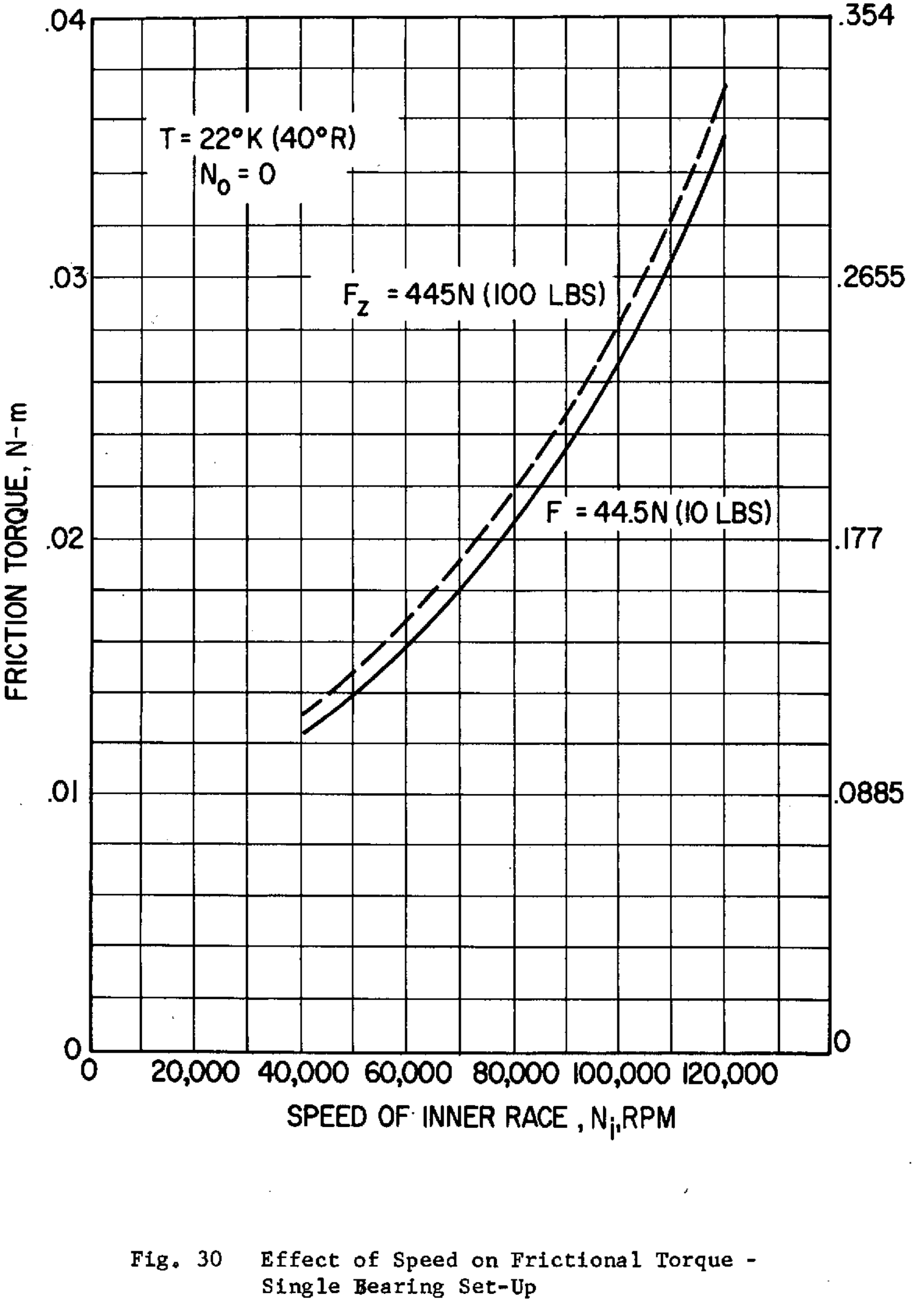

Fig. 30 Effect of Speed on Frictional Torque - Single Bearing Set-Up

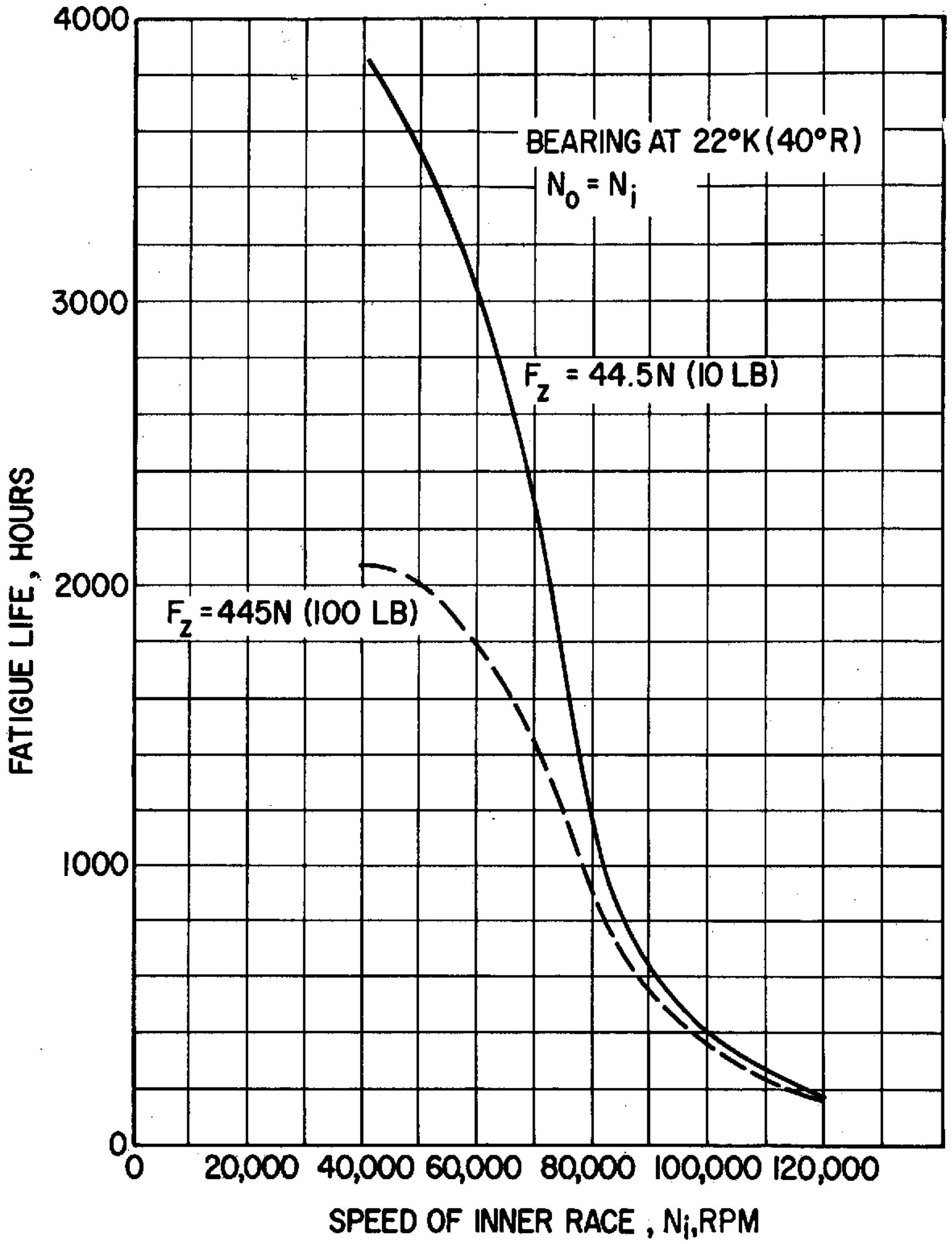

Fig. 31 Effect of Speed on Fatigue Life - Hybrid Bearing Set-Up

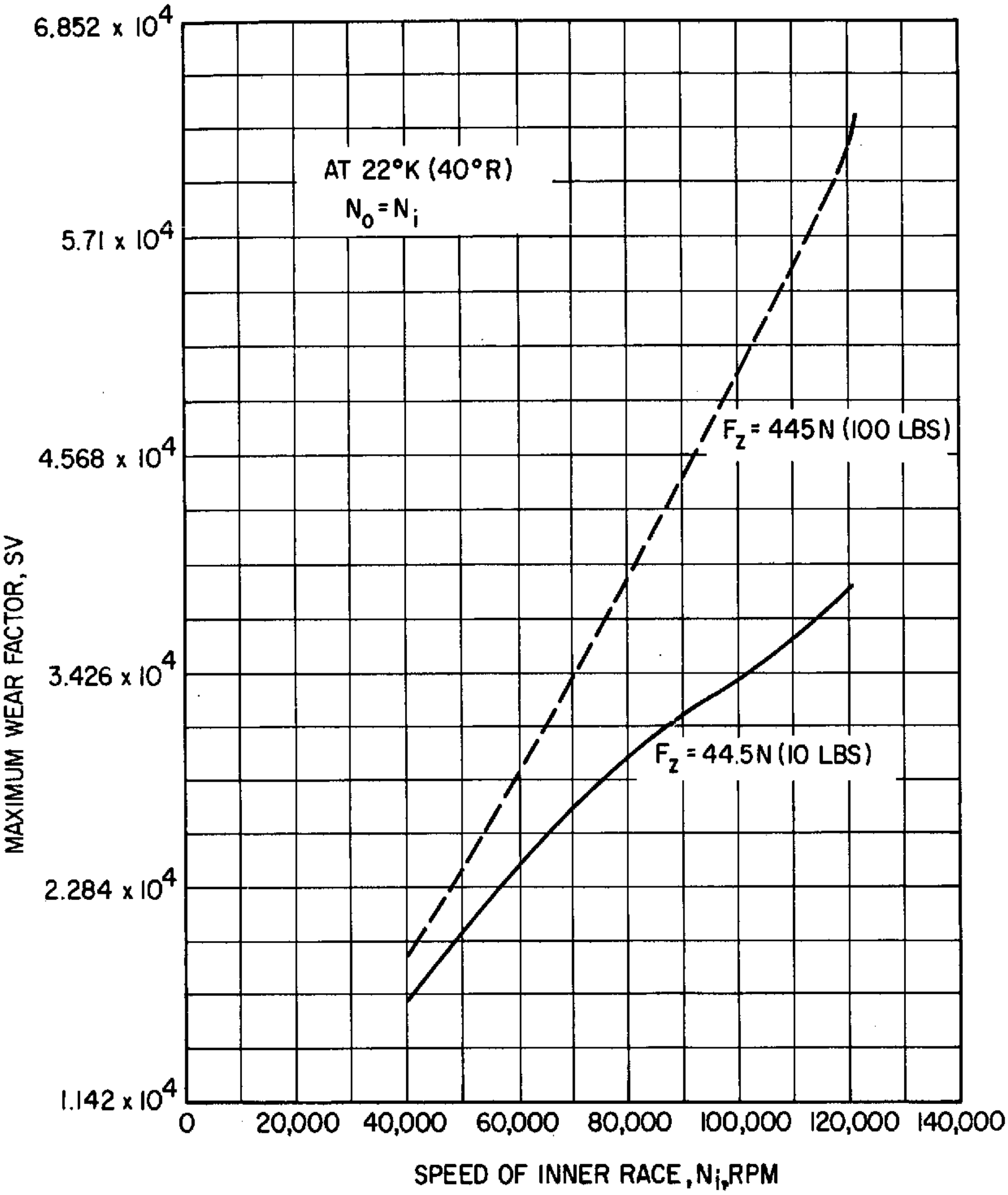

Fig. 32 Effect of Speed on Wear Factor - Hybrid Bearing Set-Up

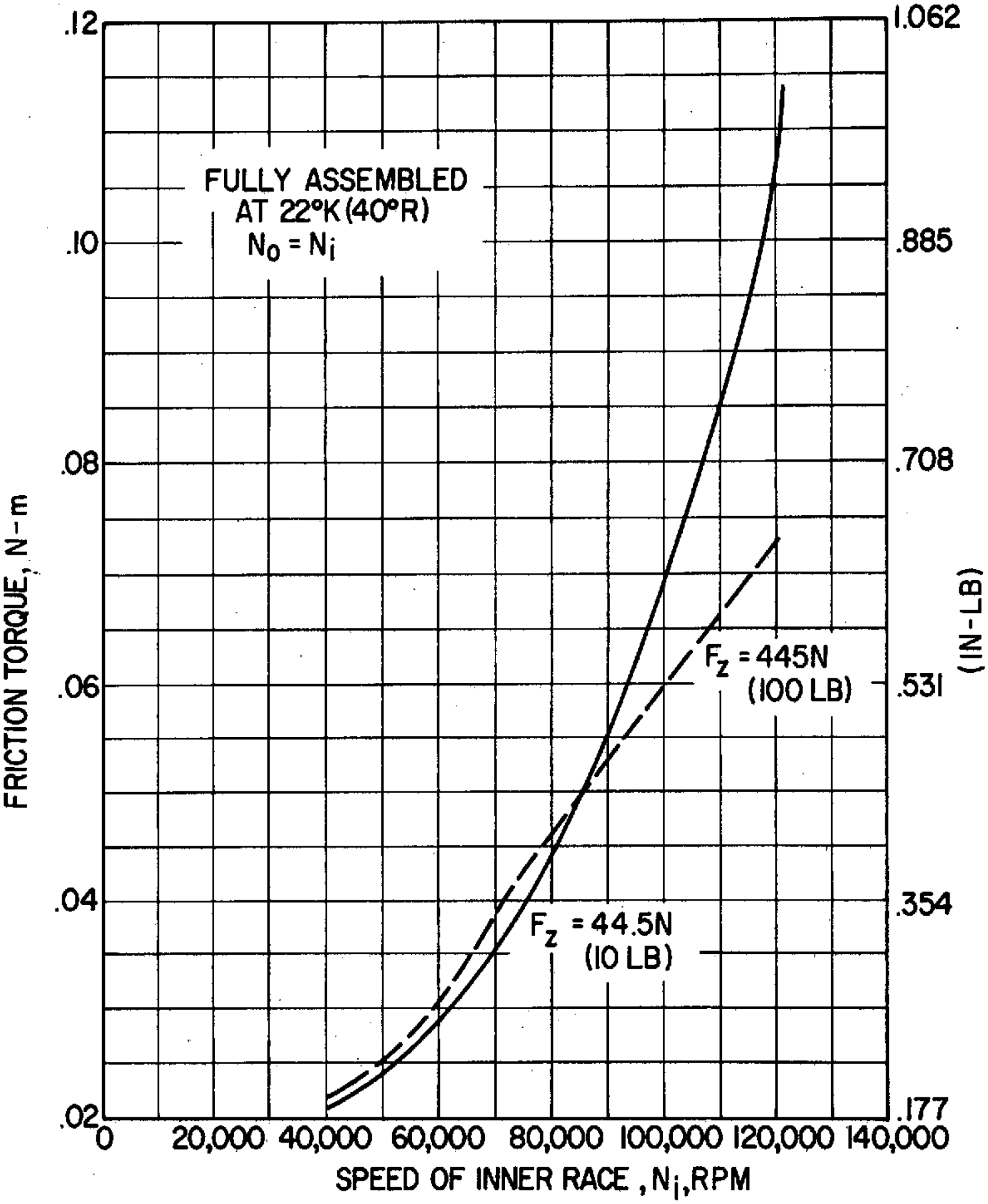

Fig. 33 Effect of Speed on Ball Bearing Frictional Torque - Hybrid Bearing Set-Up

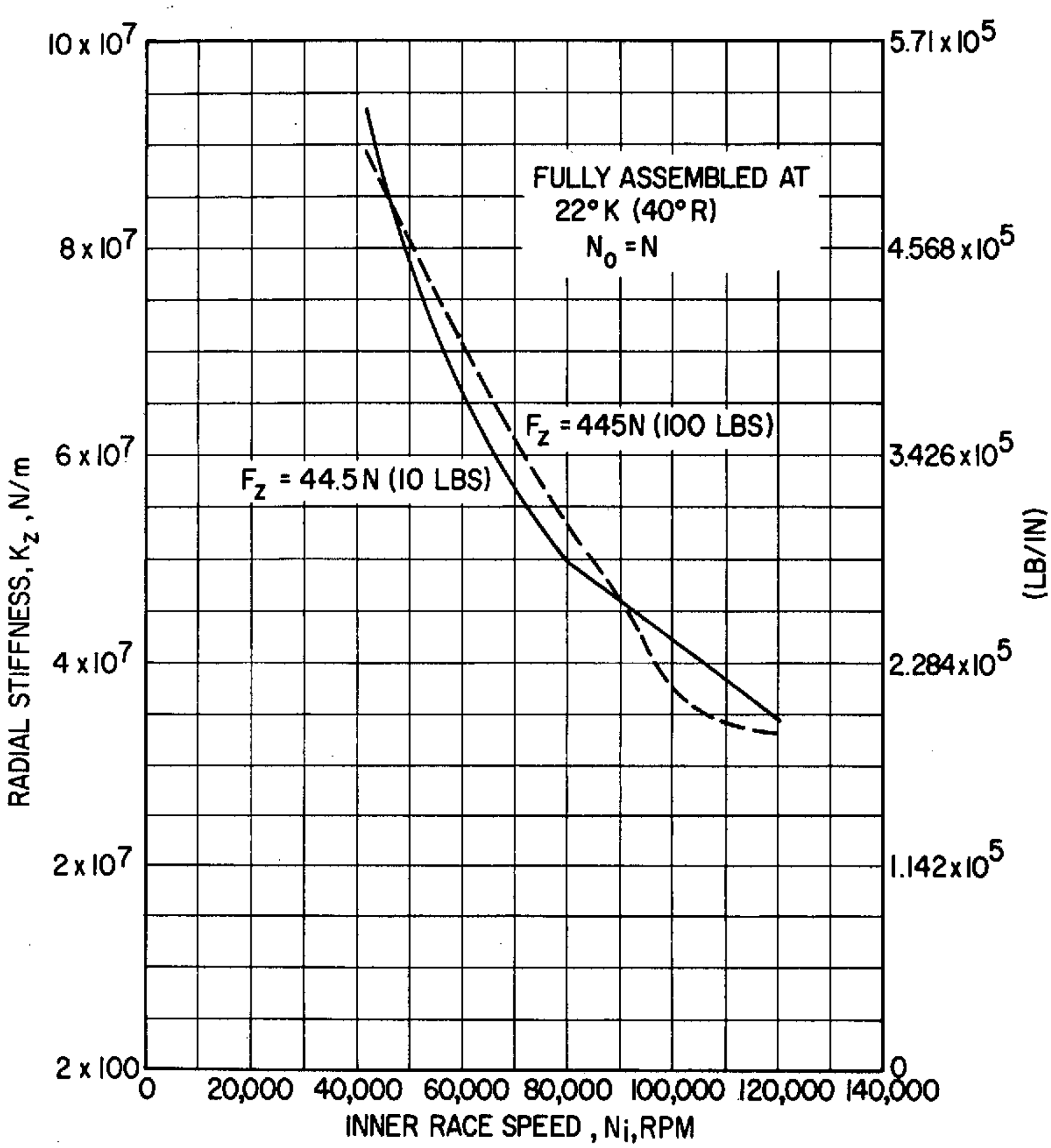

Fig. 34 Effect of Speed on Radial Stiffness - Hybrid Bearing Set-Up

The contribution of radial load (within the 44.5 N - 445. N range) to friction is minor, since the predominant frictional forces are ball inertia generated. This also explains the variation in torque with speed shown in Figure 30.

Hybrid Bearing Supported System - The performance characteristics of the hybrid bearing are presented in Figures 31 - 34. The computer calculations were based on the assumption that the outer race speed approximately equals that of the inner race. Relative growth caused by outer and inner race rotation has been accounted for, as has the effect of operations at cryogenic temperature levels. As can be seen from Figures 31 and 32, the fatigue life of the bearing is appreciably increased, and the effect of load on fatigue life between 80,000 and 120,000 rpm is negligible. The SV values, shown in Figure 32, are down by close to two orders of magnitude from those obtained with the ball bearing support system.

These results are not surprising since, theoretically speaking, once the relative velocity has decreased to zero, the fatigue life becomes infinite and the SV indicator drops to zero eliminating the probability of wear. It is this behavior of the ball bearing within a hybrid bearing set-up that renders the use of a hybrid bearing attractive.

The friction torque shown in Figure 33 exhibits characteristics which are not usually expected. Thus, up to approximately 80,000 rpm the torque is only slightly affected by the increased radial loading. Above 80,000 rpm, the torque for the 445 N (100 lb) radial load rises at a reduced rate as the speed increases; at the same time the torque of the 44.5 N (10 lb) loaded bearing keeps on increasing at a higher rate. The reason for this is that at about 80,000 rpm, the balance of forces with the 445 N (100 lb) radial load and 445 N (100 lb) preload causes one of the balls to become unloaded. At 120,000 rpm only five of the ten balls remained loaded. The other balls, having lost contact with the inner race, are thrown out against the rotating outer race and rotate with it. In reality, this behavior will cause the free balls to slide on the outer race, bringing about an increase in torque over that presented in Figure 33 for the 445 N (100 lb) radial load.

The ball bearing stiffness is not sensitive to radial load (see Figure 34), but does vary with speed, decreasing as the speed increases.

Comparing the behavior of the ball bearings selected for the two designs -- the bearings employed in the exclusively ball bearing supported system will yield lower fatigue life and higher SV values (higher wear) than the bearing employed in the hybrid system, providing the ball bearing employed in the hybrid system operates as a unit (difference between outer and inner race rotation not to exceed 1000 rpm at 120,000 rpm shaft speed). It is expected that fatigue life and wear will be critical items in this application, hence an appreciable increase in fatigue life combined with a reduction in wear should contribute to an increase in turbo-pump reliability. These factors will have to be weighed against complexity in design and rotor-dynamic stability.

The ball bearing stiffness in the hybrid mode of operation is of the same order of magnitude as that for the ball bearing mode. The stiffness variation with speed is greater in the hybrid mode, while the sensitivity to load changes appears to be somewhat more pronounced in the ball bearing mode.

The bearing torque is appreciably higher for the hybrid mode of operation. This is mainly due to increased centrifugal inertia forces. That does not necessarily mean that the power consumption is also higher since the relative speed at which the ball bearing operates in the hybrid mode is much lower than that for the ball bearing mode of operation. A detailed discussion of the hybrid bearing follows in the next section.

B. Hybrid Bearing Design

The hybrid bearing configuration selected for this application employs a duplex-mounted set of rolling-element bearings in series with a fluid-film bearing. The hybrid bearing arrangement shown in Figure 26 is designed to minimize the shortcomings of rolling-element and fluid-film bearings operating in LH_2, taking at the same time, advantage of their positive characteristics. Specifically, the hybrid bearing configuration minimizes the wear within the rolling-element bearing during operation by a reduction in the relative speed of the rolling-element bearing components. Similarly, the start-stop wear encountered on fluid-film bearings is relieved by the fact that starts and stops occur on the rolling-element bearings and as soon as the pressure within the system rises to the point where it is capable of sustaining the radial loading, the fluid-film bearings become activated. Once activated, the system operates on a fluid-film, which at least theoretically assures an infinitely high life. A detailed discussion of the fluid-film and rolling-element bearing design for the hybrid bearing is given in the following report sections.

1. Fluid-Film Bearing Component Design

An important element in the series hybrid journal bearing is the fluid-film bearing. The extremities of the environment, and the peculiar properties of liquid hydrogen give rise to some unique considerations in the design of the fluid-film bearing, as will be brought out in the following discussion. The general objectives of the design are as follows:

(a) To select optimum fluid-film bearing for present application

(b) To provide details of predicted performance and performance limits for the selected bearing

(c) To establish a basis for extrapolation of performance predictions and measurement, under test conditions, to real pump application

The steps which are being followed to meet these objectives are:

(a) Identify important physical phenomena

(b) Determine relative importance of physical phenomena

(c) Select candidate geometries

(d) Identify important design constraints

(e) Perform preliminary sizing

(f) Establish preliminary performance predictions

(g) Perform trade-off studies between candidates

(h) Select design from bearing performance and systems considerations

(i) Make detailed performance predictions over load and speed range

(j) Correlate predictions with test data

The following technical discussion will cover items (c) through (i). A qualitative and quantitative discussion of important physical phenomena (items (a) and (b) above), is given in Appendix C.

a. Selection of Candidate Designs

The viscosity of liquid hydrogen is so low that a self-acting (hydrodynamic) bearing would not be able to provide the necessary load capacity. Thus, a hydrostatic bearing, which achieves its load capacity by means of external pressurization must be used. Unfortunately, the external pressurization induces flow through the bearing and this flow, which must be provided by the pump, represents a loss to the "pump efficiency account." Thus, it is desirable to seek a hydrostatic bearing design which minimizes flow.

The two configurations which have been selected as candidates, are shown in Figure 35. They will be referred to as design A and design B. Both are orifice-restricted hydrostatic bearings with no axial drain grooves. The significance of using no axial drain grooves is that leakage flow is minimized (at a slight penalty in load capacity).

The main distinguishing features between the two designs is the width and location of the pockets. Design A has two rows of narrow pockets. Design B has a single row of wide pockets. For the purpose of analysis, each row has been considered to consist of ten (10) pockets.

The hydrostatic performance of either configuration will be very similar. Some performance differences are to be expected in the relative importance of hydrodynamic and squeeze film effects. Thus, damping and cross-coupling stiffness values may be expected to differ slightly between the two.

b. Important Design Constraints

The important constraints which must be considered in designing the fluid-film bearing are:

- Maintain liquid in bearing cavity
- Match fluid-film torque with ball bearing
- Minimize destabilizing contributions
- Provide satisfactory direct stiffness
- Maintain adequate clearance at all speeds
- Minimize flow

The need to maintain liquid in the bearing cavity means that the heat generated in the film must be removed at such a rate as to avoid boiling of the hydrogen. A temperature rise of 5.6°K (10°R) has been imposed as a maximum (50 percent of the difference between inlet and critical temperature).

The need to match fluid-film torque and ball bearing torque is fundamental to the effective operation of the hybrid bearing. The fluid-film torque should be as low as possible.

The destabilizing influence of the fluid-film bearing results from the hydrodynamic cross-coupling stiffness referred to previously. There exists, for a fluid-film bearing, characterized by a set of direct and cross-coupling stiffness and damping values, a threshold frequency, below which the effective damping provided by the bearing is negative.

If the natural frequency of the rotor-bearing system falls below this frequency, then the system is potentially unstable. The magnitude of the cross-coupling stiffness influences the threshold frequency value and the absolute magnitude of the negative effective damping which occurs below this frequency. Thus, it is desirable to minimize the cross-coupling stiffness.

To provide satisfactory direct stiffness, means that the bearing must first of all be stiff enough to carry required gravity and unbalance loads and secondly, must result in system critical speeds which are away from important operating speeds and high enough to avoid instability. Thus, the direct stiffness is an important characteristic of the bearing.

To maintain adequate clearance at all speeds, means basically that, in establishing the nominal clearance, the variation in journal diameter due to changing centrifugal effects with speed must be accounted for. The operating clearance at the highest speed must be at a minimum to keep flow down, but cannot fall below a certain value at which the temperature rise becomes intolerable.

To minimize flow is important from a pump efficiency standpoint, although, of course, the flow must be sufficiently high that the heat is adequately carried away.

c. Preliminary Sizing

The length and diameter of the fluid-film bearing are closely dictated by available space and the size of the ball bearing. The remaining design variables which may be adjusted to influence performance are clearance, pocket size, pocket axial location, and inlet orifice diameter. Of these, previous investigations of similar bearings (References 10-13) indicate that, for either configuration, the side land (dimension L_a in Figure 35) should be 25 percent of the total bearing length and that, with a large number of pockets, the total circumferential extent of all pockets in a row should be approximately 30 percent of the total circumferential extent πD (Reference 13).

Accordingly, Table 9 lists the dimensions of the bearing, either as

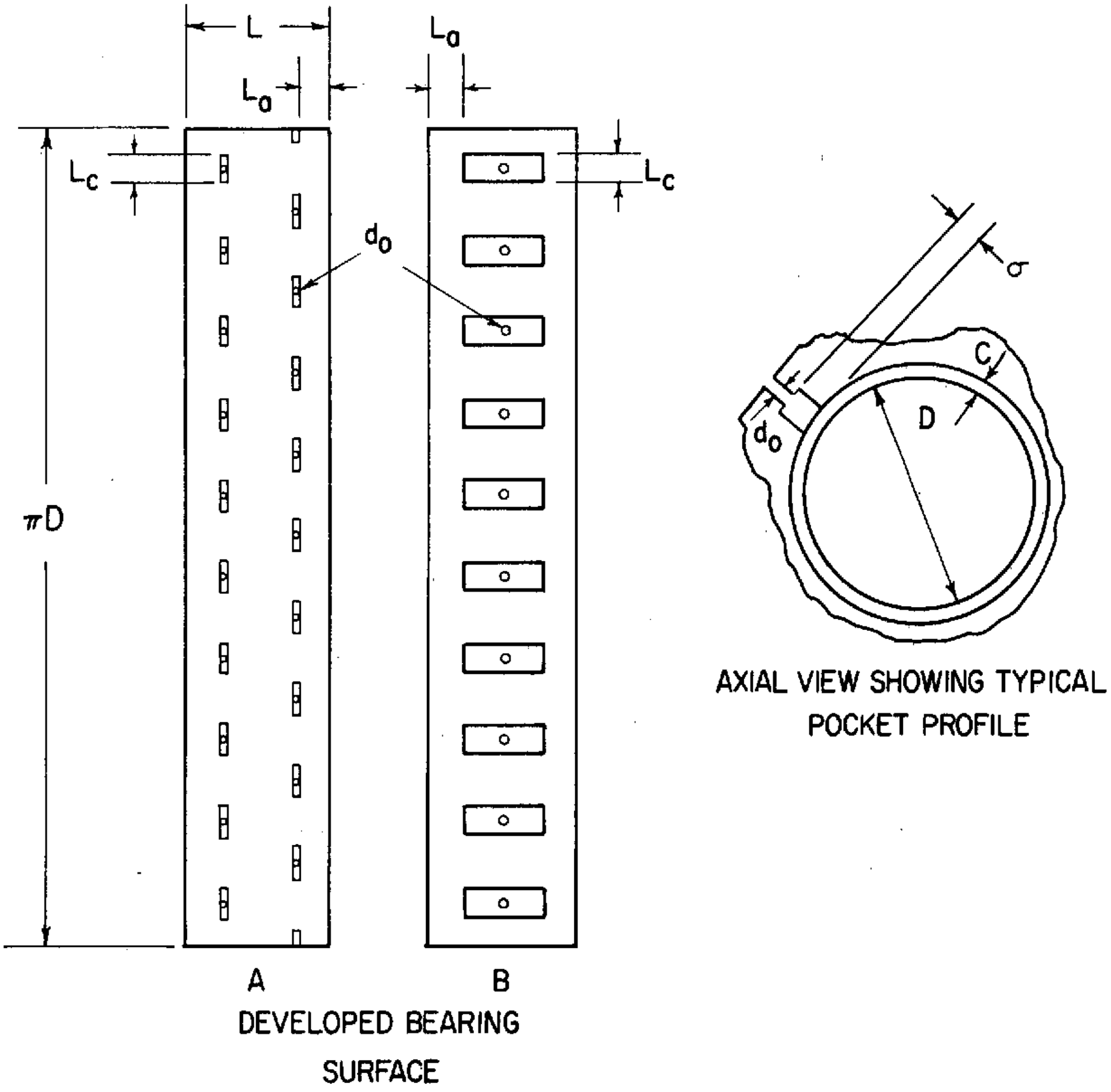

Fig. 35 Fluid-Film Bearing Candidate Geometries for Hybrid Operation

fixed values or, in the case of variables which remain to be determined by the design analysis, by a range.

TABLE 9

PRELIMINARY BEARING DIMENSIONS

Length	0.0234 Meters	(.925 inch)
Diameter	0.0419 Meters	(1.6497 inch)
Side Land	0.00638 Meters	(0.250 inch)
Pocket Length	.0039 Meters	(0.155 inch)
No. of Pockets	10 per Row	
Clearance	2×10^{-5} Meters	(.0008 inch)
Orifice Diameter	$(2.5 \text{ to } 10) \times 10^{-4}$ Meters	(.01 inch to .04 inch)

The clearance selection resulted from preliminary analysis by Dr. Constantinescu. Figure 36 shows the variation in flow and temperature rise due to friction for the A-design as determined by Dr. Constantinescu. The supply pressure was assumed to be 8.6×10^6 N/m^2 (1250 psia) and the ambient pressure 1.72×10^6 N/m^2 (250 psia). It may be seen that, below a clearance of 2×10^{-5} meters (.0008 inch), the temperature rise exceeds 5.6°K (10°R). At the same time, it is a disadvantage, from a flow standpoint, to use a larger clearance than necessary, and so the clearance at 120,000 rpm is tentatively set at 2×10^{-5} meters (.0008 inch), to minimize flow within the constraint of acceptable temperature rise. This clearance value was used during the early stages of the design process. However, the possible need to modify it if detailed performance of the bearing or rotor-bearing system so dictates is recognized.

d. Trade-Off Study Between Candidate Geometries

The two candidates, designs A and B, have been defined. Provided the number of pockets is large (> 6 per plane), the hydrostatic performance (direct stiffness and flow) is expected to be very similar for either bearing. However, the large pocket area of design B is expected to have two effects. Firstly, it will influence damping because of the

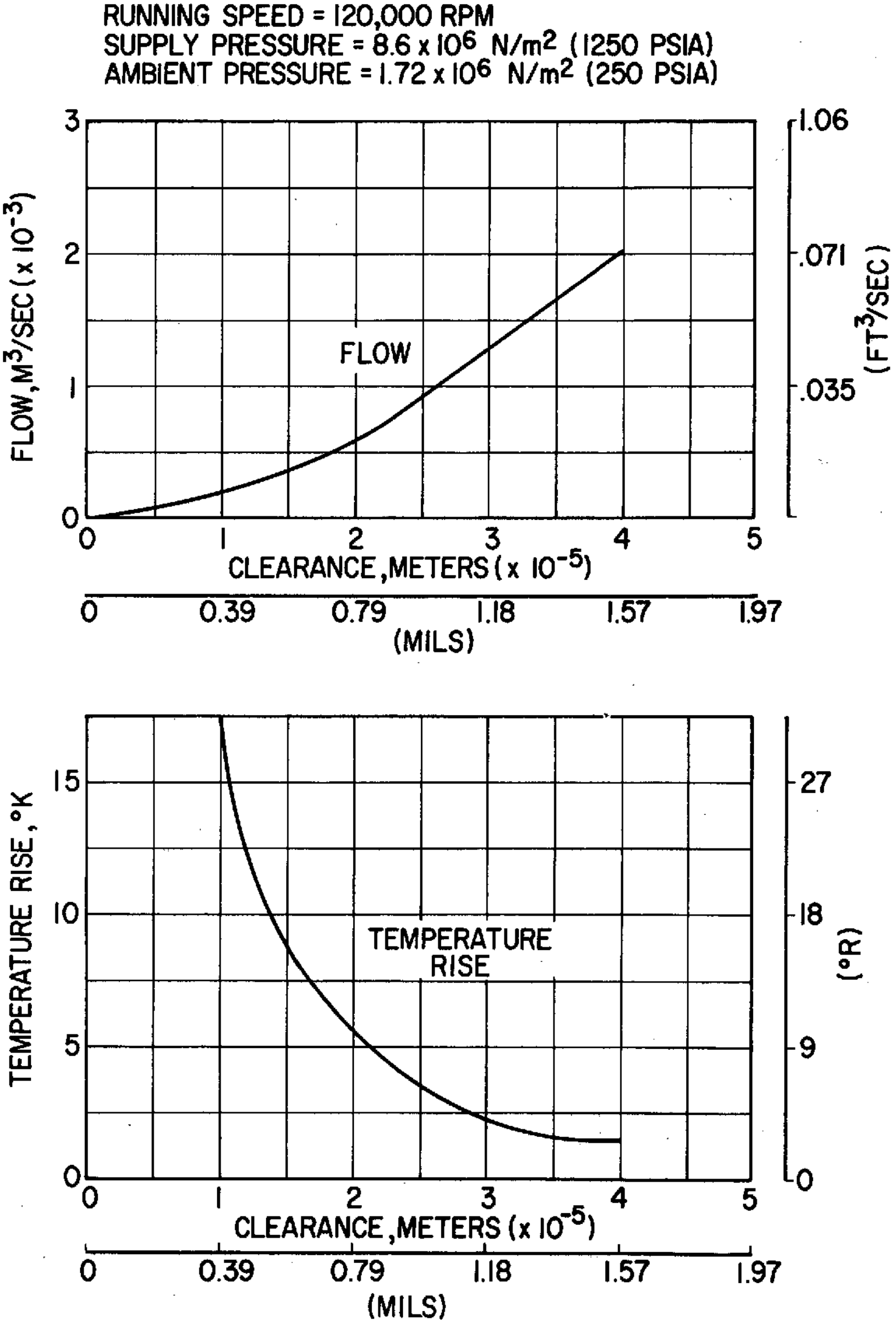

RUNNING SPEED = 120,000 RPM
SUPPLY PRESSURE = 8.6 x 10⁶ N/m² (1250 PSIA)
AMBIENT PRESSURE = 1.72 x 10⁶ N/m² (250 PSIA)

Fig. 36 Effect of Clearance on Flow and Temperature Rise of Fluid-Film Bearing larger area of wide clearance and also because of increased significance of capacitive effects with a compressible fluid. Secondly, the hydrodynamic action will be less pronounced for design B because the surface is more broken up. To provide a meaningful comparison on these accounts it was judged most important to include compressibility effects in the analysis. This was done at a penalty in absolute accuracy, since Bernoulli and time-dependent inertia effects had to be neglected. Since orifice diameter is an important factor in performance, its influence was eliminated by optimizing orifice diameters of each design for direct stiffness. Table 10 shows the results of the comparison.

As anticipated, the most significant differences occur in terms of cross-coupling stiffness and direct damping. A has higher values for both, and the advantage of A is most pronounced in terms of damping. However, since cross-coupling effects act against damping as a destabilizing effect, the advantage offered by design A is not clear-cut.

e. Design Selection

While the differences revealed in the trade-off study are not large, the A design has been selected. Even though somewhat arbitrary from a performance standpoint, the choice also reflects previous successful design experience with this configuration for a lower speed cryogenic application (Reference 11). This choice also reduces to zero the significance of the capacitive effects.

Having selected the configuration, there remains the choice of orifice diameter and clearance. Clearance is established at 2×10^{-5} (.0008 in.) meters at 120,000 rpm.

The influence of orifice diameter on stiffness at 100,000 rpm is shown in Figure 37.

The value of orifice diameter in the range $5.0 \rightarrow 7.0 \times 10^{-4}$ (.02 to .028 in.) meters promises to provide good stiffness, with an optimum close to 5.75×10^{-4} meters (.0225 in.).

TABLE 10

COMPARISON OF DESIGNS A & B

(Compressibility included; inertia effect neglected)
(Orifice Diameter Optimized)

	A	B	% Difference
Speed, rpm	120,000	120,000	---
Clearance, Meters (inches	2×10^{-5} (.0008)	2×10^{-5} (.0008)	---
Orifice Diameter, Meters (inches)	7.5×10^{-4} (.030)	1.075×10^{-3}(.045)	---
Direct Stiffness, N/m (lb/in)	2.783×10^{8} (1.59×10^{6})	2.735×10^{8}(1.56×10^{6})	1.8%
Flow, Kg/sec (lb/sec)	.110 (.242)	.117 (.257)	6.4%
Torque, N-m (lb-in)	.18 (.04)	.18 (.04)	0.
Cross-Coupling Stiffness, N/m (lb-in)	2.420×10^{7} (1.38×10^{5})	2.241×10^{7}(1.28×10^{5})	7.4%
Damping (Synchronous) N/m (lb/in)	4.264×10^{7} (2.44×10^{5})	3.537×10^{7} (2.02×10^{5})	17.0%

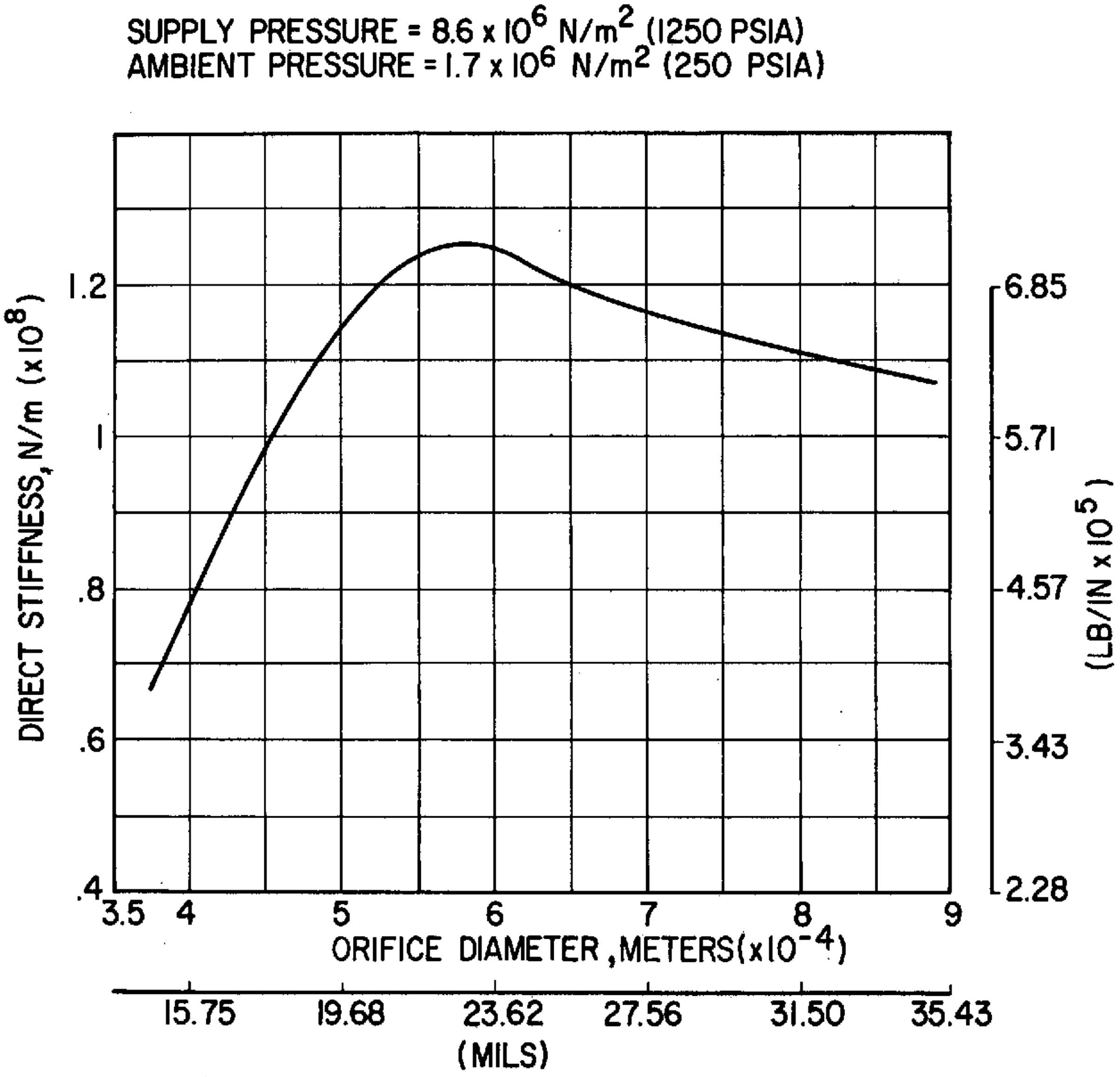

SUPPLY PRESSURE = 8.6 x 10^6 N/m^2 (1250 PSIA)
AMBIENT PRESSURE = 1.7 x 10^6 N/m^2 (250 PSIA)

Fig. 37 Fluid-Film Bearing Stiffness as a Function of Orifice Diameter (100,000 rpm)

f. Performance Predictions

In Figure 38, the influence of orifice diameter on the variation of stiffness and flow with speed is demonstrated. Superimposed on this figure is the variation of clearance with speed due to centrifugal action. Two orifice diameters [5.08 and 6.35 x 10^{-4} (.02 and .025 in.)] have been considered.

The smaller orifice size offers significantly reduced flow at low speed and a substantially higher stiffness at 120,000 rpm. This combination would appear to be advantageous, except that the mean temperature rise will now reach 5.7°K (10.3°R) at 120,000 rpm. This temperature rise is acceptable, but should be regarded as a limit, such that lower flow designs should not be considered.

The final choice of orifice diameter is 6.35 x 10^{-4}/6.00 x 10^{-4} m (0.025/0.026 in.)

Figure 39 illustrates typical variation of flow and stiffness with supply pressure at 100,000 rpm for an orifice diameter of 6.35 x 10^{-4} meters (.025 inch). The stiffness follows almost a linear variation, whereas the flow variation levels off at high pressures as a result of the increasing level of Poiseuille turbulence.

Figure 40 shows the influence of speed on fluid-film torque and on temperature rise. Comparison with the ball bearing torque predictions will show the fluid-film torque to be consistently lower within the speed range to 120,000 rpm. As the speed increases beyond 100,000 rpm, the temperature rises sharply. While acceptable up to 120,000 rpm for this configuration, the temperature rise is an important performance parameter and must be considered when contemplating future design changes which might increase the power loss or decrease the flow. Final fluid-film bearing dimensions were established upon completion of the rotor-dynamic stability studies.

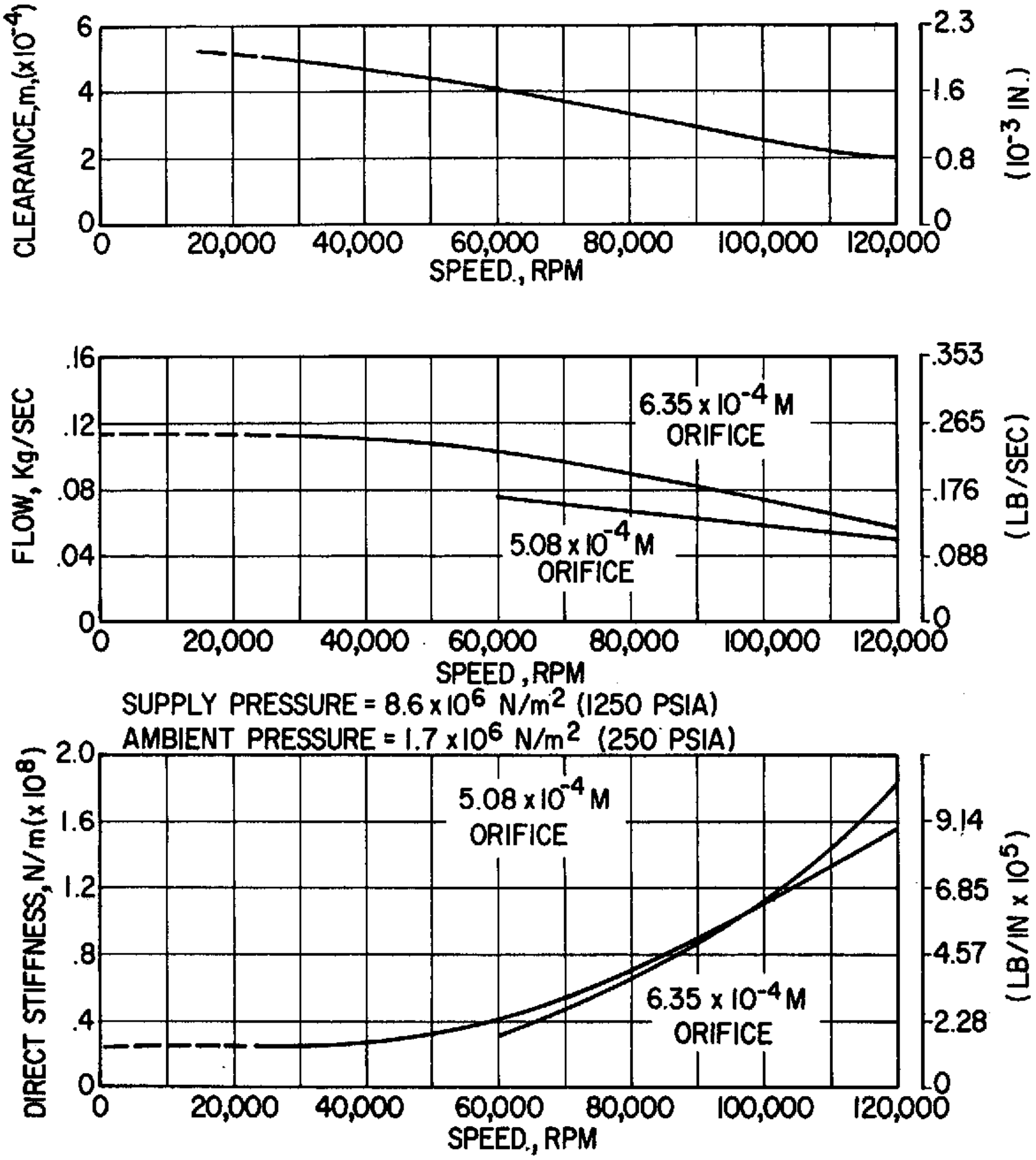

Fig. 38 Performance of Design A — Influence of Orifice Diameter and Speed

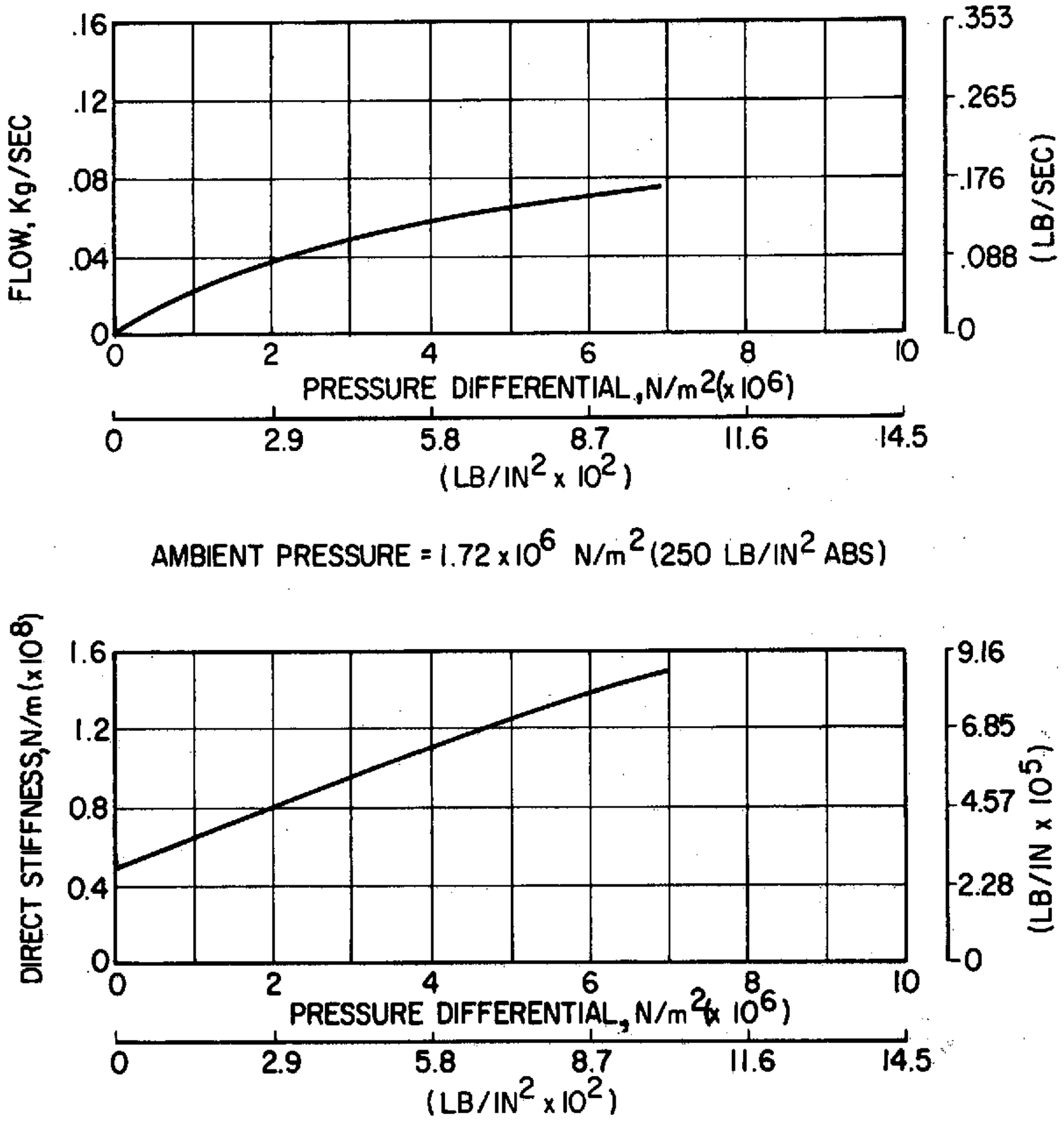

Fig. 39 Performance of Design A — Influence of Supply Pressure (100,000 rpm, 6.35×10^{-4} M Orifice)

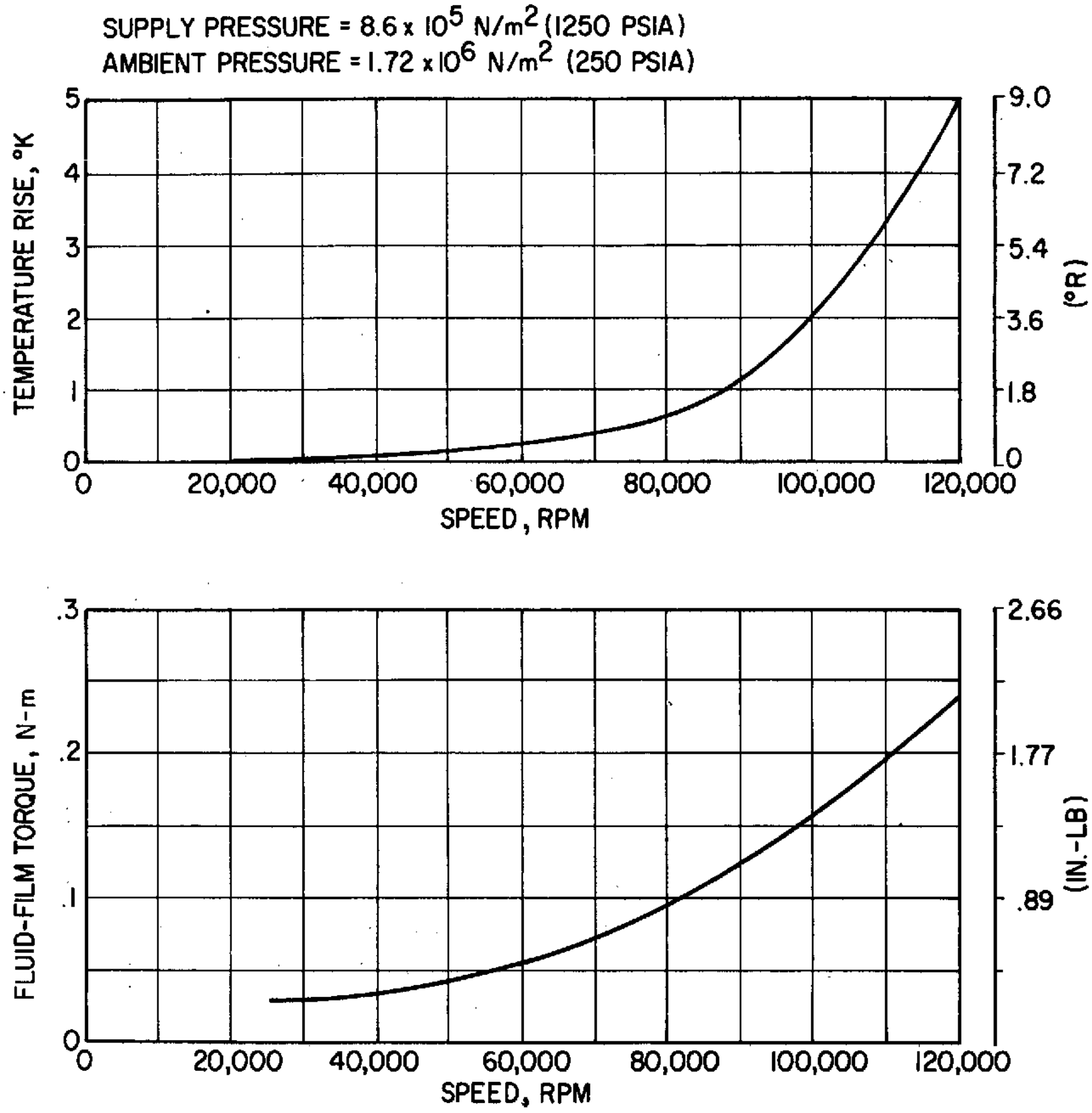

Fig. 40 Performance of Design A — Fluid-Film Torque and Temperature Rise

C-2

2. Ball Bearing Design

The design details of the ball bearing component which forms part of the hybrid bearing have been discussed in Sections A4 and A5. The component will consist of an extra-light series bearing employing a complement of ten balls, each ball being 4.76 mm (0.1875 in.) in diameter. Two ball bearings, preloaded against one another, as shown in Figure 26, will be employed. All detailed bearing dimensions and specifications are shown in Appendix D.

3. Hybrid Bearing Performance

The performance of the hybrid bearing is primarily dependent upon the torque balance between the fluid-film and duplex ball bearing set. As was previously indicated, the ball bearing acts as a clutch through which the torque required to drive the fluid-film bearing must be transmitted. To accomplish this, the torque of the ball bearing must be higher or at least equal to that of the fluid-film bearing at any given speed.

A plot of the ball bearing and fluid-film bearing torque vs. speed of the outer ring is shown in Figure 41. The ball bearing torque shown was calculated on the RECAP Program and multiplied by an experience factor of three. The ball bearing torques are based upon outer and inner ring rotation, where the speed of the outer ring is close to that of the inner ring.

The results indicate that the ball bearing has ample capacity to transmit the torque required to drive the fluid-film bearing in the hybrid design arrangement. Note that the design is conservative, and torque transmitability is possible, even without the experience factors employed to raise the ball bearing torque to realistic levels. The drop in torque with the higher radial loads at high speeds is due to the fact that the balls in the zone opposite to the radial load direction became disengaged from the inner race.

The program assumes that once the ball is disengaged, its contribution to torque drops to zero. This, in reality, will not be the case since the remaining link between the unloaded balls, the cage, and the outer race will result in additional torque transmission capability.

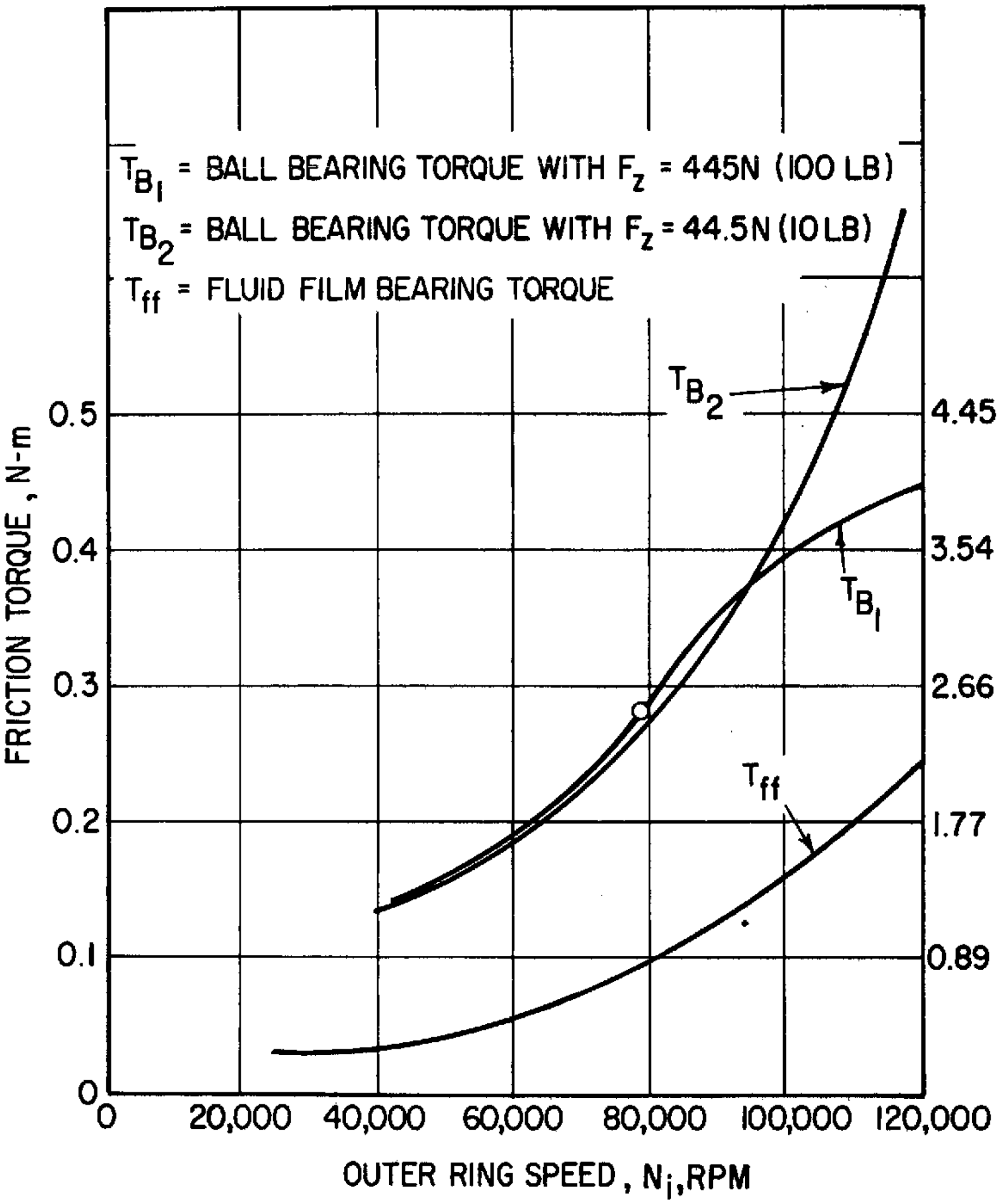

Fig. 41 Effect of Speed on Frictional Torque — Hybrid Bearing Design

C. Test Vehicle Design

To fully comply with the requirements of the small bearing technology program two related test vehicles were designed. Each of these vehicles provides unique features for evaluating particular bearing performance parameters. One test vehicle configuration is designed so it will accommodate all requirements for both single and duplex ball bearing testing. The second vehicle, derived from a majority of parts found in the ball bearing tester is fitted with the necessary parts for hybrid bearing testing.

Each of the test vehicle configurations has been extensively analyzed. A description of each configuration, including the pertinent analytical results, is found in the following report sections.

1. Ball Bearing Tester

The ball bearing tester has been designed to provide two functions. One function allows the evaluation of the test ball bearing's preload requirements at which time the rotor is supported on two single bearings. The second permits the execution of load-speed-life tests for the same bearings mounted in the form of two duplex sets.

The two test configurations, combined on one composite drawing are shown on Figure 42. All the housing parts common to both the single and duplex assemblies are identified first, and include the main housing ①, the end plate ②, the turbine nozzle spacer ③, the turbine bearing support plate ④, the turbine seal ⑤ and the turbine nozzle block ⑥. The turbine nozzle block contains both the forward driving nozzles and reversing jets required for deceleration control. In addition to the housing parts, many rotating and non-rotating components of the ball bearing tester are common to both assemblies and are intended for use in either single or duplex bearing tests.

A single rotor shaft ⑦ and drive turbine ⑧ will accommodate all test configurations and will require a minimum of replacement parts in order to satisfy any test set-up requirement. The shaft assembly is provided with a

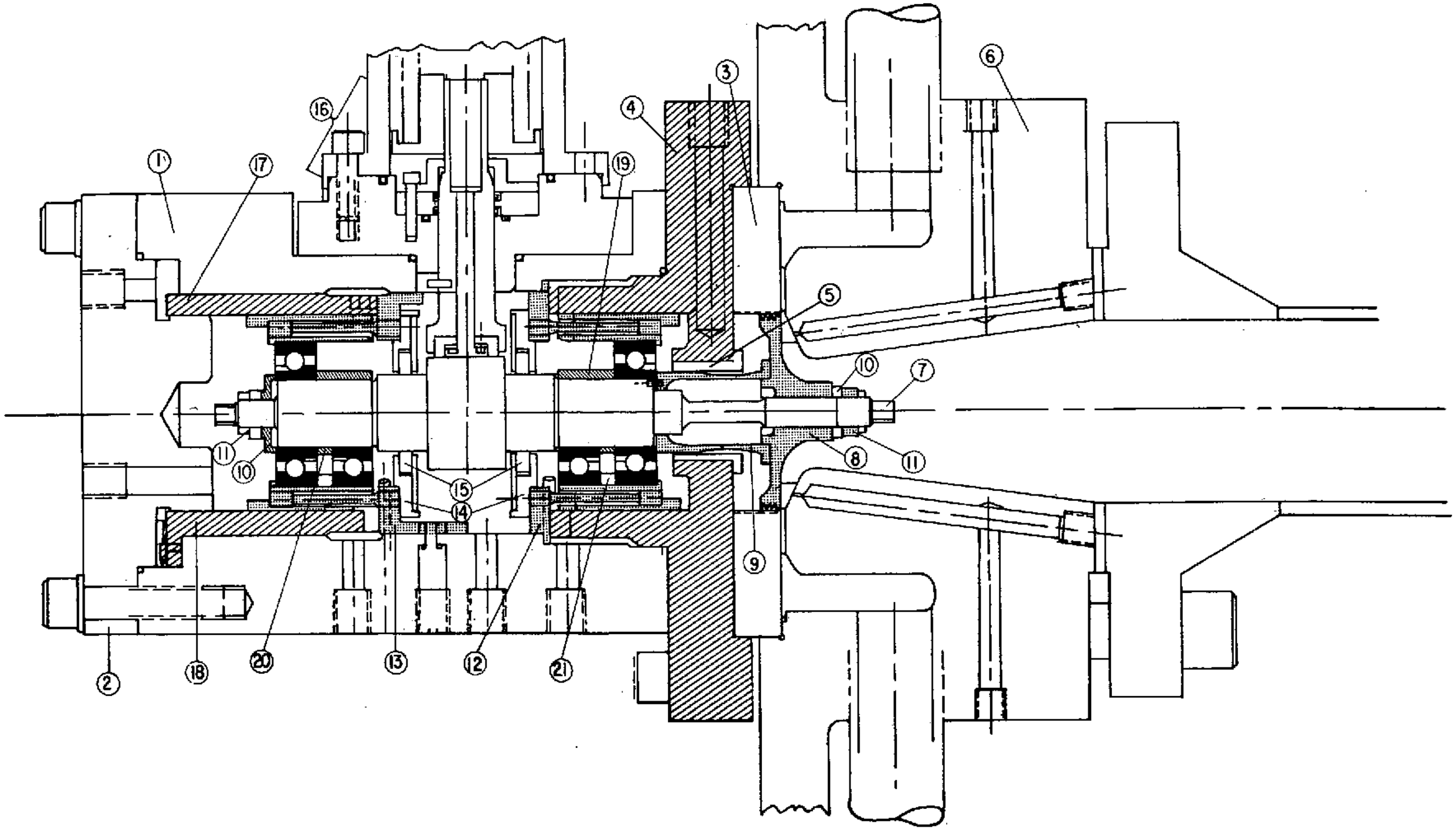

Fig. 42 Ball Bearing Tester

heat dam ⑨ in the form of a thin-walled cylinder, sized to reduce the heat flow along the shaft from the turbine to the test bearing area. The entire rotating assembly, including the test bearings and spacers are end-clamped with special washers ⑩ and nuts ⑪ .

Outer race support for the test bearings, Appendix D - MTI Specification 0232-43601-02, are provided by a similar pair of bearing mounts ⑫ and ⑬ . The bearing mount closest to the turbine ⑫ provides radial flexibility, but is end-clamped between the main housing ① and the turbine bearing support plate ④ to assure a fixed location for the rotating assembly. The bearing mount furthest from the turbine ⑬ , which also provides radial flexibility, is not clamped and is free to adjust its axial position as a result of either externally applied axial load or differential thermal expansion; an extended shoulder on bearing mount ⑬ is provided as an aid in maintaining alignment . Both bearing mounts are used for single as well as duplex bearing testing. Each bearing mount also provides the mounting surfaces for the bearing cavity seal holders ⑭ and bearing cavity seals ⑮ .

For test purposes, an axial and radial loader have been included in the vehicle design. The radial loader assembly consists of a balanced piston system identified as the radial loader assembly ⑯ ; a complete description of this assembly can be found in Appendix E. The radial loader is designed for use with both the single and duplex bearing test assemblies. In the event its use is not required, the entire assembly is removed and its penetration port sealed with a flat plate.

Axial load* is applied through a sliding piston ⑰ which is activated by the introduction of fluid to a cavity provided in the end cap ②. It is anticipated that the axial loader will only be used during single bearing tests, and that it will be replaced by a rigidly mounted spacer sleeve ⑱ when duplex bearing tests are conducted.

---

*The load pressure relationship for the axial loader is given by $F_A = 1.26 \times 10^{-3}$ ΔP where F_A is in Newtons. In the English system of units, $F_A = 1.955\ \Delta P$.

Several small rotor-mounted parts are also interchanged when switching from single to duplex testing. A single long rotor sleeve ⑲ is used in conjunction with single bearing tests, a smaller sleeve ⑳ and a combination spacer-preload spring assembly ㉑ is used when switching to duplex testing.

The spacer-preload spring is a precision-ground stepped washer which is designed to produce a 445 N (100 lb) preload at acceptable stress levels under test conditions. Adjustment of the spring thickness will provide a new preload should a different level of preload be required at some future date.

Several important design considerations were examined prior to concluding the design effort on the ball bearing tester. This report section describes the effort undertaken and the results obtained in the design.

a. Rotor Dynamics

The rotor configuration illustrated in Figure 42 was subjected to an extensive study of its dynamic behavior with respect to critical speed and unbalance response. Two model rotors, one for the single bearing and one for the duplex bearing tester were defined. These models are shown in Figure 43 (Figure 43-a shows the single bearing and Figure 43-b, the duplex tester). Each rotor model is marked to indicate calculation stations where properties of the rotors change and where the turbine's gravity center and bearing center planes are located. A separate independent calculation was performed to determine the dynamic properties of the turbine wheel. The wheel properties, which are summarized in Table 11, are used as inputs for the critical speed calculations.

TABLE 11

DRIVE TURBINE DYNAMIC PROPERTIES

Polar Mass Moment	:	1.69×10^{-5} Kg - m^2	(.058 lb-in^2)
Turbine Weight	:	0.042 Kg	(.092 lb)
Cross Section Area	:	$1.74 \times 10^{-4} m^2$	(.269 in^2)
Radius of Gyration	:	2.00×10^{-2} m	(.786 in)
Average Tangential Stress	:	1.08×10^{8} N/m^2	(15,637 lb/in^2)

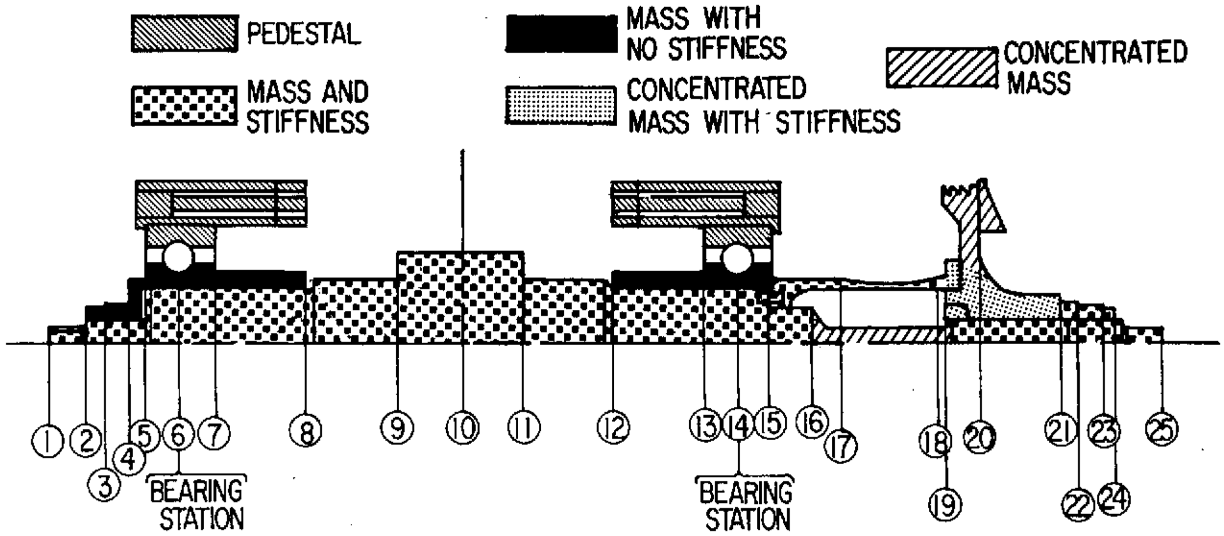

(a) Single Bearing Tester

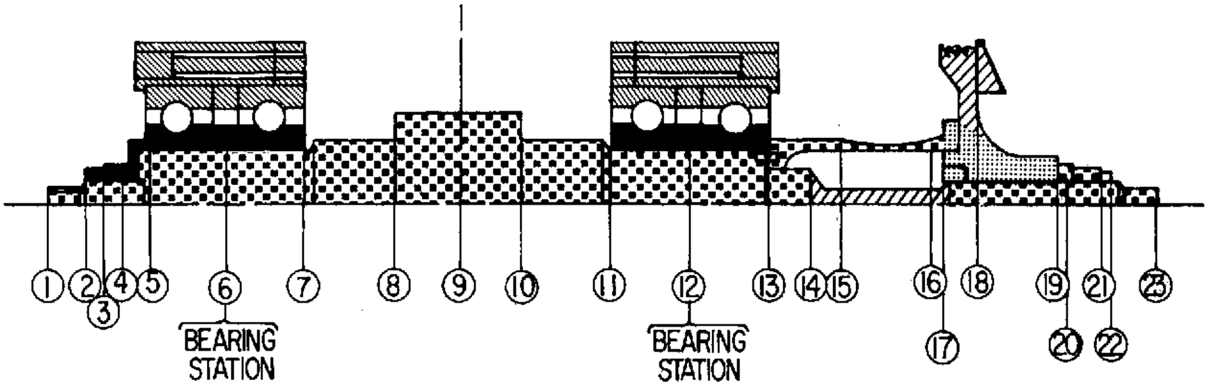

(b) Duplex Bearing Tester

Fig. 43 Dynamic Model: Ball Bearing Tester

The initial critical speed calculations for both ball bearing testers were based on the assumption that the ball bearing outer race seats were rigidly supported (infinite stiffness). Mathematically, the critical speed calculation was performed on the simplified dynamic model shown on Figure 44-a where K_b is the stiffness of either a single or a duplex bearing, M the rotor mass, I_p its polar moment of inertia, and I_t its transverse moment of inertia. Each critical speed calculation was made with the ball bearing stiffness as a dependent variable, resulting in a critical speed map that provides the speed at which a critical speed occurs for any level of ball bearing stiffness. Figure 45 shows the rigid pedestal critical speed maps for both the single and duplex bearing testers and includes the variation in bearing stiffness with speed. Interpretation of either critical speed map is obtained by following the ball bearing stiffness curve from a low to a high speed, the cross-over point where the stiffness and critical speed curves intersect indicates the actual speed at which the critical resonance occurs. As an example, the single bearing tester would experience a critical resonance condition at 90,000 rpm.

The location of critical speeds within the testing speed ranges for both the single and duplex testers is undesirable and is to be avoided when possible. One means of removing critical speeds from a specific speed range is to lower the effective stiffness of the ball bearings. For example, if the duplex bearing tester had an effective bearing stiffness of 1.00×10^8 N/m (5.72×10^5 lb/in), no critical speeds would be present above 60,000 rpm.

One method of reducing the effective ball bearing stiffness is to introduce an intermediate spring between the bearings outer race and the tester housing. A usual device employed in many ball bearing systems is a flexure-mounted ball bearing housing which provides both a soft spring mount and a damping device. Figure 44-b indicates the schematic model for the flexure mounted bearing. In this figure, K_b remains the ball bearing stiffness with the flexure or pedestal stiffness K_p, the pedestal damping B_p and the spring mount mass M_p. The actual mount

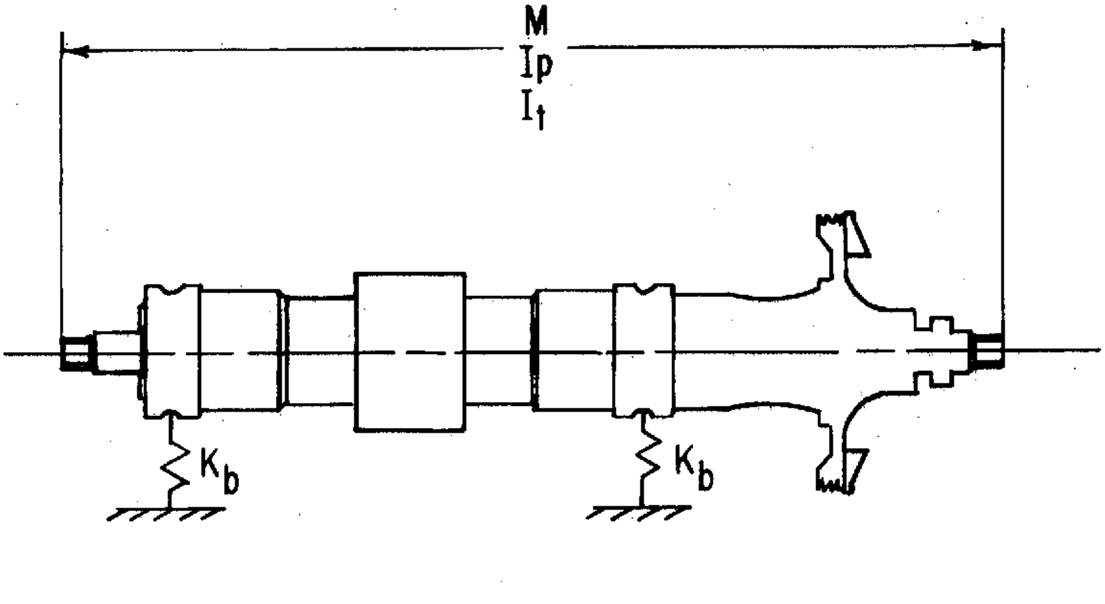

(a) Rigidly Mounted Ball Bearing

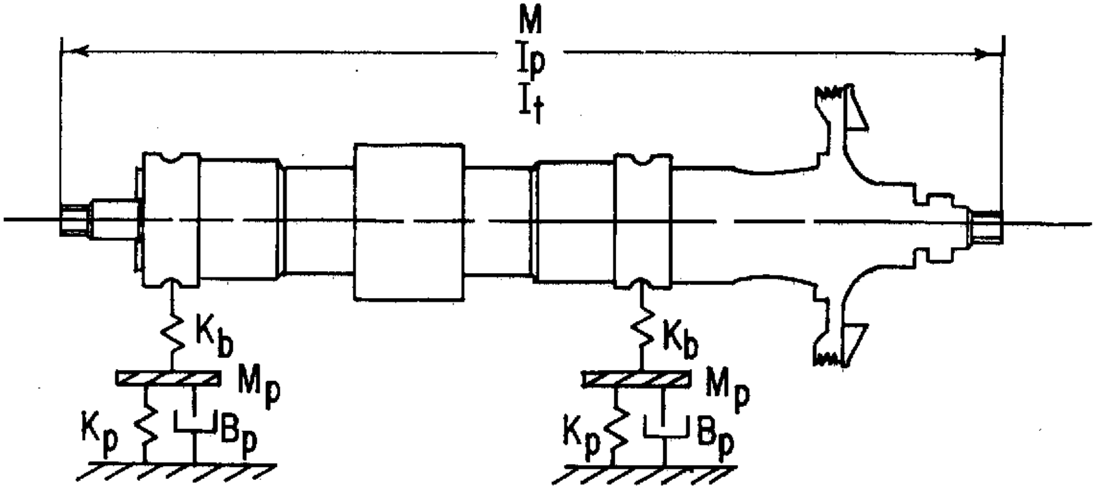

(b) Flexure Mounted Ball Bearing

Fig. 44 Critical Speed Mathematical Model

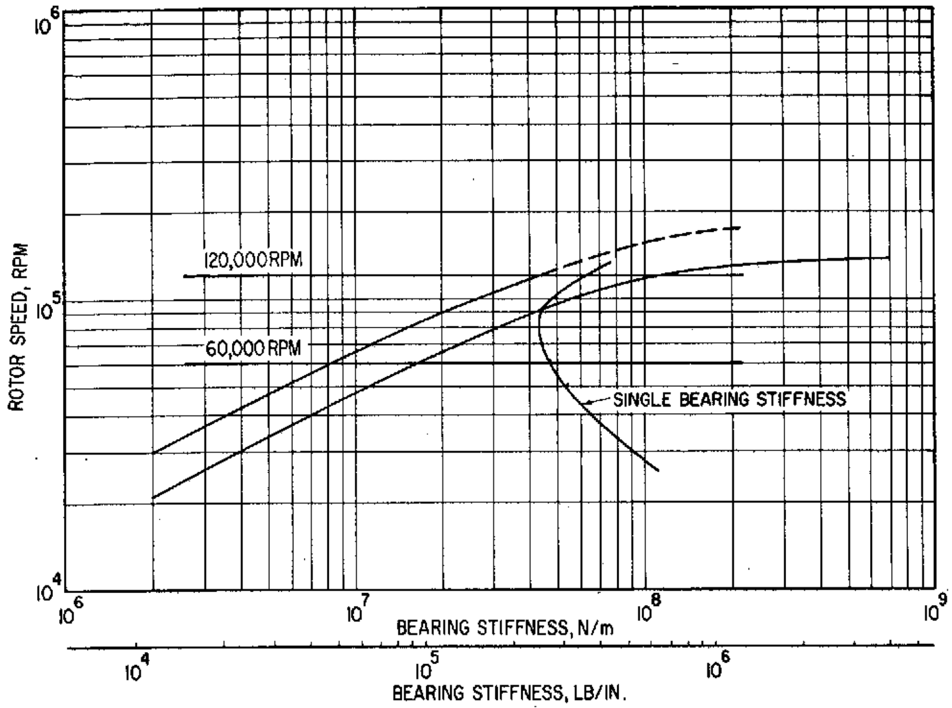

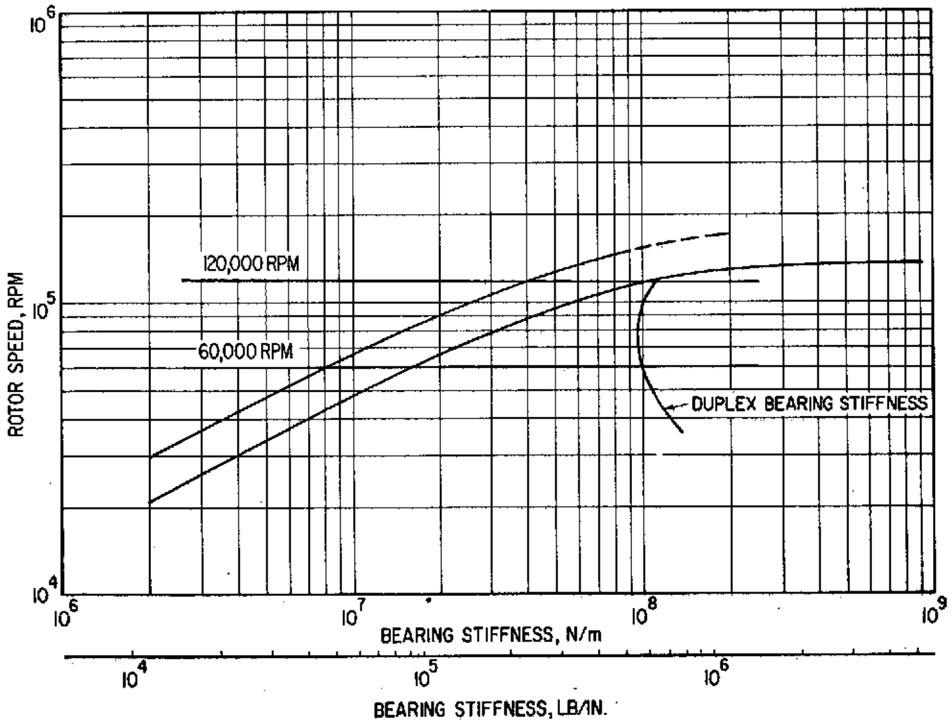

Fig. 45 Critical Speed Map: Ball Bearing Tester with Rigid Mounts

design for the ball bearing tester takes the form of a rigid cylinder into which the ball bearings are mounted, a circumferential array of axially oriented spokes to provide radial flexibility while maintaining axial rigidity and a flange for securing the bearing mount to the tester housing. The outer diameter of the rigid cylinder is manufactured with a precision surface so that it becomes a squeeze film damper when fitted into a close fitting housing bore. The configuration of the damped flexure mount for the ball bearing tester is shown in Figure 46.

The calculated spring rate of a fully assembled flexure mount is $K_p = 7.35 \times 10^6$ N/m (4.2×10^4 lb/in) with a spring supported mass of $M_p =$ 0.204 Kg (0.45 lb). The inclusion of pedestal (flexure) stiffness, K_p, and mass, M_p, in the critical speed calculations dramatically affects the critical speed map as indicated by Figure 47. The critical speed curves of Figure 47 are similar to those shown in Figure 45 with one significant change, which is the lowering of the first and second critical speed lines. For the bearing stiffness shown, no critical speed now exists over the entire test speed range of 60,000 - 120,000 rpm and the rotor-bearing system is fully capable of high-speed operation with a minimum safety margin of at least 10,000 rpm between the maximum speed of 120,000 rpm and the critical speed occuring on the duplex bearing tester. To ascertain whether the chosen flexure stiffness is adequate, a critical speed map, shown by Figure 48, was made with a constant ball bearing stiffness of 1.05×10^8 N/m (6.0×10^5 lb/in) and the flexure stiffness treated as a variable. This map shows low critical speeds at the design flexure stiffness of 7.35×10^6 N/m (4.2×10^4 lb/in) and that a substantial leeway in the flexure's radial stiffness as a result of manufacturing tolerances is permissible.

Once the critical speed behavior of the system was found to be acceptable, further calculations were performed to establish its sensitivity to rotor unbalance, and determine the rotor response characteristics.

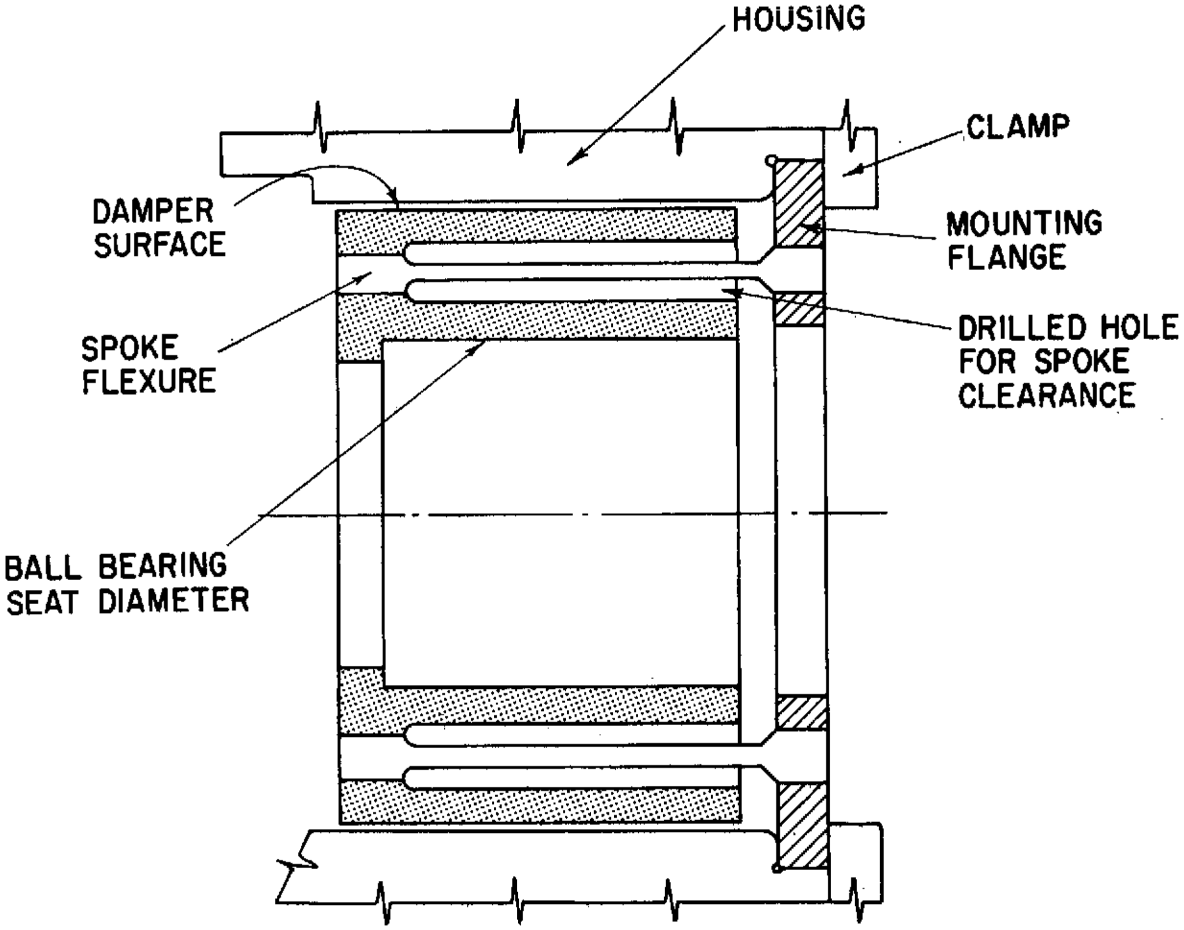

Fig. 46 Ball Bearing Flexure Mount with Squeeze Film Damper

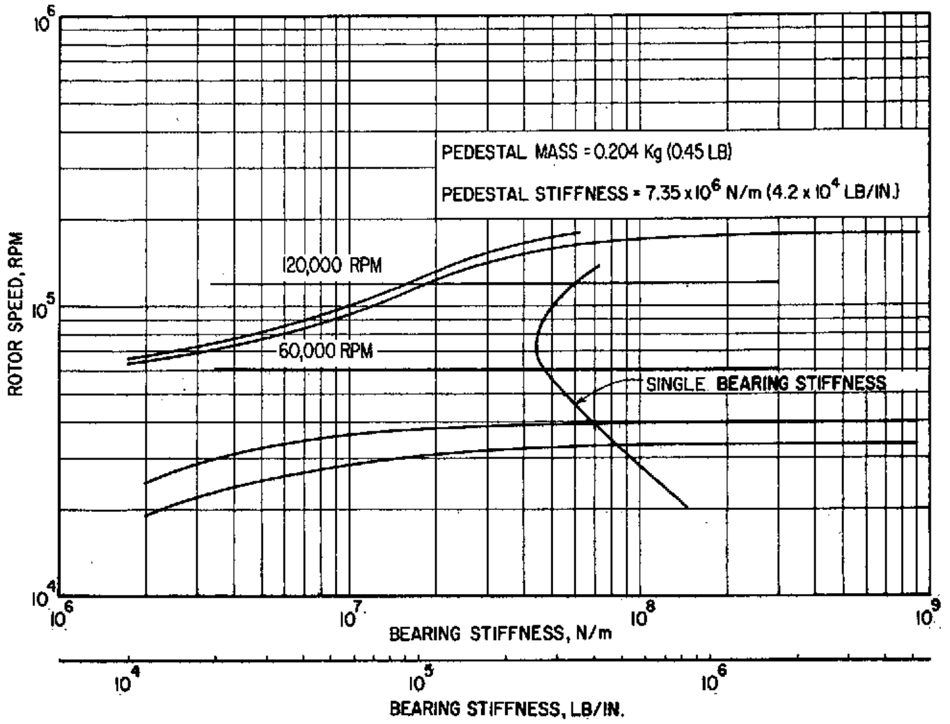

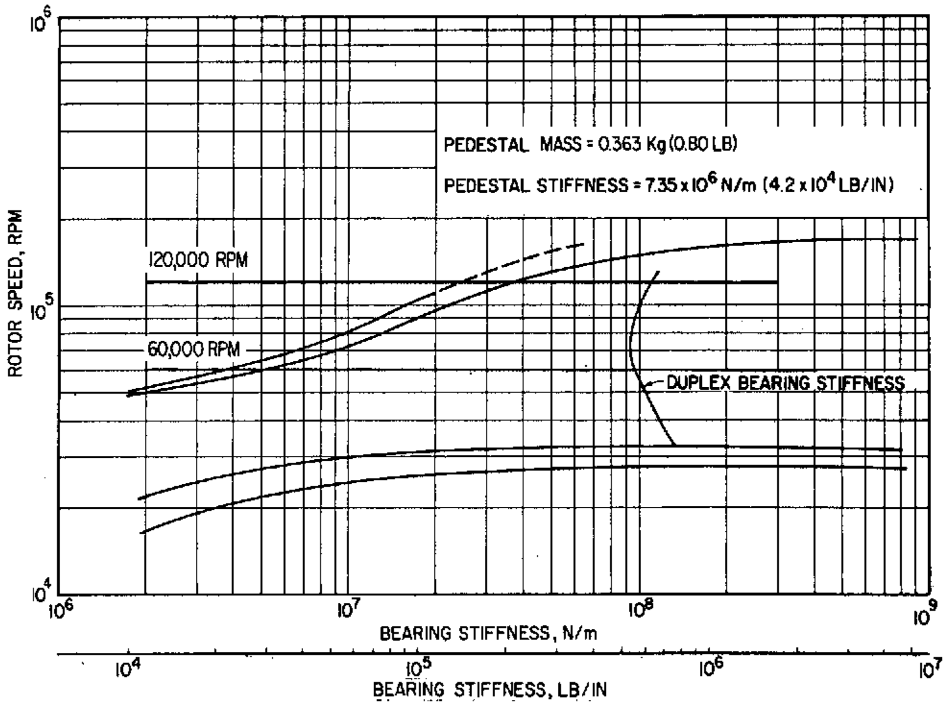

Fig. 47 Critical Speed Map: Ball Bearing Tester with Flexure Mounts

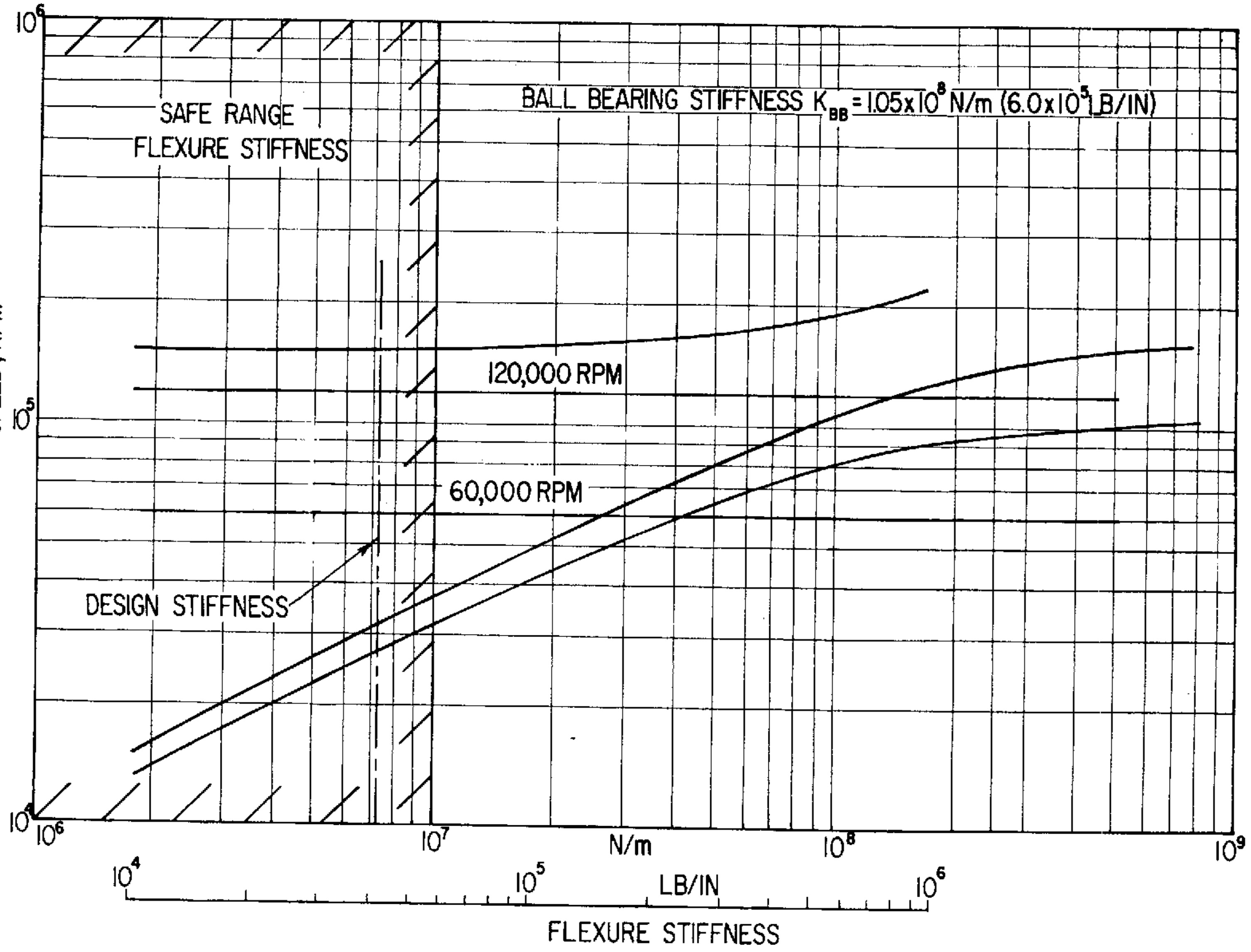

Fig. 48 Critical Speed Map: Flexure Stiffness Study

The rotor response calculations require a damping coefficient in order to provide reasonable answers. The necessary damping, provided by the action of the flexure mount, was calculated as a function of radial clearance between the mount and the tester housing. Figure 49 shows the results of the flexure damping calculations and indicates that the damper design, with the assumption of laminar flow, will provide a damping coefficient of approximately $B_p = 4.37 \times 10^2$ N-sec/m (2.5 lb-sec/in) at a radial clearance of $C = 2.04 \times 10^{-5}$ m (0.8×10^{-3} in). This damping coefficient along with the appropriate ball bearing stiffnesses indicated in Table 12 and a residual unbalance of 7.2×10^{-7} Kg-m (0.001 in-oz) at Station 20 when inputted into the unbalance response calculation, provided the response data for the single ball bearing tester. Figure 50 presents the pertinent response curves for the single bearing tester.

At no speed does the rotor excursion exceed 23.3 m/m-Kg (0.66 in/in-oz) and in the critical tester areas, such as Station 20, the turbine blade area, does the rotor excursion exceed 1.14×10^{-5} m (0.45×10^{-3} in). At test speeds between 60,000 and 120,000 rpm, rotor excursions of only 3.81×10^{6} m (0.15×10^{-4} in) are indicated.

A similar response calculation for the duplex ball bearing tester was made over the same speed range and the input parameters listed in Table 12. The only parameters significantly different from the single bearing tester were the magnitude and location of the duplex bearing spring reactions and the pedestal mass. The response curves for the duplex bearing tester at several rotor speeds are shown in Figure 51. These curves are similar in shape to the single bearing tester response curves and show acceptable excursion levels at any speed. As was indicated above, the response curves presented in Figures 9 and 10 represent the expected rotor excursions for a turbine disc unbalance of 7.2×10^{-7} Kg-m (0.001 in-oz). Rotors of a similar size and configuration as those designed for the ball bearing testers are commonly balanced to 2.16×10^{-7} Kg-m (0.3×10^{-3} in-oz). Consequently, the amplitudes indicated in Figures 50 and 51 may be multiplied by .3 to obtain more realistic estimates. A listing of the response data for

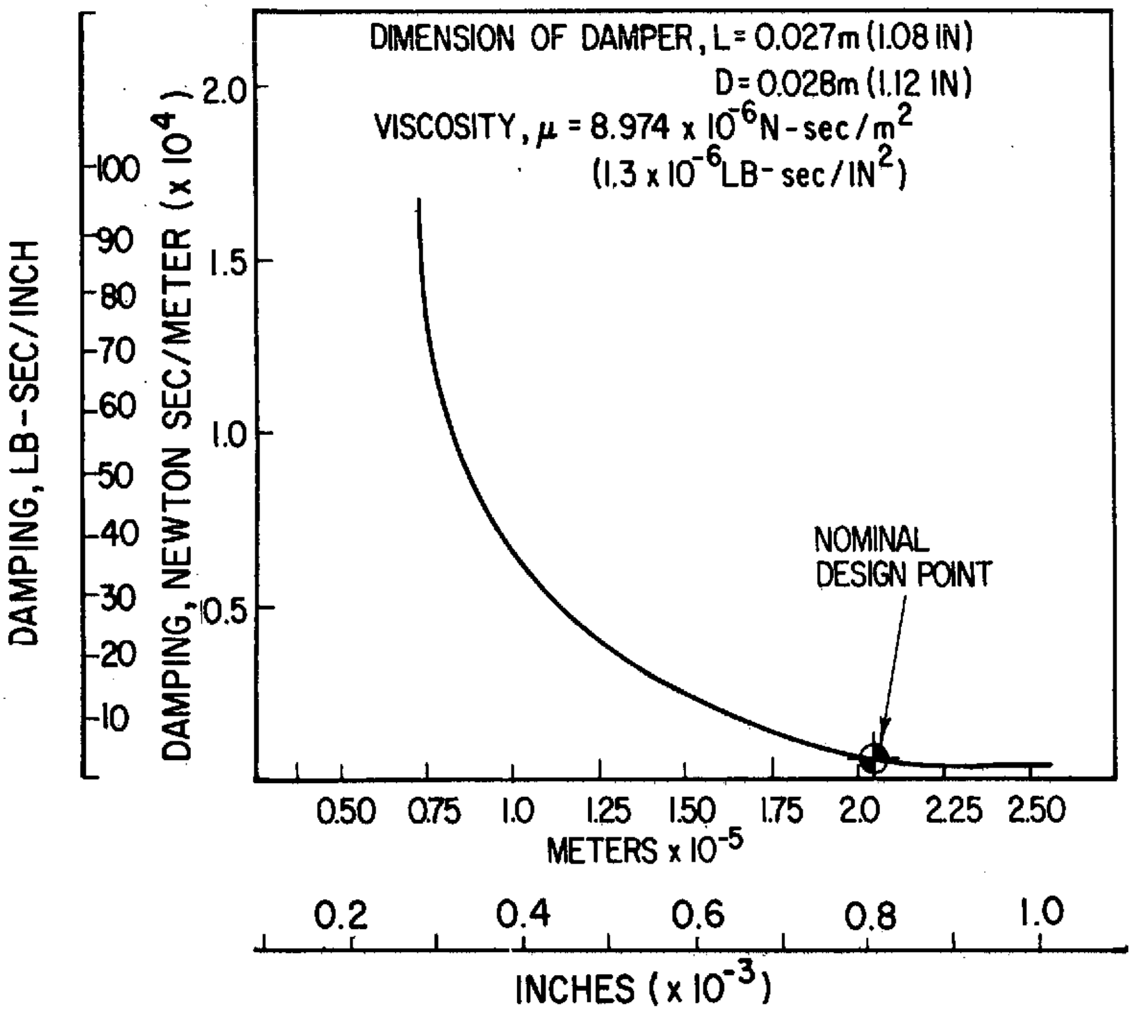

Fig. 49 Performance Characteristics - Squeeze Film Damper

TABLE 12

BALL BEARING TESTER
ROTOR DYNAMICS PARAMETERS

Speed Range 1000 RPM	Single Bearing Stiffness		Duplex Bearing Stiffness	
	10^7N/m	(10^5 lb/in)	10^8N/m	(10^6 lb/in)
0-30	6.40	(3.66)	1.28	(0.73)
30-50	5.50	(3.14)	1.10	(0.63)
50-70	4.80	(2.74)	0.96	(0.55)
70-90	4.60	(2.63)	0.92	(0.53)
90-110	5.0	(2.86)	1.00	(0.57)
110-130	5.50	(3.14)	1.10	(0.63)

Pedestal Weight – Single Bearing $M_p = 0.182$ (0.40 lb)

Pedestal Weight – Duplex Bearing $M_p = 0.363$ (0.80 lb)

Pedestal Stiffness, Both Testers $K_p = 7.35\text{x } 10^6$ N/m (4.2×10^4 lb/in)

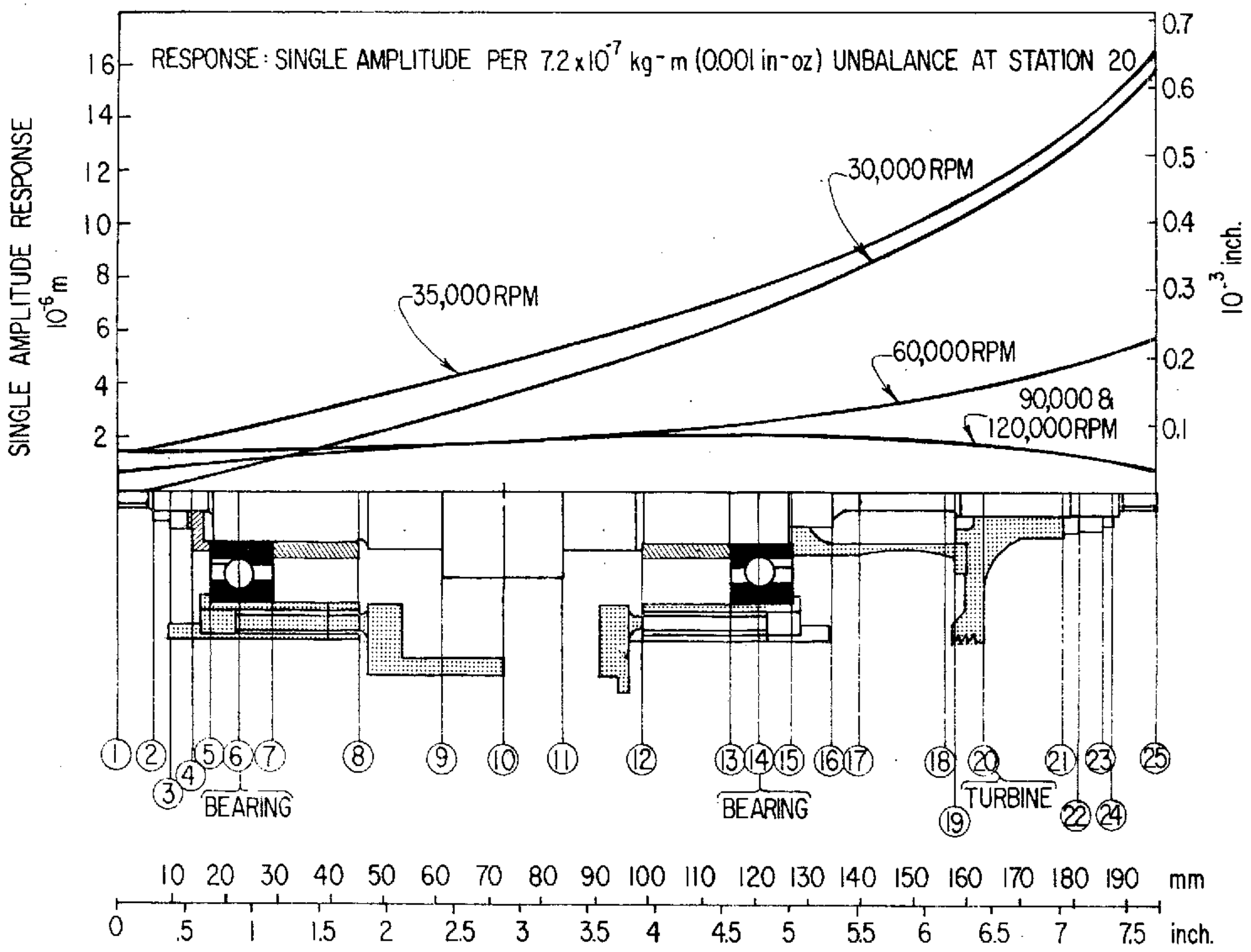

Fig. 50 Unbalance Response: Single Ball Bearing Tester

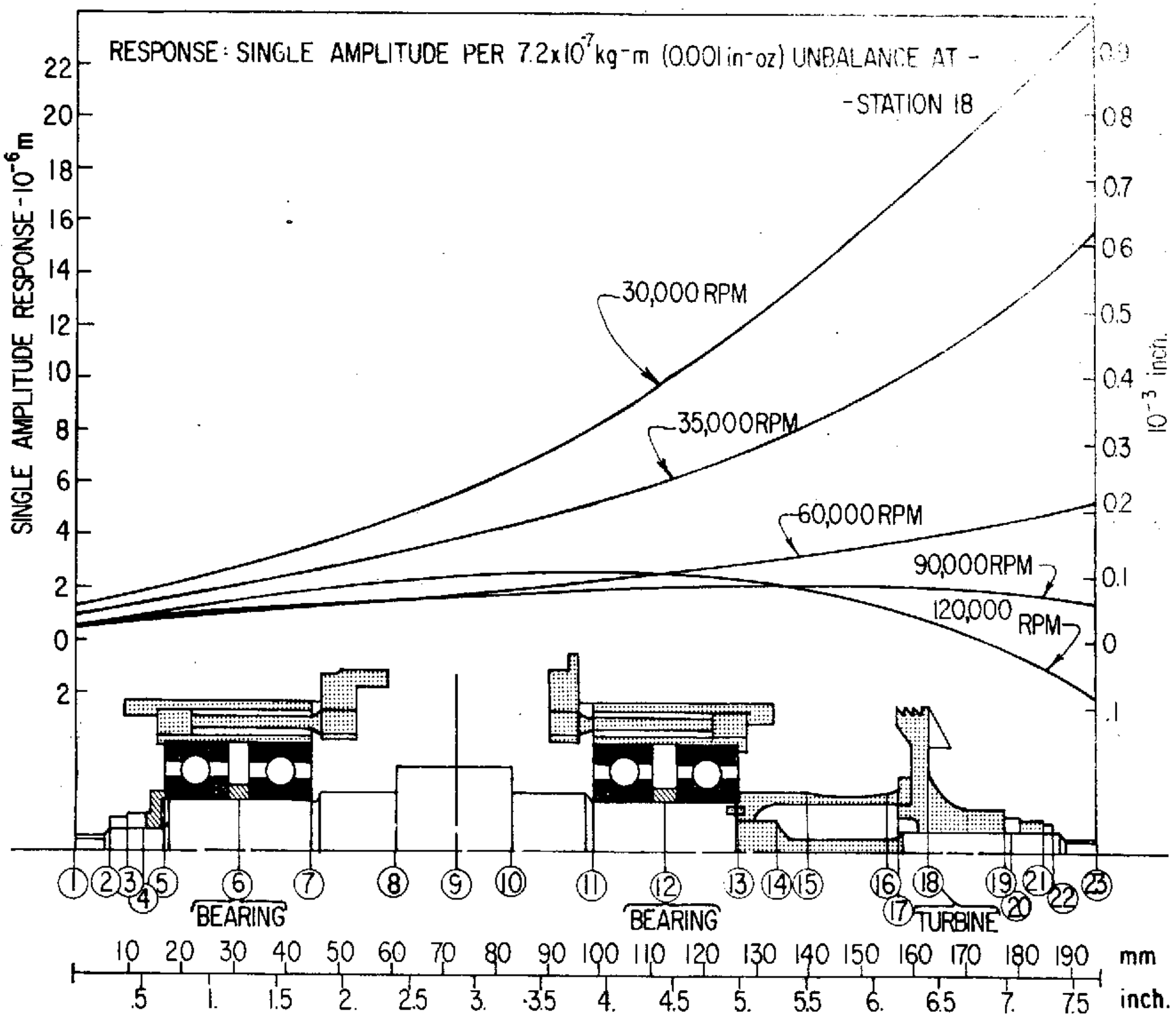

Fig. 51 Unbalance Response: Duplex Ball Bearing Tester

both the single and duplex ball bearing testers is presented in Tables 13 and 14 respectively. Included in Tables 13 and 14 are the dynamic forces sustained by the ball bearing at the speeds indicated. These forces are highest at 120,000 rpm and correspond to 107.4 N (24.1 lbs) and 89.8 N (20.1 lbs) per bearing for the single and duplex bearing systems respectively. A decrease in the residual unbalance will also result in a proportional decrease in the dynamic bearing loading.

The examination of the rotor dynamics aspects of both the single and duplex ball bearing tester final designs indicates that successful operation is possible. All critical speeds are sufficiently removed from the test speed range to preclude excessive rotor excursions during test. The conservative estimate of damping coefficients for the flexure mount combined with conservative assumptions on the level of rotor unbalance also provide reasonable assurance that the response calculation represents the maximum anticipated rotor excursions over the entire rotor speed range.

b. Thermal Analysis

An important aspect in the design of the high-speed tester operating in a cryogenic regime is the machine's ability to accommodate the low temperatures involved. The use of LH_2 as the cooling and lubricating medium for the tester's bearings further requires that the fluid itself does not absorb sufficient thermal energy to cause its bulk temperature to rise above its critical temperature. A pressure flow relationship for the LH_2 coolant is given in Appendix F. Both ball bearing testers have been subjected to a thermal analysis to assure adequate behavior. The method of analysis is described as follows:

An axi-symmetric model of the ball bearing test rig, as shown in Figure 52, was drawn. This model was analyzed using the MTI Thermal Analysis Computer Program which accepts a variety of boundary conditions, heat inputs and coolant flows. The thermal analysis program solves a system of equations representing conservation of thermal energy over each of a series of control volumes defined by a two-dimensional finite difference

TABLE 13

RESPONSE DATA — SINGLE BALL BEARING TESTER

	SINGLE AMPLITUDE ROTOR EXCURSIONS						FORCE TRANSMITTED TO PEDESTAL			
	STATION 6		STATION 14		STATION 20		STATION 6		STATION 14	
ROTOR SPEED	FREE END BEARING		TURBINE END BEARING		TURBINE		FREE END BEARING		TURBINE END BEARING	
RPM	m	(INCH)	m	(INCH)	m	(INCH)	N	(LB)	N	(LB)
5000	1.335E-08	(5.255E-07)	4.481E-08	(1.764E-06)	7.671E-08	(3.020E-06)	8.5690E-02	(1.9240E-02)	2.8766E-01	(6.4589E-02)
10000	5.575E-08	(2.195E-06)	1.931E-07	(7.603E-06)	3.284E-07	(1.293E-05)	3.5125E-01	(7.8866E-02)	1.2165E+00	(2.7314E-01)
15000	1.352E-07	(5.323E-06)	4.986E-07	(1.963E-05)	8.395E-07	(3.305E-05)	8.2457E-01	(1.8514E-01)	3.0406E+00	(6.8271E-01)
20000	2.680E-07	(1.055E-05)	1.114E-06	(4.384E-05)	1.839E-06	(7.242E-05)	1.5581E+00	(3.4983E-01)	6.4766E+00	(1.4542E+00)
25000	4.801E-07	(1.890E-05)	2.555E-06	(1.006E-04)	4.094E-06	(1.612E-04)	2.6176E+00	(5.8774E-01)	1.3931E+00	(3.1279E+00)
30000	8.918E-07	(3.511E-05)	7.038E-06	(2.771E-04)	1.075E-05	(4.234E-04)	4.4684E+00	(1.0033E+00)	3.5268E+01	(7.9187E+00)
35000	2.941E-06	(1.158E-04)	7.800E-06	(3.071E-04)	1.124E-05	(4.427E-04)	1.3215E+01	(2.9671E+00)	3.5053E+01	(7.8704E+00)
40000	4.460E-06	(1.756E-04)	4.907E-06	(1.932E-04)	8.255E-06	(3.250E-04)	1.7473E+01	(3.9232E+00)	1.9225E+01	(4.3167E+00)
45000	3.200E-06	(1.260E-04)	3.807E-06	(1.499E-04)	6.619E-06	(2.606E-04)	1.0625E+01	(2.3856E+00)	1.2636E+01	(2.8371E+00)
50000	2.336E-06	(9.198E-05)	3.211E-06	(1.264E-04)	5.311E-06	(2.091E-04)	6.5341E+00	(1.4671E+00)	8.9805E+00	(2.0164E+00)
55000	1.915E-06	(7.539E-05)	2.873E-06	(1.131E-04)	4.511E-06	(1.776E-04)	4.9027E+00	(1.1008E+00)	7.3554E+00	(1.6515E+00)
60000	1.685E-06	(6.633E-05)	2.662E-06	(1.048E-04)	3.960E-06	(1.559E-04)	4.8475E+00	(1.0084E+00)	7.6604E+00	(1.7200E+00)
65000	1.548E-06	(6.094E-05)	2.523E-06	(9.933E-05)	3.533E-06	(1.391E-04)	5.8776E+00	(1.3197E+00)	9.5800E+00	(2.1510E+00)
70000	1.462E-06	(5.755E-05)	2.425E-06	(9.549E-05)	3.172E-06	(1.249E-04)	7.5794E+00	(1.7018E+00)	1.2576E+01	(2.8237E+00)
75000	1.407E-06	(5.541E-05)	2.356E-06	(9.275E-05)	2.845E-06	(1.120E-04)	9.7786E+00	(2.1956E+00)	1.6369E+01	(3.6753E+00)
80000	1.374E-06	(5.410E-05)	2.306E-06	(9.077E-05)	2.527E-06	(9.950E-05)	1.2456E+01	(2.7968E+00)	2.0899E+01	(4.6924E+00)
85000	1.356E-06	(5.340E-05)	2.270E-06	(8.936E-05)	2.209E-06	(8.695E-05)	1.5672E+01	(3.5188E+00)	2.6223E+01	(5.8878E+00)
90000	1.351E-06	(5.317E-05)	2.245E-06	(8.837E-05)	1.879E-06	(7.398E-05)	1.9537E+01	(4.3866E+00)	3.2468E+01	(7.2900E+00)
95000	1.355E-06	(5.334E-05)	2.228E-06	(8.773E-05)	1.536E-06	(6.049E-05)	2.4212E+01	(5.4364E+00)	3.9825E+01	(8.9420E+00)
100000	1.368E-06	(5.386E-05)	2.220E-06	(8.740E-05)	1.194E-06	(4.702E-05)	2.9924E+01	(6.7188E+00)	4.8559E+01	(1.0903E+01)
105000	1.390E-06	(5.472E-05)	2.218E-06	(8.734E-05)	9.251E-07	(3.642E-05)	3.6986E+01	(8.3045E+00)	5.9039E+01	(1.3256E+01)
110000	1.421E-06	(5.593E-05)	2.224E-06	(8.756E-05)	9.393E-07	(3.698E-05)	4.5847E+01	(1.0294E+01)	7.1776E+01	(1.6116E+01)
115000	1.462E-06	(5.753E-05)	2.237E-06	(8.807E-05)	1.389E-06	(5.468E-05)	5.7173E+01	(1.2837E+01)	8.7520E+01	(1.9651E+01)
120000	1.514E-06	(5.961E-05)	2.259E-06	(8.895E-05)	2.186E-06	(8.608E-05)	7.1964E+01	(1.6158E+01)	1.0738E+02	(2.4110E+01)
125000	1.582E-06	(6.230E-05)	2.294E-06	(9.030E-05)	3.310E-06	(1.303E-04)	9.1836E+01	(2.0620E+01)	1.3311E+02	(2.9888E+01)
130000	1.672E-06	(6.583E-05)	2.345E-06	(9.233E-05)	4.856E-06	(1.912E-04)	1.1952E+02	(2.6835E+01)	1.6762E+02	(3.7636E+01)
135000	1.795E-06	(7.067E-05)	2.425E-06	(9.547E-05)	7.056E-06	(2.778E-04)	1.5996E+02	(3.5916E+01)	2.1610E+02	(4.8520E+01)

TABLE 14

RESPONSE DATA — DUPLEX BALL BEARING TESTER

	SINGLE AMPLITUDE ROTOR EXCURSIONS						FORCE TRANSMITTED TO PEDESTAL			
	STATION 6		STATION 12		STATION 18		STATION 6		STATION 12	
ROTOR SPEED	FREE END BEARING		TURBINE END BEARING		TURBINE		FREE END BEARING		TURBINE END BEARING	
RPM	m	(INCH)	m	(INCH)	m	(INCH)	N	(LB)	N	(LB)
5000	1.821E-08	(7.169E-07)	4.782E-08	(1.883E-06)	9.756E-08	(3.841E-06)	1.2450E-01	(2.7953E-02)	3.2694E-01	(7.3407E-02)
10000	7.866E-08	(3.097E-06)	2.091E-07	(8.233E-06)	4.242E-07	(1.670E-05)	5.2701E-01	(1.1833E-01)	1.4011E+00	(3.1460E-01)
15000	2.042E-07	(8.038E-06)	5.563E-07	(2.190E-05)	1.118E-06	(4.400E-05)	1.3215E+00	(2.9671E-01)	3.6000E+00	(8.0832E-01)
20000	4.620E-07	(1.819E-05)	1.317E-06	(5.187E-05)	2.604E-06	(1.025E-04)	2.8441E+00	(6.3859E-01)	8.1076E+00	(1.8204E+00)
25000	1.105E-06	(4.350E-05)	3.439E-06	(1.354E-04)	6.634E-06	(2.612E-04)	6.3497E+00	(1.4257E+00)	1.9770E+01	(4.4390E+00)
30000	2.662E-06	(1.048E-04)	9.832E-06	(3.871E-04)	1.826E-05	(7.189E-04)	1.3983E+01	(3.1396E+00)	5.1659E+01	(1.1599E+01)
35000	2.124E-06	(8.363E-05)	5.979E-06	(2.354E-04)	1.081E-05	(4.254E-04)	9.9505E+00	(2.2342E+00)	2.8008E+01	(6.2886E+00)
40000	2.369E-06	(9.328E-05)	3.726E-06	(1.467E-04)	7.348E-06	(2.893E-04)	9.6072E+00	(2.1571E+00)	1.5110E+01	(3.3926E+00)
45000	1.803E-06	(7.100E-05)	3.005E-06	(1.183E-04)	5.773E-06	(2.273E-04)	6.1462E+00	(1.3800E+00)	1.0238E+01	(2.2987E+00)
50000	1.500E-06	(5.905E-05)	2.667E-06	(1.050E-04)	4.902E-06	(1.930E-04)	4.2663E+00	(9.5799E-01)	7.5887E+00	(1.7039E+00)
55000	1.340E-06	(5.274E-05)	2.476E-06	(9.747E-05)	4.341E-06	(1.709E-04)	3.4513E+00	(7.7493E-01)	6.3791E+00	(1.4323E+00)
60000	1.248E-06	(4.914E-05)	2.359E-06	(9.287E-05)	3.932E-06	(1.548E-04)	3.5707E+00	(8.0173E-01)	6.7492E+00	(1.5154E+00)
65000	1.195E-06	(4.704E-05)	2.288E-06	(9.008E-05)	3.597E-06	(1.416E-04)	4.4500E+00	(9.9917E-01)	8.5218E+00	(1.9134E+00)
70000	1.164E-06	(4.584E-05)	2.246E-06	(8.842E-05)	3.310E-06	(1.303E-04)	5.8322E+00	(1.3095E+00)	1.1248E+01	(2.5256E+00)
75000	1.150E-06	(4.527E-05)	2.225E-06	(8.760E-05)	3.040E-06	(1.197E-04)	7.5865E+00	(1.7034E+00)	1.4679E+01	(3.2958E+00)
80000	1.148E-06	(4.518E-05)	2.221E-06	(8.744E-05)	2.776E-06	(1.093E-04)	9.6864E+00	(2.1749E+00)	1.8748E+01	(4.2095E+00)
85000	1.155E-06	(4.547E-05)	2.231E-06	(8.783E-05)	2.509E-06	(9.877E-05)	1.2159E+01	(2.7300E+00)	2.3488E+01	(5.2737E+00)
90000	1.171E-06	(4.610E-05)	2.254E-06	(8.873E-05)	2.229E-06	(8.776E-05)	1.5060E+01	(3.3815E+00)	2.8986E+01	(6.5083E+00)
95000	1.195E-06	(4.706E-05)	2.289E-06	(9.011E-05)	1.930E-06	(7.599E-05)	1.8475E+01	(4.1483E+00)	3.5376E+01	(7.9430E+00)
100000	1.228E-06	(4.835E-05)	2.337E-06	(9.199E-05)	1.608E-06	(6.329E-05)	2.2518E+01	(5.0559E+00)	4.2839E+01	(9.6186E+00)
105000	1.270E-06	(5.001E-05)	2.398E-06	(9.441E-05)	1.262E-06	(4.970E-05)	2.7339E+01	(6.1385E+00)	5.1614E+01	(1.1589E+01)
110000	1.323E-06	(5.207E-05)	2.475E-06	(9.746E-05)	9.192E-07	(3.619E-05)	3.3146E+01	(7.4422E+00)	6.2036E+01	(1.3929E+01)
115000	1.388E-06	(5.463E-05)	2.573E-06	(1.013E-04)	7.064E-07	(2.781E-05)	4.0218E+01	(9.0302E+00)	7.4542E+01	(1.6737E+01)
120000	1.468E-06	(5.780E-05)	2.692E-06	(1.060E-04)	9.129E-07	(3.594E-05)	4.8956E+01	(1.0992E+01)	8.9765E+01	(2.0155E+01)
125000	1.568E-06	(6.174E-05)	2.842E-06	(1.119E-04)	1.528E-06	(6.015E-05)	5.9930E+01	(1.3456E+01)	1.0860E+02	(2.4385E+01)
130000	1.695E-06	(6.674E-05)	3.033E-06	(1.194E-04)	2.426E-06	(9.552E-05)	7.4008E+01	(1.6617E+01)	1.3242E+02	(2.9732E+01)
135000	1.860E-06	(7.322E-05)	3.282E-06	(1.292E-04)	3.630E-06	(1.429E-04)	9.2544E+01	(2.0779E+01)	1.6332E+02	(3.6671E+01)

mesh. The mesh lines are drawn in the radial and axial directions. For the ball bearing model, 16 and 30 mesh lines were used in each of these two directions respectively. The thermal calculations result in a temperature distribution with a temperature given for each mesh point in the body.

In the course of modeling this tester, certain restrictions entering the process of fitting the model within the computer program constraints must be recognized. Firstly, the location of the LH_2 bearing coolant streams in the tester model cannot account for the total wetting of internal tester members, resulting from coolant circulation. Secondly, neither the thermal properties of the tester materials nor the generated heat transfer coefficients exactly reflect real tester conditions. A third significant restriction applies to the location of the generated friction losses. In actual operation, the clearance seal and other losses generated by the shearing of fluid are generated within the fluid itself. Current restrictions on the use of the thermal analysis program require the generation of heat to occur on the surface of a body. As a result, calculations within the boundaries of these restrictions produce abnormally high temperatures on the surface adjacent to the areas where the heat is produced. The method of analysis, therefore, tends to provide very conservative temperatures, which means that the actual temperature distribution would be better (in this case lower) than predicted. The qualitative trends in the temperature distributions are, however, valid.

The bearing coolant flows were modeled by two separate fluid streams within the body, and are identified at grid intersections by I, J numbers, where I and J are the mesh coordinate numbers in the radial and axial directions respectively. As can be seen on Figure 52, the stream corresponding to the bearing flow on the turbine side goes from point (7,19) to (7,15). The second bearing flow stream starts at (1,2) and goes through to points (1,3), (3,3), (3,5), (7,5) ending at point (7,9). Turbine flow stream originates at point (12,27) and exits at point (1,30). All pertinent thermal coefficients were evaluated by use of the MTI thermal convection coefficients program.

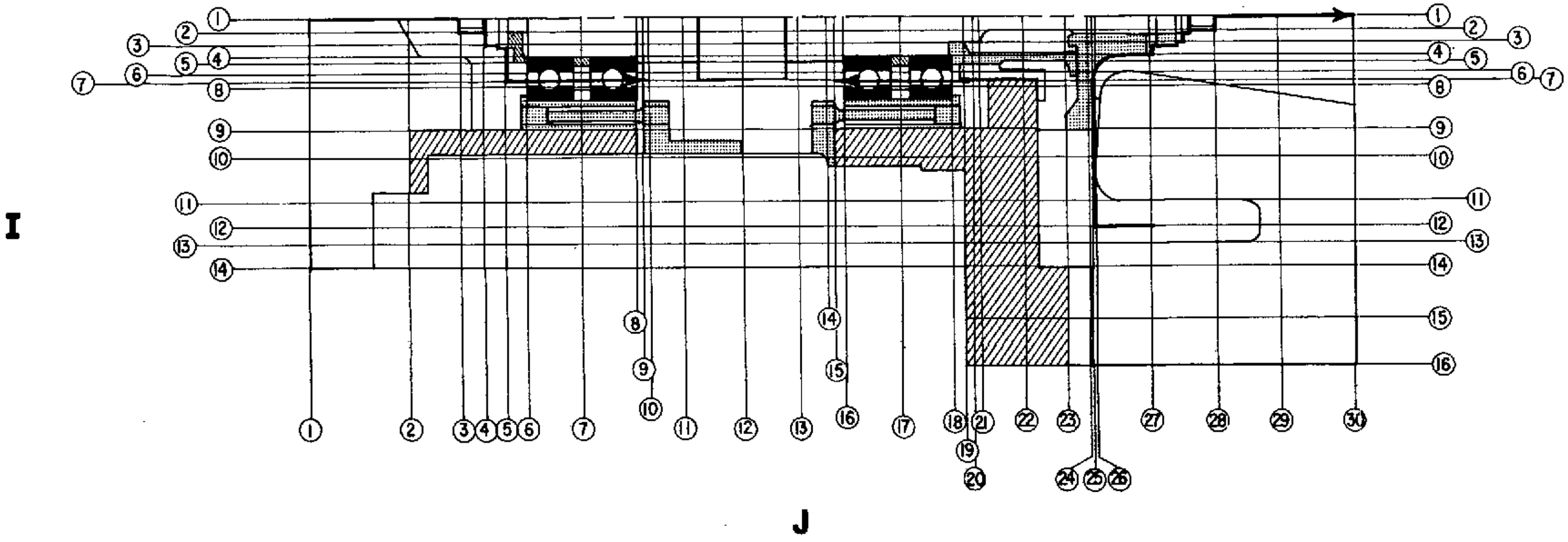

Fig. 52 Thermal Model: Ball Bearing Tester

The summary of all input parameters, both calculated and chosen, are found in Table 15.

For purposes of analysis, the calculation of temperature distribution within the test vehicle was reduced to the generation of thermal maps which provided the combined effects of:

- Rotor heat dams and thermal insulation
- Bearing Coolant flows
- Turbine flow to evaluate efficiency of the turbine heat dam
- Rotor windage loss at 120,000 rpm
- Bearing power loss at 120,000 rpm
- Fluid seal losses at 120,000 rpm

Early thermal calculations for the ball bearing testers which were made with the use of a 294°K (530°R) GH_2 radial loader supply indicated excessively high temperatures throughout the entire center portion of the tester. A change in loader supply from GH_2 to LH_2 eliminated the central shaft "heating" effect. Subsequent development calculations, including the final temperature distribution presented in this report, are based on a radial loader supply of LH_2 at 27.8°K (50°R) which is so listed in Table 15. The effects of higher surface film coefficient and skin temperature are discussed in Appendix G. The results of this analysis show no appreciable change in internal temperature distribution.

The final ball bearing tester thermal study provided a temperature distribution within the test vehicle along with the temperature rise in the LH_2 coolant flow streams. Table 16 shows the LH_2 stream temperature increases as affected by several combinations of the imposed conditions. The largest temperature rises for both the single and duplex bearing testers result from the turbine gas flow and the bearing power losses. In no case does the indicated stream temperature rise more than 6.1°C (11°F). This limited rise should not adversely affect the LH_2 coolant, providing the coolant flow rate is slightly increased.

TABLE 15

THERMAL ANALYSIS INPUT PARAMETERS — BALL BEARING TESTER

		Inlet Temperature Tin		Flow Rate		Specific Heat		Film Coefficient		Thermal Conductivity	
		K	(R)	Kg/sec	(lb/sec)	J/Kg°K	(Btu/lb-°F)	Watt/m^2 K	(Btu/hr-Ft^2-°F)	Watt/m - K	Btu/hr-Ft-°F
Fluids	LH_2 Bearing Coolant	27.8	(50)	0.091	(0.20)	9.20x 10^3	(2.20)	35000	(2000)	---	---
	Outer Housing Surface	294	(530)	---	---	---	---	.175	(0.10)	---	---
	GH_2 Turbine Annulus	294	(530)	0.082	(0.18)	1.43 x 10^4	(3.42)	341	(194.4)	0.168	(0.097)
	GH_2 Turbine Blading	---	---	0.082	(0.18)	1.43 x 10^4	(3.42)	5430	(309.5)	---	---
	GH_2 Turbine Discharge	---		0.082	(0.18)	1.43 x 10^4	(3.42)	3090	(1767)	---	---
	LH_2 Radial Loader (Rotor)	27.2	(50)	0.011	(0.025)	9.20 x 10^3	(2.20)	176	(100)	---	---
	LH_2 Radial Loader (Cavity Wall)	---		0.011	(0.025)	9.20 x 10^3	(2.20)	176	(100)	---	---
Solids	Stainless Steel	33.3	(60)	---	---	---	---	---	---	8.65	(5.0)
	Stainless Steel	44.5	(80)	---	---	---	---	---	---	11.2	(6.5)
	Stainless Steel	61.0	(100)	---	---	---	---	---	---	13.8	(8.0)
	Inconel 718	27.8	(50)	---	---	---	---	---	---	3.48	(2.0)
	T6 Aluminum	61.0	(110)	---	---	---	---	---	---	52.0	(30)
	Insulation (Epoxy Fiberglass)	NA		---	---	---	---	---	---	.348	(0.2)

TABLE 16 LH$_2$ COOLANT STREAM TEMPERATURE RISE:
BALL BEARING TESTER

	Thermal Condition	LH$_2$* Flow Rate Kg/sec	(lb/sec)	LH$_2$ Coolant Temperature Rise Free End C	(F)	Turbine End C	(F)	Assumed Losses at 120,000 rpm Watts-(Btu/hr)
Duplex	Coolant Stream Only	.091	(0.20)	0.12	(0.21)	0.122	(0.22)	None
	Coolant Plus Turbine Flow	.091	(0.20)	0.18	(0.33)	0.333	(0.60)	None
	Coolant Plus Windage	.091	(0.20)	0.18	(0.33)	0.206	(0.37)	252 (862)
	Coolant Plus Bearing Losses**	.091	(0.20)	4.36	(7.87)	3.77	(6.78)	4100 (13927 per bearing)
	Coolant Plus Seal Losses	.091	(0.20)	0.13	(0.24)	0.155	(0.28	90.4 (308)
	All the Above plus LH$_2$ Loader @ 27.8 °K (50°R) & 0.011 Kg/sec (0.025 lb/sec)	.091	(0.20)	5.00	(9.00)	4.45	(8.00)	All Above
Single	Coolant Stream Only	.045	(0.10)	0.24	(0.43)	0.24	(0.43)	None
	Coolant Plus Turbine Flow	.045	(0.10)	0.37	(0.66)	0.66	(1.20)	None
	Coolant Plus Windage	.045	(0.10)	0.37	(0.67)	0.41	(0.74)	252 (862 Btu/hr)
	Coolant Plus Bearing Losses**	.045	(0.10)	5.05	(9.05)	4.35	(7.82)	4100 (13927 per bearing)
	Coolant Plus Seal Losses	.045	(0.10)	0.27	(0.49)	0.31	(0.56)	90.4 (308 Btu/hr)
	All the Above plus LH$_2$ Loader @ 27.8°K (50°R) & 0.011 Kg/sec (0.025 lb/sec)	.045	(0.10)	6.10	(11.0)	5.56	(10.0)	All Above

* Flow rate is per coolant stream
(0.2 lb/sec) for the duplex tester
(0.1 lb/sec) for the single bearing tester

** Bearing Power Loss = 0.650 N-m (5.75 in-lb) four bearings at 120,000 rpm
2/3 outer race - 1/3 inner race, 1/2 power used for single bearing tester

The results of the temperature distribution calculation for the ball bearing tester are shown in Figure 53. Several conclusions can be derived from the temperature map, these are:

1. The effectiveness of the heat dam is demonstrated by the very large axial temperature gradient indicated between the turbine wheel and the turbine end ball bearing seat. The lack of a radial gradient between the shaft and heat dam indicates that no thermally induced distortions of the turbine wheel will occur.
2. To maintain the coolant streams below the critical temperature at the exit from the bearing, provisions should be made for either an increase of the stream flow (above 0.091 Kg/sec (0.20 lb/sec) or a decrease in the inlet stream temperature below 27.8°K (50°R).
3. A less satisfactory range of temperatures is shown to exist along the boundary between the flexure mounts, (Items 12 and 13 on Figure 42) and the housing. The temperatures shown in these locations are less satisfactory because they represent levels in excess of the LH_2 critical temperature. At these temperature levels, the performance of the dampers may be affected by the existance of a mixed phase rather than the single LH_2 phase upon which the calculations are based. Since the major heat source is associated with the turbine inlet temperatures, the introduction of thermal insulation between the turbine and nozzle box housing should help to maintain this damper temperature at sub-critical levels.

In summary, the temperature trends presented in Figure 53 indicate the need for some modifications to the original tester design. These are:

- Provide a turbine heat dam by selecting an insulating material for the turbine spacer block (Item 3, Figure 1)
- Examine the possibility of decreasing the inlet temperature below the initial levels in the test stand

TEMPERATURES ARE IN °K(°R)

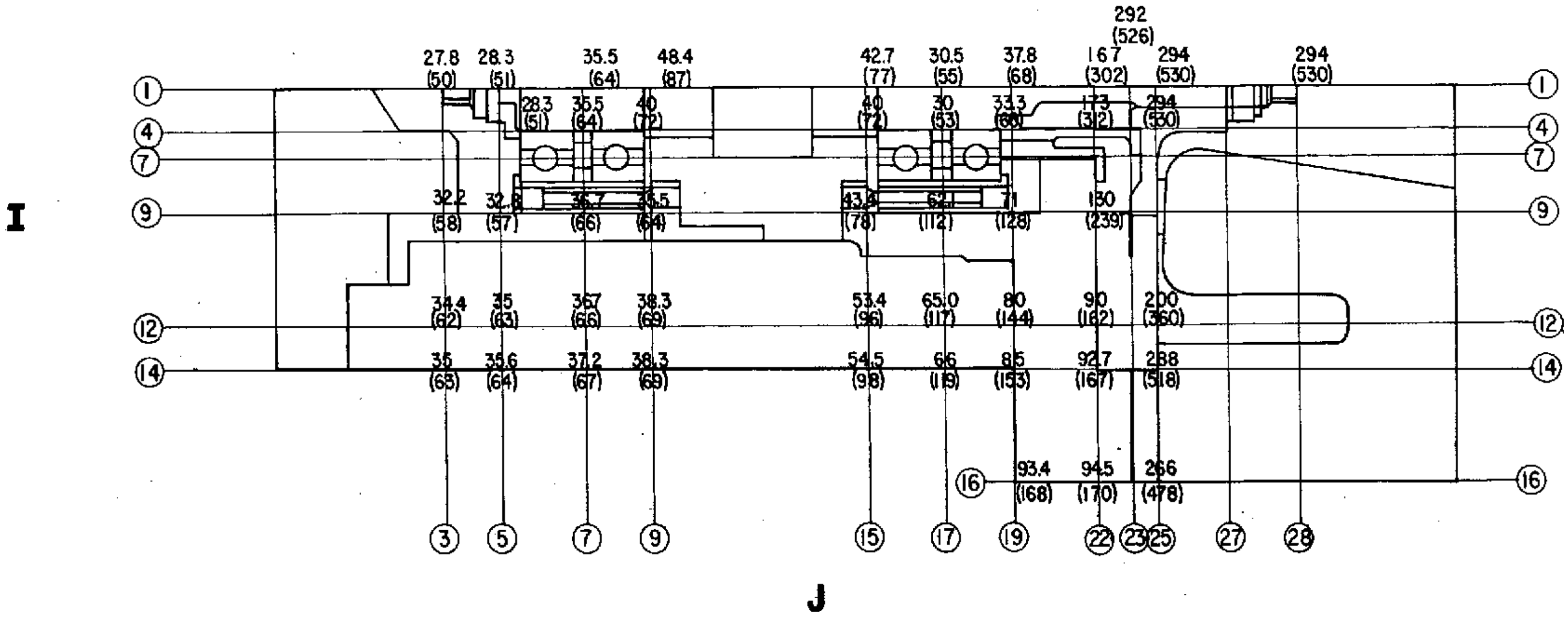

Fig. 53 Temperature Distribution: Ball Bearing Tester at 120,000 rpm

Provisions for these modifications have been either included in the test vehicle design details, or taken into consideration in the facility build-up.

2. Hybrid Bearing Tester

A companion tester design, which parallels that of the ball bearing tester, employs a relatively new bearing concept for cryogenic machines. This bearing type (as described in Section A) consists of a hydrostatic fluid-film bearing operating in parallel with a ball bearing. A test vehicle incorporating the hybrid bearing has been designed and is presented in Figure 54. Many parts used in this tester assembly are the same as those used for the ball bearing tester; these parts are identified by the ball bearing tester numbers (see Figure 42), but will not be described here. New parts, unique to the hybrid tester will be described and assigned identification numbers sequentially after the ball bearing tester parts.

New parts, specifically designed for the hybrid bearing tester, include the turbine end and free end hydrostatic bearing flanges ㉒ and ㉓ . These parts, designed to fit in the spaces provided for ball bearing tester parts, contain the hydrostatic journal bearings and are manufactured to provide ample lubricant passes for directing pressurized LH_2 to the hydrostatic bearings. The turbine end hydrostatic bearing flange also carries a hydrostatic thrust bearing for support of unbalanced axial loads. The two hydrostatic bearing flanges ㉒ and ㉓ are the only non-rotating parts to be replaced when converting from ball bearing to hybrid bearing testing.

The rotating assembly contains several new parts for accommodating the hybrid bearing. A smaller duplex ball bearing [Appendix D - MTI Specification 0232-43601-01] as well as the axial thrust runner requires narrower shaft spacers including new mid-bearing spacers ㉔ , and new inboard spacers ㉖ and ㉗ . The addition of the thrust runner ㉘ requires a new heat dam ㉙ .

Each hybrid bearing assembly consists of two extra-light series ball bearings, a mid-bearing spacer ㉔ , a hydrostatic journal sleeve ㉕ , and a preload spring. The preload spring is located between the sides of outer races of

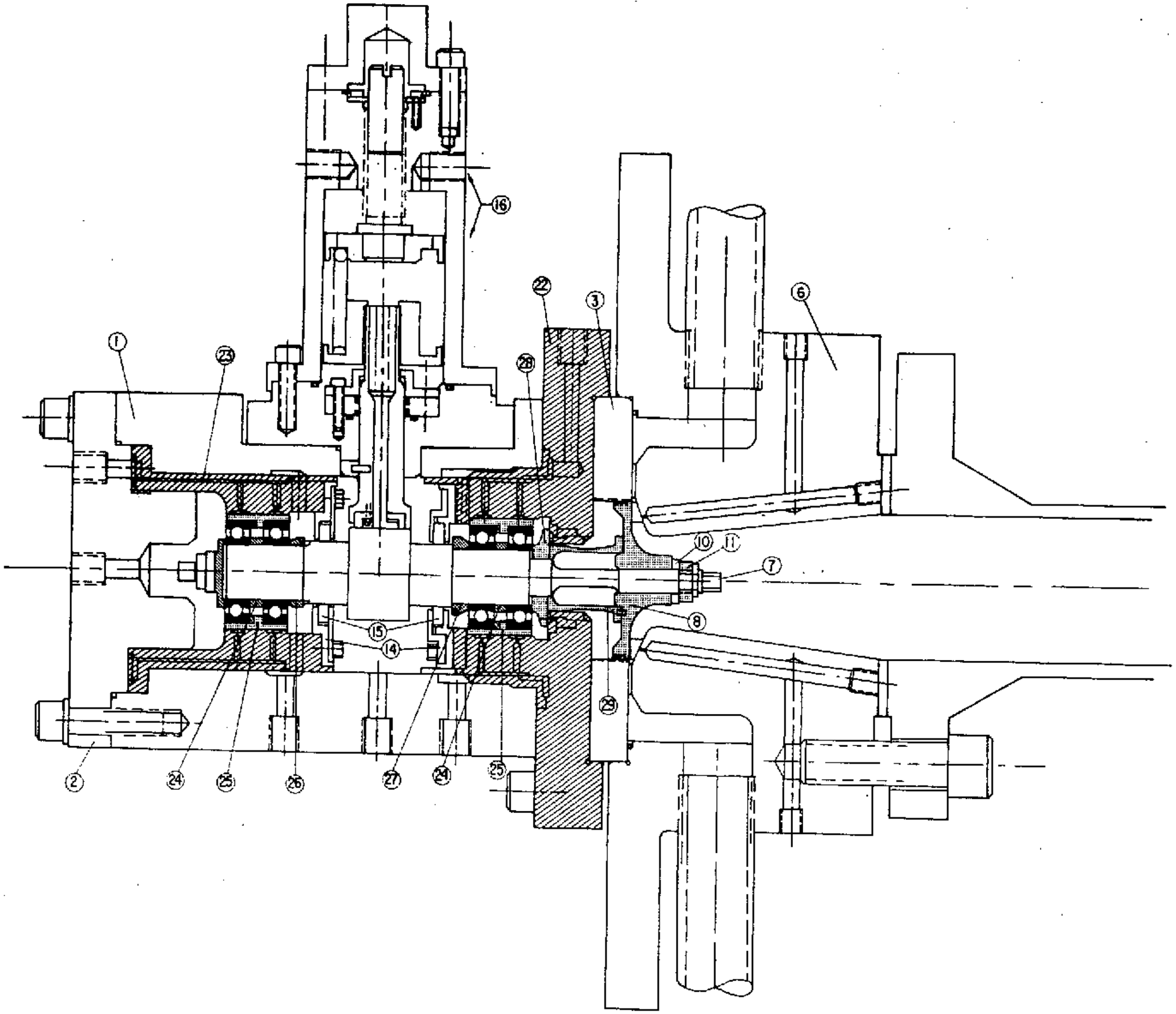

Fig. 54 Hybrid Bearing Tester

the test ball bearing in each duplex bearing set. The axial thickness difference between the unrestrained preload spring and the mid-bearing spacer determines the level of preload imposed on the bearings. A preload spring compression, which provides a 100 lb preload at assembly, has been shown in Section A to be more than sufficient to permit successful ball bearing performance throughout the entire test range. The installed assembly of the hybrid bearing is illustrated in Figure 55.

The hybrid bearing (including the hydrostatic journal bearing) requires an axially unrestrained installation to function properly. This type of installation means that close contact axial positioning devices such as bumpers must not be used, because their use imposes a thrust load on the hybrid bearing set which ultimately prevents proper operation of the fluid-film bearing component.

To relieve the hybrid bearings from the test vehicle thrust load, a thrust runner has been designed. The runner is located between the rotor shoulder and a shortened heat dam, as shown on Figure 54, Item 28 . The physical size of the thrust runner, as well as its performance characteristics are shown on Figure 56. Since the thrust bearing is unidirectional, the control of pressures which affect tester thrust unbalance must be established at levels which insure a positive thrust on the bearing. The tester design requires the maintenance of a 1.66×10^6 N/m^2 (240 lb/in^2) turbine discharge pressure regardless of the turbine supply. The desired maximum thrust load is set at 66.7 N (15 lb) thereby establishing a minimum flow rate of 5.20×10^{-3} Kg/sec (1.15×10^{-2} lb/sec) at a film thickness of 1.6×10^{-5} m (7.0×10^{-4} in). The maximum thrust load occurs during acceleration and will decrease as the turbine supply pressure is decreased. At zero speed, the thrust load will reduce to 30.9 N (6.9 lb) resulting in a flow increase to 6.15×10^{-3} Kg/sec (1.36×10^{-2} lb/sec).

a. Rotor Dynamics

The hybrid bearing tester, illustrated in Figure 56 was investigated to determine its dynamic behavior as indicated by its critical speeds and unbalanced response. The rotor model used for these analyses is shown

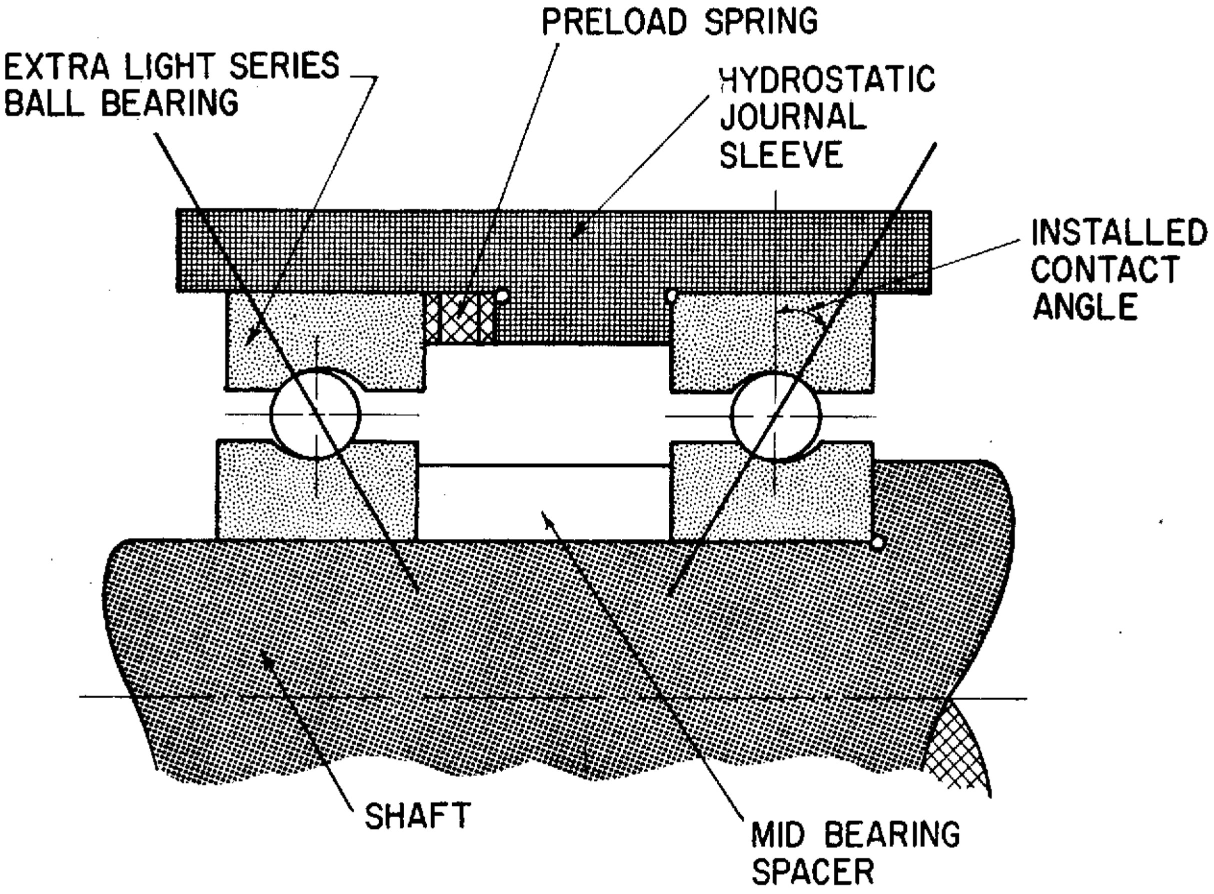

Fig. 55 Installed Hybrid Bearing Assembly

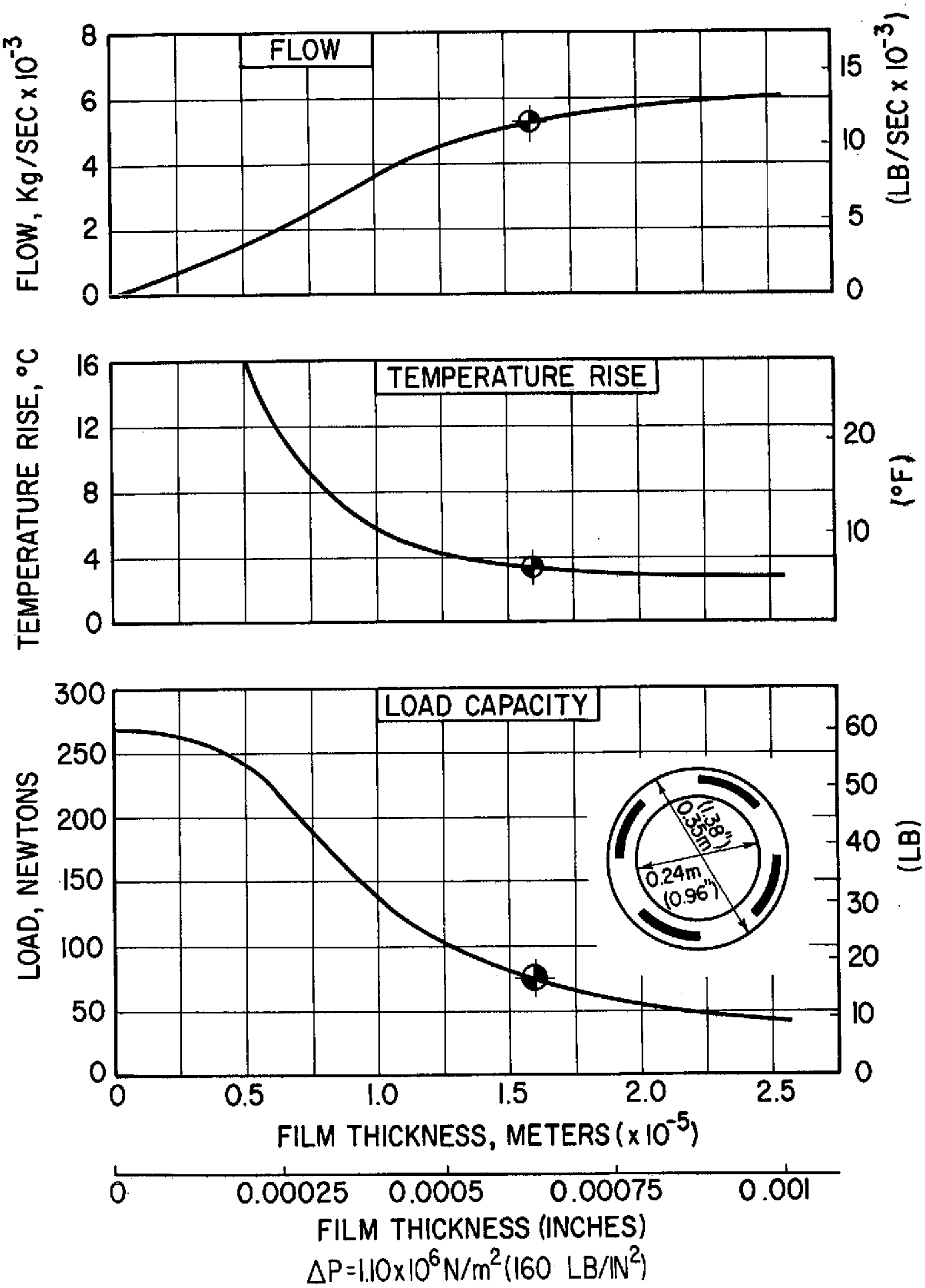

Fig. 56 Performance Characteristics of the Hybrid Bearing Tester Thrust Bearing

in Figure 57 and is represented mathematically by the rotor bearing system pictured in Figure 58 where M is the rotor mass, I_p its polar moment of inertia, and I_t its transverse moment of inertia. The turbine wheel is represented by the dynamic properties previously listed in Table 11. The remaining rotor dynamic parameters are listed in Table 17. The hybrid bearing is represented by the ball bearing stiffness K_b, the duplex bearing outer races and the hydrostatic journal sleeve mass M_p, the fluid-film damping B_p and stiffness K_p. Figure 59 shows the critical speed map for the hybrid bearing and includes the changes in ball bearing stiffness with speed.

Five hydrostatic bearing stiffnesses, representing the results of five different hydrostatic bearing supply pressures overlay the critical speed map to indicate the possible operational tracking of the hybrid bearing. A sixth curve representing $\Delta P \approx N^2$ curve is also included in Figure 59 to show a ramped supply pressure. The obvious indication of performance shown by Figure 59 is that a critical speed must be driven through at high speed for any fixed level of hydrostatic bearing pressure above 1.72×10^6 N/m^2 (250 lb/in^2). In addition, all testing in the area of 100,000 to 120,000 rpm would occur exactly on a critical speed at the higher bearing pressures leaving only pressures at or below 1.72×10^5 N/m^2 (250 lb/in^2) as the most probable pressure level permissible for safe high-speed tester operation. Several questions relating to the hybrid bearing design are raised as a result of the necessity of operating above or close to a high-speed critical speed. The three most important questions to be answered are:

- Can geometric changes improve the stability?
- Will the rotor operate in a stable mode?
- What unbalance response can be expected should the final design leave the critical speed map unaltered?

The answer to the first and second question was obtained by evaluating several changes in hydrostatic bearing geometry with the use of MTI's Rotor System Stability Program. This program was used because any rotating machine supported on fluid-film bearings operating above

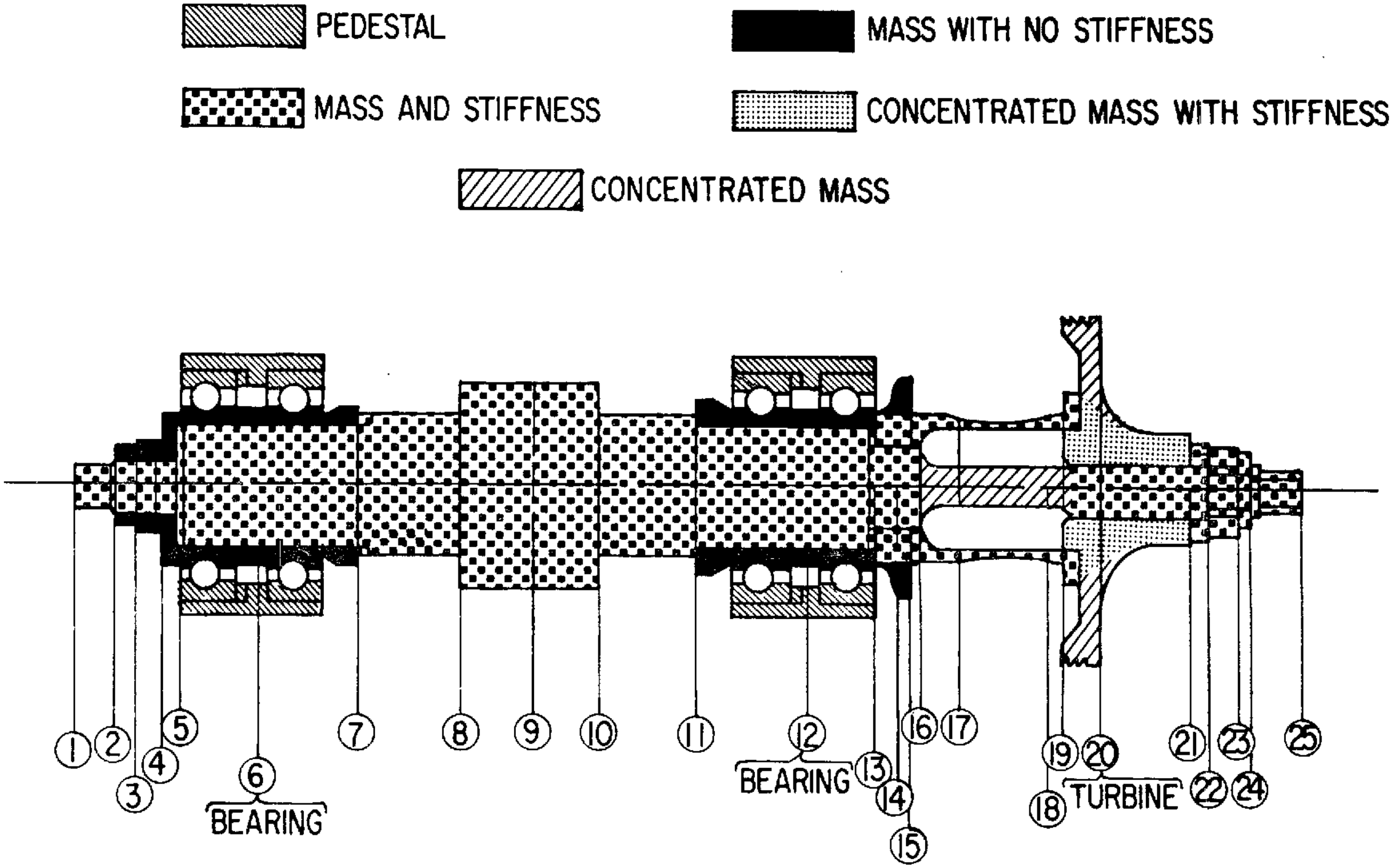

Fig. 57 Dynamic Model: Hybrid Bearing Tester

TABLE 17 HYBRID BEARING TESTER ROTOR DYNAMICS PROPERTIES

$\Delta P = 1.72 \times 10^6$ N/m^2 (250 lb/in^2)

HYBRID BEARING STIFFNESS

Speed Range	Ball Bearing Stiffness (K_b)		Hydrostatic Bearing Stiffness (K_p)	
10^3 rpm	10^8 N/m	(10^6 lb/in)	10^7 N/m	(10^5 lb/in)
5-25	2.45	(1.40)	0.26	(0.80)
30-45	1.82	(1.04)	1.02	(1.07)
50-65	1.44	(0.82)	1.40	(1.48)
70-85	1.05	(0.60)	2.08	(2.17)
90-105	0.91	(0.52)	3.43	(3.62)
110-125	0.66	(0.38)	5.21	(5.80)

HYDROSTATIC BEARING DAMPING (B_p)

$B_{xx} = B_{yy}$	
10^2 N sec/m	(lb sec/in)
10.2	(5.73)
13.9	(7.97)
19.1	(10.9)
29.7	(16.4)
46.6	(26.7)
89.0	(50.2)

Pedestal Mass $M_p = 0.104$ Kg (0.23 lb). B_{xx} and B_{yy} are damping coefficients in the x and y direction respectively for the overall damping coefficient B_p.

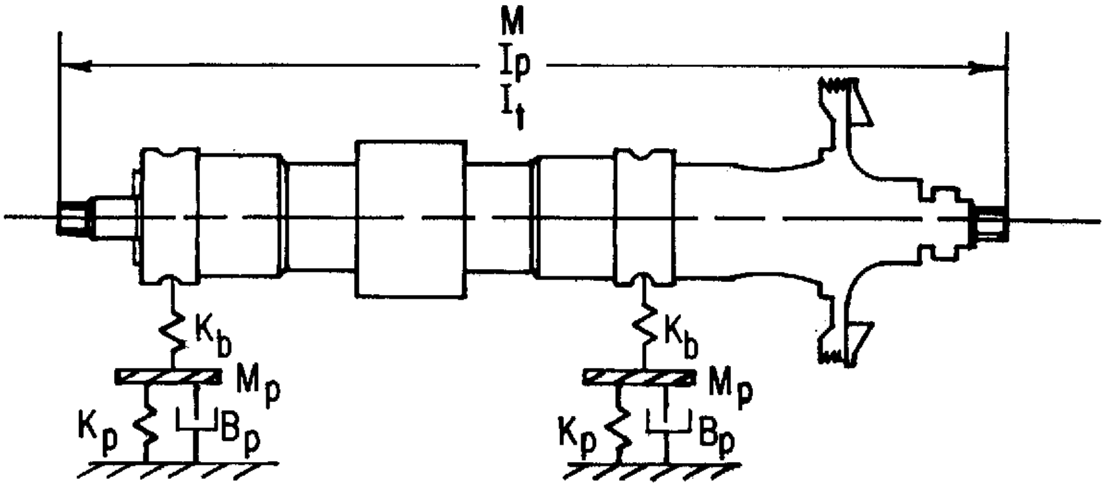

Fig. 58 Critical Speed Mathematical Model: Hybrid Bearing Tester

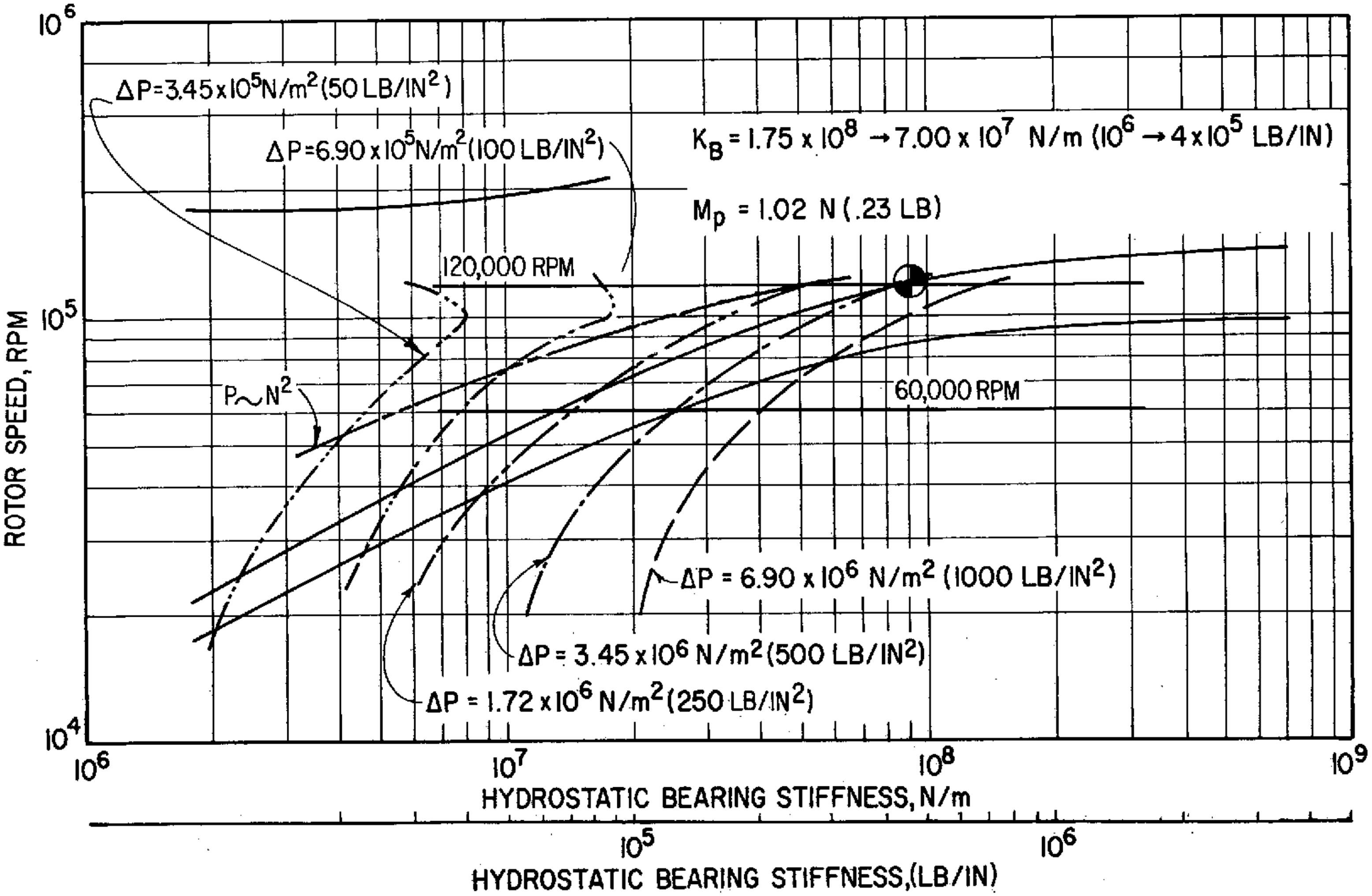

Fig. 59 Critical Speed Map: Hybrid Bearing Tester

twice its first critical speed is susceptible to rotor instabilities which are highly sensitive to changes in bearing characteristics.

At any operating speed of a rotor-bearing system, there is a system natural frequency, ν (in general, non-synchronous with the rotational speed), which can be excited and which has an amplitude decay exponent, λ. Amplitude growth is described by the expression $e^{\lambda t}$, where t is the time. In the commonly referred to logarithmic decrement $\delta = -2\pi\lambda/\nu$, if δ is positive (λ negative) the system is stable (adequately damped) and any induced vibrations will decay. As δ turns negative (rotor instability threshold speed) the rotor becomes unstable and susceptible to internal or external excitation forces.

Table 18 provides a listing of the bearing variations investigated and the resulting bearing performance. The criterion for selecting the most promising bearing design is based on which geometry provides the greatest positive value of log decrement. From Table 18, the bearing geometry with the highest probability of success is the bearing previously selected in Section B, but operating at a reduced supply pressure of $\Delta P = 1.72 \times 10^6$ N/m^2 (250 lb/in^2). The flow rate requirement for the bearing is now 0.022 kg/sec (0.05 lb/sec) resulting in an anticipated temperature rise of 10.6°C (19°F). The introduction of LH_2 to the hybrid bearing at 22.2°K (40°R) will assure that the temperature rise through the bearing will not raise the LH_2 temperature above its critical value. The temperature rise of 10.6°C (19°F) at a tester speed of 120,000 rpm results from a calculation which assumes the entire hydrostatic bearing loss is absorbed by the LH_2. A more likely condition whereby a significant amount of this energy is transferred to the surrounding metal and not into the fluid stream would reduce the calculated rise in temperature.

An added advantage in operating at the low supply pressure is the substantial reduction in LH_2 requirements the lower pressure provides. The calculated flow rate of 0.022 kg/sec (0.05 lb/sec) per bearing is (1/4) one-quarter the flow rate required by the ball bearing tester,

TABLE 18 HYDROSTATIC BEARING GEOMETRY AND SUPPLY PRESSURE EVALUATION SUMMARY

Supply Pressure ΔP		Clearance* (C)		Length (L)		Log Decrement δ	Temperature Rise ΔT		Flow Rate (Q)	
N/m^2	(lb/in^2)	mm	(in)	mm	(in)		°C	(°F)	Kg/sec	(lb/sec)
6.90×10^6	(1000)	.025	(.001)	22.0	(.9)	.154	4.30	(7.75)	.052	(.12)
6.90×10^6	(1000)	.025	(.001)	14.6	(.6)	.108	2.62	(4.72)	.056	(.13)
6.90×10^6	(1000)	.051	(.002)	22.0	(.9)	.087	1.81	(3.26)	.105	(.24)
3.45×10^6	(500)	.025	(.001)	22.0	(.9)	.193	6.50	(11.7)	.035	(.08)
3.45×10^6	(500)	.038	(.0015)	22.0	(.9)	.115	3.46	(6.23)	.056	(.13)
1.72×10^6	(250)	.025	(.001)	22.0	(.9)	.260	10.60	(19.1)	.022	(.05)
1.72×10^6	(250)	.025	(.001)	14.6	(.6)	.058	6.00	(10.8)	.026	(.06)
1.72×10^6	(250)	.038	(.0015)	22.0	(.9)	.013	5.31	(9.43)	.039	(.09)

---

*Clearance sized at 100,000 rpm.

thereby leaving a significant flow rate margin for cooling the ball bearing portion of the hybrid bearing.

The stability analysis of the hybrid bearing tester has answered the first two questions raised by the critical speed study; namely, that the basic geometry of the hydrostatic bearing is best left as originally sized and that operation of the tester along the 1.72×10^6 kg/m^2 (250 lb/in^2) stiffness line on Figure 59 will produce the most potentially stable operation. The answer to the third question lies in the results of the rotor response calculations.

The unbalanced rotor response of the hybrid bearing rotor-bearing system depends on the accuracy of the input parameters derived from the hybrid bearing calculations. The calculated performance characteristics of the hybrid bearing described in Section B were further refined to provide values of stiffness and damping at several reduced supply pressures including $\Delta P = 1.72 \times 10^6$ N/m^2 (250 lb/in^2). In addition to the nominal synchronous values of stiffness and damping, an added improvement to the response calculations was taken by including the effects of damping cross-coupling. It should be noted that the response calculations are based on an unbalance of 7.2×10^{-7} kg-m (0.001 oz-in) located at the turbine's gravitational center; this level of unbalance is, as already discussed in the preceding section, close to three times higher than will actually be attained. With the lower residual unbalance, the calculated response amplitudes will be accordingly reduced by the same amount. The response curves in Figure 60 and the response data listed in Table 19 both show maximum rotor excursion occurs outside the bearing areas and primarily affect turbine blade tip clearances. The rotor excursions, when considering the actual achievable rotor unbalance, represent tractable amplitudes and should not prevent successful operation of the hybrid tester.

The dynamic bearing loads transmitted through the bearings to the pedestals are also listed in Table 19. The maximum load occurs at the turbine end bearing, at a shaft speed of 110,000 rpm and is equal to 222N (50 lb). This radial load which lies well within the 0 - 445 N

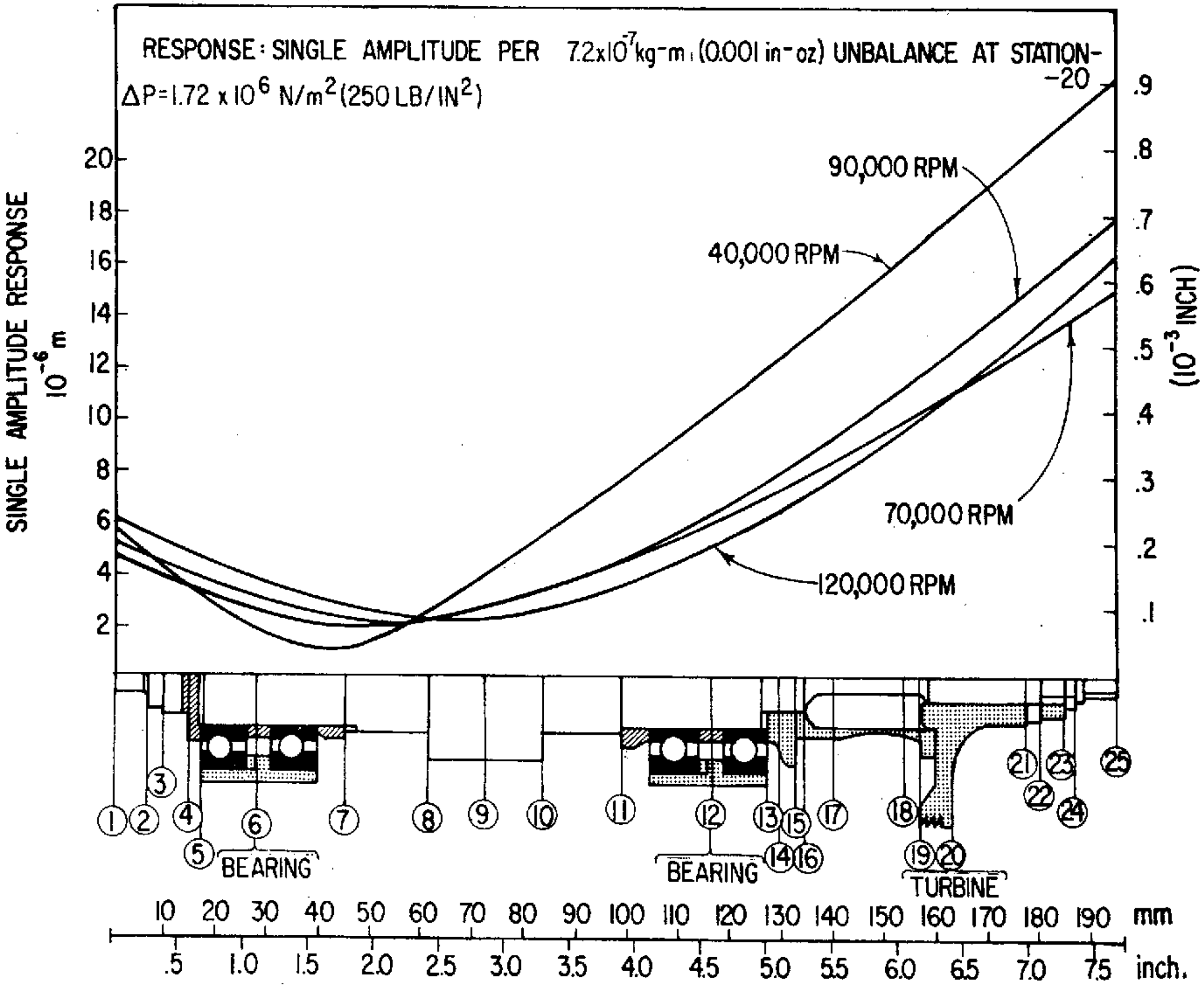

Fig. 60 Unbalance Response: Hybrid Bearing Tester

TABLE 19

RESPONSE DATA – HYBRID BEARING TESTER

	SINGLE AMPLITUDE ROTOR EXCURSIONS						FORCE TRANSMITTED TO PEDESTAL			
	STATION 6		STATION 12		STATION 20		STATION 6		STATION 12	
ROTOR SPEED	FREE END BEARING		TURBINE END BEARING		TURBINE		FREE END BEARING		TURBINE END BEARING	
RPM	m	(INCH)	m	(INCH)	m	(INCH)	N	(LB)	N	(LB)
5000	1.419E-08	(5.585E-07)	4.072E-08	(1.603E-06)	7.841E-08	(3.087E-06)	1.078E-01	(2.4208E-02)	3.094E-01	(6.9462E-02)
10000	6.065E-08	(2.388E-06)	1.771E-07	(6.971E-06)	3.386E-07	(1.333E-05)	4.470E-01	(1.0037E-01)	1.303E+00	(2.9265E-01)
15000	1.509E-07	(5.940E-06)	4.547E-07	(1.790E-05)	8.613E-07	(3.391E-05)	1.072E+00	(2.4064E-01)	3.218E+00	(7.2258E-01)
20000	3.091E-07	(1.217E-05)	9.820E-07	(3.866E-05)	1.834E-06	(7.220E-05)	2.099E+00	(4.7140E-01)	6.610E+00	(1.4841E+00)
25000	5.900E-07	(2.323E-05)	2.039E-06	(8.026E-05)	3.736E-06	(1.471E-04)	3.771E+00	(8.4673E-01)	1.276E+01	(2.8640E+00)
30000	7.559E-07	(2.976E-05)	2.703E-06	(1.064E-04)	5.004E-06	(1.970E-04)	5.775E+00	(1.2966E+00)	1.990E+01	(4.4690E+00)
35000	1.353E-06	(5.328E-05)	5.578E-06	(2.196E-04)	1.008E-05	(3.967E-04)	9.064E+00	(2.0352E+00)	3.337E+01	(7.4924E+00)
40000	2.020E-06	(7.953E-05)	1.010E-05	(3.978E-04)	1.765E-05	(6.948E-04)	1.241E+01	(2.7856E+00)	4.556E+01	(1.0229E+01)
45000	2.031E-06	(7.995E-05)	7.907E-06	(3.113E-04)	1.337E-05	(5.263E-04)	1.462E+01	(3.2822E+00)	4.518E+01	(1.0145E+01)
50000	1.923E-06	(7.569E-05)	8.659E-06	(3.409E-04)	1.520E-05	(5.985E-04)	1.892E+01	(4.2484E+00)	6.205E+01	(1.3932E+01)
55000	2.409E-06	(9.484E-05)	6.662E-06	(2.623E-04)	1.156E-05	(4.551E-04)	2.140E+01	(4.8043E+00)	5.818E+01	(1.3063E+01)
60000	3.117E-06	(1.227E-04)	5.428E-06	(2.137E-04)	9.792E-06	(3.855E-04)	2.366E+01	(5.3130E+00)	5.273E+01	(1.1840E+01)
65000	3.178E-06	(1.251E-04)	4.646E-06	(1.829E-04)	8.793E-06	(3.462E-04)	2.515E+01	(5.6479E+00)	4.836E+01	(1.0858E+01)
70000	2.921E-06	(1.150E-04)	5.883E-06	(2.316E-04)	1.903E-05	(4.305E-04)	3.535E+01	(7.9370E+00)	8.432E+01	(1.8932E+01)
75000	3.198E-06	(1.259E-04)	5.192E-06	(2.044E-04)	1.004E-05	(3.952E-04)	3.837E+01	(8.6146E+00)	7.977E+01	(1.7910E+01)
80000	3.137E-06	(1.235E-04)	4.722E-06	(1.859E-04)	9.350E-06	(3.681E-04)	4.080E+01	(9.1609E+00)	7.640E+01	(1.7154E+01)
85000	2.985E-06	(1.175E-04)	4.407E-06	(1.735E-04)	8.773E-06	(3.454E-04)	4.269E+01	(9.5861E+00)	7.429E+01	(1.6681E+01)
90000	3.289E-06	(1.295E-04)	6.043E-06	(2.379E-04)	1.263E-05	(4.971E-04)	6.633E+01	(1.4892E+01)	1.454E+02	(3.2654E+01)
95000	3.421E-06	(1.347E-04)	5.593E-06	(2.202E-04)	1.204E-05	(4.739E-04)	7.189E+01	(1.6141E+01)	1.410E+02	(3.1656E+01)
100000	3.401E-06	(1.339E-04)	5.245E-06	(2.065E-04)	1.153E-05	(4.539E-04)	7.716E+01	(1.7325E+01)	1.379E+02	(3.0963E+01)
105000	3.338E-06	(1.314E-04)	4.973E-06	(1.958E-04)	1.109E-05	(4.366E-04)	8.205E+01	(1.8423E+01)	1.362E+02	(3.0577E+01)
110000	3.856E-06	(1.518E-04)	5.530E-06	(2.177E-04)	1.197E-05	(4.711E-04)	1.169E+02	(2.6241E+01)	2.259E+02	(5.0725E+01)
115000	3.904E-06	(1.537E-04)	5.136E-06	(2.022E-04)	1.138E-05	(4.482E-04)	1.287E+02	(2.8887E+01)	2.184E+02	(4.9032E+01)
120000	3.899E-06	(1.535E-04)	4.811E-06	(1.894E-04)	1.090E-05	(4.290E-04)	1.399E+02	(3.1422E+01)	2.115E+02	(4.7498E+01)
125000	3.874E-06	(1.525E-04)	4.549E-06	(1.791E-04)	1.047E-05	(4.124E-04)	1.499E+02	(3.3666E+01)	2.055E+02	(4.6139E+01)

(0-100 lb) assumed in the original bearing calculations, will be further decreased with lowered residual unbalance.

b. Thermal Analysis

The hybrid bearing tester, like the ball bearing tester, was subjected to a comprehensive thermal analysis and like the ball bearing tester, was analyzed using all the power losses and liquid and gaseous fluid streams concurrently. The complexity of the thermal model of the hybrid tester resulting from both the interaction of many flow streams and its complicated geometry required many assumptions in order to fit the model within the computer program restraints. Along with the similar difficulties in modeling discussed for ball bearing tester, the hybrid bearing tester hydrostatic bearing LH_2 supply flow stream model could not account for fluid flow in the region between the two rows of pockets (see Section B for a complete description of the hydrostatic bearing geometry). As a result of the assumptions made, the quantitative accuracy of the temperature calculations is in doubt, although the qualitative temperature trends are valid.

Figure 61 shows the thermal model used for the hybrid bearing temperature distribution calculations. In addition to the coolant and turbine gas and radial loader flow streams, which are similar to the ball bearing tester, four new flow streams identified by grid, I, J numbers as (a) one-half hydrostatic supply at free end of bearing, (12,6) to (10,6) to (10,4); (b) one-half hydrostatic supply at free end of bearing, (12,10) to (10,10) to (10,12); (c) one-half hydrostatic supply at turbine end bearing, (12,20) to (10,20) to (10,18), and (d) one-half hydrostatic supply at turbine end bearing, (12,24) to (10,24) to (10,26), are included to simulate the hydrostatic bearings LH_2 supply paths. A composite listing of the input parameters used in the hybrid bearing thermal analysis are presented in Table 20.

The LH_2 flow to the thrust bearing was not included in the thermal mapping and therefore does not appear in Table 20. The decision not to include the thrust bearing flow was based on the inability to

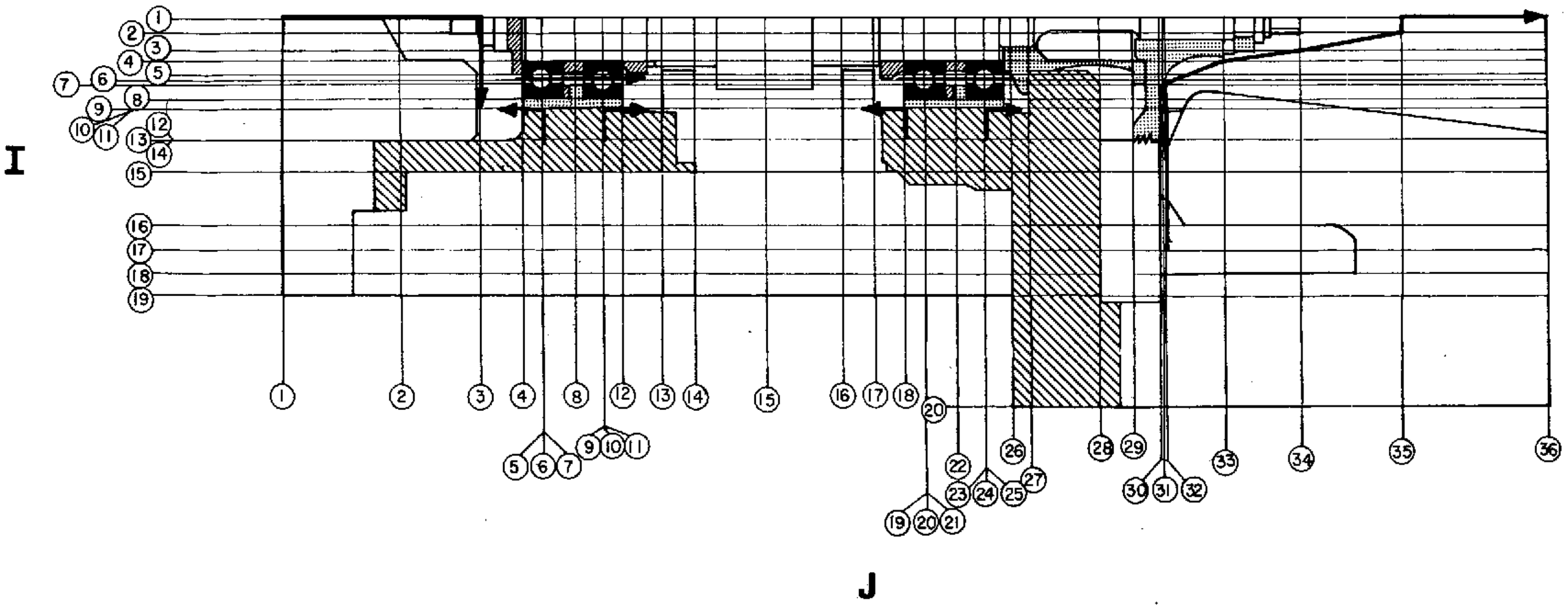

Fig. 61 Thermal Model: Hybrid Bearing Tester

TABLE 20

THERMAL ANALYSIS INPUT PARAMETERS HYBRID BEARING TESTER

		Inlet Temperature		Flow Rate		Specific Heat		Film Coefficient		Thermal Conductivity	
		^{o}K	(^{o}R)	Kg/sec	(lb/sec)	$J/Kg^{o}K$	$\left(\frac{Btu}{lb\ ^{o}F}\right)$	$\frac{Watt}{m^2\ ^{o}K}$	$\left(\frac{Btu}{hr\text{-}ft^2\text{-}^{o}F}\right)$	$\frac{Watt}{m\ -\ ^{o}K}$	$\left(\frac{Btu}{hr\text{-}ft\text{-}^{o}F}\right)$
Fluids	LH_2 Bearing Coolant (Free End)	27.8	(50)	0.045	(0.10)	9.2×10^3	(2.2)	35000	(20000)	----	----
	LH_2 Bearing Coolant (Turbine End)	27.8	(50)	0.045	(0.10)	9.2×10^3	(2.2)	35000	(20000)	----	----
	LH_2 Hydrostatic Supply (Per Stream)	27.8	(50)	0.011	(0.025)	9.2×10^3	(2.2)	28000	(16000)	----	----
	GH_2 Turbine Annulus	294	(530)	0.082	(0.18)	1.43×10^4	(3.42)	341	(194.4)	0.168	(0.097)
	GH_2 Turbine Blading	---	---	0.082	(0.18)	1.43×10^4	(3.42)	5430	(3095)	----	----
	GH_2 Turbine Discharge	---	---	0.082	(0.18)	1.43×10^4	(3.42)	3090	(1767)	----	----
	LH_2 Radial Loader	27.8	(50)	0.012	(0.025)	9.2×10^3	(2.2)	176	(100)	----	----
Solids	Stainless Steel	33.3	(60)	----	----	----	----	----	----	8.65	(5.0)
	Stainless Steel	44.5	(80)	----	----	----	----	----	----	11.2	(6.5)
	Stainless Steel	61.0	(100)	----	----	----	----	----	----	13.8	(8.0)
	Inconel 718	27.8	(50)	----	----	----	----	----	----	3.48	(2.0)
	T6 Aluminum	61.0	(110)	----	----	----	----	----	----	52.0	(30)
	Insulation (Epoxy Fiberglass)	NA		----	----	----	----	----	----	.348	(0.2)

provide a sufficient grid density in the thrust bearing area to accommodate the necessary flow stream. To balance the lack of a flow stream at the thrust bearing, the thrust bearing frictional power loss was not included in the thermal calculations.

The thermal analyses for the hybrid tester provides a temperature map of the complete tester and the temperature rise for all flow streams (both cooling and hydrostatic bearing supply). A listing of the temperature rise for each flow stream is presented in Table 21.

The largest flow stream temperature rises are indicated at the hydrostatic bearing supplies which exit the bearing toward the free-end of the rotor. The maximum indicated stream temperature rise is approximately 14.5°C (26°F). This value is larger than the bulk rise of 11°C (19°F), calculated as if the total bearing loss at 120,000 rpm was used to raise the stream temperature. This anomaly is largely due to the inability to exactly model the hydrostatic supply. The temperature rise can be expected to be significantly lower in the actual tester.

The temperature distribution in the hybrid bearing tester, using power losses calculated at a rotor speed of 120,000 rpm is shown in Figure 62. [In many aspects the hybrid tester temperature distribution resembles the results obtained for the ball bearing machines. The temperature distribution at the heat dam (Item 29 of Figure 53), shows the anticipated high axial gradient].

The temperature map also indicates some metal temperatures in excess of the LH_2 critical temperature. The major contributor to the generation of these higher temperatures is identical to that stated for the ball bearing testers, i.e., the location of generated heat along a machine surface rather than in a flow stream where the heat is actually generated.

As previously discussed, the difficulty in developing an exact thermal model that will fit the existing computer program results in temperature

TABLE 21

LH_2 COOLANT STREAM AND HYDROSTATIC BEARING SUPPLY TEMPERATURE RISE

Flow Stream	LH_2 Flow Rate Kg/Sec	(lb/sec)	LH_2 Temperature Rise Free End C	(F)	LH_2 Temperature Rise Turbine End C	(F)
Coolant Stream	0.056	(0.12)	2.38	(4.3)	—	—
Coolant Stream	0.056	(0.12)	—	—	.84	(1.5)
Hydrostatic Supply (a)+	0.011	(0.025)	14.5	(26)	13.2	(24)
(b)+	0.011	(0.025)	7.8	(14)	8.4	(15)

+Left Row of Pockets Designated as "a" Supply
Right Row of Pockets Designated as "b" Supply

ASSUMED LOSSES

● Windage	252 Watts (862 BTU/hr)
● Seals	90.4 Watts (308 Btu/hr)
● Hydrostatic Bearing*	2440 Watts (8359 BTU/hr)

*Loss Distributed Equally Between Journal and Bearing Surfaces

TEMPERATURES ARE IN °K(°R)

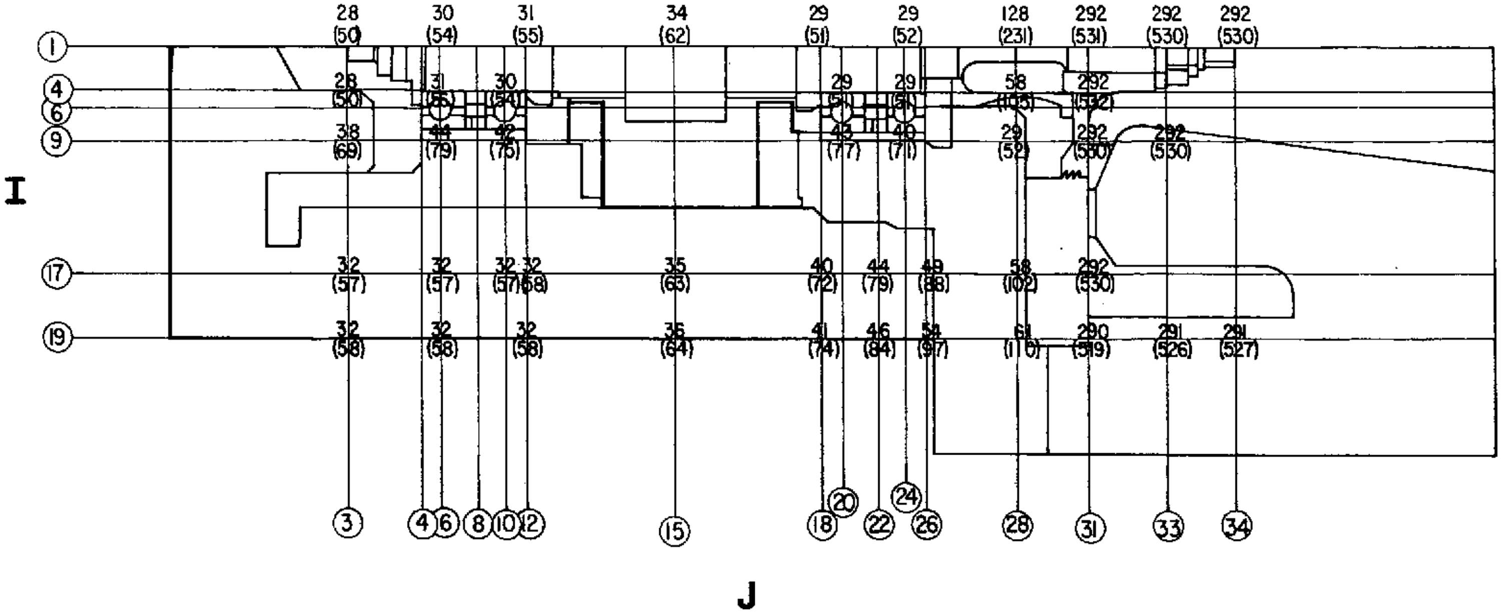

Fig. 62 Temperature Distribution: Hybrid Bearing Tester

levels much higher than would be experienced by the actual machine. Moreover, the introduction of additional streams, such as the hydrostatic feed paths, without a further increase in the grid density (decrease in spacing between stations) may seriously curtail the accuracy of the calculated temperatures. Unfortunately, a further increase in the grid density was not possible due to the inherent limitations of the thermal program used. In general, the conclusions drawn in Section C-1 apply also to the hybrid tester configuration.

3. Special Common Parts

Several specialized components which are common to both test vehicles require a specific design effort. These component designs are described in the following report section.

a. Seal Design

The seals incorporated in both test rig designs are of the non-contact clearance type and are used to isolate and direct the flow of various gases and liquids required by the testers during operation. In the ball bearing tester shown in Figure 63, four different leakage paths are identified. All these leakage paths are restricted by seals consisting either of floating rings, labyrinth, or laminar annular restrictors.

Two identical floating ring seals ① located between the radial loader cavity and the test bearing cavity are installed to maintain a 1.72×10^6 N/m^2 (250 lb/in^2) bearing cavity pressure, thereby insuring a positive leakage of liquid hydrogen from the bearing cavity to the loader cavity which is to be maintained at 1.66×10^6 N/m^2 (240 lb/in^2). These seals are to be employed only when gaseous hydrogen is used to activate the radial loading device. The use of liquid hydrogen in the radial loader will eliminate the necessity for seals in location ①. A fixed clearance seal ② separates the turbine end cavity from the turbine back space. This seal serves the same function as the shaft seals (Item ②), which is the maintenance of a 1.72×10^6 N/m^2 (250 lb/in^2) bearing cavity pressure and a positive leakage path of

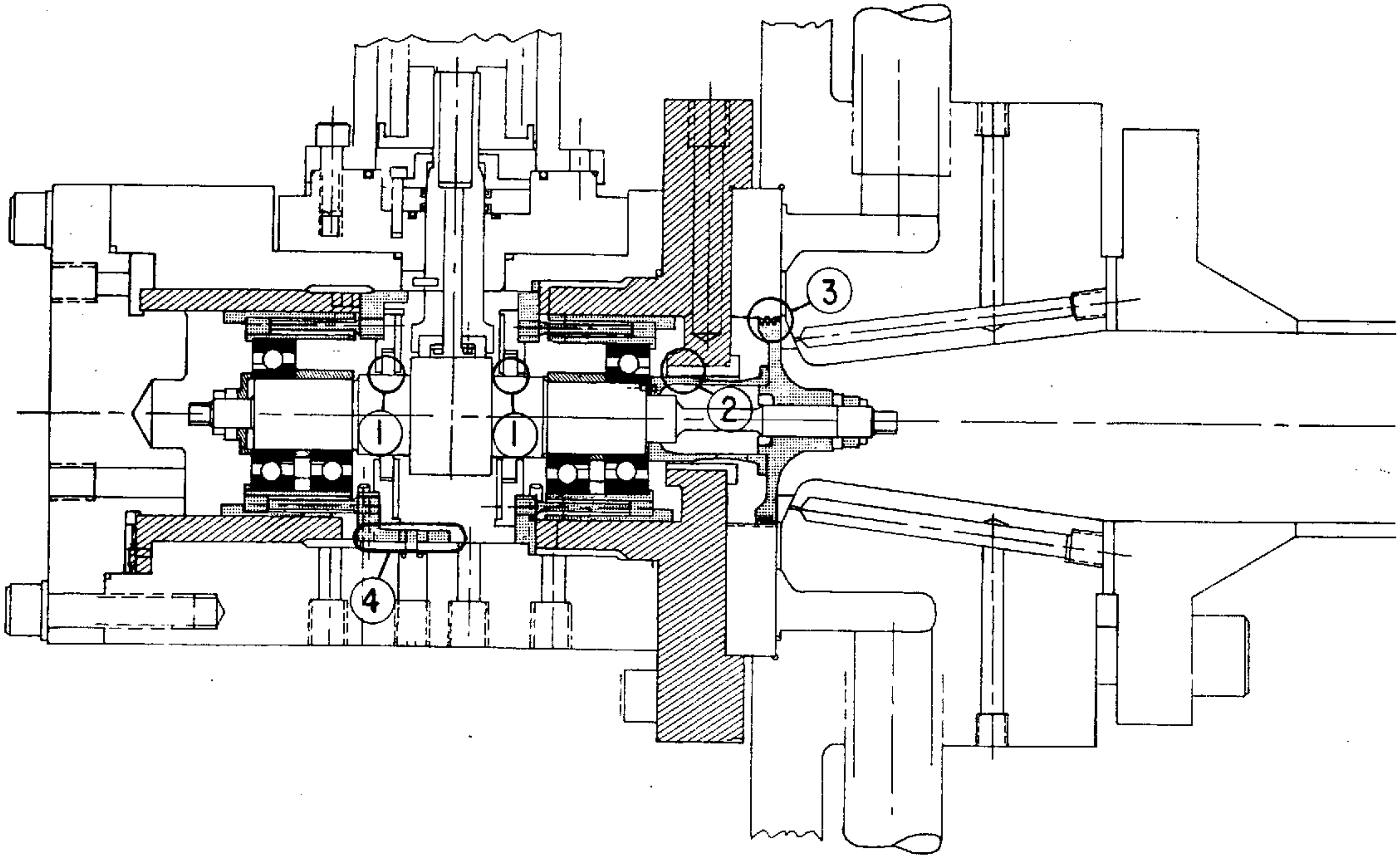

Fig. 63 Tester Seal Identification

liquid hydrogen into gaseous hydrogen behind the turbine wheel. The third leakage path is through a labyrinth seal at the turbine tip ③. This seal is used to prevent the high turbine supply pressure from acting against the back of the turbine wheel. The leakage through this seal is speed dependent due to centrifugal growth of the aluminum turbine wheel.

The cavity in the back of the turbine wheel, which is isolated between seals ② and ③, is vented to the turbine outlet duct that is maintained at 1.65×10^6 N/m^2 (240 lb/in^2). This arrangement in addition to minimizing leakage through the imposition of a 6.9×10^4 N/m^2 (10 lb/in^2) pressure drop across seal ②, also controls the hydraulic thrust load acting on the rotor (see Appendix H).

The leakage path ④ occurs between the bearing mount (Item ⑬ of Figure 52 and the housing). Leakage across this path is again the result of 6.9×10^4 N/m^2 (10 lb/in^2) ΔP across the bearing mount between the bearing cavity and the loader cavity. Again, should LH_2 be used in the radial loader, this leakage path will be eliminated.

The leakage rates through the three seals (①,②, &③), and the clearance leakage (④), have been calculated versus a number of variables (i.e., pressure drop, clearance and/or downstream temperature). Calculation of flows for conditions in the subsonic regime was carried out by use of the MTI generalized bearing/seal program. This program takes into account compressibility of the fluid, and nonlinear turbulence. A value of viscosity evaluated at the mean temperature and pressure is shown in Figure 64. The pressure drop due to the acceleration of the flow into a seal entrance was neglected for the subsonic regime of operation. The values adopted here are thus conservative.

For high velocities compared to the speed of sound, the flow is less than or equal to the choked flow. This can be obtained by the nozzle flow equation evaluated at the critical pressure ratio:

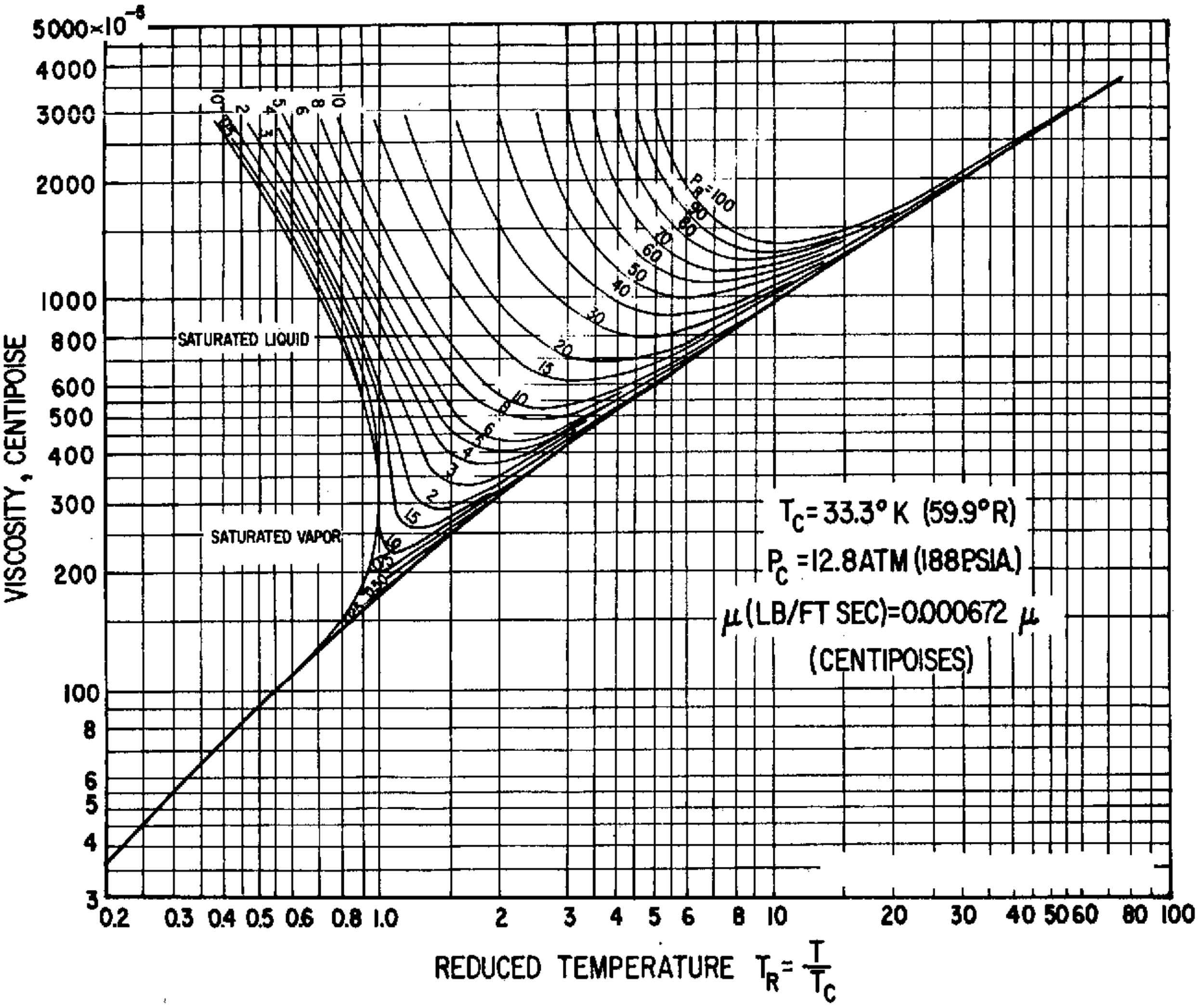

Fig. 64 Viscosity Chart for Hydrogen

$$\left(\frac{P_2}{P_1}\right)_{cr} = \left(\frac{2}{\gamma + 1}\right)^{\gamma/\gamma-1}$$

The flow is given by:

$$Q = C_D \, A \left\{ 2P_1\rho_1\left(\frac{P_2}{P_1}\right)^{2/\gamma} \left(\frac{\gamma}{\gamma - 1}\right) \left[1 - \left(\frac{P_2}{P_1}\right)_{cr}^{\frac{\gamma-1}{\gamma}}\right]\right\}^{1/2}$$

where A is the minimum flow area and C_D the discharge coefficient. A value of $C_D = 1$, was used to obtain a conservative leakage rate.

The calculated results for the selected seal designs are summarized in Table 22. The anticipated total hydrogen leakage rate is expected to be 0.038 Kg/sec (0.070 lb/sec) of which 28 percent is liquid, in a system which employs all four seals. The use of LH_2 instead of GH_2 in the radial loader will eliminate seals ① and ④, hence the total hydrogen leakage rate will be .025 Kg/sec (0.56 lb/sec) of which about 11 percent will be LH_2.

TABLE 22

SEAL LEAKAGE RATES

Seal Ident.	Flow Medium	Temperature °K	(°R)	Radial Clearance mm	(in)	Leakage Rate Kg/sec	(lb/sec)
1	LH_2	27.8	(50)	0.025	(0.001)	6.35×10^{-3}	(.014)
2	LH_2	27.8	(50)	0.025	(0.001)	2.71×10^{-3}	(.006)
3	GH_2	29.4	(350)	0.075	(0.003)	2.27×10^{-2}	(.05) at 120,000
4	LH_2	27.8	(50)	0.012	(0.0005)	0.091×10^{-3}	(.0002)

Total Leakage: 0.032 Kg/sec (0.070 lb/sec)
72 percent gaseous, 28 percent liquid

A complete set of graphs providing leakage rates for all seal calculations is found in Appendix I. The leakage through path No. 4 is not presented graphically since it is a singular point.

All leakage calculations as well as the general discussion of the seals apply equally well to the single ball bearing, duplex ball bearing and hybrid testers. The only exception is the seal location in position ② in Figure 63. In the hybrid version, the sealing in this position is accomplished by the thrust plate (Item 28 in Figure 54), the characteristics of which are discussed in Section C-2. The net leakage rate shall, however, remain at the 2.7×10^{-3} Kg/sec (.006 lb/sec) level.

b. Turbine Design

The drive turbine design for the hybrid and ball bearing testers was based on the following initial specifications:

Power - 11,900 watts (16 HP) max.
Max. Speed - 120,000 rpm
Acceleration - 50,000 rpm/sec
Gas Supply - GH_2: 1.66×10^7 N/m^2 (2400 lb/in^2) and 21.1°C(70°F)

The maximum power required by the turbine was obtained from the following sources:

1. Torque to Accelerate
2. Torque to Sustain
    a. Bearing Losses
    b. Windage Losses
    c. Seal Function Losses
3. Safety Margin

The rotor polar moment of inertia generated by the rotor dynamics computer program is $I_p = 6.28 \times 10^{-5}$ $Kg\text{-}m^2$ (0.23 $lb\text{-}in^2$). In order to overcome inertia and to sustain the 50,000 rpm/sec acceleration to 120,000 rpm requires a turbine torque of .339 N-m (3 in-lb). Bearing loss calculations show a sustaining torque requirement of 0.555 N-m (4.92 in-lb) at 120,000 rpm, and seal and windage loss calculations indicate a torque to be supplied by the turbine at 120,000 rpm is

0.026 N-m (0.24 in-lb). The maximum turbine power requirement is thus 11,900 watts (16 HP). This number includes all power losses plus the acceleration requirements.

The design of a GH_2 turbine presents a somewhat unusual problem in that the sonic velocity of hydrogen is about four times that of air, the limiting aerodynamic criteria is not Mach No., but one of limiting wheel stresses. For reasons of design flexibility and low cost manufacture, it is advantageous to use the cantilever radial in-flow type turbine. This type of turbine, however, does have higher inherent stresses than the full bladed radial in-flow type. Considering further the use of a high strength wrought aluminum alloy, such as forged 2014-T6, the turbine tip speed is limited to 1300 ft/sec, depending on the final length of the cantilevered blade section. In this regard, it should be noted that when the turbine exhausts to atomospheric pressure, a very large blade length is necessary to pass the required mass flow. To bring the stress level within safe limits, it was necessary to reduce the blade height. A shorter blade in turn required high turbine back-pressures (higher gas density) to maintain the specified power output. After several trials, the design values shown in Table 23 were arrived at. The back-pressure was elevated to 1.66×10^6 N/m^2 (240 lb/in^2). The turbine flow rate, generated power and pressure requirements as functions of speed are shown in Figures 65, 66 and 67.

The elevated back-pressures, in addition to providing for the required turbine power output, contributes, also, as explained in preceding sections, to the reduction of test vehicle leakage and hydraulic thrust loads. However, the need to maintain this pressure at a constant level when the turbine flow is varied, will require a variable size orifice at the turbine exhaust. The automatic adjustment to the exhaust orifice area, in conjunction with turbine supply pressure to maintain the desired torques and speeds will have to be provided for in the control system layouts.

TABLE 23

TURBINE DESIGN VALUES

	Accelerating	Sustaining			
Speed: RPM	120,000	120,000	90,000	60,000	30,000
Torque: N-m (in-lb)	0.96 (8.5)	0.62 (5.5)	0.38 (3.4)	0.20 (1.8)	0.085 (.75)
Power: WATTS (HP)	11,900 (16.2)	7820 (10.5)	3620 (4.85)	1280 (1.72)	268 (.36)
Pressure Ratio:	1.35	1.2	1.108	1.044	1.014
Back Pressure Orifice Dia.: m (in)	113 (.444)	106 (.415)	92 (.362)	75.7 (.298)	53.5 (.211)
Enthalphy Drop: Joule (BTU)	$1.57x10^5$ (149)	$9.6x10^4$ (91)	$5.39x10^4$ (51)	$2.32x10^4$(22)	$7.4x10^3$ (7)
Supply Pressure: N/m^2 abs (lb/in^2)	$2.23x10^6$ (323)	$1.99x10^6$ (288)	$1.83x10^6$ (265)	$1.73x10^6$(250)	$1.64x10^4$ (244)
Mass Flow Rate: Kg/sec (lb/sec)	$6.99x10^{-2}$(.152)	$5.66x10^{-2}$ (.125)	$4.29x10^{-2}$(.0945)	$2.90x10^{-2}$(.064)	$1.45x10^{-2}$(.032)

TURBINE CONSTANTS

Turbine Inlet Dia.: m (in)	5.70×10^{-2} (2.2)
Turbine Exhaust Dia.: m (in)	4.06×10^{-2} (1.6)
Inlet Blade Height: m (in)	1.09×10^{2}(.043)
Exhaust Blade Height: m (in)	2.28×10^{-2} (.090)
Turbine Back Pressure N/m^2 (lb/in^2)	1.66×10^{6} (240)
Inlet Temperature: °K (°R)	294. (530)
Turbine Efficiency:	.65
Number of Nozzles:	19
Number of Buckets:	30

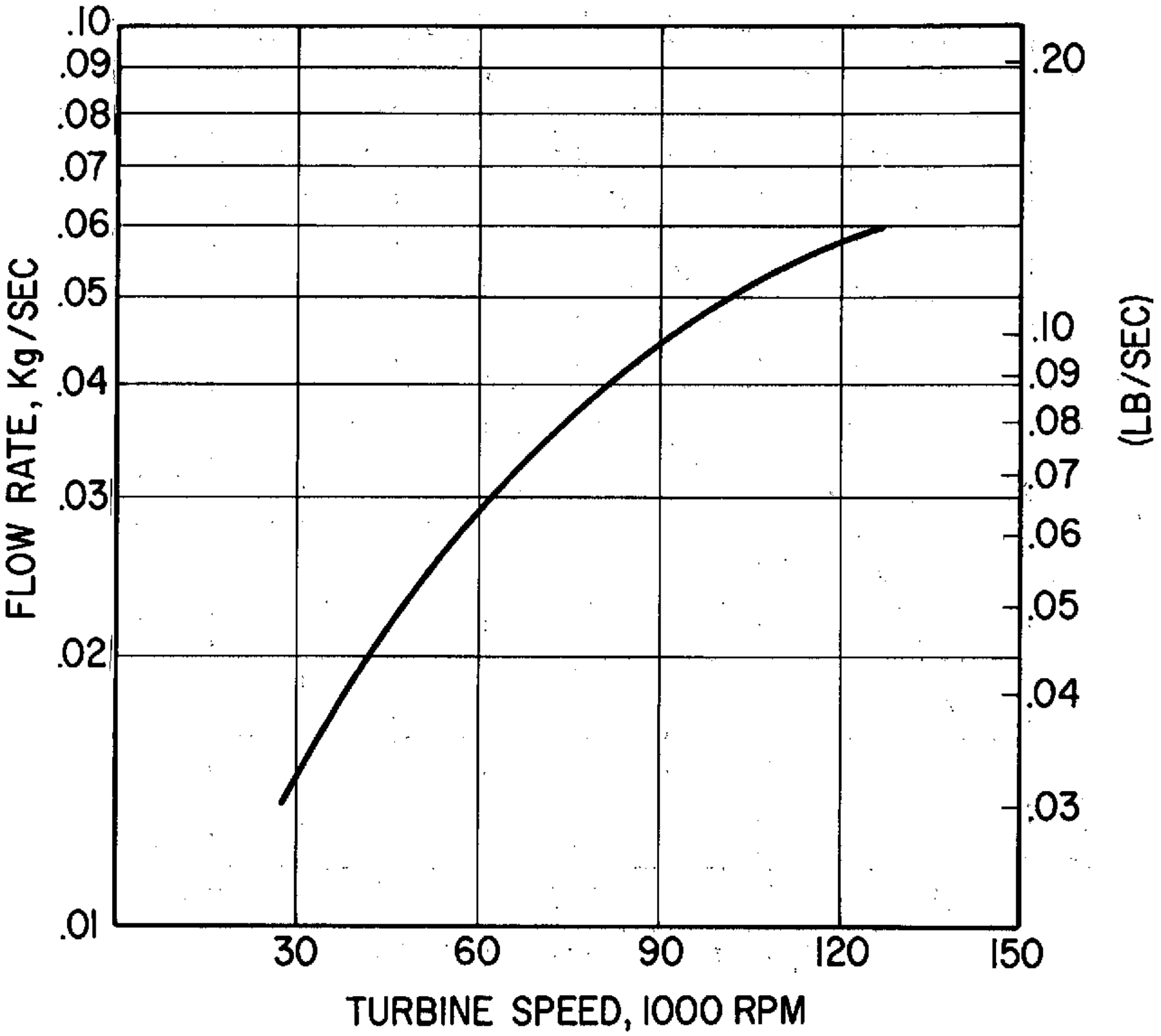

Fig. 65 Turbine Flow for Sustained Operation

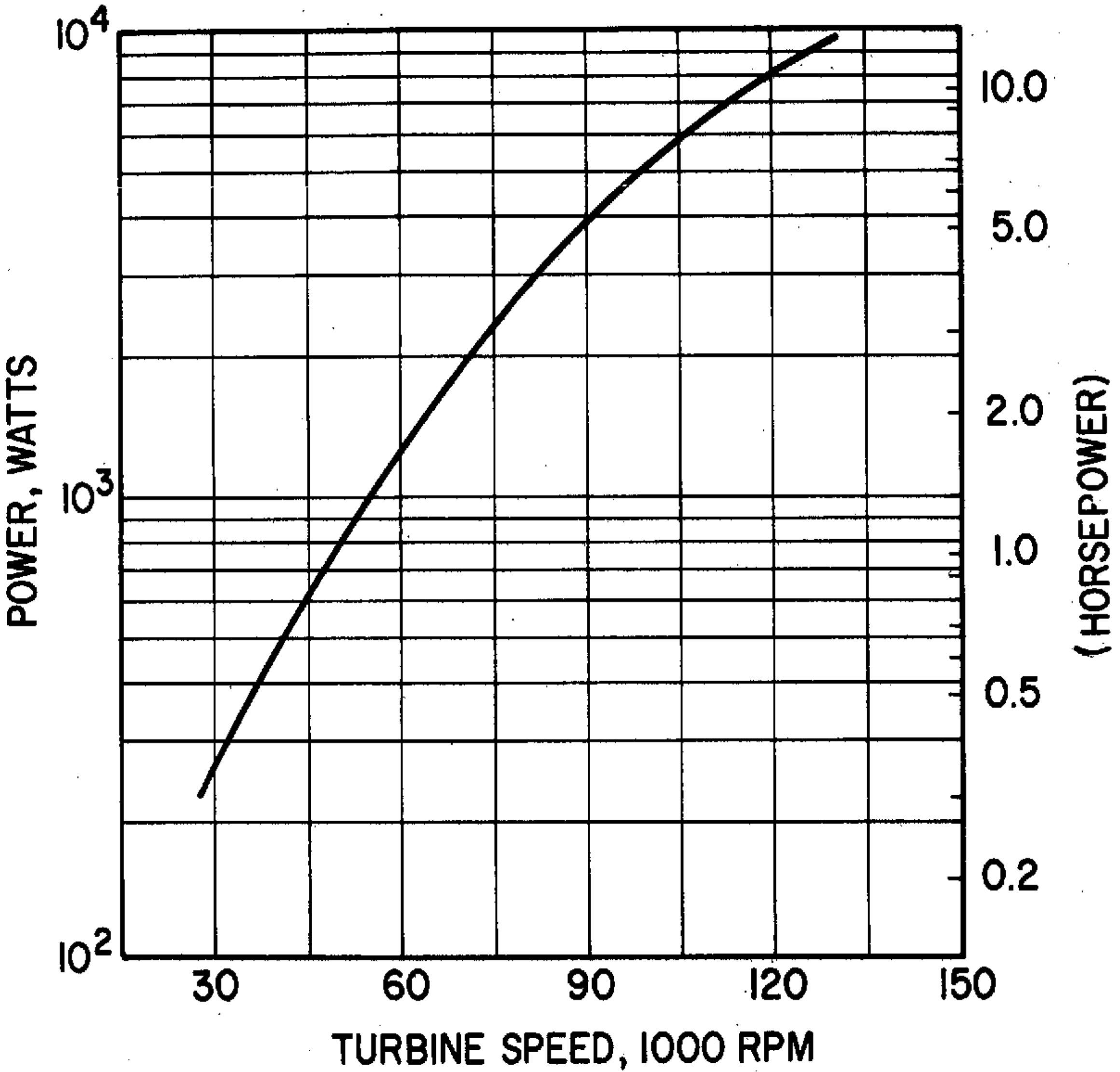

Fig. 66 Turbine Power at Sustained Operation

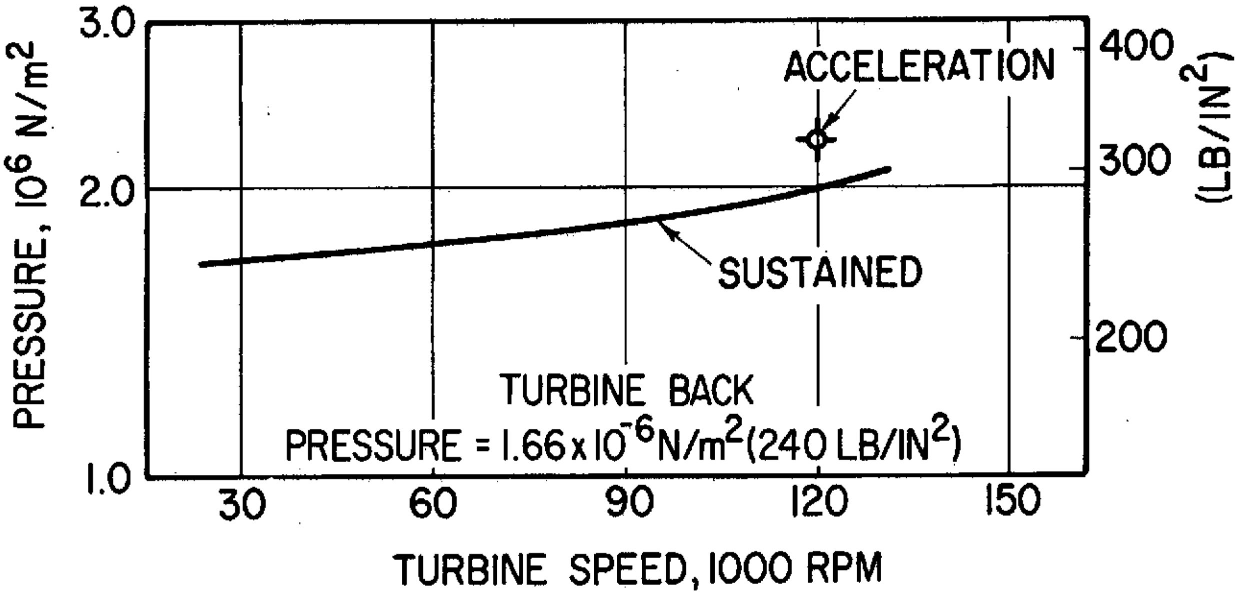

Fig. 67 Turbine Supply Pressure Requirements for Sustained Operation

c. Instrumentation

Proper evaluation of both the ball bearing and hybrid bearing tester performance relies on the accurate measurement of many test parameters. Table 24 lists the parameters to be measured, the location of the primary sensor and the type of instrument to be employed. The selected instrument locations are identified by number on two tester layouts; Figure 68 for the ball bearing, and Figure 69 for the hybrid bearing. In cases where the primary sensor is external to the tester, the instrument attachment provision is listed rather than the instrument type. Selection of instrument types is based on the compatibility of the selected instrument with cryogenic hydrogen.

Particular attention has been paid to those instruments which are to be permanently installed within the tester housing. The ball bearing outer race thermocouples will be installed into the flexure mounts in juxtaposition with the ball bearings' outer races. These thermocouples will be assembled from individual 2.54×10^{-4} m (0.010 in) diameter chromel and constantan wires, each having a 7.53×10^{-5} m (0.003 in) thick teflon insulation jacket. Two thermocouples will be installed at each bearing making a maximum of eight (8) thermocouples to be installed for the ball bearing testers. The hybrid bearing tester ball bearings have rotating outer races and as such are not capable of being thermally monitored, however, a pair of thermocouples will be installed in the non-rotating part of the free end hybrid bearing. The remaining temperatures of interest, internal to the testers, shall be obtained with sheathed 1/16 diameter platinum resistance thermocouples which will penetrate the tester housing through sealing gland fittings at the 1/8 NPT ports provided on several tester parts.

Rotor and pertinent bearing speeds will be measured with the use of photo-electric devices. Each speed measurement listed will require a separate optical fibre bundle and transducer amplifier to convert six (6) pulses per revolution signals to rpm equivalents. Two additional photosensitive probe locations are provided in the hybrid bearing tester to permit the measurement of the hybrid journal sleeve lateral motion. The two probe locations will be at the free end bearing and circumferentially displaced by 90°.

TABLE 24

INSTRUMENTATION LIST

	Measurement	Location Preload Tester	 Duplex Tester	 Hybrid Tester	Type
1	Inner Race Speed	Rotor: Turbine End	Rotor: Turbine End	Rotor: Turbine End	Fiber Optic Sensor
2	Cage Speed	Rotor: Free End	Rotor: Free End	Rotor: Free End	Fiber Optic Sensor
3	Outer Race Speed			Rotor: Free End	Fiber Optic Sensor
4	Ball Bearing Temp.	Outer Race 2 Brgs.	Outer Race 4 Brgs.		Platinum Resistance Thermocouple
5	Vibration	Housing — Both Ends	Housing — Both Ends	Housing — Both Ends	Accelerometer
6	Axial Load	Free End Bearing Mt.			Strain Gage
7	Radial Load	Free End Bearing Mt. Loader Piston	Free End Bearing Mt. Loader Piston	 Loader Piston	Strain Gage Pressure Transducer
8	Bearing Coolant Temperature	Adjacent to Bearing Inlet and Outlet	Adjacent to Bearing Inlet and Outlet	Adjacent to Bearing Inlet and Outlet	1/8 NPT Port Provided
9	Bearing Coolant Pressures	At Supply and Discharge Ports	At Supply and Discharge Ports	At Supply and Discharge Ports	1/8 NPT Port Provided
10	Coolant Flow Rate	External	External	External	
11	Bearing Supply Pressure			From Internal Manifold	1/8 NPT Port Provided
12	Bearing Supply Flow Rate			External	
13	Bearing Supply Temperature			External	
14	Bearing Recess Pressure			External	1/8 NPT Port Provided
15	Rotor Lateral Motion			Hydrostatic Bearing Sleeve - Free End	Fiber Optic Sensor

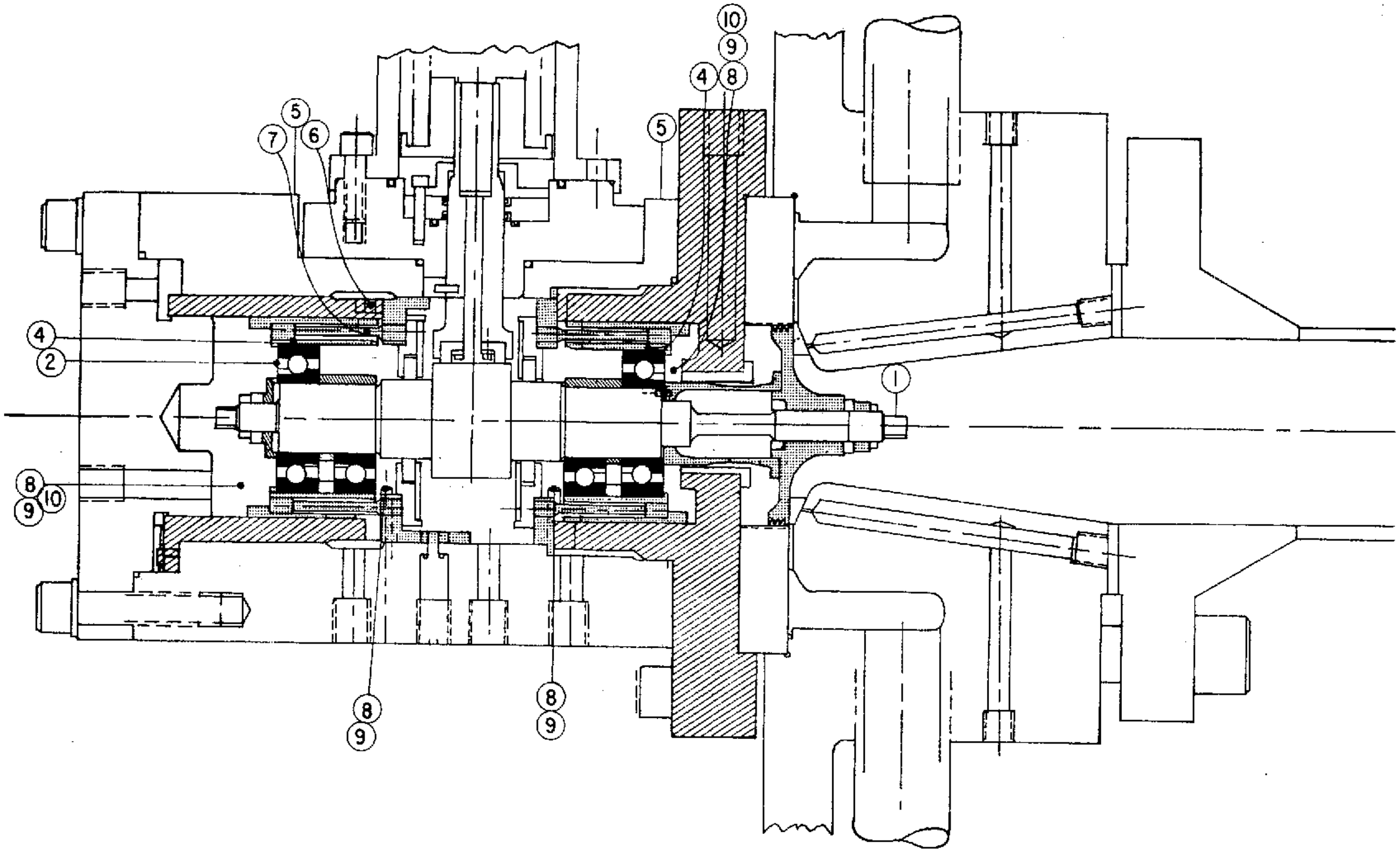

Fig. 68 Ball Bearing Tester Instrumentation

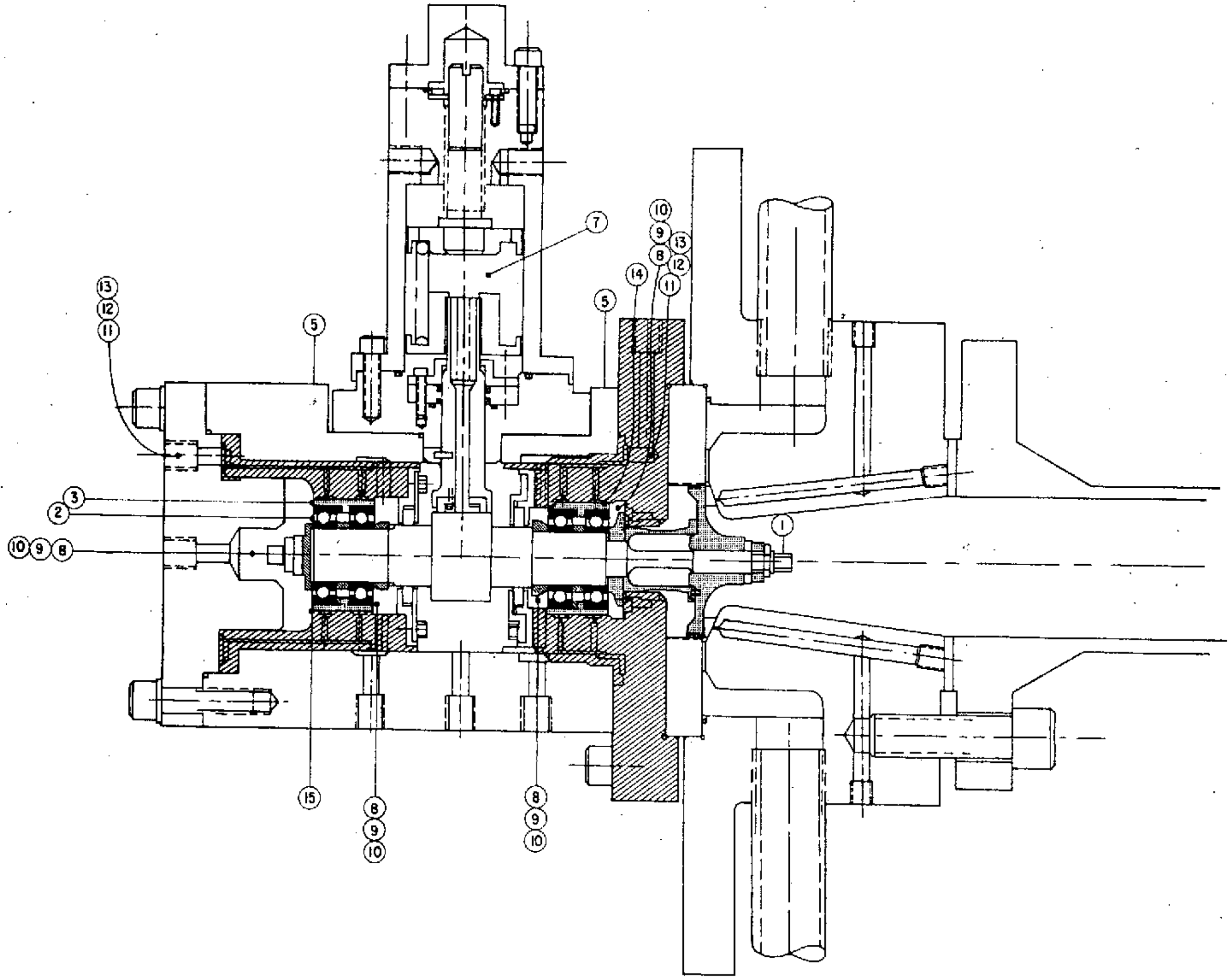

Fig. 69 Hybrid Bearing Tester Instrumentation

Both radial and axial loads imposed on the ball bearing tester will be measured with strain gage instrumentation. An axial load spring will be installed between the free end flexure mount (Item ⑬, Figure 42) and the loader piston (Item ⑰, Figure 42). Four strain gages operating into a full bridge will provide the necessary strain information for determining the applied axial load. The strain gages will be attached in pairs at the maximum bending stress location of the load spring in order to maximize the strain reading. The positive and negative reading strain gages share alternate positions on the bridges. When arranged in this configuration, they will provide both maximum output and temperature compensation.

Radial load is similarly measured on the ball bearing tester with the installation of four (4) strain gages on two spokes of the free end flexure mount. Two gages will be attached to the maximum stress point on each of two spokes, aligned with the radial load. Alternate connections of the positive and negative reading gages on a full bridge will maximize the strain readings resulting from radial load and provide for temperature compensation.

In addition to load and speed, it is anticipated that close monitoring of the supply pressures and temperatures will be desired. To assist in obtaining these data, 1/8 NPT ports for the necessary pressure and temperature sensor fittings are provided in both the ball bearing and hybrid testers.

d. Materials

The following specific materials requirements are important in the design of both the ball and hybrid bearing testers.

1. Dimensional stability of the bearings and structural parts
2. Erosion and corrosion resistance
3. Sliding compatibility of the materials, including sliding under start-stop conditions and during a high-speed rub
4. Matched coefficients of thermal expansion between the bearings, the shaft and housing, throughout the operating temperature range

The third item on this list is perhaps the most critical one, and though all four requirements need to be satisfied, it may be necessary in any trade-off of requirements to emphasize this one. This is particularly true for the hybrid bearing tester journal bearings. The ball bearing material selection has been discussed in Section A-2.

Table 25 details some of the existing liquid hydrogen sliding bearing material experience (References 1 & 2). The materials most readily adaptable to the fluid-film bearing component of the hybrid bearing are those run by Rocketdyne. These materials consisted of chrome plate vs. silver plate deposited on the basic materials of construction. The advantage of using plated films rather than solid inserts is obvious, since the plating permits the selection of the substrate materials on the basis of strength, stability, and thermal matching considerations. Chrome plate and silver plate are, furthermore, easy to apply, as well as economical to repair, should any accidental damage occur during the tests. The hybrid journal sleeve, made of 440 C stainless steel for thermal compatibility with the test ball bearings, will be hard chrome plated. Bearing bores of the hydrostatic bearing flanges (Item ㉒ of Figure 54) will be silver plated as per AMS-2412. The plating will be held to a final thickness of 2.54×10^{-5} – 7.62×10^{-5} m (0.001 - 0.003 inch).

The remainder of all the tester parts with the exclusion of the rotating assembly (rotor, spacers, heat dam, turbine wheel and fasteners) will be made of 316 stainless steel. Selection of the 316 stainless steel alloy is based on the following reasons:

- All 300 series stainless steels are recommended for cryogenic temperatures
- 316 stainless steel is readily available
- Notch strength of 316 at cryogenic temperatures ranks among the highest of all 300 series stainless steels
- Thermal expansion coefficient slightly higher than 440 C stainless steel to permit ease of assembly at room temperature

TABLE 25 LIQUID HYDROGEN HYDROSTATIC BEARING MATERIALS EXPERIENCE

Company	Materials	Results	Reference
Pratt and Whitney	1. Bearing B-10 Lead bronze bushing Tungsten carbide coated Inconel 718 journal	Success	2
	2. Bearing B-10 lead bronze bushing Tungsten carbide coated AMS 6260 journal	Success	2
Aerojet General	Inconel 718 coated with tungsten carbide journal and bearing	Failure	3
Rocketdyne	Silver plated bearing with chrome-plated journal	Success	

Inconel 718 is specified for all rotating tester parts with the exception of the turbine wheel. Two primary reasons for the selection of Inconel are its relatively high impact strength at cryogenic temperatures (approximately 40 times higher than 440 C stainless steel), combined with only a 25 percent larger thermal expansion coefficient, as compared to 440 C. No other stainless steel combines the high impact strength at cryogenic temperatures necessary for the tester rotor with a thermal expansion coefficient close to 440 C. Although many stainless steels have high impact strengths at low temperatures, the large thermal expansion rates (as much as 180 percent more than 440 C) preclude their use as shafting, since excessive interferences between the ball bearings and the rotor would be required during room temperature assembly.

The turbine wheel design specifies 2014-T6 forged aluminum as its material for the following reasons:

- Turbine wheel's predominant operating temperature will be at or near 294°K (530°R) and so cryogenic temperatures are not major design criteria
- The overhung turbine design dictates a light weight turbine wheel
- 2014-T6 forgings have been successfully employed for high-speed turbine wheels in the past

All static seals installed in tester areas where cryogenic temperatures are anticipated are specified to be 321 stainless steel, unvented standard wall "O"-rings with a $2.54 \times 10^{-4}/5.08 \times 10^{-4}$ m (0.001/0.002 in) thick silver plate. In those areas of the testers where temperatures are at or near 294°K (530°R), fluorinated polymer "O"-rings are used.

Table 26 lists the cryogenic properties of all the major component materials used in the manufacture of both testers.

TABLE 26

MATERIAL PROPERTIES OF TESTER PARTS AT CRYOGENIC TEMPERATURES

Item	Material	Density		Youngs Modulus		Thermal Expansion Coefficient		Thermal Conductivity*	
		Kg/m^3	(lb/in^3)	N/m^2	(lb/in^2)	m/m	(in/in)	W/m-°F	(Btu/hr-ft-°R)
Shaft, Spacers, Heat Dam	Inconel 718	8.20×10^3	(0.296)	2.16×10^{11}	(31.3×10^6)	-233×10^{-5}		3.48	(2.00)
Housing, Loaders, Flexure Mount	316 Stainless Steel	7.85×10^3	(0.283)	2.07×10^{11}	(30.0×10^6)	-290×10^{-5}		8.6 13.8	(5.0) (8.0)
Hybrid Journal Sleeve	AISI 440C	7.85×10^3	(0.283)	2.07×10^{11}	(30.0×10^6)	-175×10^{-5}		8.6	(5.0)
Turbine Wheel	Aluminum 2016-T6	2.77×10^3	(0.100)	7.57×10^{10}	(11.0×10^6)	$24.1 \times 10^{-6}/°K$	($12.1 \times 10^{-6}/°F$)	52.0	(30.0)

*Thermal Conductivity Listed Corresponds to Calculated Average Vehicle Temperatures.

CONCLUSIONS & RECOMMENDATIONS

The design study performed within the scope of this work resulted in finalized designs of rolling-element bearings, hybrid bearings, and a test vehicle for the development of bearing technology for advanced turbo-pump applications. Two angular contact ball bearing designs have been produced, one for the use in ball bearing rotor support systems, and another for use in hybrid bearing systems. The designs differ in size and internal geometry, because of the differing performance requirements inherent in the two concepts.

The general design trends indicate a high degree of sensitivity of the bearing life to load and speed changes. In order to maximize the life potential of each rolling-element bearing, both externally imposed loads, as well as speeds, should be minimized. Because the given conditions of operation extend beyond present-day experience, no quantitative life predictions are possible at this time.

The analytical results indicate that the hybrid bearing should be capable of successful operation in a hybrid mode since the ball bearing possesses ample capacity to transmit the torque required to drive the fluid-film bearing at the given design speeds.

Each of the tester (ball bearing and hybrid) designs has indicated no major deficiency which could seriously impair their operation. The critical speeds and rotor response calculations indicate, in most instances, well-bounded, stable operation at the desired test speeds, with low amplification of response when transmitting through a critical. The most serious weak spot is found in the hybrid bearing tester response, where the supply pressures may have to be limited to a maximum of 3.45×10^6 N/m^2 (500 psia) to avoid rotor instabilities.

Results of the thermal studies are less conclusive, primarily because of difficulties encountered in the modeling of a rather complex thermal system. It is apparent that some modification, on the test stand, of coolant flow design levels for tester cooling will be necessary in order to satisfy all thermal requirements.

Mechanically, all tester designs are now complete and detailed. No additional adjustments in the external fluid supplies, beyond those mentioned in this report are envisioned and, therefore, more detailed planning for the test facility can now proceed. To summarize the fluid requirement for all three tester configurations, Table 27 is presented.

In addition to the liquid flow requirements, several critical absolute and differential pressures must be maintained for satisfactory performance. These are:

- Turbine Discharge Pressure $P = 1.66 \times 10^{6}$ N/m^2 (240 lb/in^2)
- Turbine Back-Pressure $P = 1.66 \times 10^{6}$ N/m^2 (240 lb/in^2)
- Radial Loader Cavity Pressure (when in use with GH_2) $P = 1.66 \times 10^{6}$ N/m^2 (240 lb/in^2)
- Internal Tester Pressure $P = 1.72 \times 10^{6}$ N/m^2 (250 lb/in^2)
- Coolant Supply Pressure (Approx.) $\Delta P = 1.72 \times 10^{8}$ N/m^2 (2.5 lb/in^2)
- Hybrid Journal Supply Pressure $\Delta P = 1.72 \times 10^{6}$ N/m^2 (250 lb/in^2)
- Hybrid Tester Thrust Bearing $\Delta P = 1.10 \times 10^{6}$ N/m^2 (160 lb/in^2)
- Turbine Supply Pressure $P_{max} = 2.24 \times 10^{6}$ N/m^2 (325 lb/in^2)
- Maximum Radial Loader Supply Pressure $\Delta P = 8.96 \times 10^{6}$ N/m^2 (1300 lb/in^2)
- Maximum Axial Loader Supply Pressure $\Delta P = 1.72 \times 10^{6}$ N/m^2 (250 lb/in^2)

This report completes the design phase performed under Tasks I, II and III of the original contract.

TABLE 27

SUMMARY OF LH_2 BEARING TESTER FLUID REQUIREMENTS

	Single Bearing Tester		Duplex Bearing Tester		Hybrid Tester	
	10^{-3} Kg/sec	(lb/sec)	10^{-3} Kg/sec	(lb/sec)	10^{-3} Kg/sec	(lb/sec)
LIQUID HYDROGEN						
Bearing Coolant (Net)	90.6	(0.200)	181.2	(0.400)	90.6	(0.200)
Bearing Supply (Net)	NA		NA		4.53	(0.100)
Radial Loader (Max)	1.13	(0.0025)	1.13	(0.0025)	1.13	(0.0025)
TOTAL LH_2	91.73	(0.2025)	182.33	(0.4025)	91.73	(0.3025)

GASEOUS HYDROGEN TO TURBINE - 70 x 10^{-3} Kg/sec (0.152 lb/sec)

REFERENCES

1. Young, W. E. and Reddecliff, J. M., "Investigation of Hydrostatic Bearings for Use in High-Pressure Cryogenic Turbopumps - Final Report, " May 1967, AFAPL TR-67-130.

2. Roesch, E. and Accinelli, J.B., "Feasibility Demonstration of a 90 mm LH_2 Hydrostatic Radial Bearing for Turbopump Application," Reports 7740R-70-o11 and 774-70-012.

3. NASA Space Vehicle Design Criteria, "Liquid Rocket Engine Turbo-pump Bearings," NASA SP-8048, March 1971.

4. Harris, T. A., "Rolling Bearing Analysis," J. Wiley, New York, 1966.

5. Winn, L.W., "Examination of 60mm and 65mm Bore Ball Bearings After Tests in Liquid Hydrogen in ANSC Pump Simulator," MTI 71TR19, SNPC 76-10.

6. Brewe,E.E., Scibbe, H.W., Wisander, D.W., "Performance of High-Speed Ball Bearings with Lead and Lead-Alloy-Plated Retainers in Liquid Hydrogen at 1.2 Million DN," ASME Paper No. 73-Lub-22.

7. Winn, L.W., "Evaluation of Hybrid-Hydrostatic Bearing Program," MTI 70TR45, SNPC-75, June 1970.

8. Jones, A.B., "A General Theory for Elastically Constrained Ball and Radial Roller Bearings under Arbitrary Load and Speed Conditions," ASME Journal of Basic Engineering, pp. 309-320 (June 1960).

9. Leveille, A.R., Murphy, J.J., "Determination of the Influence of Static Loads on the Output Torque of Instrument Ball Bearings," presented at the International Ball Bearing Symposium,Charles Stark Draper Laboratory, Inc., Cambridge, Mass., June 5-7, 1973.

10. Reddecliffe, J.M. and Vohr, J.H., "Hydrostatic Bearings for Cryogenic Rocket Engine Turbopump," Journal of Lubrication Technology, July 1969, pp. 557-573.

11. Winn, L.W. and Smalley, A.J., "Final Report, MK-25 LH_2 Pump Hybrid Bearing Design," Prepared for SNPO-AEC, MTI Report No. 71TR19.

12. Finkin,E.F., Smalley, A.J. and Winn, L.W., "Design of Hydrostatic Bearings for the ANSC-LH_2 Pump," MTI 72TR18. Prepared under Contract SNPC-76, Modification No. 8, April 1972.

13. Alston, R.L., O'Donoghue, J.P., "The Effect of the Number of Recesses on the Performance of Externally Pressurized Multirecess Journal Bearings," Tribology, May 1971, pp. 94-96.

14. Elrod, H.G., Ng, C.W., "A Theory for Turbulent Fluid-Films and Its Application to Bearings, "Journal of Lubrication Technology, Trans. ASME, Vol. 89 - Series F. No. 3, July 1967, p. 346.

REFERENCES (Continued)

15. RPI-MTI, "Design of Gas Bearings," Volume I and II, Gas Bearing Design Course, August 1967.

NOMENCLATURE

A	Area, m^2 (in^2)
B	Width, m (in)
B_{10}	Ball Bearing Fatigue Life, hours
B_p	Pedestal Damping, N-sec/m (lb-sec/in)
B_{xx}	Damping (x Axis), N-sec/m (lb-sec/in)
B_{xy}	Cross Damping, N-sec/m (lb-sec/in)
B_{yy}	Damping (y Axis), N-sec/m (lb-sec/in)
C	Bearing Clearance (radial), m (in)
C_D	Cage Clearance (diametral), m (in)
C_p	Specific Heat J/Kg °K (BTU/lb°R)
D	Diameter, m (in)
$D_{1,2..n}$	Sequential Diameters, m (in)
d	Ball Diameter, m (in)
d_o	Orifice Diameter, m (in)
e	Cage Eccentricity, m (in)
F	Force, N (lb)
$\overline{F}$	Force (dimensionless)
F_A	Axial Force, N (lb)
F_f	Film Force, N (lb)
F_p	Pressure Force, N (lb)
F_r	Radial Force, N (lb)
F_s	Spring Force, N (lb)
F_z	Radial Load, N (lb)
f_i	Inner Race Curvature
f_o	Outer Race Curvature

NOMENCLATURE (Continued)

GH_2	Gaseous Hydrogen
G_X	Average Viscosity Correction
H	Shoulder Height, m (in)
$\overline{H}$	Head Rise, m (ft)
h	Film Thickness, m (in)
I_p	Polar Moment of Inertia, Kg-m^2 (in-lb-sec^2)
I_t	Transverse Moment of Inertia, Kg-m^2 (in-lb-sec^2)
$\overline{K}$	Stiffness, dimensionless
K_{BB}	Ball Bearing Stiffness, N/m (lb/in)
ΔK_{xx}	Reduction in Stiffness, N/m (lb/in)
K_b	Bearing Stiffness, N/m (lb/in)
K_p	Pedestal Stiffness, N/m (lb/in)
K_z	Radial Stiffness of Ball Bearing, N/m (lb/in)
k	Thermal Conductivity, Watts/m °K (BTU/hr-ft °F)
L	Length, m (in)
L_a	Side Land on Journal Bearing, m (in)
L_c	Pocket Width, m (in)
LH_2	Liquid Hydrogen
M	Mass, kg (lb)
M_p	Pedestal Mass, kg (lb)
N	Rotation Speed, rpm
N_i	Inner Race Speed, rpm
N_o	Outer Race Speed, rpm
N_s	Specific Speed, rpm
ΔP	Differential Pressure, N/m^2 (lb/in^2)
P	Pressure, N/m^2, (lb/in^2)

NOMENCLATURE (Continued)

P_c	Critical Pressure, N/m^2 (lb/in^2)
P_r	Reduced (Normalized) Pressure, dimensionless
P_D	Radial Play in Ball Bearing, m (in)
P_E	Axial Play in Ball Bearing, m (in)
Q	Flow Rate, Kg/sec (lb/sec)
R	Radius, m (in)
S	Hertzian Stress, N/m^2 (lb/in^2)
T	Temperature, °K (°R) °K - Absolute Temperature Kelvin °R - Absolute Temperature Rankine
ΔT	Differential Temperature, °K (°R)
T_B	Ball Bearing Torque, N-m (in-lb)
T_c	Critical Temperature, °K, (°R)
T_{ff}	Fluid-Film Bearing Torque, N-m (in-lb)
T_R	Reduced (Normalized) Temperature, dimensionless
T_s	Stream Temperature
t	Time, sec
V	Velocity of Spin, ft/sec
v	Volumetric Flow, m^3/sec (ft^3/sec)
w	Cage Mass, g (oz)
Z	Heat Flow Rate, watts (Btu/hr)
z	Heat Reluctance, watts/°K (Btu/hr °R)
α	Contact Angle, degrees
α_1	Initial Contact Angle, degrees
γ	Polytropic Exponent
δ	Log Decrement

NOMENCLATURE (Continued)

λ	Amplitude Decay Exponent
μ	Viscosity, N-sec/m^2 (lb-sec/in^2)
ν	Natural Frequency, sec
ξ	Fraction of Total Bearing Area
ρ	Density, Kg/m^3 (lb/in^3)
σ	Pocket Depth, m (in)
ψ	Heat Transfer Film Coefficient, Watt/m^2(°K) (Btu/hr ft^2 °R)
ω	Rotational Frequency, sec

APPENDIX A

TABLE A-1

PROPERTIES OF BEARING, CAGE AND SHAFT MATERIALS

Material	Modulus Of Elasticity N/m^2 (lb/in^2)	Poissons Ratio	Density Kg/m^3 (lb/in^3)	Thermal* Expansion Cm/Cm (in/in)
AISI 440 C	2.16×10^{11} (31.3×10^6)	0.30	$.783 \times 10^4$ (0.283)	-175×10^{-5}
Inconel 718	2.16×10^{11} (31.3×10^6)	0.30	$.819 \times 10^4$ (0.296)	-233×10^{-5}
Ti-SAE-2.5 Sn	1.17×10^{11} (17×10^6)	0.31	$.448 \times 10^4$ (0.162)	-175×10^{-5}
Armalon	0.15×10^{11} (2.2×10^6)	0.10	$.124 \times 10^4$ (0.045)	-400×10^{-5} -1300×10^{-5} **

---

*Thermal Expansion is given at 13.3°K (40°R)

**The Expansion of Armalon is lower on the diameter than across the ring thickness. Note corresponding values.

APPENDIX B

BEARING LOAD ESTIMATES IN LH_2 TURBO-PUMPS

This Appendix presents calculations of an estimate of the bearing loads anticipated in a typical LH_2 turbo-pump, the basic characteristics of which were provided by NASA Program Management.

The turbo-pump consists of a 3-stage centrifugal compressor and a high-speed (100,000 rpm +) turbine driven pump. Each stage generates a pressure rise of about 1500 psi. The pressure rise within the wheel for a 45° vane back-sweep design is about 55 percent of the overall stage pressure rise. Hence, the pressure difference effecting the axial thrust forces is about (.55) (1500) = 825 psi, per stage. The net thrust area of the 3.85 diameter impellers is about 10 square inches indicative that very large potential thrust forces are possible in the pump. In addition, a substantial thrust load ($\approx$ 1000 lbs.) is generated by the 2-stage turbine.

While it is possible to reduce the net thrust forces by the proper positioning of labyrinth seals with controlled inter-stage seals, the net loads will always be higher than what would be considered acceptable. For this reason, the use of a balance piston design is not only desirable but, indeed, mandatory.

Radial Loads

Pumps and compressors having uniform area collectors or cross-over channels have no net radial loads. However, with volute type collectors some net radial load generally results. In pumps with volute collectors, the static pressure distribution around the impeller periphery changes at constant speed. At "normal" or "best efficiency" flow it is theoretically uniform (zero net radial load) but as the flow rate changes from this value, the pressure distribution becomes non-uniform, producing a net thrust on the impeller in the radial plane.

Extensive experiments have been conducted over the years to establish design guidelines for estimating the radial loads. Figure B-1 shows a typical characteristic for estimating the magnitude of the radial load when the pump has a single

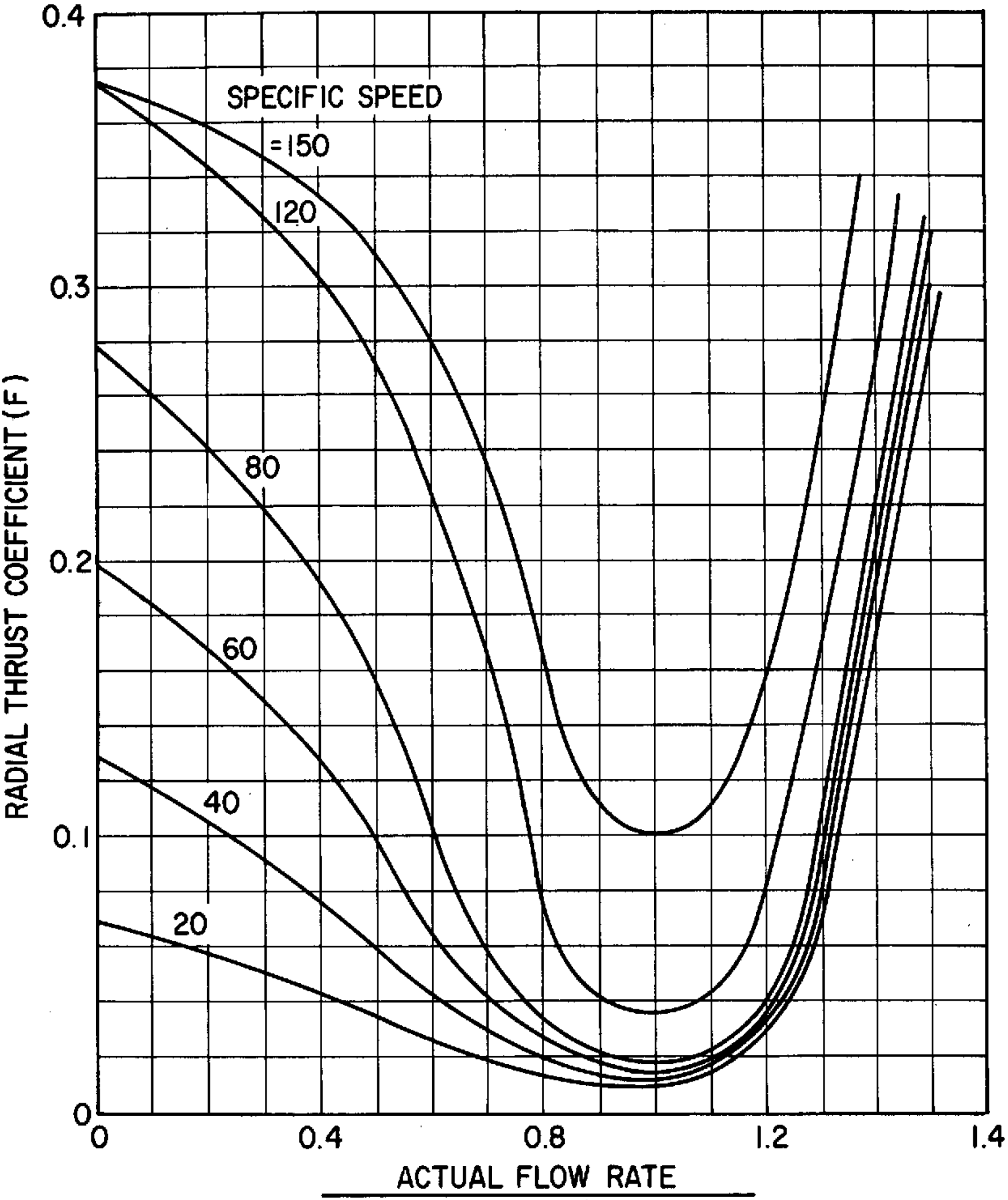

Fig. B-1 Radial Thrust in Centrifugal Pumps volute diffuser. Using this relationship, the following represents the estimated radial load.

$$N_s = \text{Specific Speed} = \frac{N\,Q}{H\,(6.95 \times 10^{-2}} \quad (\frac{N\,Q}{H\,3/4} \text{ in English units })$$

where

Q = Volume Flow = $3.6 \times 10^{-2} m^3/sec$ ($1.27\ ft^3/sec$)

$\overline{H}$ = Head Rise - ft = 13,500 m (44,500 ft)

therefore

N_s = 37.8 (considered low)

Assuming a ± 20 percent flow variation from design flow results in a "F_r" factor (Figure B-1) of .02 - hence,

$$F_r = \frac{\overline{F}\,\overline{H}\,DB}{4.58x10^{-4}} \quad (\frac{\overline{F}\,\overline{H}\,DB}{2.3} \text{ in English units})$$

where

F_r = Net Radial Load on Rotor - N (lbs)

$\overline{F}$ = Load Coefficient (Figure B-1)

D = Impeller Diameter, m (in)

B = Impeller Width, m (in)

$\overline{H}$ = Head, m (ft)

The above relationship was established for water pumps - hence, a head correction must be made for the relative fluid densities. For a density ratio between LH_2 and water of ρ_{LH_2}/ρ_{water} = .077

therefore

$\overline{H}$ = 891 m (3500 ft)

and with

$\overline{K}$ = .02

D = .0976 m (3.85 in)

B = 4.75×10^{-3} m (.187 in)

F_r = 98 N (22 lbs)

Assuming approximately 50 percent margin, it is recommended that a net radial load of 134 N (30 lbs) be used for bearing selection. Since the 134 N (30 lbs) load is closer to the large bearing, it will see 102 N (23 lbs) load and the smaller bearing 31.1 N (7 lbs).

It is, of course, recognized that by going to a double volute design, the net radial load from off-design diffuser effects is eliminated.

APPENDIX C

FLUID-FILM BEARINGS - IMPORTANT PHYSICAL PHENOMENA

The primary physical phenomena which influence performance are listed in Table C-1. All of these are accounted for in the design analysis.

TABLE C-1

PRIMARY PHYSICAL PHENOMENA

- Hydrostatic Action
- Poiseuille Turbulence
- Couette Turbulence
- Centrifugal Growth of Journal
- Frictional Heat Generation
- Convective Heat Transfer

They are briefly discussed in the following paragraphs:

Hydrostatic action is the means by which an external pressure source is utilized to provide load capacity and stiffness. Fluid is fed to the bearing under pressure through an inlet resistance (in this case an orifice in each pocket). The fluid flows axially through the bearing clearance space which offers a second resistance to its flow. The inlet and film resistances are of similar magnitude, so that the pressure at the inlet to the bearing film tends to lie midway between supply pressure and outlet pressure. Under concentric conditions the film resistance does not vary circumferentially and the circumferential pressure distribution is uniform. When the journal moves eccentric in its clearance shape, the film resistance varies circumferentially and a circumferential pressure distribution is set up which acts to oppose the eccentricity of the journal. By adjusting the relative magnitudes of inlet and film resistances the stiffness and load carrying capacity may be adjusted to meet design requirements. In design analysis of the bearing a line source approximation (15) is used to represent the discrete hydrostatic supply pockets. This approximation basically implies the assumption that the number of pockets is large. References 10 and 13 in the main text illustrate clearly that above 6 pockets, increasing the number of pockets has very little influence on performance. Thus, the number of 10 pockets employed in the fluid-film bearing fully satisfies the implied assumption.

Poiseuille turbulence occurs because the kinematic viscosity of liquid hydrogen is low. The pressure induced velocity of the fluid through the clearance space leads to Reynolds numbers of order 25000. As a result, the effective viscosity is increased. This is clearly a non-linear phenomenon. It is handled in design analysis as a non-linearity on the basis of work by Ng and Elrod (14).

Couette turbulence again results from low kinematic viscosity but the fluid velocity in this case is that induced by relative surface motion between journal and housing. Since pressure flow mean velocities are generally higher than mean fluid velocities induced by surface rotation in this bearing, Couette turbulence takes a role of lesser significance than Poiseuille turbulence.

Centrifugal growth of the journal is a significant effect because of the "thin ring" nature of the ball bearing outer race and because of the high speeds of operation. As was shown in Section A, the radial clearance may reduce by over 2.5×10^{-5} meters (.001") between static and 120,000 rpm operation.

Frictional heat generation describes the result of shearing the fluid-film by relative velocity of the journal and housing. Convective heat transfer is the predominant mechanism whereby the heat is carried away. Thus, a flow of liquid hydrogen through the bearing is necessary to avoid boiling. The mean temperature rise through the bearing is calculated by equating frictional heat generation to the heat carried away by the hydrogen.

Table C-2 lists a number of physical phenomena which may also have some influence on bearing performance, but may be regarded as of secondary order. Included in this table is an indication of how the phenomenon in question affects performance, and a range of the likely magnitudes of the effect.

As indicated, the most important of these effects are included in most of the design analyses performed. The magnitude of other effects has been assessed by separate analysis, and a decision was made not to include them in the design analysis. The implication of neglecting these effects is considered to be acceptable. The meaning of the items of Table C-2 is discussed below.

Hydrodynamic action refers to the forces generated in the fluid-film bearing due to surface motion induced flow in a circumferentially-varying clearance space. The nature of hydrodynamic effects is to induce a force which acts at right angles to the journal displacement vector and, therefore, implies a cross-coupling stiffness. The magnitude of the hydrodynamic force lies in the range 15-30 percent of the hydrostatic force in this application. The particular significance of hydrodynamic action is that, because of the cross-coupling, it can be a destabilizing influence. Hydrodynamic forces are included in the output of the design analysis and should be accounted for in rotor-dynamic analysis.

Bernoulli inertia effects refer to the losses in static pressure which can occur at points in the fluid-film where significant acceleration takes place; specifically, there is a significant acceleration as the fluid leaves the pockets either in design A, or design B. Because this is an intermediate resistance (between inlet and film) which is affected by the local film clearance, it acts to modify the stiffness of the film. Bernoulli inertia effects reduce the optimum hydrostatic stiffness of the bearing, but if the bearing has an orifice diameter significantly larger than optimum, the inlet inertia effects can act to improve the stiffness.

Time dependent inertia effects describe the fact that, when there is normal relative motion between journal and housing, there are dynamic pressures induced to provide the necessary fluid acceleration. These pressures tend to reduce the direct stiffness of the fluid-film bearing under dynamic conditions. These effects are included in the design analysis according to an approximate treatment developed by Dr. Constantinescu.

$$\Delta K_{xx} = - \frac{\alpha\rho \ \omega^2 C^2 G_x B_{xx}}{\mu}$$

where :

TABLE C-2

SECONDARY PHYSICAL PHENOMENA

PHENOMENON	EFFECT	MAGNITUDE
HYDRODYNAMIC ACTION	CROSS-COUPLING STIFFNESS DESTABILIZING INFLUENCE	15 - 30 PERCENT OF DIRECT STIFFNESS
BERNOULLI INERTIA EFFECTS	EXTRA INLET RESISTANCE REDUCTION IN STIFFNESS	20 - 30 PERCENT STIFFNESS REDUCTION
TIME-DEPENDENT INERTIA EFFECTS	REDUCTION IN STIFFNESS	10 - 15 PERCENT
STEADY COMPRESSIBILITY EFFECTS	REDUCTION IN STIFFNESS	2 - 5 PERCENT
TIME-DEPENDENT COMPRESSIBILITY EFFECTS	REDUCTION IN DAMPING	10 - 30 PERCENT
PRESSURE DEPENDENT VISCOSITY	REDUCTION IN STIFFNESS	5 PERCENT
CONDUCTIVE HEAT TRANSFER	REDUCTION IN TEMPERATURE RISE	5 - 15 PERCENT

(✓ Included in Performance Predictions)

ΔK_{xx} is the reduction in stiffness to account for dynamic inertia effects (N/m), (lb/in)

ρ is fluid density Kg/m^3 (lb/in)

ω is frequency of vibration (rad/sec)

C is the clearance, m (inches)

G_x is the average viscosity correction coefficient to account for turbulence

μ is viscosity, Newton sec/m^2 (lb-sec/in^2)

B_{xy} is damping, Newton sec/m (lb-sec/in)

α is the fraction of the total bearing area over which clearance C applies

Compressibility effects relate to the fact that the density of liquid hydrogen varies slightly with pressure. The term steady compressibility effects is used to refer to the influence that density variations have upon stiffness. It is found that, due to compressibility, there is a slight reduction in stiffness of under 2 - 5 percent of the stiffness calculated, neglecting compressibility effects. The term time-dependent compressibility effects refers, firstly, to the fact that the fluid can now undergo compression when there is normal relative velocity of journal and housing, and secondly, to the fact that trapped volumes of fluid such as in a pocket can cause a phase shift due to capacitive action. The result is to reduce the damping relative to a value calculated on the basis of incompressible squeeze film action. In extreme cases (very large pockets) the capacitive action can lead to negative damping.

The term pressure dependent viscosity refers to the fact that the viscosity of liquid hydrogen is influenced by pressure. Between 1.72×10^{-6} (250) and 1.81×10^{-5} N/m^2 (1250 psi), the viscosity can approximately double. Since this is the largest pressure difference which will be seen in the current test vehicle, the influence on stiffness of a factor of two variation in viscosity was investigated. The stiffness variation did not exceed 5 percent. This very mild sensitivity is a result of the turbulence effects. The effective viscosity does not vary as rapidly as the actual viscosity under turbulent conditions.

Conductive heat transfer represents an additional path for heat loss from the fluid-film when there is heat generated by friction. Dr. Constantinescu investigated the effect of conduction and showed it contributed most strongly when the clearance (and hence the flow) was small, as shown in Table C-3.

TABLE C-3

TEMPERATURE RISE BASED ON
CONVECTION AND CONDUCTION
FOR DESIGN A (V.N. CONSTANTINESCU)

C, meters (inches)	10^{-5}	(.0004)	2×10^{-5}	(.0008)	3×10^{-5}	(.0012)
T (convection only) °K (°R)	17.76	(32.0)	5.43	(9.8)	2.39	(4.3)
T (convection + conduction)	12.87	(23.2)	4.81	(8.6)	2.26	(4.1)
Difference, percent	27.50	(49.5)	11.40	(20.5)	5.40	(9.7)

The percentage range of 5 - 15 percent specified in Table C-2 is considered to cover the likely range of discrepancy for reasonable clearances if conduction effects are neglected. Note that by neglecting conduction effects, a pessimistic value for temperature rise is obtained.

APPENDIX D

MTI BEARING MANUFACTURING SPECS
NUMBER 0232-43601-01
(Revision 1)

1.0 SCOPE

This specification, together with the enclosed Figure 1 establishes the requirements for the design, manufacture and packaging of a 20-mm extra-light series ball bearing for use in liquid hydrogen applications.

2.0 APPLICABLE DOCUMENTS

The following documents shall form part of this specification to the extent specified herein. If the requirements of this specification and those listed below differ, the requirements of this basic specification shall govern. The applicable issue of the following documents shall be the issue in effect on date of invitation to bid.

MIL-STD 100 MIL-D-1000 Form 3 USAS Y-14.5	Drawing Specifications
AFBMA Standard 12	Revision No. 3, June 1969 - Annular Bearing Engineering Committee Standards
AFBMA Standards for Sec. 10, Rev. 5 December 1964	Balls - Anti-Friction Bearing Manufacturers Association Ball Standards
AMS 5618	Corrosion Resistant Steel - SAE 51 440 C (Ball Bearing)
AMS 5630 C	Corrosion Resistant Steel - SAE 51 440 C (Cages Only)
AMS 6444 B	Par. 6.3 Inclusion Rating
AMS 4909	Plate Stock (Titanium 5 Al, 2.5 Sn)

3.0 OPERATING REQUIREMENTS

3.1	Speeds:	Operating - 120,000 rpm
3.2	Loads:	Radial Operating Load - 222N (50 lb) max. Thrust Load - 2220N (500 lb) max.
3.3	Acceleration:	50,000 rev/min/sec
3.4	Minimum Expected Life:	10 Hours
3.5	Environmental Media:	LH_2 @ 23.8/29.5°K (43/53°R) and 1.38/1.72 x 10^{-6} N/m^2 (200/250 lb/in^2 abs)
3.6	Number of Start-Stop Cycles:	1.38/1.72 x 10^6 N/m^2 (200/250 lb/in^2 abs)

4.0 DESIGN REQUIREMENTS

4.1 Bearing Tolerances - have been established per ABEC Class 7 P specifications.

4.2 Materials

4.2.1 Inner Ring - 440 C per AMS 5618 C Consumable Electrode Vacuum Melted (CEVM).

Minimum Rockwell C Hardness @ 58. Surface finish of raceway 2.03 x 10^{-7} m (8 μ-in) circumferentially. Waviness - 7.64 x 10^{-7} m(30 μ-in) max. peak.

4.2.2 Outer Ring - 440 C per AMS 5618 C Consumable Electrode Vacuum Melted (CEVM). Surface finish of raceway same as in 4.2.1. Minimum Rockwell C Hardness @ 58.

4.2.3 Balls - 440 C per AMS 5618 C Consumable Electrode Vacuum Melted (CEVM). Minimum Rockwell C Hardness @ 58. Surface finish 5.09 x 10^{-8} m (2 μ-in) maximum.

4.2.4 Cage - Two types of cages shall be made of two different materials, i.e., 440 C corrosion resistant steel (35 to 40 RC) and Titanium 5 Al 2.5 Sn alloy both per AMS 4909 specifications. Initial surface finish prior to plating 4.05x10^{-7}m(16μ-in) rms.

Cages to be plated with P-77 (87.5 Pb, 10 Sn, 2.5 Cu) by Gould, Inc. of Cleveland, Ohio. Prior to plating, the surfaces are to be cleaned and flashed per Gould's specifications. The plating is to be applied 3.05×10^{-5} m (1.2×10^{-3} in) thick over the entire surface. Balance cages to 3.6×10^{-7} Kg-m (5.0×10^{-4} oz-in) after plating. Material to be removed on cage bore.

4.2.5 Heat Number - The heat number for all races and balls to be included with certification for each bearing.

4.2.6 Surface Hardness - The surface hardness of all rolling-elements and raceways shall be 58-63 RC.

4.2.7 Stabilization - Stabilize material through repeated chilling in LN_2 and tempering, per I.T.I. specifications.

4.2.8 Demagnetization - All bearing materials shall be thoroughly demagnetized upon completion of bearing manufacturing process.

4.3 Internal Geometry

4.3.1 Balls - The balls shall be of AFBMA Grade 10. Ten balls per bearing of 4.76×10^{-3} m (0.1875 in).

4.3.2 Unmounted Contact Angle - The nominal unmounted contact angle shall be 26°. The angle tolerances are established by the race and diametral clearance tolerances.

4.3.3 Race Curvature - Inner Race - 54%
Outer Race - 52%

4.3.4 Bearing Shoulders - Inner race shoulder and outer race shoulder as specified in Figure D-1. Allow sufficient snap at inner race low shoulder for handling and disassembly with a temperature gradient not to exceed 97.5°C (200°F).

4.3.5 Diametral Clearance - The diametral clearance shall fall within $4.70 - 6.22 \times 10^{-5}$ m (.00185 - .00245 in) when measured under 22.2 N (5 lb) gage load applied in one direction, and then in the opposite direction.

4.3.6 Axial Clearance - The axial clearance, when measured under a 22.3 N (5 lb) gage load applied in one direction and reversed in the other direction, shall not exceed 2.26 - 2.59 x 10^{-4} m (0.0089 - 0.0102 in).

4.3.7 Dimensional Measurements - All dimensions are to be certified at 21.1 ± 1.1°C (70° ± 2°F).

4.3.8 Face Location - Face A shall be in the same plane as Face B within 2.54 x 10^{-6} m (1.0 x 10^{-4} in) with bearing under a 22.2 N (5 lb) axial load. The faces opposed to Faces A and B shall be in the same plane within 2.54 x 10^{-6} m (.0001 in) with the load at 22.2 N (5 lb).

4.3.9 Race Edges - The inner ring race edges shall be relieved to permit short excursions of the ball contact ellipse beyond the raceway limits without ball creasing.

4.4 Markings

4.4.1 Face Markings - Mark Face A with "A" and Face B with "B" as shown in Figure D-1. Mark Faces A and B with assigned serial number, and supply part number.

4.4.2 Mark location of the high point of inner race eccentricity.

4.4.3 Markings to be performed with electrolytic etch per MIL-STD-130 D.

4.5 Cleanliness and Packaging

4.5.1 Cleanliness - Cleanliness to be per MIL-P-116, level II. Do not use cleaning agents containing H_20.

4.5.2 Packaging - Package per fabrication order instructions.

4.6 General

Only the item described on the enclosed drawing and within this document is approved by Mechanical Technology Incorporated for use in applications justified hereon. A substitute item shall not be used without prior approval of MTI or NASA.

MTI BEARING MANUFACTURING SPECS
NUMBER 0232-43601-02
(Revision 1)

1.0 SCOPE

This specification, together with the enclosed Figure D-2, establishes the requirements for the design, manufacture and packaging of a 20-mm light series ball bearing for use in liquid hydrogen applications.

2.0 APPLICABLE DOCUMENTS

The following documents shall form part of this specification to the extent specified herein. If the requirements of this specification and those listed below differ, the requirements of this basic specification shall govern. The applicable issue of the following documents shall be the issue in effect on date of invitation to bid.

MIL-SRD-100 MIL-D-1000 Form 3 USAS Y-14.5	Drawing Specifications
AFBMA Standard 12 Rev. No. 3, June 1969-	Annular Bearing Engineering Committee Standards
AFBMA-Standards for Balls, Sec. 10 Rev. 5, Dec. 1964	Anti-Friction Bearing Manufacturers Association - Ball Standards
AMS 5618	Corrosion Resistant Steel - SAE 51 440 C (Ball Bearing)
AMS 5630 C -	Corrosion Resistant Steel - SAE 51 440 C (Cage Only)
AMS 6444 B -	Par. 6.3 Inclusion Rating
MIL-T-9047 -	Bar and Forging Stock

3.0 OPERATING REQUIREMENTS

3.1 Speed: Operating - 120,000 rpm

3.2 Loads: Radial Operating Load - 44.5 - 445 N (10 - 100 lb) max.
Thrust Load - 2230 N (500 lbs) max.

3.3 Acceleration: 50,000 rev/min/sec

3.4 Minimum Expected Life: 10 Hours

3.5 Environmental Media: LH$_2$ @ -420 to -430°F
200 to 250 psia

3.6 Number of Start-Stop Cycles: 300

4.0 DESIGN REQUIREMENTS

4.1 Bearing Tolerances - have been established per ABEC Class 7 - P specifications.

4.2 Materials

4.2.1 Inner Ring - 440 C per AMS 5618 C Consumable Electrode Vacuum Melted (CEVM).
Minimum Rockwell C Hardness @ 58. Surface finish of raceway 2.03 x 10^{-7} m (8 μ-in) circumferentially. Waviness - 7.64 x 10^{-7} m(30 μ-in)max. peak.

4.2.2 Outer Ring - 440 C per AMS 5618 C Consumable Electrode Vacuum Melted (CEVM). Surface finish in raceway same as in 4.2.1. Minimum Rockwell C Hardness @ 58.

4.2.3 Balls - 440 C per AMS 5618 C Consumable Electrode Vacuum Melted (CEVM). Minimum Rockwell C Hardness @ 58. Surface finish - 5.09 x 10^{-8} m (2 μ-in) maximum.

4.2.4 Cage - Cages shall be made of laminated glass fabric, impregnated with Teflon. Cage material specifications will be supplied at a later date. Back-up cages shall be made of 440 C stainless steel (35-40 RC) per AMS 5630 C specifications. Steel cage surface finish shall be 4.05 - 8.10 x 10^{-7} m (16 μ-in) rms.

Steel cages to be plated with P-77 (87.5 Pb, 10 Sn, 2.5 Cu) by Gould, Inc. of Cleveland, Ohio. Prior to plating, the surfaces are to be cleaned and flashed per Gould's specifications. The plating is to be applied 3.05 x 10^{-5} m (1.2 x 10^{-3} in) thick over the entire surface. Balance cages to 3.6 x 10^{-7} Kg-m (0.0005 oz-in) after plating. Material to be removed on cage bore.

4.2.5 Heat Number - The heat number for all races and balls to be included with certification for each bearing.

4.2.6 Surface Hardness - The surface hardness of all rolling-elements, raceways shall be 58 - 63 RC.

4.2.7 Stabilization - Stabilize material through repeated chilling in LN_2 and tempering per I.T.I. specifications.

4.2.8 Demagnetization - All bearing materials shall be thoroughly demagnetized upon completion of bearing manufacturing process.

4.3 Internal Geometry

4.3.1 Balls - The balls shall be of AFBMA Grade 10. Nine balls per bearing of 6.35 x 10^{3} m (0.2500 in) diameter.

4.3.2 Unmounted Contact Angle - The nominal unmounted contact angle shall be 24°. The angle tolerances are established by the race and diametral clearance tolerances.

4.3.3 Race Curvature - Inner Race - 56%
Outer Race - 52%

4.3.4 Bearing Shoulders - Inner race shoulder is as shown on drawing. Outer race shoulder is as shown on drawing D-2. Allow sufficient snap at low end of inner race low shoulder for handling and disassembly with a temperature gradient not to exceed 97.5°C (200°F).

4.3.5 Diametral Clearance - The diametral clearance shall fall within 6.85 - 8.37 x 10^{-5} m (.0027 - .0033 in) when measured under 22.3N (5 lb) gage load applied in one direction, and then in the opposite direction.

C-3

4.3.6 Axial Clearance - The axial clearance, when measured under a 22.3 N (5 lb) gage load applied in one direction and reversed in the other direction, shall not exceed 3.81 - 4.32 x 10^{-4} m (.015 - .017 in).

4.3.7 Dimensional Measurements - All dimensions are to be certified at 21.1 ± 1.1°C (70° ± 2°F).

4.3.8 Face Location - Face A shall be in the same plane as Face B, within 2.54 x 10^{-6} m (1.0 x 10^{-4} in) with bearing under a 22.2 N (5 lb) axial load. The faces opposed to Faces A and B shall be in the same plane within 2.54 x 10^{-6} (1.0 x 10^{-4} in) with the load at 22.2 N (5 lb).

4.3.9 Race Edges - The inner ring race edges shall be relieved to permit short excursions of the ball contact ellipse beyond the raceway limits without ball creasing.

4.4 Markings

4.4.1 Face Markings - Mark Face A with "A" and Face B with "B" as shown in Figure D-2. Mark Faces A and B with assigned serial number, and supply part number.

4.4.2 Mark location of the high point of inner race eccentricity.

4.4.3 Markings to be performed with electrolytic etch per MIL-STD-130 D.

4.5 Cleanliness and Packaging

4.5.1 Cleanliness - Cleanliness to be per MIL-P-116, level II. Do not use cleaning agents containing H_2O.

4.5.2 Packaging - Package per fabrication order instructions.

4.6 General

Only the item described on the enclosed drawing and within this document is approved by Mechanical Technology Incorporated for use in applications justified hereon. A substitute item shall not be used without prior approval by MTI or NASA.

REPRODUCIBILITY OF THE ORIGINAL PAGE IS POOR

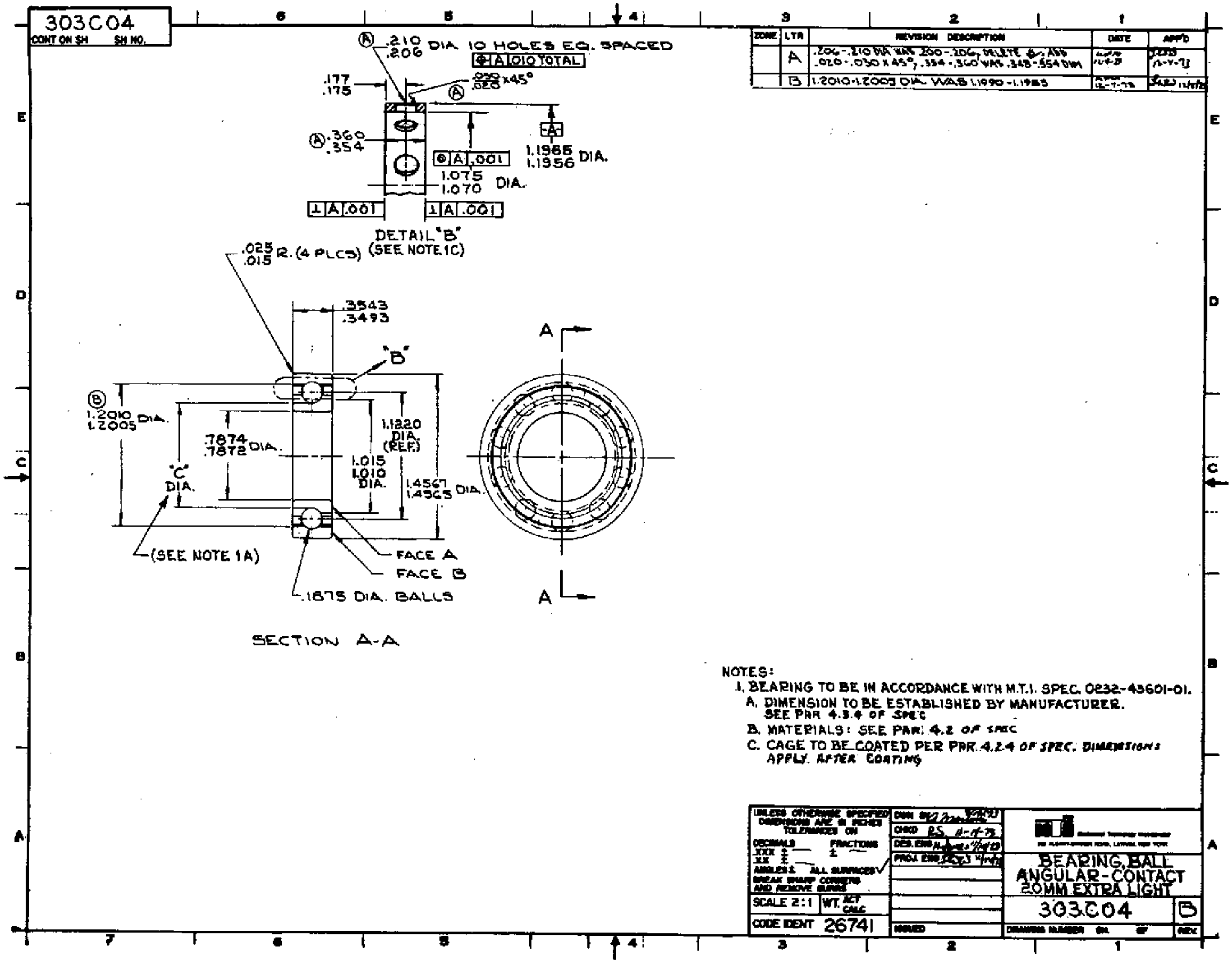

Fig. D-1 20-mm Extra-Light Series Ball Bearing Design

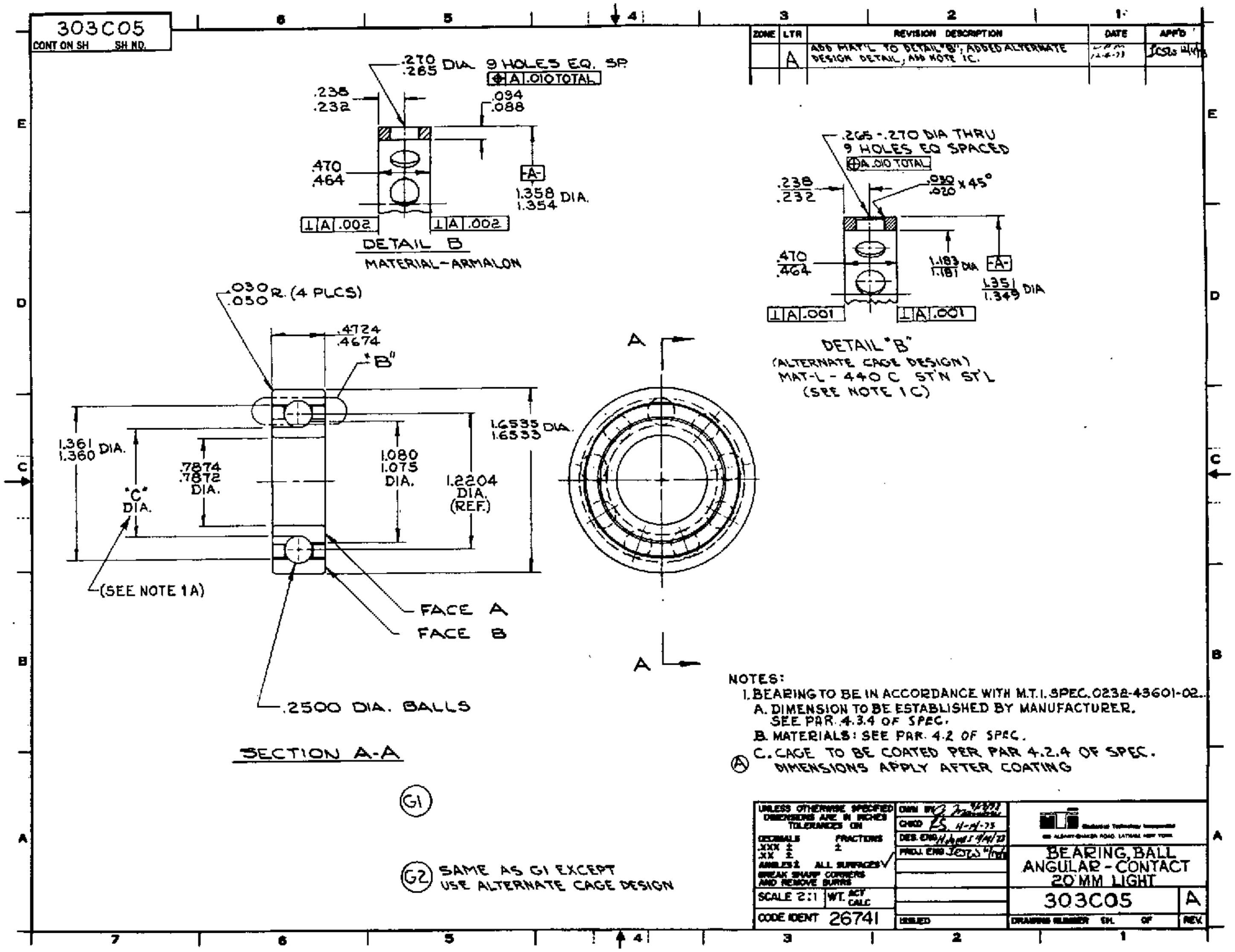

NOTES:

1. BEARING TO BE IN ACCORDANCE WITH M.T.I. SPEC. 0232-43601-02.
   - A. DIMENSION TO BE ESTABLISHED BY MANUFACTURER. SEE PAR. 4.3.4 OF SPEC.
   - B. MATERIALS: SEE PAR. 4.2 OF SPEC.
   - Ⓐ C. CAGE TO BE COATED PER PAR 4.2.4 OF SPEC. DIMENSIONS APPLY AFTER COATING

Fig. D-2 20-mm Light Series Ball Bearing Design

APPENDIX E

RADIAL PISTON LOADER
ANALYTICAL SUMMARY

For the purpose of analysis, the radial loader "piston" (Figure E-1) is considered to have three (3) forces acting on it.

- The spring force, F_s, which is directed towards the shaft, and is essentially constant for the very small displacements undergone by the piston.
- The pressure force, F_p, which acts downwards on the piston, due to the inlet pressure, P_1, acting on the difference in area between the piston O.D. and the loader pad I.D.
- The fluid-film force, F_f, which acts upwards on the piston, due to the pressure distribution between the inlet pressure, P_1, and the ambient pressure, P_2. For LH_2 this force is a complicated function of $(P_1 - P_2)$ and the film thickness,h. The complexity arises because of inertia effects and turbulence in the film. A computer program is available to calculate this force, (MTI Program - EMGROV).

The forces may be defined as follows:

$$F_s = 44.5 \text{ N } (10 \text{ lb}) \qquad (1)$$

$$F_p = \frac{\pi}{4} (D_1^2 - D_3^2) (P_1 - P_2) \qquad (2)$$

$$F_f = f \, ((P_1 - P_2), h, D_2, D_3) \qquad (3)$$

and to produce equilibrium of the piston:

$$F_f = F_s + F_p \qquad (4)$$

(Note that by using $(P_1 - P_2)$ throughout, the ambient pressure forces may be treated as zero).

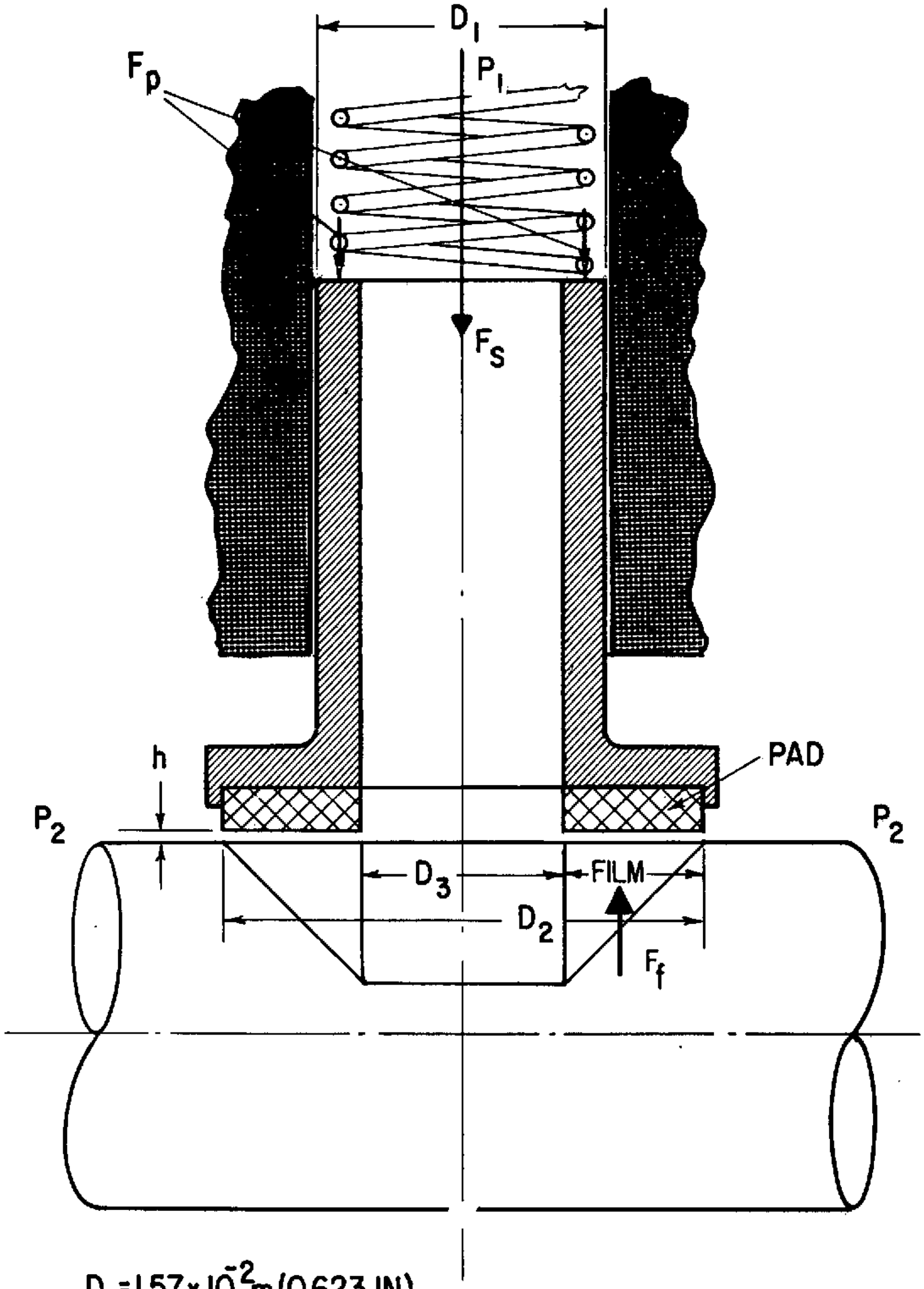

$D_1 = 1.57 \times 10^{-2}$ m (0.623 IN)
$D_2 = 2.16 \times 10^{-2}$ m (0.850 IN)
$D_3 = 1.52 \times 10^{-2}$ m (0.600 IN)

Fig. E-1 Radial Loader Schematic

Thus, for a given value of $(P_1 - P_2)$, we must find the equilibrium value of h, to satisfy equation [4].

The force on the shaft, F_r, is then:

$$F_r = F_f + \frac{\pi}{4} D_3^2 (P_1 - P_2) \tag{5}$$

and the flow, Q, is also calculated by the MTI computer program, (EMGROV).

Dimensions of the piston are:

$D_1 = 1.57 \times 10^{-2}$ m (0.623 in)

$D_2 = 2.16 \times 10^{-2}$ m (0.850 in)

$D_3 = 1.52 \times 10^{-2}$ m (0.600 in)

Figure E-2 illustrates the variation of film force with film thickness for four (4) different values of $\Delta P = (P_1 - P_2)$, and shows how the equilibrium values of film thickness are determined for a LH_2 loader supply.

Figure E-3 illustrates the variation of LH_2 flow through the film as a function of film thickness. The equilibrium film thickness values are ringed for each curve. The equilibrium flow rates extracted from Figure E-3 are listed together with their respective equilibrium film thicknesses and radial shaft loads in Table E-1.

The film thickness, flow, and shaft forces at equilibrium are plotted against supply pressure in Figures E-4 and E-5.

Important Points Are:

1. A reverse in slope of the film force vs. film thickness curves occurs at film thicknesses above 5.00×10^{-6} m (200×10^{-6} in). The positive slope region is not a possible operating region, since it is statically unstable. The piston will seek the lower film thickness equilibrium point.

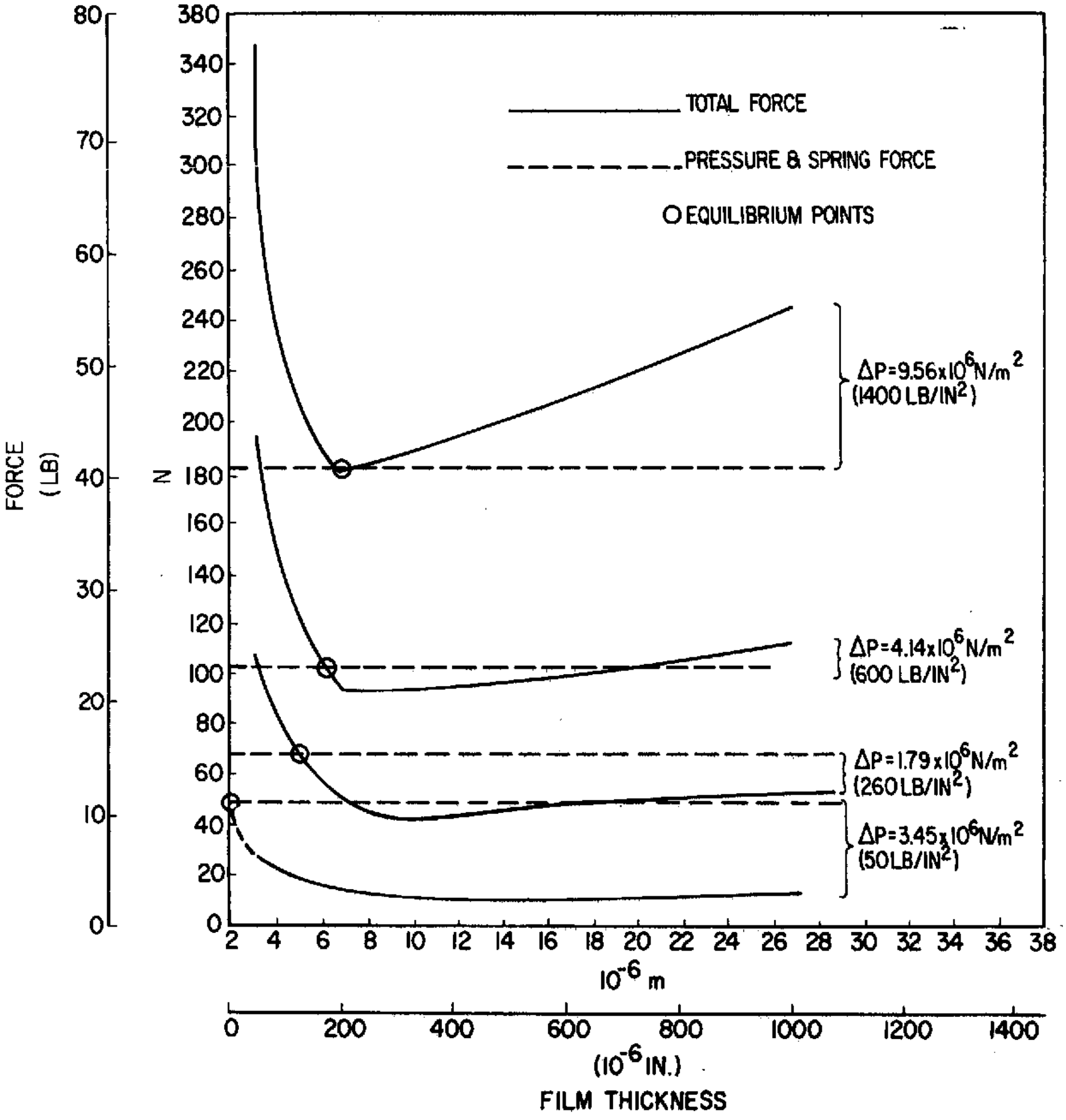

Fig. E-2 Film Force — Film Thickness Relationship — LH_2 Supply

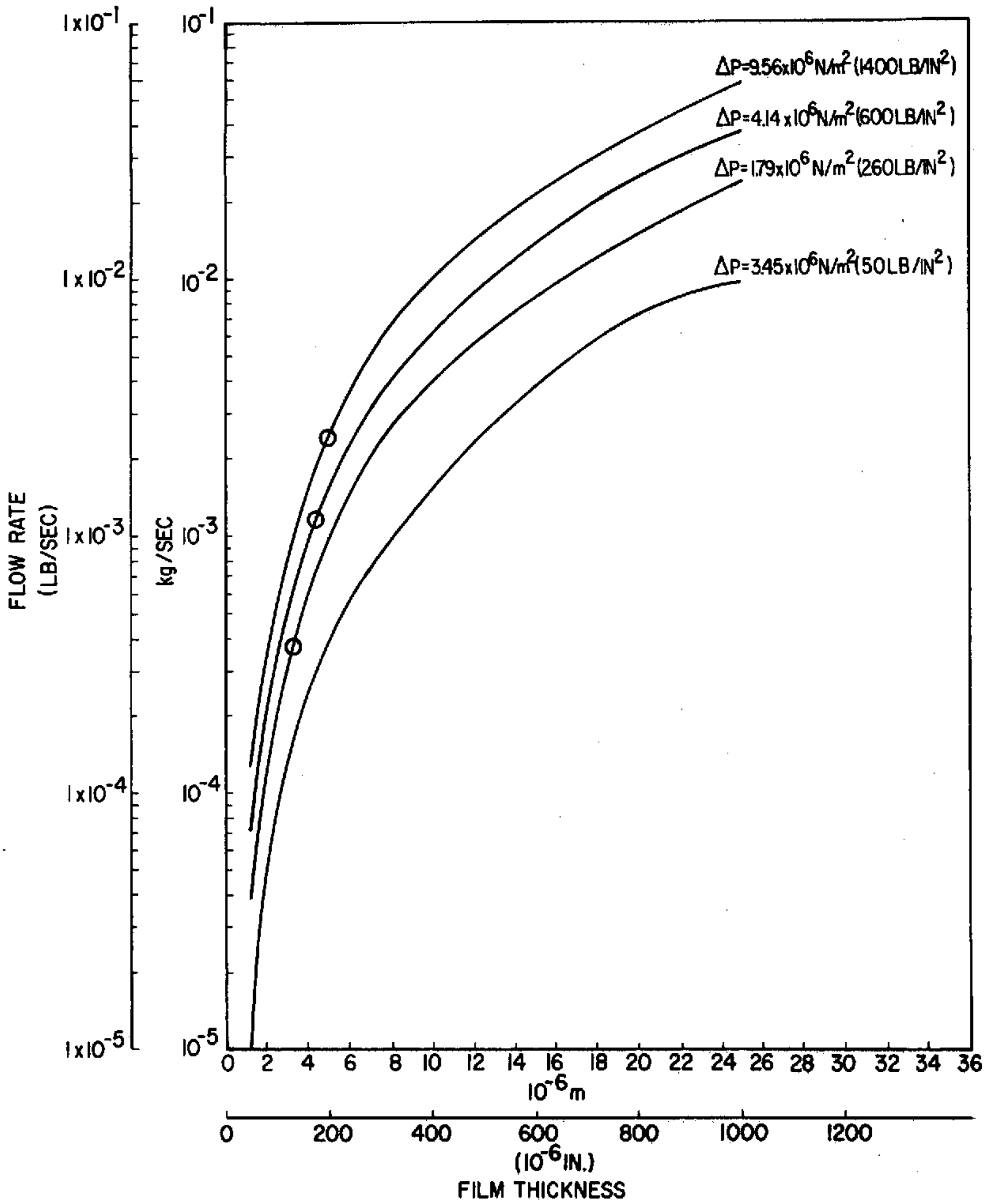

Fig. E-3 Flow Rate — Film Thickness Relationship — LH_2 Supply

TABLE E-1 LOADER PERFORMANCE VALUES
LH_2 SUPPLY

$(P_1 - P_2)$	Equilibrium Film		Equilibrium Flow		Shaft Force, F_r	
(ΔP)	m	(in)	Kg/sec	(lb/sec)	N	(lb)
1.80×10^6 N/m^2 (260 lb/in^2)	3.26×10^{-6}	(128×10^{-6})	1.64×10^{-4}	(3.6×10^{-4})	395	(89)
4.15×10^6 N/m^2 (600 lb/in^2)	4.45×10^{-6}	(175×10^{-6})	5.45×10^{-4}	(1.2×10^{-3})	859	(193)
9.67×10^6 N/m^2 (1400 lb/in^2)	4.84×10^{-6}	(190×10^{-6})	1.09×10^{-3}	(2.4×10^{-3})	1940	(437)
3.45×10^5 N/m^2 (50 lb/in^2)	2.54×10^{-7}	(10×10^{-6})	0	(0)	111	(25)

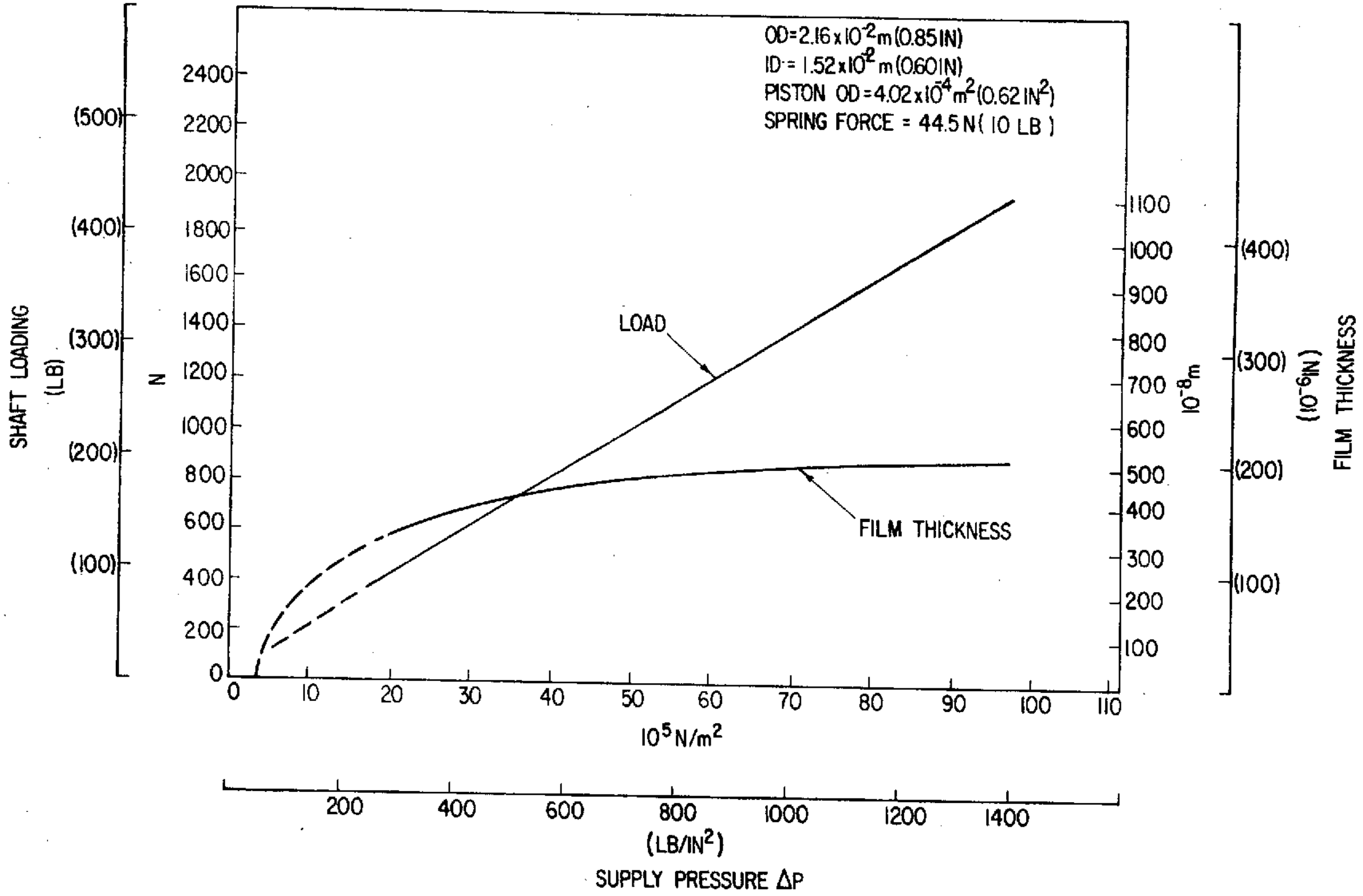

Fig. E-4 Radial Loader Shaft Load - Film Thickness Relationship LH_2 Supply

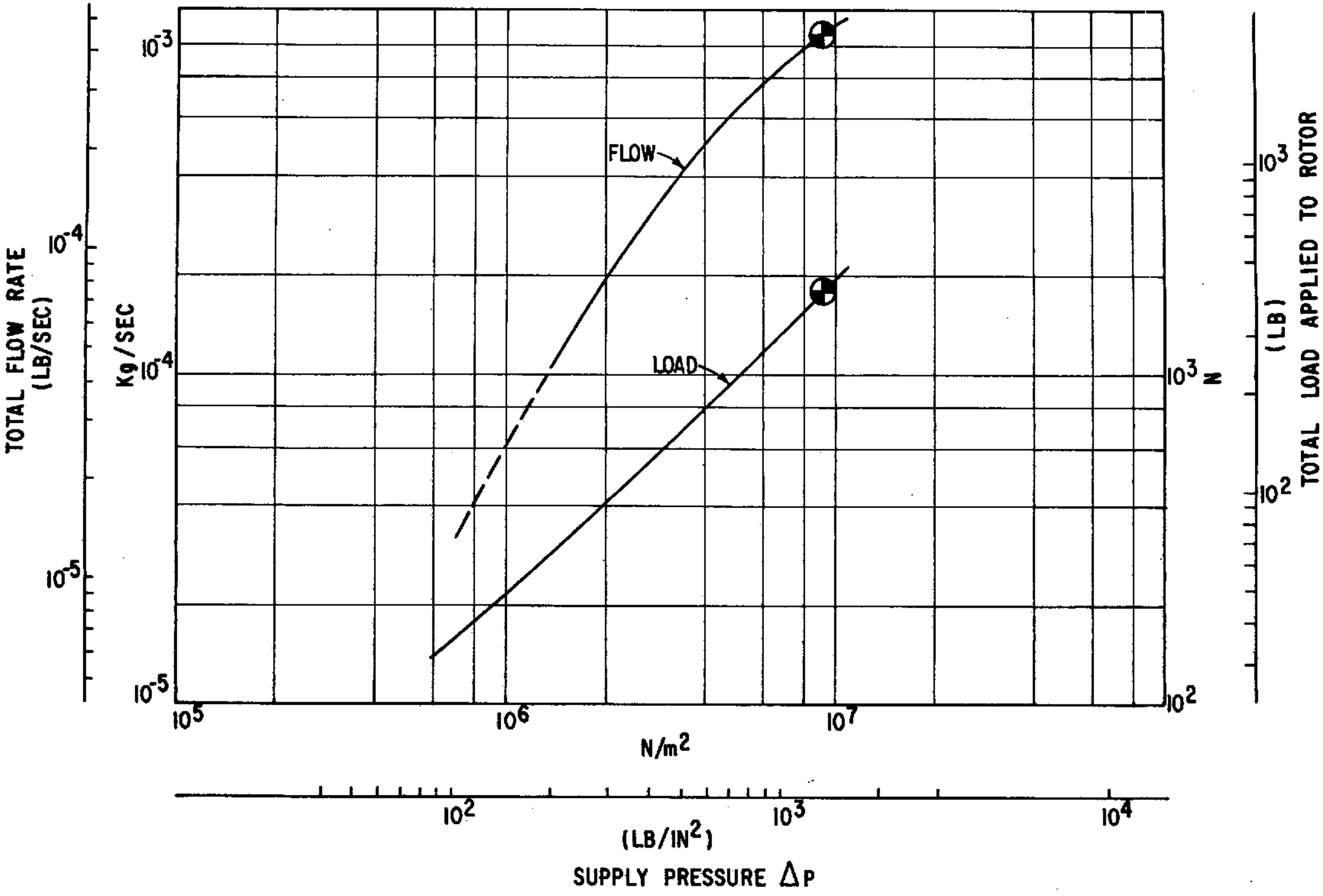

Fig. E-5 LH_2 Radial Loader Performance

2. There is little that can be done to shift the region of equilibrium film thickness under 5.00×10^{-6} m (200×10^{-6} in). This is really dictated by the very low viscosity of liquid hydrogen.
3. The flow through the film is, therefore, reasonably well determined. If more flow is needed for control purposes, the provision of a leakage path through the side of the piston offers one possible method of increasing the flow.
4. The equilibrium film thickness for a 3.45×10^5 N/m^2 (50 lb/in^2) ΔP is obviously unrealistic. This limits the loader at the low end of its shaft force range, to somewhere between 111 N (25 lb) and 396 N (89 lb).
5. Decreasing the spring force to 22 N (5 lb) would extend the operative range of the loader at the low end of the shaft force range. Decreasing the spring force would also introduce some uncertainty into how the piston loader would behave at high pressures. Above a certain limiting value of ΔP, the film force would always be larger than the (spring + pressure) force, whatever the film thickness, as predicted by analysis. Under these conditions the loader may work but its performance cannot be predicted.

The previously described LH_2 radial loader analysis can be modified somewhat in order to provide performance information for the loader when it is supplied with GH_2. The relationship between forces and pressures remains unchanged; the significant change occurs in the value of film force, F_f, and flow rate, Q, which are now affected by compressibility as well as inertia effects and turbulence in the film. A computation sequence similar to that followed for the LH_2 loader produces the flow rates, and film force at an equilibrium film thickness for several levels of loader ΔP.

The calculated values of film force, F_f, can now be combined with their related pressures in equation [5] to generate a new curve of radial load, F_r, as a function of supply pressure, P_1. Figure E-6 provides the relationship between the loader supply pressure and the resulting radial load and flow. Figure E-7 provides the loader's operating film thickness as a function of supply pressure.

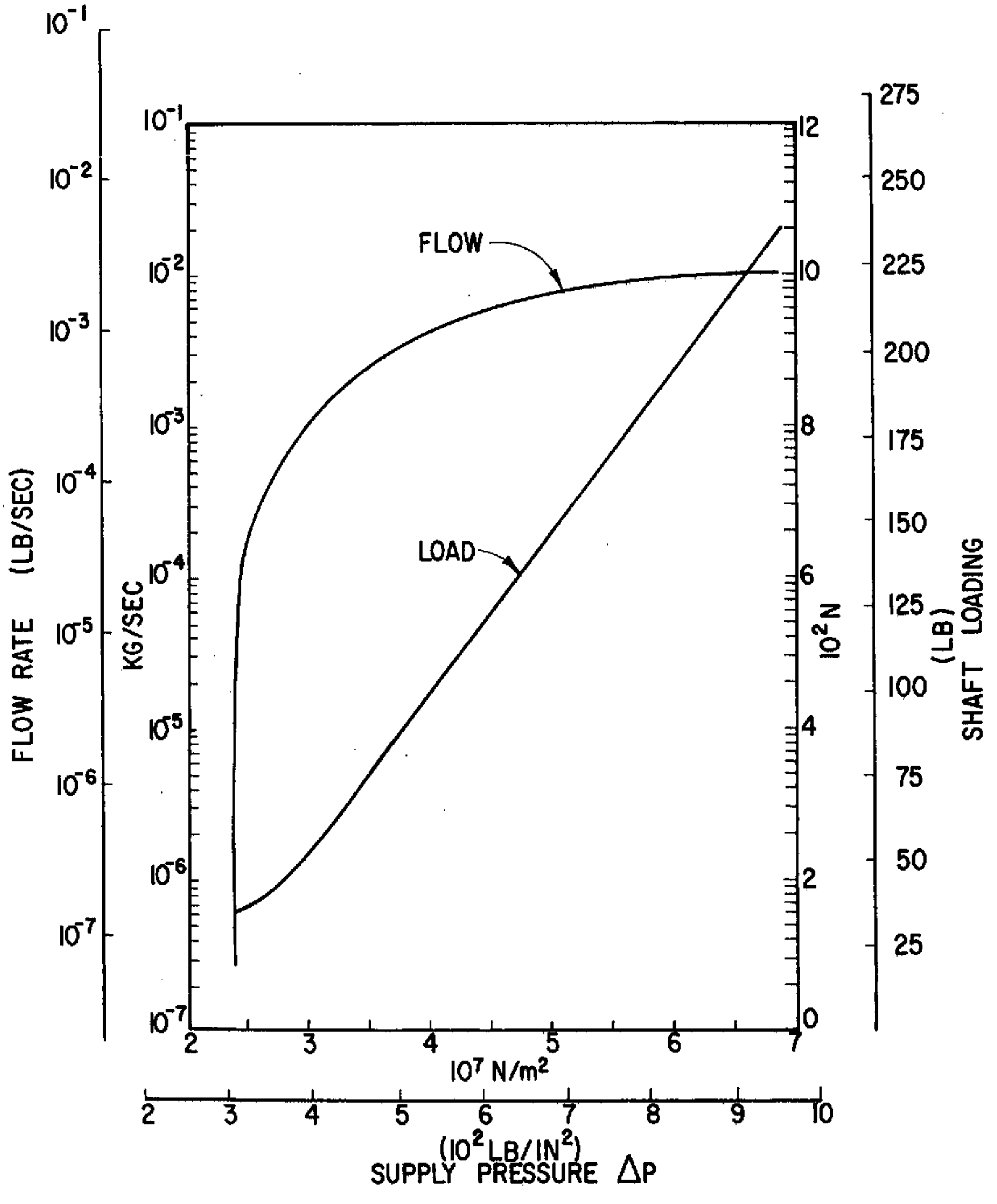

Fig. E-6 GH_2 Radial Loader Performance

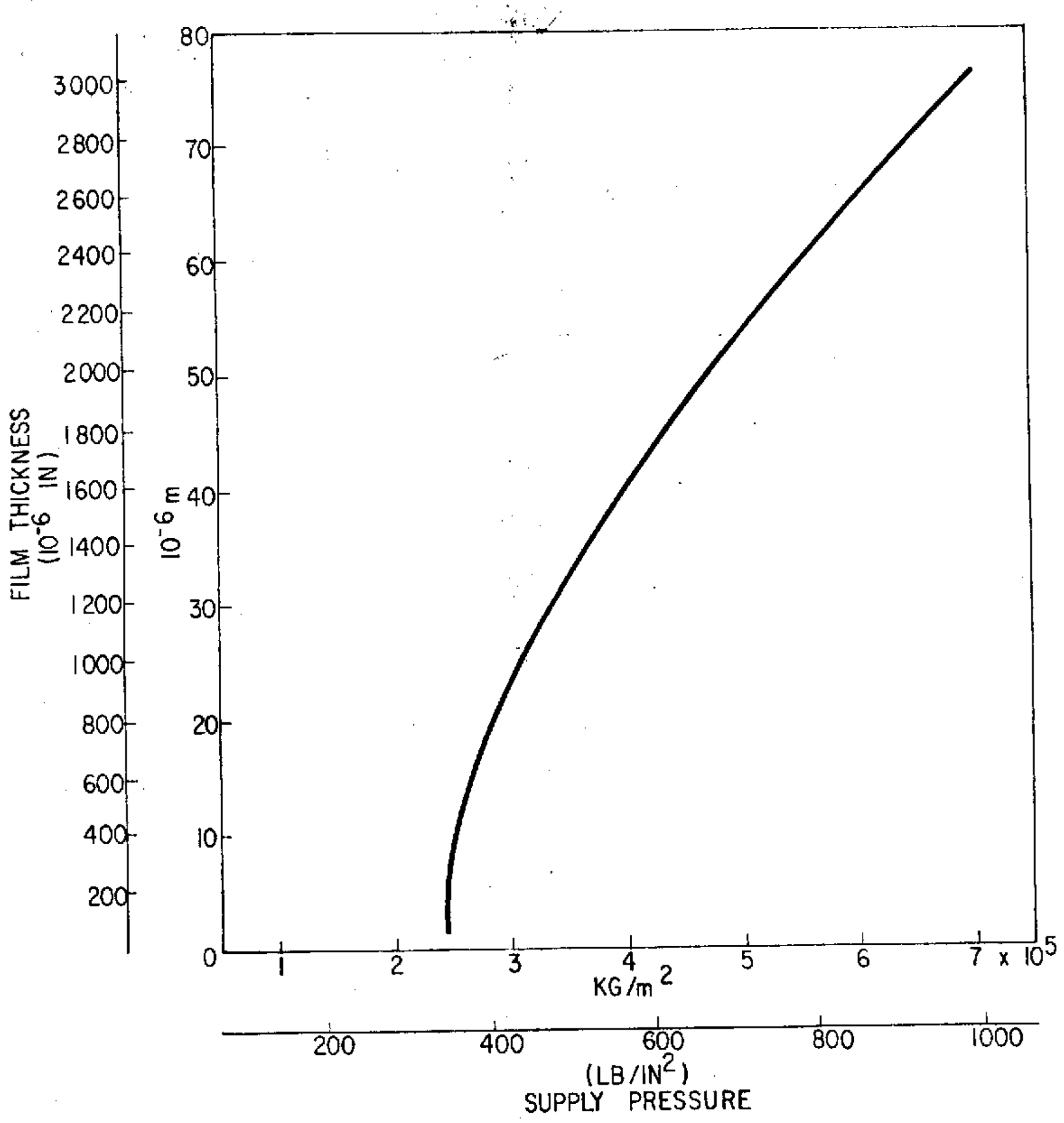

Fig. E-7 GH_2 Radial Loader Film Thickness - Supply Pressure Relationships

The load pressure relationship shown in Figure E-6 is linear, thereby permitting the extrapolation of the load curve up to the maximum required radial load of 2000 N (400 lbs).

APPENDIX F

COOLANT STREAM PRESSURE LOSSES

Pressure loss calculations were carried out to determine the pressure required to circulate LH_2 through the ball bearings and the hybrid bearing. Figure F-1 shows the pressure loss results for the coolant losses through the ball bearings.

Flow tubes in the hybrid bearing supply lines are sized to provide the following maximum losses:

• Turbine End Bearing	1.36×10^4 N/m^2 (2.0 lb/in^2)
• Free End Bearing	1.70×10^4 N/m^2 (2.5 lb/in^2)
• Thrust Bearing	2.04×10^3 N/m^2 (0.3 lb/in^2)

Pressure losses are calculated from housing exterior to upstream side of orifices.

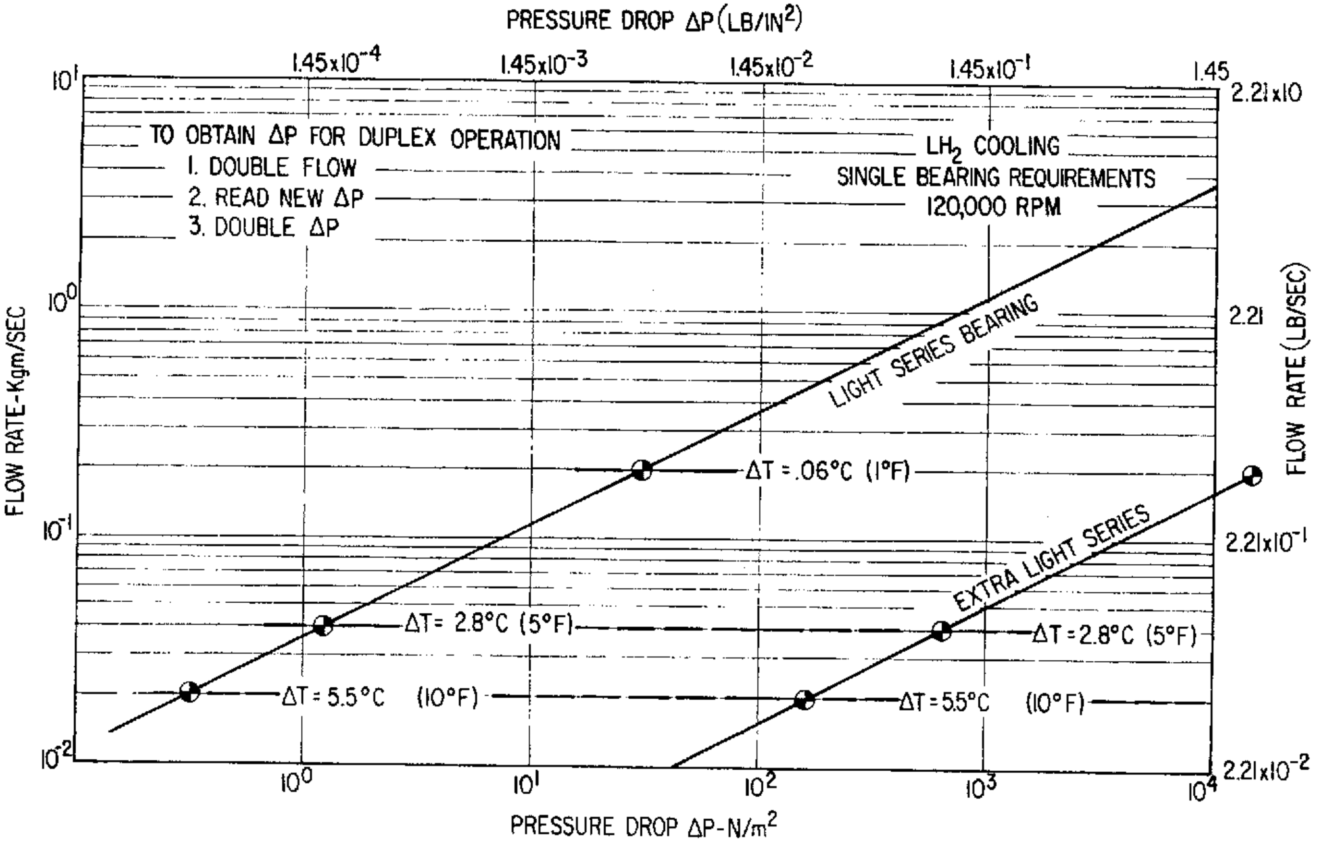

Fig. F-1 Coolant Flow Pressure Loss

APPENDIX G

EFFECTS OF HIGHER FILM COEFFICIENT AND SKIN TEMPERATURE ON TEST VEHICLE

A review of the thermal calculations for the LH_2 testers to determine the effects of a 75°C (167°F) skin temperature and a higher surface film coefficient on the temperature distribution within the tester.

For these calculations, only bulk thermal effects are assumed for the following conditions:

A. Temperatures

1. Ambient Temperature T_1 = 277°K (530°R)
2. Outer Surface (Initial) T_{21} = 19.4°K (67°R)
3. Outer Surface (Final) T_{22} = 75°K (167°R)
4. LH_2 (Input) T_s = 10°K (50°R)

B. Film Coefficients

1. Outer Surface (Initial) ψ_{11} = $.18 \frac{W}{m^2 {}^\circ K}$ (0.1 Btu/hr-ft^2-°R)
2. Outer Surface (Final) ψ_{12} = $1.8 \frac{W}{m^2 {}^\circ K}$ (1.0 Btu/hr-ft^2-°R)
3. Interface LH_2 to Metal $\psi_{21} = \psi_{22}$ = $3500 \frac{W}{m^2 {}^\circ K}$ (2000 Btu/hr-ft^2-°R)

C. Material Properties

1. Tester Housing Conductivity k = $10.4 \frac{W}{m\text{-}{}^\circ K}$ (6.5 Btu/hr-ft-°R)
2. LH_2 Specific Heat C_p = $9.21 \times 10^3 \frac{J}{{}^\circ K}$(2.2 Btu/lb-°R)
3. LH_2 Flow Rate ΣQ = 0.18 Kg/sec (0.40 lb/sec)

D. Geometry

1. Tester OD D_1 = 0.18 m (5.0 in)

2. Tester ID D_2 = 0.057 m (2.25 in)

3. Tester Length L = 0.20 m (7.75 in)

A simplified thermal model of the LH_2 tester can be represented by the following nodal diagram

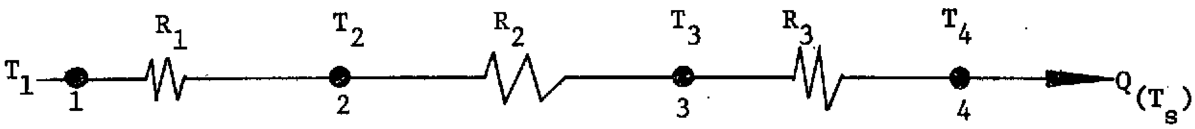

where

$R_1 = \psi_1 A_1$ = Thermal resistance of outer diameter air film (Air to Metal)

$R_2 = \dfrac{k\ A_1}{L}$ = Thermal resistance of tester housing material

$R_3 = \psi_2 A_2$ = Thermal resistance of inner film (metal to LH_2)

T_3 = Inner surface metal temperature

T_4 = LH_2 stream temperature

For calculation purposes

$A_1 = \pi D_1\ L = 7.9 \times 10^{-2}\ m^2\ (0.85\ ft^2)$

$A_2 = \pi D_2\ L = 3.53 \times 10^{-2}\ m^2\ (0.38\ ft^2)$

and

$R_{11} = \psi_{11} A_1 =$ 0.045 W/°K (0.085 Btu/hr-°R)

$R_{12} = \psi_{12} A_1 =$ 0.45 W/°K (0.850 Btu/hr-°R)

$$R_2 = \frac{k\ A_1}{L} = 25.4\ \mathrm{W/°K}\quad (48\ \mathrm{Btu/hr\text{-}°R})$$

$$R_3 = \psi_3 A_2 = 403\ \mathrm{W/°K}\quad (760\ \mathrm{Btu/hr\text{-}°R})$$

The nodal equations are solved by the summation of heat flows at each nodal point so that

$$\Sigma Z_2 = 0 = R_1(T_2 - T_1) + R_2\ (T_2 - T_3)$$

$$\Sigma Z_3 = 0 = R_2(T_3 - T_2) + R_3\ (T_3 - T_4)$$

$$\Sigma Z_4 = 0 = R_4(T_4 - T_3) + \Sigma Qc_p\ (T_4 - T_s)$$

which reduces to

$$\begin{bmatrix} R_1 + R_2 & -R_2 & 0 \\ -R_2 & R_2 + R_3 & -R_3 \\ 0 & -R_3 & R_3 + \Sigma QC_p \end{bmatrix} \begin{bmatrix} T_2 \\ T_3 \\ T_4 \end{bmatrix} = \begin{bmatrix} R_1T_1 \\ 0 \\ \Sigma QC_pT_s \end{bmatrix}$$

The above determinent, when solved for T_2, T_3, and T_4, yields

$$T_2 = \frac{(R_1T_1)(R_2{+}R_3)(R_3{+}\Sigma Qc_p) + R_2R_3\ \Sigma Qc_pT_s - R_3^2\ (R_1T_1)}{[(R_1{+}R_2)(R_2{+}R_3)(R_3{+}R_4)(R_3{+}\Sigma Qc_p)] - [R_3^2\ (R_1{+}R_2) + R_2^2\ (R_3{+}\Sigma Qc_p)]}$$

$$T_3 = \frac{(R_3)(\Sigma Qc_pT_s)(R_1{+}R_2) + R_2(R_1T_1)(R_3{+}\Sigma Qc_p)}{[\ (R_1{+}R_2)(R_2{+}R_3)(R_3{+}R_4)(R_3{+}\Sigma Qc_p)] - [R_3^2\ (R_1{+}R_2) + R_2^2\ (R_3{+}\Sigma Qc_p)]}$$

$$T_4 = \frac{(R_1{+}R_2)(R_2{+}R_3)(\Sigma Qc_pT_s)(R_1T_1)(R_2)(R_3) - R_2^2\ \Sigma Qc_pT_s}{[(R_1{+}R_2)(R_2{+}R_3)(R_3{+}R_4)(R_3{+}\Sigma Qc_p)] - [R_3^2\ (R_1{+}R_2) + R_2^2\ (R_3{+}\Sigma Qc_p)]}$$

For the initial (ψ_{11}) parameters listed previously (T_2 is a dependent not an independent variable for these calculations). The nodal temperatures are:

T_2 = 10.5°K (50.90 °R) (Outer Diameter)

T_3 = 10.05°K (50.03°R) (Inner Diameter)

T_4 = 10.01°K (50.01°R) (LH_2 Discharge)

A second set of temperatures, based on an outer film coefficient of $h_{12} = 1.8 \frac{W}{m^2 °K}$ (1.0 Btu/hr-ft^2-°R), is

T_2 = 15.0°K (59.00°R) (Outer Diameter)

T_3 = 10.35°K (50.65°R) (Inner Diameter)

T_4 = 10.05°K (50.12°R) (LH_2 Discharge)

The resulting temperatures, both for the initial and final coefficients are not quantitatively accurate but do, qualitatively, demonstrate the very small effects on temperature that result from an order of magnitude change in external film coefficient.

An alternate method of evaluating the effect of skin temperature and external film coefficient on the LH_2 final temperature is to calculate the net increase in heat input from

$$\Sigma Z = Z_2 - Z_1 = \psi_{12} A_1 (T_1 - T_{22}) - \psi_{11} A_1 (T_1 - T_{21})$$

for the previously listed parameters

$$\Sigma Z = (1.8)(7.9\text{x}10^{-2})(277-75)-(.18)(7.9\text{x}10^{-2})(277-19.4)$$
$$[(1.0)(.85)(530-167) - 0.1\ (.85)(530-67)]$$

or

$$\Sigma Z = 78.7 \text{ Watts } (268 \text{ Btu/hr})$$

If it is assumed that this increase of energy input is totally removed by the LH_2 coolant and does not cause an increase in tester metal temperature then from

$$\Sigma Z = \Sigma Q \; C_p \; \Delta T$$

$$78.7 = (.18)(9.21 \times 10^{-3}) \; (\Delta T)$$

or

$$\Delta T = 0.048°C \; (0.087°F)$$

It is unlikely that the total added energy input will be conducted through the tester's metal housing and as a result, the temperatures within the tester will adjust upward. Under any circumstances, however, no adverse effects from adjustment in either film coefficient or skin temperature should be expected.

APPENDIX H

HYBRID BEARING TESTER THRUST BALANCE

The objective of this calculation is to size the diameter of the turbine tip seal to assure a positive thrust load at any rotor speed. Figure H-1 illustrates the geometry and pressure force locations.

P_1 = Turbine Discharge Pressure = 1.66×10^{-6} N/m^2 (240 lb/in^2)
P_2 = Average Turbine Blade Pressure = $(P_5 + P_4)\frac{1}{2}$
P_3 = Internal Tester Pressure = 1.72×10^{-6} N/m^2 (250 lb/in^2)
P_4 = Turbine Wheel Back Pressure = 1.66×10^{-6} N/m^2 (240 lb/in^2)
$P_5{}^*$ = Turbine Inlet Pressure = 1.80×10^{-6} N/m^2 (261 lb/in^2)

The net pressure unbalance acting on the turbine wheel must be directed so that the thrust bearing is always loaded. Two extreme load conditions exist.

1. During acceleration when $P_5 = 1.80 \times 10^{-6}$ N/m^2 (261 lb/in^2)
2. Zero speed where $P_2 = P_5 = 1.66 \times 10^{-6}$ N/m^2 (240 lb/in^2)

A summation of loads yields

$$\frac{\pi}{4}\left[P_1 D_3^2 + P_2(D_4^2 - D_3^2) - P_5(D_4^2 - D_1^2) - P_4(D_1^2 - D_2^2) - P_3 D_2^2\right] + F_T = 0 \qquad [1]$$

When solved for D, the above equation becomes

$$D_1 = \left[\frac{-\frac{4}{\pi}Ft - \{D_3^2(P_1 - P_2) + D_4^2(P_2 - P_5) + D_2^2(P_4 - P_2)\}}{(P_5 - P_4)}\right]^{1/2} \qquad [2]$$

$^*P_5$ is the inlet pressure at the turbine wheel tip and is lower than the turbine inlet pressure by the pressure loss through the nozzle box. Acceleration, not sustained pressure, is used for the calculations.

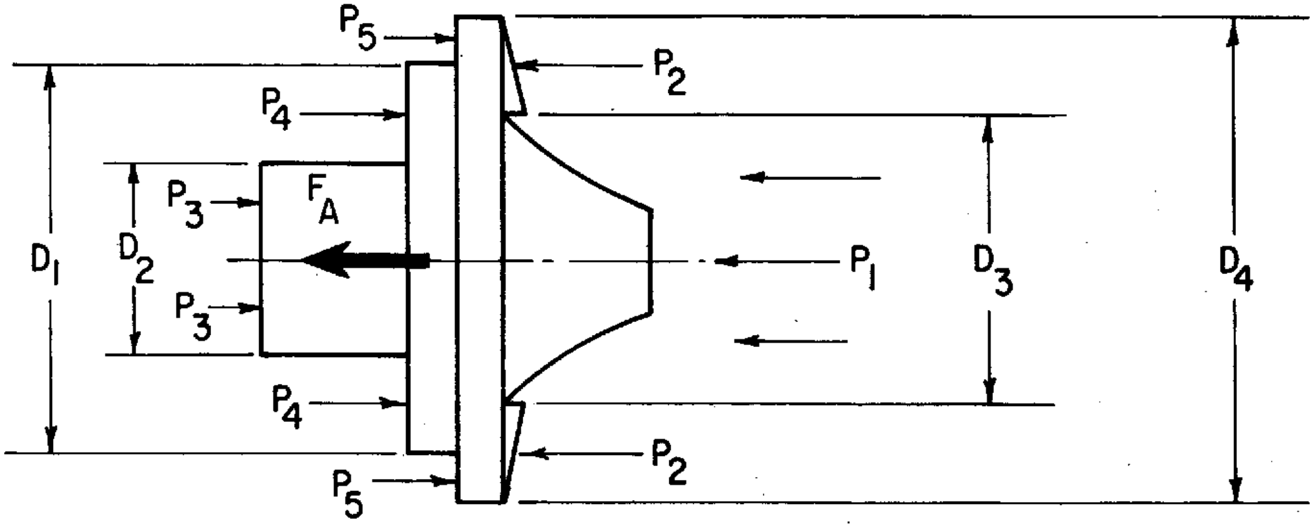

D_1 = TURBINE SEAL DIAMETER

D_2 = SHAFT SEAL DIAMETER = 2.38×10^{-2} m (0.936 IN.)

D_3 = TURBINE BLADE I.D. = 4.13×10^{-2} m (1.624 IN.)

D_4 = TURBINE TIP DIAMETER = 5.56×10^{-2} m (2.216 IN.)

Fig. H-1 Turbine Wheel Geometry and Pressure Locations

For the conditions listed above D_1 = .0482 m (1.893 in) and at this seal diameter, other conditions of turbine supply yield the following forces.

P_1		F_T	
N/m^2	(lb/in^2)	N	(lb)
1.93×10^{-6}	(280)	57.4	(12.9)
2.00×10^{-6}	(290)	64.0	(14.4)
2.07×10^{-6}	(300)	70.7	(15.9)

Figure H-2 presents a curve of thrust load as a function of turbine blade inlet pressure. At the zero (0) speed condition $P_2 = 1.66 \times 10^{-6}\ N/m^2$ $(240\ lb/in^2)$ yields a thrust load of F_T = 30.9 N (6.9 lb).

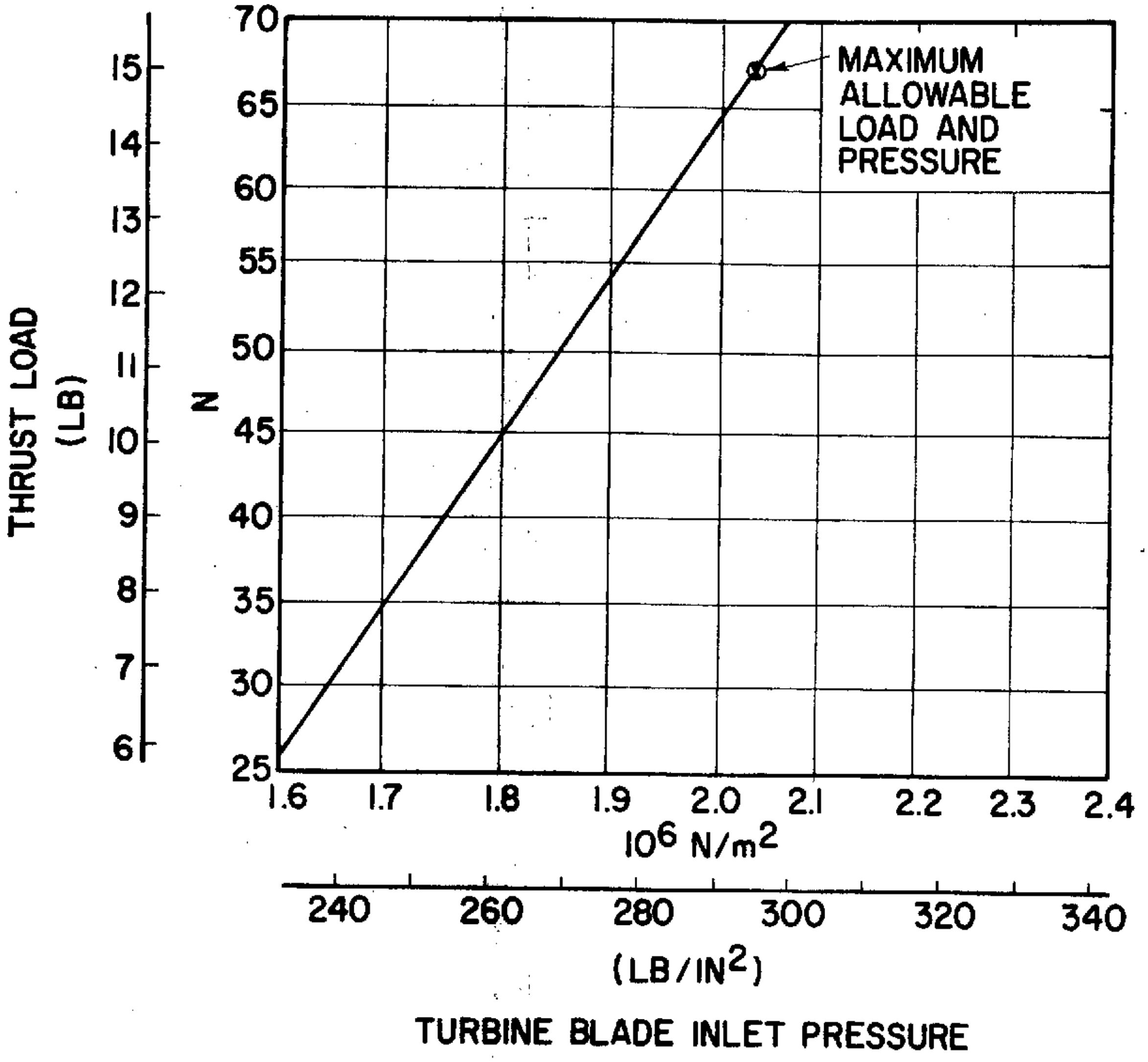

Fig. H-2 Thrust Balance — All Bearing Testers

APPENDIX I

SEAL LEAKAGE CALCULATIONS

Figures I-1 through I-3 present the flow curves calculated for the several leakage paths indicated in the main text.

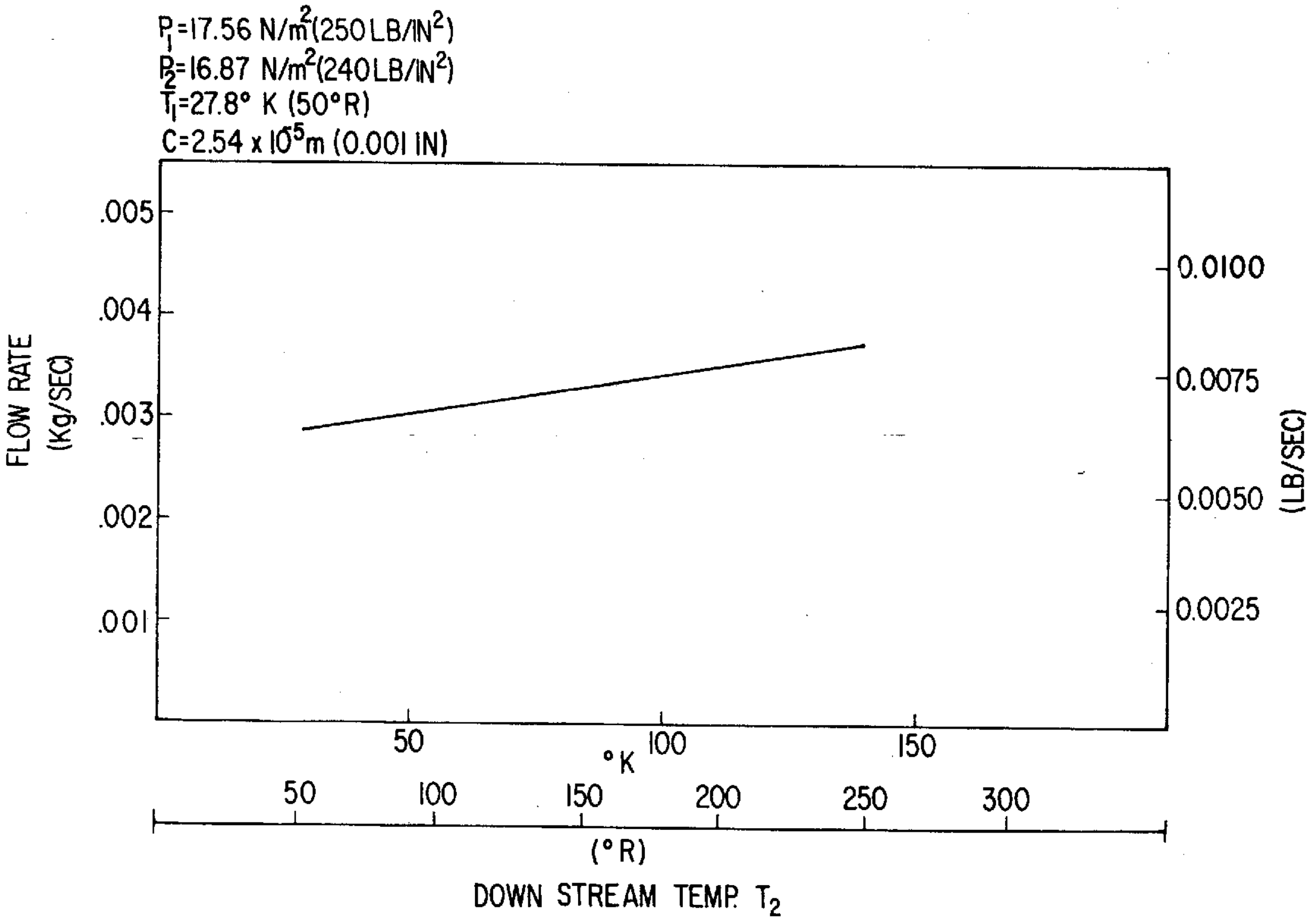

Fig. I-1 Shaft Seal Leakage

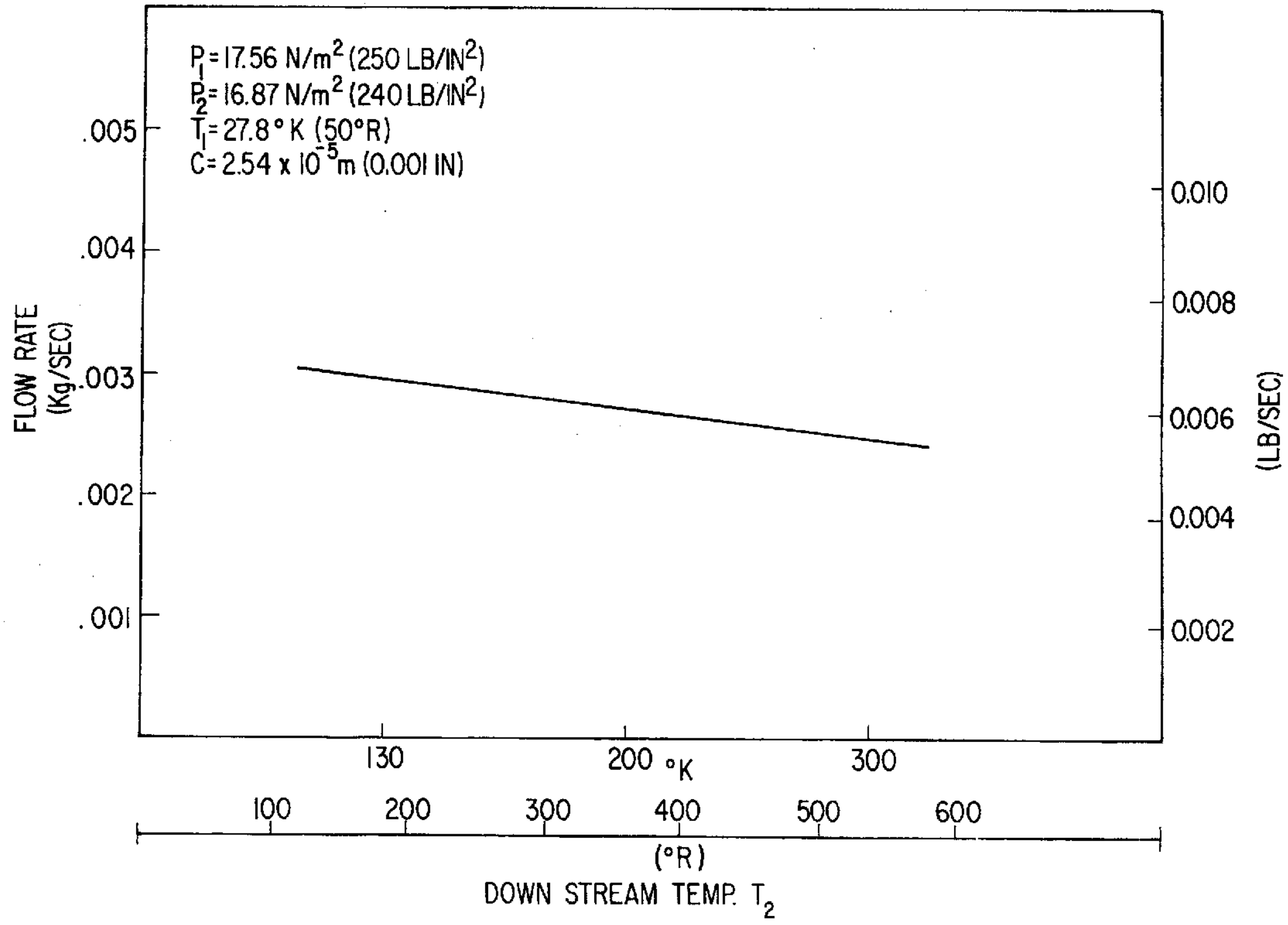

Fig. I-2 Heat Dam Leakage

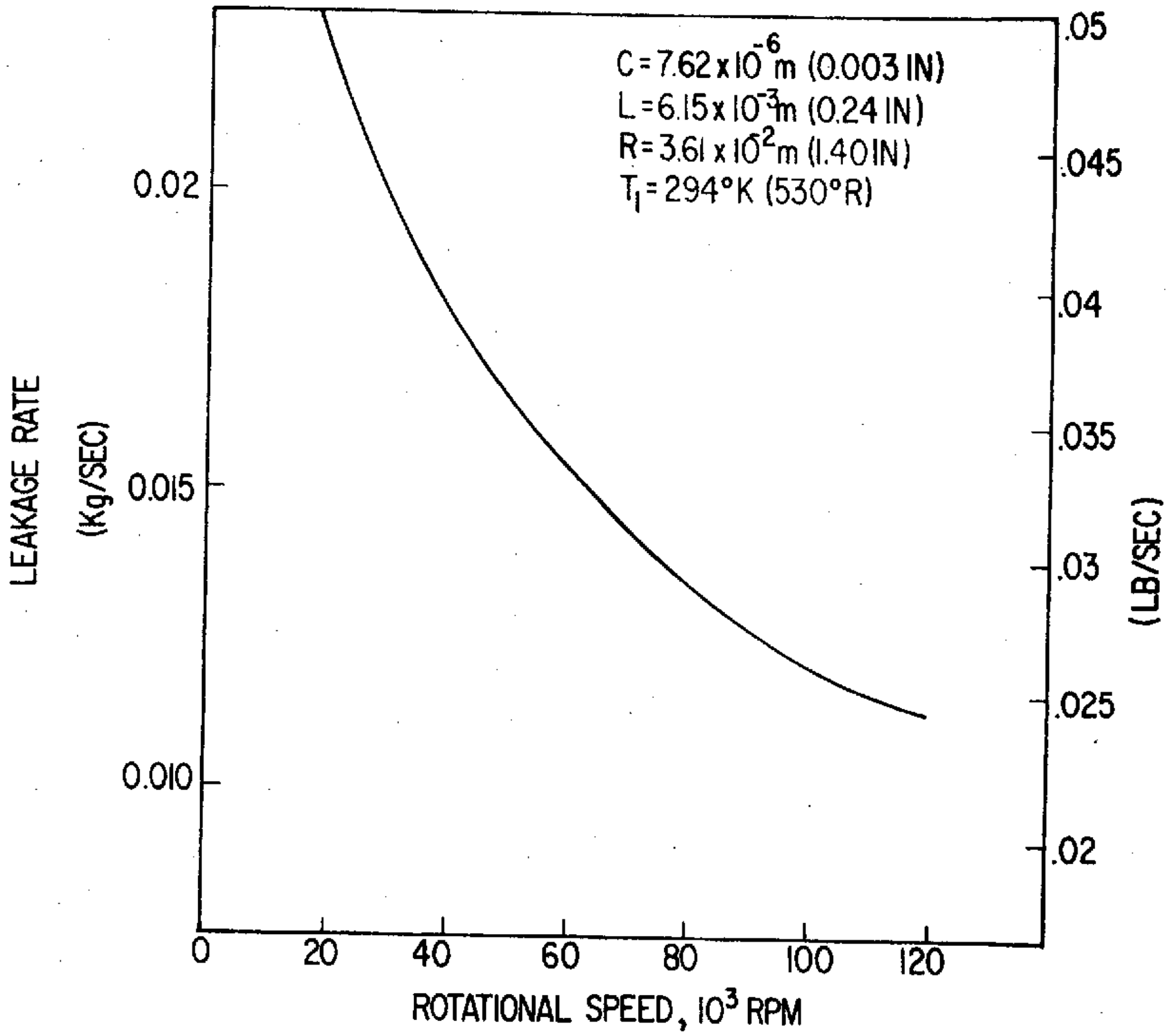

Fig. I-3 Labyrinth Seal Leakage

DISTRIBUTION LIST FOR FINAL REPORT

NAS3-17773 MTI CR-134615

National Aeronautics & Space Administration
Lewis Research Center
21000 Brookpark Road
Cleveland, Ohio 44135

Attention:

Contracting Officer, MS 500-313
E. A. Bourke, MS 500-205 (5)
Technical Utilization Office, MS 3-16
Technical Report Control Office, MS 5-5
AFSC Liaison Office, MS 501-3 (2)
Library, MS 60-3 (2)
Office of Reliability & Quality Assurance, MS 500-211
N. T. Musial, MS 500-113
C. J. Morgan, Project Manager, MS 500-203 (19)

Director, Manned Space Technology, RS
Office of Aeronautics & Space Technology
NASA Headquarters
Washington, D. C. 20546

Director, Space Prop. and Power, RP
Office of Aeronautics & Space Technology
NASA Headquarters
Washington, D. C. 20546

Director, Launch Vehicles & Propulsion, SV
Office of Space Science
NASA Headquarters
Washington, D. C. 20546

Director, Materials & Structures Div., RW
Office of Aeronautics & Space Technology
NASA Headquarters
Washington, D. C. 20546

Director, Advanced Missions, MT
Office of Manned Space Flight
NASA Headquarters
Washington, D. C. 20546

Director, Physics & Astronomy Programs, SG
Office of Space Science
NASA Headquarters
Washington, D. C. 20546

Director, Planetary Programs, SL
Office of Space Science
NASA Headquarters
Washington, D. C. 20546

Office of Aeronautics & Space
Technology, R
NASA Headquarters
Washington, D. C. 20546

NASA
Ames Research Center
Moffett Field, California 94035
Attention: Library

NASA
Flight Research Center Library
P.O. Box 273
Edwards, California 93523

Dir., Technology Utilization Div.
Office of Technology Utilization
NASA Headquarters
Washington, D. C. 20546

Office of the Director of Defense
Research & Engineering
Washington, D. C. 20301
Attn: Office of Asst. Dir.
(Chem. Technology)

NASA Scientific & Technical
Information Facility
P. O. Box 33
College Park, Maryland 20740
Attn: NASA Representative (10)

NASA
Goddard Space Flight Center
Greenbelt, Maryland 20771
Attn: Library

National Aeronautics & Space Administration
John F. Kennedy Space Center
Cocoa Beach, Florida 32931
Attn: Library

National Aeronautics & Space Administration
Langley Research Center
Langley Station
Hampton, Virginia 23365
Attn: Library

National Aeronautics & Space Administration
Manned Spacecraft Center
Houston, Texas 77001
Attn: Library

National Aeronautics & Space Administration
George C. Marshall Space Flight Center
Huntsville, Alabama 35912
Attn: Library

Jet Propulsion Laboratory
4800 Oak Grove Drive
Pasadena, California 91103
Attn: Library

Defense Documentation Center
Cameron Station
Building 5
5010 Duke Street
Alexandria, Virginia 22314
Attn: TISIA

Air Force FTC (FTAT-2)
Edwards Air Force Base, California 93523
Attn: Library

Air Force Office of Scientific Research
Washington, D.C. 20333
Attn: Library

Advanced Research Projects Agency
Washington, D.C. 20525
Attn: Library

Aeronautical Systems Division
Air Force Systems Command
Wright-Patterson Air Force Base,
Dayton, Ohio
Attn: Library

Air Force Missile Test Center
Patrick Air Force Base, Florida
Attn: Library

Air Force Systems Command
Andrews Air Force Base
Washington, D.C. 20332
Attn: Library

Air Force Rocket Propulsion Laboratory (RPR)
Edwards, California 93523
Attn: Library

Space & Missile Systems Organization
Air Force Unit Post Office
Los Angeles, California 90045
Attn: Technical Data Center

Office of Research Analyses (OAR)
Holloman Air Force Base, New Mexico 88330
Attn: Library
RRRD

U. S. Air Force
Washington, D.C.
Attn: Library

Commanding Officer
U. S. Army Research Office (Durham)
Box CM, Duke Station
Durham, North Carolina 27706
Attn: Library

U. S. Army Missile Command
Redstone Scientific Information Center
Redstone Arsenal, Alabama 35808
Attn: Document Section

Bureau of Naval Weapons
Department of the Navy
Washington, D.C.
Attn: Library

Commander
U. S. Naval Missile Center
Point Mugu, California 93041
Attn: Technical Library

Commander
U. S. Naval Weapons Center
China Lake, California 93557
Attn: Library

Commanding Officer
Naval Research Branch Office
1030 E. Green Street
Pasadena, California 91101
Attn: Library

Director (Code 6180)
U. S. Naval Research Laboratory
Washington, D.C. 20390
Attn: Library

Picatinny Arsenal
Dover, New Jersey 07801
Attn: Library

Air Force Aero Propulsion Laboratory
Research & Technology Division
Air Force Systems Command
United States Air Force
Wright-Patterson AFB, Ohio 45433
Attn: APRP (Library)

Space Division
Aerojet-General Corporation
9200 East Flair Drive
El Monte, California 91734
Attn: Library

Aerojet Liquid Rocket Company
P. O. Box 15847
Sacramento, California 95813
Attn: Technical Library 2484-2015A

Aeronutronic Division of Philco Ford Corp.
Ford Road
Newport Beach, California 92663
Attn: Technical Information Department

Aerospace Corporation
2400 E. El Segundo Blvd.
Los Angeles, California 90045
Attn: Library-Documents

Astropower Laboratory
McDonnell-Douglas Aircraft Company
2121 Paularino
Newport Beach, California 92163
Attn: Library

Battelle Memorial Institute
505 King Avenue
Columbus, Ohio 43201
Attn: Report Library, Room 6A

Bell Aerosystems, Inc.
Box 1
Buffalo, New York 14240
Attn: Library

Boeing Company
Space Division
P.O. Box 868
Seattle, Washington 98124
Attn: Library

Chemical Propulsion Information Agency
Applied Physics Laboratory
8621 Georgia Avenue
Silver Spring, Maryland 20910

Chrysler Corporation
Space Division
P.O. Box 29200
New Orleans, Louisiana 70129
Attn: Librarian

General Dynamics/Convair
P. O. Box 1128
San Diego, California 92112
Attn: Library

Missiles and Space Systems Center
General Electric Company
Valley Forge Space Technology Center
P. O. Box 8555
Philadelphia, Pa. 19101
Attn: Library

General Electric Company
Flight Propulsion Lab. Department
Cincinnati, Ohio
Attn: Library

Grumman Aircraft Engineering Corporation
Bethpage, Long Island, New York
Attn: Library

Ling-Temco-Vought Corporation
P. O. Box 5907
Dallas, Texas 75222
Attn: Library

Lockheed Propulsion Company
P. O. Box 111
Redlands, California 92374
Attn: Library, Thackwell

Marquardt Corporation
16555 Saticoy Street
Box 2013 - South Annex
Van Nuys, California 91409

Denver Division
Martin-Marietta Corporation
P. O. Box 179
Denver, Colorado 80201
Attn: Library

Rocketdyne Division
North American Rockwell Inc.
6633 Canoga Avenue
Canoga Park, California 91304
Attn: Library, Department 596-306

Space & Information Systems Division
North American Rockwell
12214 Lakewood Blvd.
Downey, California
Attn: Library

Western Division
McDonnell Douglas Astronautics
5301 Bolsa Ave
Huntington Beach, California 92647
Attention: Library

United Aircraft Corporation
Pratt & Whitney Division
Florida Research & Development Center
P. O. Box 2691
West Palm Beach, Florida 33402
Attn: Library